ACTIVE VIBRATION CONTROL OF A FLEXIBLE BASE MANIPULATOR

A Dissertation Presented to The Academic Faculty

By

Lynnane E. George

In Partial Fulfillment
Of the Requirements for the Degree
Doctor of Philosophy in Mechanical Engineering

Georgia Institute of Technology July 2002

Copyright © 2002 by Lynnane Ellis George

Active Vibration Control of a Flexible Base Manipulator

| Approved: | |
|--------------------------|--|
| Dr. Wayne Book, Chairman | |
| Dr. Anthony Calise | |
| Dr. Al Ferri | |
| Dr. William Singhose | |
| Dr. David Taylor | |
| Date Approved: | |

DEDICATION

To my grandparents:

Iva Frances Adamson

Dolzey Paul Borel

ACKNOWLEDGEMENTS

Intellectual and Technical Support

First, I would like to thank my advisor, Dr. Wayne Book, for the advice and guidance over the years working on this project. In addition, I would like to thank my committee members for suggestions, advice, and guidance along the way. The Intelligent Machine Dynamics Lab group also provided me many opportunities to present my work and get feedback on various aspects of this project. In particular, I would like to thank my long-term office mates, Davin Swanson, L.J. Tognetti, and Saghir Munir, for the many hours of discussion, advice, and assistance.

Personal Support

My husband, Tom George, has always been there and supportive throughout our years of marriage. In addition, I would like to thank my parents Herschel and Joyce Ellis, for their support in many ways over the years.

Financial Support

Partial funding for this work was provided by the Air Force Institute of Technology U.S.

Air Force Academy Faculty Preparation Program and the HUSCO/Ramirez Endowed

Chair for Fluid Power and Motion Control

Disclaimer

The views expressed in this document are those of the author and do not reflect the official policy or position of the United States Air Force, Department of Defense, or U.S.

Government

TABLE OF CONTENTS

| DEDICATION | iii |
|---|----------|
| ACKNOWLEDGEMENTS | iv |
| LIST OF TABLES | ix |
| LIST OF FIGURES | x |
| LIST OF SYMBOLS AND NOMENCLATURE | xvii |
| SUMMARY | xx |
| CHAPTER I: Introduction | 1 |
| 1.1 Motivation | 1 |
| 1.2 Problem Overview | 4 |
| 1.3 Contributions | |
| 1.4 Organization and Overview | 6 |
| CHAPTER II: Literature Review | |
| 2.1 Introduction | 10 |
| 2.2 Flexible and Rigid Manipulator Modeling | 11 |
| 2.2.1 Flexible Robot Modeling 2.2.2 Rigid Robot Modeling | 11 13 |
| 2.2.2 Rigid Robot Modeling 2.2.3 Coupled Macro/Micromanipulator Models | |
| 2.3 General Macro/Micromanipulator Control Approaches | |
| 2.4 Control and Coupling of Free-Flying Space Robots | |
| 2.5 Micromanipulator Vibration Damping Techniques | 26 |
| 2.5.1 Energy Dissipation Methods | 27 |
| 2.5.2 Inertial Damping Control | 29 |
| 2.6 Limitations of Previous Research | |
| CHAPTER III: Flexible Base Manipulator Modeling | 38 |
| 3.1 Introduction | 38 |
| 3.2 Flexible Base Model | 39 |
| 3.2.1 Assumed Modes | 40 |
| 3.2.2 Kinetic and Potential Energy | 44 |

| 3.3 Flexible Base Rigid Manipulator Model |
|--|
| 3.4 Coupled Macro/Micromanipulator Model |
| CHAPTER IV: Interaction Force and Torques and Inertial Singularities |
| 4.1 Introduction |
| 4.2 Inertia Forces and Torques and Inertial Singularities 4.2.1 Performance Measure for Inertial Damping 4.2.2 Interaction Force Performance |
| 4.2.3 Interaction Torque Performance 4.2.4 Combined Performance |
| 4.3 Nonlinear Rigid Interaction Force and Torque Effects 4.3.1 Amplitude Effects |
| 4.4 CG Method to Identify Critical Interaction Force Effects |
| 4.5 Conclusions |
| CHAPTER V: Control Scheme |
| 5.1 Introduction |
| 5.2 Performance Index |
| 5.3 Vibration Controller |
| 5.3.1 Vibration Control Gains |
| 5.4 Controller Performance |
| 5.4.1 Controllability 5.4.2 Ideal Rigid Robot Model Control Performance |
| 5.4.2 Ideal Rigid Robot Model Control Performance 5.4.3 Alternate Contoller Form |
| 5.4.4 Simulations of Single Degree of Freedom Controller |
| 5.4.5 Hydraulics Dominated Rigid Robot Model Control Performance |
| CHAPTER VI: Simulations |
| 6.1 Introduction |
| 6.2 Single Flexible Link Macromanipulator with Anthropomorphic Rigid Robot |
| 6.3 Simulation Results |
| 6.3.1 Disturbance Rejection |
| 6.3.2 Interaction Torque Effects |
| 6.3.3 Multi-Link Macromanipulator Simulations |
| 6.3.4 Combined Position and Vibration Control Performance |
| 6.4 Hydraulic Actuator Effects |
| CHAPTER VII: Experimental Work |
| 7.1 Introduction |

| 7.2 Experimental Testbed | 1 |
|---|---|
| 7.2.1 Rigid Robot Independent Joint Controllers | 1 |
| 7.2.2 Macromanipulator | 1 |
| 7.3 Interaction Forces and Torques | 1 |
| 7.3.1 Single Degree of Freedom Interaction Forces and Torques | 1 |
| 7.3.2 Multi-Degree of Freedom Interaction Forces and Torques | 1 |
| 7.4 Multi-Degree of Freedom Vibration Damping | 1 |
| 7.4.1 Disturbance Rejection | 1 |
| 7.4.2 Combined Movement and Vibration Control | 2 |
| 7.5 Implementation Issues | 2 |
| 7.5.1 Acceleration Data | 2 |
| 7.5.2 Hydraulics Effects | 2 |
| 7.5.3 Joint Torque Effects | 2 |
| CHAPTER VIII: Conclusions | 2 |
| 7.1 Conclusions | 2 |
| 7.2 Contributions | 2 |
| 7.3 Recommendations for Future Research | 2 |
| APPENDIX A: Equations of Motion | 2 |
| REFERENCES | 2 |
| VITA | 2 |

LIST OF TABLES

| Table | Title | Page |
|-------|---|------|
| 6-1 | Simulated Point-to-Point Motion | 150 |
| 7-1 | Model Parameters for Second Order Approximation of Moog Servovalves | 169 |
| 7-2 | Feedforward Dead Zone and Drift Compensator | 171 |
| 7-3 | Selected Gains for Independent Joint Controllers | 172 |
| 7-4 | Dimensions and Properties of Experimental Robot | 174 |
| 7-5 | Modes of Vibration on Experimental Testbed | 180 |
| 7-6 | Damping Ratios for Macromanipulator Free Vibration Modes | 181 |
| 7-7 | Single Degree of Freedom Interaction Force and Torque Test Cases | 187 |
| 7-8 | Summary of Active Damping Controller Disturbance Rejection | 199 |
| A-1 | Denavit-Hartenberg Parameters for Anthropomorphic Robot | 217 |
| A-2 | Denavit-Hartenberg Parameters for Spherical Robot | 238 |
| A-3 | Denavit-Hartenberg Parameters for Wrist | 241 |

LIST OF FIGURES

| <u>Figure</u> | | <u>Page</u> |
|---------------|---|-------------|
| 1-1 | Macro/Micro Manipulator | 2 |
| 1-2 | Flexible Base Manipulator | 2 |
| 1-3 | Overview of Control Scheme | 8 |
| 3-1 | Flexible Link Model Notation | 41 |
| 3-2 | Flexible Base Rigid Robot | 49 |
| 3-3 | Flexible Base Single Link Rigid Robot | 50 |
| 3-4 | Notation Used for Recursive Newton-Euler Algorithm | 53 |
| 4-1 | 3 DOF Anthropomorphic Robot | 60 |
| 4-2 | 3 DOF Spherical Robot | 61 |
| 4-3 | 3 DOF Wrist Robot | 61 |
| 4-4 | 6 DOF Anthropomorphic Robot with Wrist | 62 |
| 4-5 | Force Performance – 3 DOF Anthropomorphic Robot | 66 |
| 4-6 | Force Performance – 3 DOF Spherical Robot | 67 |
| 4-7 | Force Performance – 3 DOF Wrist Robot | 68 |
| 4-8 | Torque Performance – 2 DOF Anthropomorphic Robot | 73 |
| 4-9 | Torque Performance – 3 DOF Spherical Robot | 74 |
| 4-10 | Torque Performance – 3 DOF Wrist Robot | 75 |
| 4-11 | Combined Force and Torque Performance – 3 DOF Anthropomorphic Robot | 76 |

| 4-12 | Combined Force and Torque Performance – 3 DOF Spherical Robot | 77 |
|------|---|-----|
| 4-13 | Anthropomorphic Robot Coriolis Forces | 80 |
| 4-14 | Anthropomorphic Robot Centrifugal Forces | 81 |
| 4-15 | Anthropomorphic Robot Inertia Forces | 81 |
| 4-16 | Spherical Robot Coriolis Torques | 83 |
| 4-17 | Spherical Robot Centrifugal Torques | 84 |
| 4-18 | Spherical Robot Inertia Torques | 84 |
| 4-19 | Anthropomorophic Interaction Forces, Large Inertia Effects | 85 |
| 4-20 | Anthropomorphic Interaction Forces, Near Singularity Case 2 | 86 |
| 4-21 | Anthropomorphic Interaction Forces, Large Centrifugal Effects | 87 |
| 4-22 | Anthropomorphic Configuration with Large Nonlinear Forces | 88 |
| 4-23 | Effect of Reducing Joint Amplitudes on Nonlinear Effects | 90 |
| 4-24 | Alternate Inverse Kinematic Configurations for Anthropomorphic Robot | 93 |
| 5-1 | Combined Position and Base Vibration Control Scheme | 95 |
| 5-2 | Linearized Single Degree of Freedom Control Scheme | 112 |
| 5-3 | Pole-Zero Map of Closed Loop System | 116 |
| 5-4 | Root Locus for Increasing Vibration Control Feedback Gains | 118 |
| 5-5 | Root Locus for Increasing Position Control Feedback Gains | 118 |
| 5-6 | Root Locus with Poor Selection of Vibration and Rigid Position Controllers | 121 |
| 5-7 | Root Locus with Better Selection of Vibration and Rigid Position Controllers | 121 |

| 5-8 | Effect of Choosing Vibration Control Zero too Large | 122 |
|------|--|-----|
| 5-9 | Effect of Choosing Vibration Control Zero too Small | 122 |
| 5-10 | Root Locus for Velocity Feedback, Ideal Model | 123 |
| 5-11 | Alternate Form of Vibration Controller | 124 |
| 5-12 | Pole-Zero Map of Alternate Controller | 125 |
| 5-13 | Single Degree of Freedom Matlab Simulation | 126 |
| 5-14 | Single Degree of Freedom Flexible Base Manipulator | 126 |
| 5-15 | Simulated Base Motion Due to an Applied Disturbance | 127 |
| 5-16 | Simulated Joint Motion with Inertial Damping Due to an Applied Disturbance | 128 |
| 5-17 | Simulated Commanded Joint Motion | 128 |
| 5-18 | Simulated Base Vibration Due to Commanded Joint Motion | 129 |
| 5-19 | Simulated Inertial Damping Performance with Velocity Feedback | 129 |
| 5-20 | Actuator Dominated Linearized Rigid Robot Model | 130 |
| 5-21 | Form of Vibration Controller for Hydraulics Dominated Robot | 131 |
| 5-22 | Root Locus for Increasing Vibration Control Gains, Hydraulics Model | 132 |
| 5-23 | Root Locus for Increasing Position Control Gains, Hydraulics Model | 133 |
| 6-1 | Matlab Simulation | 137 |
| 6-2 | Anthropomorphic Robot Configuration [45°,20°,-70°] | 141 |
| 6-3 | Simulated Base Vibration Due to an Applied Disturbance | 141 |
| 6-4 | Simulated Joint Motion Due to an Applied Disturbance | 142 |
| 6-5 | Simulated Total End Point Position Due to an Applied Disturbance | 142 |

| 6-6 | Simulated Base Vibration Due to an Applied Disturbance, Large Vibration Control Gains | 143 |
|------|---|-----|
| 6-7 | Simulated Joint Motion Due to an Applied Disturbance, Large Vibration Control Gains | 144 |
| 6-8 | Simulated Base Vibration with Robot in a Region with Large Nonlinear Effects | 145 |
| 6-9 | Simulated Joint Motion with Robot in a Region with Large Nonlinear Effects | 146 |
| 6-10 | Simulated Base Vibration with Interaction Forces and Torques Modeled, Configuration [45°,45°,-70°] | 147 |
| 6-11 | Simulated Base Vibration With Interaction Forces and Torques Modeled, Configuration [-90°,45°,-70°] | 148 |
| 6-12 | Simulated Base Vibration x Due to Point-to-Point Motion | 151 |
| 6-13 | Simulated Base Vibration y Due to Point-to-Point Motion | 152 |
| 6-14 | Simulated Base Vibration z Due to Point-to-Point Motion | 152 |
| 6-15 | Simulated Joint 1 Motion During Point-to-Point Motion | 153 |
| 6-16 | Simulated Joint Motion during Point-to-Point Motion | 153 |
| 6-17 | Simulated Total End Point Position x During Point-to-Point Motion | 154 |
| 6-18 | Simulated Total End Point Position y During Point-to-Point Motion | 155 |
| 6-19 | Base Vibration x with Reduced Gains for Damping Controller | 157 |
| 6-20 | Root Locus for Single Degree of Freedom Ideal Linearized Model | 157 |
| 6-21 | Hydraulics Dominated Single Degree of Freedom Model | 158 |
| 6-22 | Baseline Performance with Joint 2 Hydraulics Model | 160 |
| 6-23 | Phasing of Joint Actuation and Base Vibration, Hydraulics Model | 160 |

| 6-24 | Effect of Increasing Phase Lag on Hydraulics Model Vibration Performance | 161 |
|------|---|-----|
| 6-25 | Phasing of Joint Actuation and Base Vibration, Hydraulics Modeled with Higher Order Dynamics | 162 |
| 7-1 | Laboratory Setup | 166 |
| 7-2 | Experimental Rigid Robot | 168 |
| 7-3 | Independent Joint Controller | 168 |
| 7-4 | Joint 1 Response to D/A Output of -100 | 170 |
| 7-5 | Dead Zone Phenomenon in Hydraulic Servovalve | 172 |
| 7-6 | Root Locus Design for Independent Joint Controllers | 173 |
| 7-7 | Macromanipulator Base Mounting | 175 |
| 7-8 | Overall Macro/Micromanipulator Testbed | 176 |
| 7-9 | Free Vibration x Due to an Applied Disturbance x | 177 |
| 7-10 | Frequency Content of x Vibration Due to an Applied Disturbance x | 178 |
| 7-11 | Position x Due to an Applied Disturbance x | 179 |
| 7-12 | Frequency Content of x Position Data Due to an Applied Disturbance x | 179 |
| 7-13 | Position y Due to an Applied Disturbance x | 181 |
| 7-14 | Braced Micromanipulator | 184 |
| 7-15 | Predicted and Measured Interaction Forces at the Base of the Micromanipulator Due to Joint 1 Harmonic Motion | 185 |
| 7-16 | Predicted and Measured Interaction Torques at the Base of the Micromanipulator Due to Joint 1 Harmonic Motion | 186 |

| 7-17 | Predicted and Measured Interaction Forces Due to Joints 1,2, and 3 Actuating Simultaneously | 188 |
|------|--|-----|
| 7-18 | Frequency Content of Force y Data Due to Joints 1,2,and 3 Actuating Simultaneously | 189 |
| 7-19 | Anthropomorphic Robot Configuration [0°, 87°, 56°] | 190 |
| 7-20 | Interaction Forces Due to Joints 1 and 2 Actuating Near an Inertial Singularity | 190 |
| 7-21 | Frequency Content of Force Data due to Joints 1 and 2 Actuating Near an Inertial Singularity | 191 |
| 7-22 | Anthropomorphic Robot Configuration [0°,38°,0°] | 192 |
| 7-23 | Interaction Forces with Large Centrifugal Effects Due to Joints 1, 2, and 3 Actuating Simultaneously | 192 |
| 7-24 | Frequency Content of Force x data with Large Centrifugal Effects | 193 |
| 7-25 | Interaction Torques due to Joints 1, 2, and 3 in Configuration $(0^{\circ},38^{\circ},0^{\circ})$ | 193 |
| 7-26 | Frequency Content of Interaction Torque Data Due to Joints 1, 2, and 3 | 194 |
| 7-27 | Block Diagram of Multi-Degree of Freedom Vibration Damping | 197 |
| 7-28 | Vibration Control Due to an Applied Disturbance | 200 |
| 7-29 | Joint Response Due to an Applied Disturbance | 200 |
| 7-30 | Base Vibration Due to Commanded Movement | 202 |
| 7-31 | Joint Motion during Commanded Point-to-Point Movement with Vibration Control | 202 |
| 7-32 | Base Vibration Due to Commanded Movement in Region with Predicted Poor Inertial Damping Performance | 203 |
| 7-33 | Low Frequency Tracking of Joint 2 | 206 |

| 7-34 | High Frequency Tracking of Joint 2 | 206 |
|------|--|-----|
| 7-35 | Testbed Configuration with Poor Inertial Damping Performance | 208 |

LIST OF SYMBOLS AND NOMENCLATURE

a_i,d_i: Length of link i of the rigid robot

 $B_f(\boldsymbol{\theta})$: Rigid manipulator interaction force inertia matrix

 $B_{\tau 0}(\theta)$: Rigid manipulator interaction torque inertia matrix

 $B(\theta)$: Total rigid robot interaction inertia matrix= $\begin{bmatrix} B_f(\theta) \\ B_{r0}(\theta) \end{bmatrix}$

 $B_{\tau}(\theta)$: Rigid manipulator inertia matrix

C(q): Macromanipulator translational damping matrix

 $C_r(\mathbf{q})$: Macromanipulator rotational damping matrix

CG: Center of gravity

DOF: Degree of freedom

 \mathbf{F}_{IF} : Interaction forces between the micro and macromanipulator= $\left[F_x \ F_y \ F_z\right]^T$

 I_{jkk} : Moment of inertia of link j of the rigid robot about the k^{th} axis

ID: Inverse dynamics function

J(q): Macromanipulator mass moment of inertia matrix

 K_{i} : Vibration control feedback gain for i^{th} macromanipulator DOF

 $K(\boldsymbol{q})$: Macromanipulator translational stiffness matrix

 $K_r(\mathbf{q})$: Macromanipulator rotational stiffness matrix

m_i: Mass of the ith link of the rigid robot

 $M(\mathbf{q})$: Macromanipulator mass matrix

 $N_{Cf}(\boldsymbol{\theta})$: Rigid robot centrifugal interaction force matrix

 $N_{C\tau 0}(\theta)$: Rigid robot centrifugal interaction torque matrix

 $N_f(\theta)$: Total rigid robot nonlinear interaction force matrix (centrifugal and coriolis)

 $N_{Rf}(\theta)$: Rigid robot coriolis interaction force matrix

 $N_{R\tau 0}(\boldsymbol{\theta})$: Rigid robot coriolis interaction torque matrix

 $N_{\tau 0}(\boldsymbol{\theta})$: Total rigid robot nonlinear interaction torque matrix (centrifugal and coriolis)

PD: Proportional and derivative controller

PID: Proportional, derivative, and integral controller

PI: Performance Index

q: Flexible manipulator generalized coordinates

 $\tilde{\mathbf{q}}$: Flexible manipulator generalized coordinates linearized about an operating point

Q: Generalized force applied by the micromanipulator to the macromanipulator

 \mathbf{r}_{cg} : Position vector to the overall CG of the robot

R_iⁱ⁻¹: Rotation matrix of frame i with respect to frame i-1

T: Kinetic Energy

V: Potential Energy

W_f: Flexible robot weighting matrix

W_r: Rigid robot weighting matrix

 \mathbf{x}_{f} : Flexible base translational motion = $[\mathbf{x} \ \mathbf{y} \ \mathbf{z}]^{T}$

X_i: Amplitude of vibration of the ith mode of the flexible base

x_d: Desired rigid robot end point position

δ: Disturbance force

ζ: Damping ratio

 $\pmb{\theta}$ or $\pmb{\theta}_a$: Actual rigid manipulator joint variables= $\left[\theta_1 \; \theta_2 \; \theta_3 \; ... \theta_n\right]^T$

 $\tilde{m{\theta}}$: Rigid manipulator joint variables linearized about an operating point

 $\pmb{\theta_d} \text{: Desired rigid manipulator joint variables} = \left[\theta_{1d} \; \theta_{2d} \; \theta_{3d} \; \ldots \theta_{nd}\right]^T$

 $\boldsymbol{\theta}_f$: Flexible base rotational motion= $[\boldsymbol{\theta}_x \ \boldsymbol{\theta}_y \ \boldsymbol{\theta}_z]^T$

 θ_i : Rigid robot ith joint angle

 $\boldsymbol{\tau}$: Rigid robot joint actuation torques= $\left[\tau_1 \ \tau_2 \ \tau_3 \ ... \tau_n\right]^T$

 $\pmb{\tau}_{IF}$: Interaction torques between the micro and macromanipulator= $\left[\tau_x\,\tau_y\,\tau_z\right]^T$

 ω_i : Natural frequency of the i^{th} mode of the flexible base

SUMMARY

A rigid (micro) robot mounted serially to the tip of a long, flexible (macro) robot is often used to increase reach capability, but flexibility in the macromanipulator can make it susceptible to vibration. A rigid manipulator attached to a flexible but unactuated base was used to study a scheme to achieve micromanipulator positioning combined with vibration damping of the base. Inertial interaction forces and torques acting at the base of the rigid robot were studied to determine how to use them to damp the base vibration.

The ability of the rigid robot to create inertial interactions varies throughout the workspace. There are also "inertial singularity" configurations where the robot loses its ability to create interactions in one or more degrees of freedom. A performance index was developed to quantify this variation in performance and can be used to ensure the robot operates in joint space configurations favorable for inertial damping. When the performance index is used along with appropriate vibration control feedback gains, the inertia effects, or those directly due to accelerating the rigid robot links, have the greatest influence on the interactions. By commanding the link accelerations out of phase with the base vibration, energy will be removed from the system. This signal is then added to the rigid robot position control signal. Simulated and measured interaction forces and torques generated at the base of a rigid robot are compared to verify conclusions drawn about the controllable interactions. In addition, simulated and experimental results demonstrate the combined position control and vibration damping ability of the scheme.

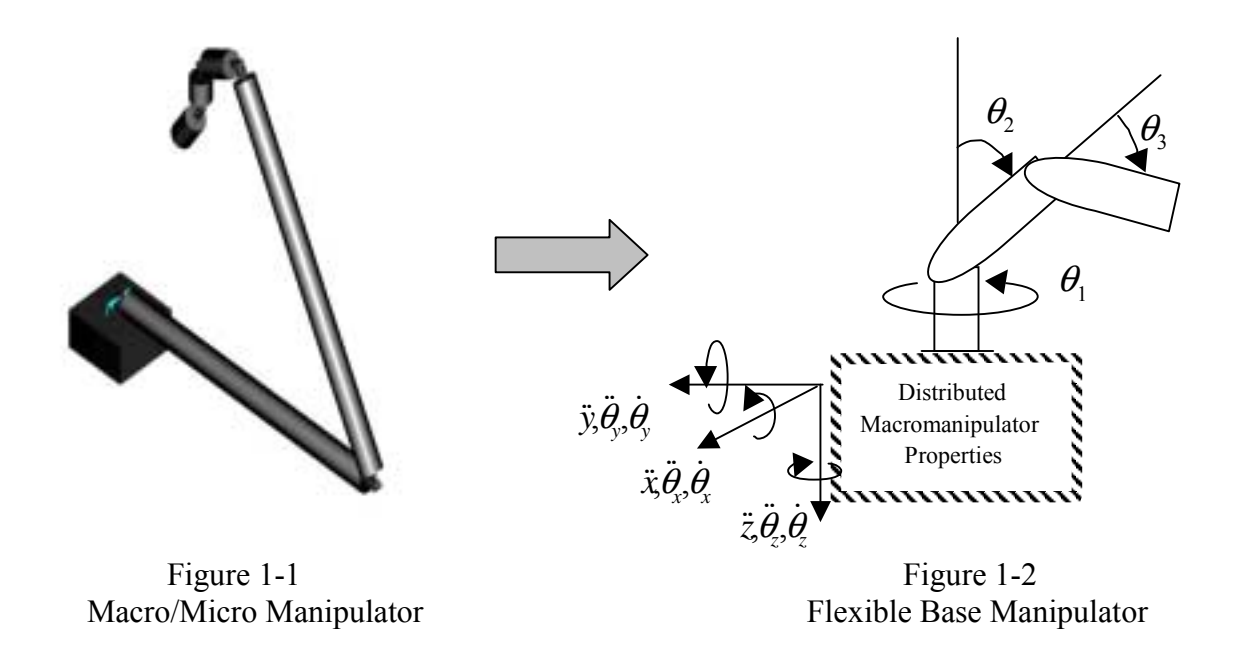
CHAPTER I

INTRODUCTION

1.1 Motivation

The objective of this research was to develop a combined position and enhanced vibration control scheme for a rigid manipulator attached to a flexible base. The configuration is similar to a macro/micromanipulator (Figure 1-1), which has links that are long and lightweight with a rigid robot attached serially to the end. Macro/micro manipulators are desirable for certain uses, because the macromanipulator can provide long reach capability by moving the robot to the general area of interest where it can then be used for fine-tuned positioning. These are often used to perform tasks that humans may be incapable of doing or that are dangerous for humans.

One application is in the nuclear industry where macro/micromanipulators are used to remove nuclear waste from underground storage tanks [25]. In the application described in the reference, a 39 foot, seven degree of freedom long-reach manipulator was used with a rigid end effector to clean seven storage tanks at Oak Ridge National Laboratory from 1996-2000. Two end effectors were used: one type measured the radiation field, while the other scarified the tank walls.



Another growing application is in space, where long reach capability is needed, but weight is crucial [41,56,77,93]. The space shuttle has used a remote manipulator system (RMS), or Canadarm, which was initially launched and used in 1981. One problem is that approximately 1/3 of the time spent by astronauts in operation of the RMS is spent waiting for vibration to decay [41]. The second-generation system, Space Station Remote Manipulator System, or Canadarm 2, is a seven-jointed arm that was designed to maneuver large payloads around the International Space Station. It will sometimes be used with the Special Purpose Dexterous Manipulator to provide specific maintenance tasks.

The problem is that flexible links are difficult to control and are susceptible to vibration induced by movement of the robot itself or by external disturbances. The many degrees of freedom involved make control of the coupled system a complex task. This

research considers the base of the rigid robot to be flexible, where the base motion is similar to that due to vibration at the tip of a flexible macromanipulator with locked joints (Figure 1-2). It is assumed for this work the joints of the macromanipulator are not actuating so the only vibration in the system is due to externally applied disturbances or motion of the rigid manipulator.

Many researchers have tackled the problem of developing control schemes to eliminate unwanted vibration in flexible manipulators. One area involves determining trajectories that will avoid or minimize inducing vibration; however, these schemes are not useful for controlling vibration once it occurs. The macromanipulator actuators are not a good option for vibration damping due to bandwidth limitations and non-collocation of the actuators and end point vibration. This creates a non-minimum phase problem due to time delays, further exacerbated by flexibility in the link(s). In addition, since only gross positioning capability is really needed for the macromanipulator, it is an unnecessary increase in cost and system complexity to use its actuators for vibration control in addition to their already difficult task.

The use of the rigid manipulator to damp vibration in the macromanipulator has proven to be a promising area. The micromanipulator produces inertial forces and torques that act as disturbances to the macromanipulator under decoupled control. Under coupled control, these inertial effects can be used as damping forces and torques and applied directly to the tip of the macromanipulator. This also makes the system minimum phase, further reducing the complexity of the control task. In addition, it is much easier to provide high bandwidth actuators for a small robot arm than for a large

one, so its actuators can respond more quickly and efficiently to provide large inertial forces and torques. Previous methods of damping vibration in this manner include energy dissipation methods and inertial damping methods. The goal here is to command the rigid robot to act as an active vibration damper, damping the motion of the macromanipulator at the natural frequencies of the system. These along with other methods of controlling macro/micromanipulators are discussed in more detail in Chapter 2.

1.2 Problem Overview

In this work, the rigid robot control scheme must perform the dual task of damping unwanted base vibration (macromanipulator vibration) while providing position control of the rigid robot. On the one hand, if the motion of the micromanipulator or combined system is completely prescribed by the task, this method is not useful. However, under circumstances where the task will allow small movements of the rigid robot to damp the vibration, this technique can be very effective. After all, if the system is vibrating uncontrollably the system performance is impacted. The controlled interactions are collocated with the vibration at the tip of the macromanipulator, and the rigid robot can respond quickly to create the inertial damping forces and torques. The goal here is to reduce the vibration as quickly and efficiently as possible so the system can continue with its task. This method requires no hardware modifications other than some type of measurement of the vibration.

Most of the literature addresses macro/micromanipulator position control or vibration control alone, but few researchers address both. The authors that have addressed both assume limited base flexibility, thereby limiting the applicability of the work. In addition, simulations and hardware demonstrations have been limited mostly to planar translational vibration. Finally, operation throughout the workspace has not been addressed, in particular at locations where coupling effects between the macro and micromanipulator are unsuited to vibration damping.

The control scheme described in this dissertation was tested in simulations and experiments in two main scenarios. The first was with the robot operating at a desired joint space configuration and tested its ability to damp vibration induced by an applied disturbance. The second scenario was for point-to-point motion where the rigid robot is moving from an initial to a final joint space configuration in a given time period. Both of these allow flexibility in choosing between alternate inverse kinematic joint space configurations. If the joint space configuration of the rigid robot is a prescribed part of the control scheme, another method of damping may be required.

1.3 Contributions

The contributions of this thesis are:

1. Extension of the macro/micromanipulator control problem to multiple degrees of freedom by considering the analogous problem of a rigid manipulator mounted on a flexible base.

- 2. Investigation of inertial singularities and variation in inertial damping performance throughout the workspace.
- 3. Development of a control scheme that provides active base vibration damping in parallel with rigid robot position control and establishment of appropriate vibration control gain limits.
 - 4. Verification of the above via simulation.
- 5. Experimental work including verification of the accuracy of the interaction force and torque predictions and demonstration of the effectiveness of the control scheme on a realistic multi-degree of freedom testbed.

1.4 Organization and Overview

This dissertation is organized in the following manner:

Chapter 1 discusses the motivation of the research, contributions of the work, and outlines the dissertation.

Chapter 2 reviews the current state of literature on the subject of macro/micromanipulator control and limitations of previous research.

Chapter 3 describes modeling of the flexible base manipulator. A Lagrangian approach with a finite number of assumed modes was used to represent the flexible manipulator, while a recursive Newton-Euler formulation was used to derive expressions for the interaction forces and torques acting between the macro and micromanipulator. The general form of these interactions is:

$$\begin{split} \mathbf{F}_{IF} &= B_f(\boldsymbol{\theta}) \ddot{\boldsymbol{\theta}} + N_f(\dot{\boldsymbol{\theta}}_i \dot{\boldsymbol{\theta}}_j, \boldsymbol{\theta}) + G_f(\boldsymbol{\theta}) + C_f(\boldsymbol{\theta}) \ddot{\mathbf{q}} + N_{fc}(\dot{\mathbf{q}}, \mathbf{q}, \dot{\boldsymbol{\theta}}, \boldsymbol{\theta}) \\ \boldsymbol{\tau}_{IF} &= B_{\tau 0}(\boldsymbol{\theta}) \ddot{\boldsymbol{\theta}} + N_{\tau 0}(\dot{\boldsymbol{\theta}}_i \dot{\boldsymbol{\theta}}_j, \boldsymbol{\theta}) + G_{\tau 0}(\boldsymbol{\theta}) + C_{\tau 0}(\boldsymbol{\theta}) \ddot{\mathbf{q}} + N_{\tau 0c}(\dot{\mathbf{q}}, \mathbf{q}, \dot{\boldsymbol{\theta}}, \boldsymbol{\theta}) \end{split} \tag{1-1}$$

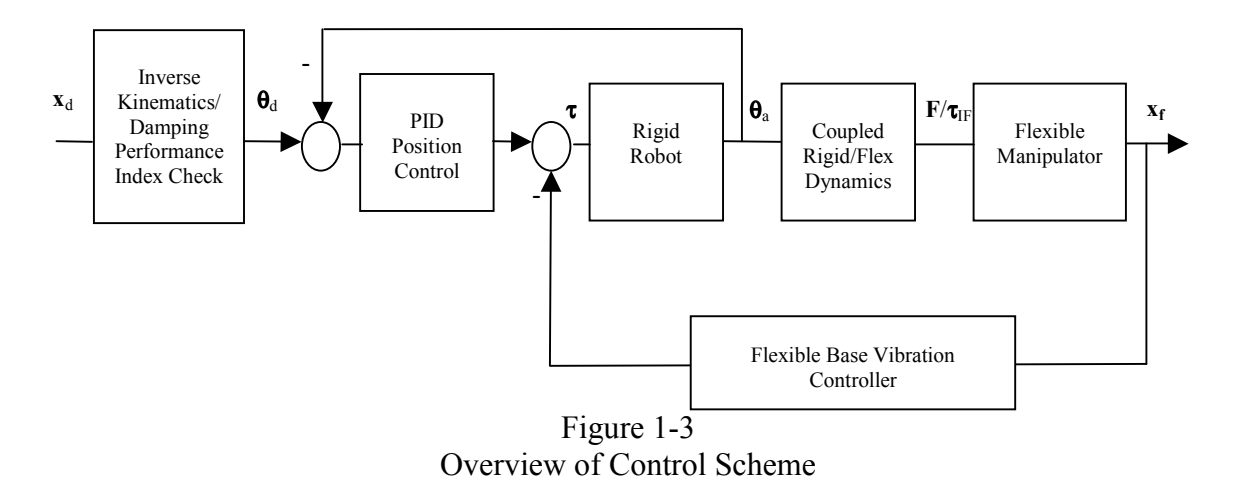
where θ represents the rigid robot joint variables and \mathbf{q} represents the flexible manipulator generalized coordinates. The rigid robot configuration, θ , joint velocities and accelerations, and flexible base velocities and accelerations drive the interactions. The goal was to study these interactions in order to determine how to use them in the control scheme to damp the macromanipulator vibration.

Chapter 4 discusses in more detail the controllable interactions, or the first two terms in each equation in 1-1. A performance measure is introduced which predicts the effectiveness of the rigid robot in creating these interactions. The rigid inertia effects $(B_f(\theta))$ and $B_{\tau 0}(\theta)$ are particularly important for two reasons. First, the rigid robot must have enough inertia to effectively apply interaction forces and torques to the macromanipulator. The ratio of the rigid inertia to flexible inertia effects becomes an important part of the performance index, discussed in Chapter 5. Second, there are joint workspace configurations where these matrices become singular. These "inertial singularities" represent physical limitations in that an inertia force or torque cannot be created in one or more degrees of freedom. The variation in performance is driven by the joint space configuration of the rigid robot, so the performance measure can be used to choose joint space configurations better suited for inertial damping. The inertia effects dominate the interactions in most non-singular configurations. However, the nonlinear rigid effects may also become significant in certain cases and these are also discussed here.

The control scheme is discussed in Chapter 5. The overall schematic is shown in Figure 1-3. The flexible base vibration controller takes the form:

$$\mathbf{\tau} = -ID(\mathbf{\theta}) * K\dot{\mathbf{x}} \tag{1-2}$$

where $ID(\theta)$ represents an inverse dynamics function [4,19] designed to cancel the significant rigid robot dynamics and \mathbf{x} represents the motion of the flexible base. The rigid robot motion will be commanded to absorb the vibration energy of the flexible base.



Chapter 6 discusses simulations of vibration damping of a three degree of freedom anthropomorphic robot mounted on a flexible base. Simulations demonstrating disturbance rejection as well as the use of the performance index in predicting better joint space configurations for vibration damping during commanded motion are presented.

Chapter 7 discusses the experimental testbed and presents results from two areas of testing. First, predicted and measured interaction forces and torques generated at the base of a rigid three degree of freedom anthropomorphic robot are presented, which verified many of the results presented in Chapter 4. Second, the ability of the controller to damp vibration on a multi-degree of freedom testbed was tested. The macromanipulator consists of two flexible links in a fixed joint configuration. Three links of a six degree of freedom micromanipulator were used for vibration damping. Some promising results are presented demonstrating overall vibration energy from the system. However, several implementation issues arose that limited the effectiveness of the scheme on the testbed. These are discussed in more detail as well as proposed means of addressing these issues for future work.

Chapter 8 summarizes the results and suggests area of further research. Finally, Appendix A includes the equations for the interaction forces and torques for four typical robot configurations.

CHAPTER II

LITERATURE REVIEW

2.1 Introduction

This chapter reviews the general topic of macro/micromanipulator control. Macro/micromanipulators were introduced in the early 1980s as a means of improving endpoint control of flexible manipulators, which were becoming more common for applications where long reach capability was needed. Positioning errors due to flexibility and other inaccuracies in the links of the macromanipulator are compensated for by the micromanipulator.

First, literature on modeling flexible and rigid manipulators is reviewed. Since this in itself is a very broad area, the research discussed here is specifically relevant to modeling combined flexible/rigid systems. Next, general methods of controlling macro/micromanipulators are discussed. The problem that becomes quickly apparent is the large number of degrees of freedom involved and complexity of the resulting control problem. The links of the macromanipulator are susceptible to vibration, so there are additional degrees of freedom that need to be controlled as well as the rigid coordinates. One option to reduce the complexity of the problem is to decouple control of the rigid and flexible robots. In this case, the macromanipulator provides gross positioning while the rigid robot provides the fine-tuned positioning. However, there are also problems with this technique. The rigid robot produces inertial forces and torques which can act as disturbances to the macromanipulator and worsen the vibration problem. In addition, with larger and more flexible macromanipulators, vibration amplitudes can become too large for the rigid robot to compensate for. Thus another area of research evolved which focused on methods of commanding the micromanipulator to reduce vibration in the macromanipulator. One way is to command the rigid robot using trajectories that will reduce these disturbances. An alternate approach is to use the disturbances to damp the vibration, which is the basis of the work described in this dissertation. The current state of research in this area is reviewed as well as limitations of the work performed thus far.

In addition, there has been a great deal of related research in the area of space robotics. This area has not been widely recognized as being related to the problem of earth-based macro/micromanipulator control. However, the approach taken in this thesis, where the rigid robot is considered attached to a flexible base, is very similar to space robotics research that considers a rigid robot mounted to a floating base (spacecraft). Some of the applicable space robotics research is also reviewed here.

2.2 Flexible and Rigid Manipulator Modeling

2.2.1 Flexible Robot Modeling

There are many methods available to model flexible link robots. Since the links are distributed parameter systems, their motion is described by partial differential equations instead of ordinary differential equations and hence modeling can become very

challenging. In addition to the nonlinear rigid dynamics commonly found in robotic systems, flexible manipulators also exhibit elastic behavior.

Book [8] developed a recursive Lagrangian approach for modeling flexible link robots. Describing the position of a point on a flexible link requires both rigid and elastic coordinates, so he suggested the use of 4 x 4 transformation matrices for more compact representation. By choosing a finite number of assumed modes to model the elastic motion, the position of a point along each flexible link can be written in terms of the rigid and flexible coordinates. Expressions for kinetic and potential energy of the system can then be developed. The kinetic energy terms consist of translational and rotational energy of each link. Potential energy terms consist of elastic bending, gravity, and shearing deformation effects.

Several authors have considered the relative importance of the energy terms and under what circumstances certain effects may be neglected [46,52,72,83]. Most authors involved in modeling flexible manipulators assume Euler-Bernoulli bending theory applies. When this is the case, rotational inertia terms may be assumed negligible, and potential energy terms only need to include elastic bending and gravity effects [83]. The resultant equations are integrated over the spatial variable and used with Lagrange's equations to derive the equations of motion. One advantage of this method is that the energy terms can include as much or as little detail as needed. Modal damping may also be added if desired. Regardless of the method used to derive them, the equations of motion take the form:

$$M_b(\mathbf{q})\ddot{\mathbf{q}} + C_b(\mathbf{q},\dot{\mathbf{q}}) + K_b\mathbf{q} + G_b(\mathbf{q}) = \mathbf{Q}$$

 $M_h = inertia matrix$

 C_h = nonlinear, coupling, and viscoelastic effects

 $K_h = \text{stiffness matrix}$

 G_h = gravitational effects

 \mathbf{Q} = generalized forces

$$\mathbf{q} = \begin{bmatrix} \mathbf{x}_f \\ \mathbf{\theta}_r \end{bmatrix} = \begin{bmatrix} \text{flexible coordinates} \\ \text{rigid joint coordinates} \end{bmatrix}$$
 (2-1)

The generalized forces are the joint actuation torques and contact forces and torques. In the case of a macro/micromanipulator, the contact forces and torques will be those created by the micromanipulator.

Lee [32], Lew [34], and Obergfell [53] used this method to model a two-link flexible robot at Georgia Tech called RALF (Robot Arm, Large and Flexible). Other examples of modeling a single flexible link can be found in Cannon [15], Loper [42], Nataraj [52], and Smart and Wiens [72].

2.2.2 Rigid Robot Modeling

Common methods of modeling rigid robots are a Lagrangian approach or a Newton-Euler formulation. Detailed descriptions of both methods can be found in Craig [18], McKerrow [48], or Sciavicco and Siciliano [61]. The equations of motion take the form:

$$B_{\tau}(\theta)\ddot{\theta} + N_{\tau}(\dot{\theta}, \theta)\dot{\theta} + G_{\tau}(\theta) = \tau$$

 $\theta = \text{rigid joint coordinates}$
 $B_{\tau}(\theta) = \text{symmetric, positive definite inertia matrix}$
 $N_{\tau}(\theta, \dot{\theta}) = \text{centrifugal and coriolis effects}$
 $G_{\tau}(\theta) = \text{gravitational effects}$
 $\tau = \text{joint actuation torques}$ (2-2)

2.2.3 Coupled Macro/Micromanipulator Models

One method of modeling macro/micromanipulators is using the recursive Lagrangian approach mentioned above and treating the last few links as rigid. However, this quickly becomes long and tedious. Lew [34] developed a more efficient method of deriving the equations of motion of two robots connected serially. He concentrated on identifying the coupling dynamics between the two manipulators assuming known models for each. The coupled equations of motion take the form:

$$\begin{bmatrix} M_b + M_{b/r}(\mathbf{q}, \boldsymbol{\theta}) & M_{br}(\mathbf{q}, \boldsymbol{\theta}) \\ M_{br}^T(\mathbf{q}, \boldsymbol{\theta}) & B_r(\boldsymbol{\theta}) \end{bmatrix} \begin{bmatrix} \ddot{\mathbf{x}}_f \\ \ddot{\boldsymbol{\theta}} \end{bmatrix} + \begin{bmatrix} C_b \dot{\mathbf{x}}_f + C_{br}(\dot{\mathbf{q}}, \mathbf{q}, \dot{\boldsymbol{\theta}}, \boldsymbol{\theta}) \\ N_r(\dot{\boldsymbol{\theta}}, \boldsymbol{\theta}) + C_{b/r}(\dot{\mathbf{q}}, \mathbf{q}, \dot{\boldsymbol{\theta}}, \boldsymbol{\theta}) \end{bmatrix} + \begin{bmatrix} K_b & 0 \\ 0 & 0 \end{bmatrix} \begin{bmatrix} \mathbf{x}_f \\ \boldsymbol{\theta} \end{bmatrix} = \begin{bmatrix} 0 \\ \boldsymbol{\tau} \end{bmatrix}$$
(2-3)

The notation used here is slightly different from the notation used in [34] and his papers [35-40] in order to be consistent with the notation used in equations 2-1 and 2-2. M_b , C_b , and K_b represent macromanipulator properties and are defined along with \mathbf{q} in equation 2-1. B_{τ} and N_{τ} represent the rigid robot dynamics and are defined along with $\mathbf{\theta}$ in equation 2-2. $M_{b/r}$ and M_{br} are coupling inertia matrices, and C_{br} and $C_{b/r}$ are nonlinear coupling terms (gravitational effects are included in the nonlinear terms). It is further

assumed the macromanipulator is not actuating so the only joint torques and rigid coordinates that vary are those associated with the rigid robot. Most of the macro/micromanipulator control literature uses this form of the coupled equations of motion as a baseline model.

Sharf [63] introduced a means of effectively decoupling the macro and micromanipulator models by finding expressions for the reaction forces acting between the two bodies. This is equivalent to equation 2-3, the only difference being the explicit definition of the interactions.

2.3 General Macro/Micromanipulator Control Approaches

The control of flexible manipulators has been studied extensively. Control of the distributed, nonlinear systems is difficult and researchers have examined end point sensing, robust control, vibration suppression, and command shaping techniques, among others, to better control them. Book [9,10] discussed many of the problems associated with controlling flexible manipulators. As discussed in section 2.2.1, modeling is difficult but achievable if the system modes of interest can be limited to a finite number of modes. The control problem is extremely complicated for many reasons. First, flexible manipulators are susceptible to vibration, either induced by movement of their long, flexible links or external disturbances. Second, the number of control variables (joint variables) is less than the number of mechanical degrees of freedom, which include both the rigid and flexible coordinates. Third, the dominant closed loop poles of the system do not become more stable with increasing position control feedback gains. This

limits the achievable bandwidth to about 1/3 that of a rigid manipulator [10]. Thus, lower bandwidth actuators are typically used and they may not be fast enough to respond to the vibration. In addition, the actuators are located at the joints of the macromanipulator while the vibration of concern is at the end point. This non-collocation issue further complicates the control problem. Non-minimum phase dynamics can result and, combined with the many other control issues associated with flexible manipulators, may threaten system stability.

Sharon, Hogan, and Hardt introduced macro/micromanipulators in the early 1980s as a means of improving endpoint control of flexible manipulators [64,65]. They showed that a rigid robot mounted serially to a flexible manipulator could be used to compensate for position errors caused by macromanipulator flexibility and other inaccuracies. The end point position control bandwidth was chosen to be approximately 15 times the first natural frequency of the macromanipulator. Since the micromanipulator inertia is relatively small, it can respond quickly to the rapid transients of the macromanipulator vibration.

Much of the research in the control of macro/micromanipulators involves designing specialized coupled control schemes. The many degrees of freedom involved combined with additional challenges associated with controlling the flexible links make coupled control a difficult task. These control schemes fall into three general categories. First are schemes where both the macromanipulator and micromanipulator are controlled concurrently. The complexity of these schemes makes them difficult to implement but may be the only solution in some cases. The second area involves decoupled

macromanipulator control schemes designed to control or reduce the vibration. Since flexible manipulators have been in use for many years, there is a large pool of applicable research that can help reduce vibration, including input shaping. A third area considers the decoupled micromanipulator controller. These include schemes that use the rigid robot to compensate for macromanipulator position error as well as schemes that actively use the micromanipulator to reduce the vibration. The latter is the basis for this research and the background in this area is described in more detail in the next section.

One well-known method of improving trajectory tracking is to use an inverse dynamics function to cancel undesirable system dynamics. Bayo and Moulin [4] and Devasia and Bayo [19] considered the control of flexible manipulators through the solution of the system inverse dynamics. However, one major problem with applying this method to a flexible link robot is that it is a non-minimum phase system. When the dynamics are inverted the inverse dynamics model contains both positive and negative real eigenvalues.

Kwon and Book [31] investigated inverse dynamic trajectory tracking for a single-link flexible manipulator. Their goal was to develop a time domain inverse dynamics method that enabled a flexible manipulator to follow a given end point trajectory accurately without overshoot or residual vibration. They first modeled the manipulator using the assumed modes method described in section 2.2.1 and developed the inverse dynamics model. The tracking controller combined an inverse dynamics function for feedforward control with a joint feedback controller. They worked around the non-minimum phase issue by extending the solution set to include a non-causal solution and

split the inverse dynamics into causal and anticausal parts. They showed in simulation and experiment the effectiveness of the controller in producing fast, vibration-free motion of a single flexible link manipulator. This work provided a valuable contribution in showing that, with an understanding of the unique problems associated with flexible systems, inverse dynamics could be implemented on them.

Several researchers have considered ways to reduce the complexity of combined macro/micromanipulator control schemes. Singh and Schy [69] used a control law that decouples the rigid and elastic behavior. They considered a PUMA-type robot with three rotational joints mounted on a space vehicle, where the first two links are rigid and the last link flexible. The elastic dynamics are further decomposed into two subsystems modeling the transverse vibration of the elastic link in two orthogonal planes. A proportional-integral-derivative (PID) controller is used on the joint angle errors. Two fictitious forces acting at the tip of the flexible link are used to damp the elastic oscillations. The scheme was shown effective and robust to modeling errors in simulation. However, practical implementation would require a realistic way to provide the elastic control forces.

Lew considered a different strategy of bracing the macromanipulator [34]. He developed a hybrid controller for flexible link manipulators that make contact with the environment at more than one point and proved its stability. He was able to show effective position and force tracking control. Experimental work was performed at Georgia Tech with a rigid robot mounted on the end of a two link flexible manipulator

and demonstrated that the use of this technique could effectively reduce vibration in the macromanipulator in the planar case.

Yim and Singh [90] used an inverse control law combined with a predictive control law for a macro/micromanipulator. The inverse control law was used for end point trajectory control of the rigid micromanipulator and is based on the inversion of the input/output map. The predictive controller was used for end point control of the flexible macromanipulator. It was developed for precise trajectory tracking and designed so the flexible dynamics remained stable. The controller was derived by minimizing a quadratic function of the tracking error, elastic deflection, and input control torques. The stability of the scheme was proven and its effectiveness demonstrated via simulations. They also considered the same predictive control law [89,91] except with a sliding mode controller for the micromanipulator. The micromanipulator control scheme was variable structure control, which is more insensitive to modeling errors. The sliding mode controller was developed with the sliding surface functions of tip position, its derivative, and the integral of the tracking error. Its purpose was to ensure precise trajectory tracking of the end effector. Simulations of a single flexible link with a two rigid link micromanipulator indicated that good end point trajectory control and elastic mode stabilization is achievable.

Another wide area of research involves input shaping or trajectory modification techniques to avoid inducing vibration during commanded moves. These techniques reduce vibration in a system by convolving an impulse sequence with the desired command. When the impulse sequence is chosen properly, the resulting reduction in

vibration can be drastic, even in the presence of modeling uncertainties. The only information required is the basic properties of natural frequencies and damping ratios of the modes of concern.

Singer and Seering [68] reshaped an impulse input into two impulses, where the second was delayed by ½ the period of vibration to be avoided. The shaper was placed outside the feedback loop. When more than two pulses are used, sensitivity to modeling errors is reduced. The effectiveness of the technique was evaluated on a Space Shuttle Remote Manipulator System (RMS) simulator at Draper Laboratory and showed a factor of 25 reduction in endpoint residual vibration for typical moves of the RMS. Banerjee [3] also showed the effectiveness of input shaping techniques on a shuttle experiment with a very flexible payload. Simulated spin up and slew motion of the shuttle with two 150-meter long flexible antenna booms indicated much less residual vibration in the flexible antennas when the motion was commanded with a three impulse shaper.

Singhose, Singer, and Seering showed that input shaping leads to much better performance than other filtering techniques (Butterworth, notch, etc.) [70]. In particular, they compared the impulse sequence length, residual vibration, and robustness to uncertainties in the system model. Each method was used to shape a step command given to a harmonic oscillator. The results clearly indicated the input shapers are significantly shorter, yield considerably less vibration, and are far more insensitive to modeling errors than the filters. Singhose and Singer [71] also showed that the use of input shapers does not significantly affect trajectory tracking. These techniques could be

applied to the macromanipulator to reduce vibration created by its motion, or applied to the micromanipulator, or both.

Command shaping is a closely related area except typically refers to a scheme that has a variable delay between pulses. This is important for flexible manipulators because the natural frequencies of the system and required delay between pulses vary with workspace location. Magee and Book [45] applied command shaping techniques to reduce vibration induced by the motion of a rigid robot mounted on a flexible base. They used a finite impulse response filter on the micromanipulator joint position error. A general three term filter was developed that can produce both positive and negative filter coefficients depending on the delay time value. Experimental work was performed using a small articulated robot attached to a much larger, flexible robot. The smaller robot was commanded to move under proportional-derivative (PD) control with and without the filter. The use of the filtering method resulted in a vibration amplitude reduction of nearly 60%. Input and command shaping techniques can be very useful for reducing vibration created by commanded movement of the robot. However, they require information about the system and only help in the case of vibration induced by the manipulator itself. Vibration caused by external disturbances remains unchecked.

Xie, Kalaycioglu, and Patel [87] developed an algorithm to command the correct macromanipulator actuator pulses at the end of a maneuver to cancel observed vibration. This algorithm was designed specifically for the Space Shuttle Remote Manipulator System (RMS). As noted in Chapter 1, the RMS is a realistic example of a flexible manipulator and moving it tends to induce vibration. The technique described in this

paper is termed "pulse active damping." The concept is to excite vibration exactly opposite the observed vibration so cancellation is achieved. This concept is similar to input shaping except that it is applied to the system once the vibration is initiated and measured. Real-time system identification is then performed to acquire the natural frequencies and damping ratios of the system. The desired joint torque needed at the shoulder to cancel the oscillations is applied at half the natural frequency of the vibration (180° out of phase), thereby canceling it. Although this technique was shown to be effective in simulation, the large inertia of the flexible arms, non-collocation of the macromanipulator actuators and the end point, and limited actuator bandwidths could make it challenging to implement.

Other researchers studied the use of the micromanipulator to compensate for displacement errors caused by the macromanipulator flexibility. Ballhaus and Rock [2] developed a scheme where the macromanipulator would move the rigid robot within range of the desired end point position. If the desired relative tip position was within reach, a low gain PD controller was used to command the final micromanipulator position. If not, the rigid robot was set to a nominal position. Experimental work on two .52-meter flexible links with a two degree of freedom rigid micromanipulator demonstrated the effectiveness of this technique. The low endpoint gains ensured low interactions. However, the authors also noted that with increasing gains the interaction forces increase and can lead to instability.

Yoshikawa, Hosoda, Doi, and Murakami [94] developed an endpoint tracking control algorithm that consists of a PD macromanipulator controller for global positioning

combined with a dynamic trajectory tracking control law for the micromanipulator. The micromanipulator control scheme was designed to account for the dynamics of the system with a nonlinear state compensator, which linearizes the closed loop system. The ability of the method to achieve precise positioning was demonstrated on a small-scale laboratory setup consisting of a macromanipulator with two flexible links and a two link rigid robot for the micromanipulator. However, with larger and more flexible macromanipulators with larger amplitudes of vibration, these techniques become less effective. In addition, the base vibration remains uncontrolled.

2.4 Control and Coupling of Free-Flying Space Robots

Another wide area of study that has some applicability to macro/micromanipulator control has been in the analysis and control of free-flying space robots. Although some principles are different since space robots do not have a fixed inertial base, some aspects of this research can be applied. Some of these concepts have already begun to be applied to some of the control techniques discussed in section 2.5.

Much work has been done to understand the dynamic interactions between a robot and a free-floating base. Torres, Dubowsky, and Pisoni [77,78] developed a "coupling map" as an analytical tool to describe dynamic interaction between a space manipulator and its base. The coupling map was formed from the translational inertia of the coupled macro/micromanipulator weighted by the stiffness of the macromanipulator. This provides a measure of the inertia forces acting between the two bodies and a measure of the strain energy of the flexible system. It could then be used to find paths of low energy

coupling that would result in little interference between the robot and its base, or "hot spots" where the degree of coupling is large. Its effectiveness was evaluated experimentally on a three link planar manipulator mounted to a flexible beam.

Xu and Shum [88] proposed a coupling factor to characterize the degree of dynamic coupling between a spacecraft and a robot mounted to it. The goal was to use this factor to find robot motions that minimize the interference to the spacecraft. Jiang [28] proposed a dynamic compensability measure and dynamic compensability ellipsoid to quantify the degree of coupling between a robot and a flexible space structure. The compensability measure predicted the ability of the robot to compensate for the endeffector position error resulting from the flexible displacements. This measure was used to find the additional joint motion that would compensate for the end effector error.

Papadopoulos and Dubowsky [56] discussed the problem of "dynamic singularities" in free-floating space manipulators. The spacecraft is assumed uncontrolled and will move in response to manipulator motion. They first assume a fixed inertial base at the center of mass of the system and find the Jacobian of the end effector written in terms of a coordinate system with its origin there (J*). When J* is not of full rank, the robot is in a workspace location where it is unable to move its end-effector in an inertial direction. These dynamic singularities depend upon the inertia properties of the robot and are also path dependent. They are a function of the manipulator joint space only and do not depend on spacecraft orientation. The singularities consist of the typical kinematic singularities plus infinitely more dynamically singular configurations. These are similar

to "inertial singularities" discussed later in this dissertation, where the rigid robot cannot create an interaction force or torque in one or more degrees of freedom.

Yoshida, Nenchev, and Uchiyama [93] considered vibration suppression control of a flexible space structure consisting of a robot mounted on a free-floating base. There are two parts to this work: reactionless motion control path planning and a vibration control subtask. The first subtask involves a technique called "reaction null space" where robot trajectories are selected to avoid creating dynamic reaction forces at the base of the manipulator. This paper considers the interactions between the two as a generic wrench, which is a function of the robot parameters, joint velocities, and joint accelerations. This quantity is then integrated to define the coupling momentum of the system. The reaction null space consists of trajectories that keep the coupling momentum constant so the interaction wrench is zero. In order for these paths to exist, the robot must have kinematic or dynamic redundancy, a selective reaction null space (when base flexibility is only an issue in limited degrees of freedom), or a singular rigid inertia matrix. Reactionless paths were determined for a simulated space based robot and verified to be effective on their experimental testbed, which consisted of a two link rigid robot mounted on a planar flexible base.

They also noted that the orthogonal complement of the reaction null space could be used to achieve maximum coupling, and thus could be useful for the vibration suppression subtask. Here they assume the robot is initially stationary so nonlinear effects are negligible. Furthermore, the flexible deflections are assumed small so the inertia submatrices are functions of the rigid joint variables only. The vibration control

subtask commands the rigid inertia effects proportional to the base velocity so damping is added to the system. This is similar to concepts by Lew and Moon [35-38] and Sharf [63] that will be discussed in section 2.5.

Yoshida and Nenchev [92] linked the field of space robots with the flexible base manipulator control problem. They compared several types of what they termed "underactuated mechanical systems", including a flexible base manipulator and a free-floating manipulator, and pointed out similarities and differences between the two. The free-floating robot was considered mounted to an inertia, while the flexible base manipulator was considered a rigid robot mounted to a mass-spring-damper system. The additional difference is the existence of a base constraint force for the flexible base manipulator. They pointed out the "reaction null space" is a common concept between the configurations. Thus, this concept could be valuable in the case of a redundant macro/micromanipulator to avoid or reduce disturbances created by commanded movements.

2.5 Micromanipulator Vibration Damping Techniques

The complexity of the control schemes required for macro/micromanipulator control reviewed in section 2.3 led to an area of research in which the micromanipulator is used to actively damp vibration in the macromanipulator. The control scheme becomes much less complex and the rigid robot actuators are typically able to respond more quickly to the vibration. The rigid robot can apply forces and torques directly to tip of the macromanipulator where the vibration is usually largest, and this also results in nearer

collocation of the actuators and the vibration. This technique can be used to reduce vibration that exists in the system or is induced by robot motion or external disturbances.

2.5.1 Energy Dissipation Methods

Torres, Dubowsky, and Pisoni [79] introduced a method entitled Pseudo-Passive Energy Dissipation (P-PED) for macro/micromanipulator vibration control. They assume locked macromanipulator joints while the micromanipulator performs its functions, so the system can be considered a redundant rigid manipulator mounted on a highly flexible supporting structure. The rigid manipulator is first moved into place, and then the controller is switched to the P-PED gains. These gains are chosen to maximize the energy dissipated by the rigid robot, essentially commanding the actuators of the robot to behave as passive linear springs and dampers during this phase of control. This method was shown effective in two degrees of freedom. However, this scheme is only applicable to a limited class of problems; i.e. those that allow the micromanipulator to be used exclusively for vibration damping when under P-PED control. After the P-PED controller eliminates the vibration, the original system controller is used. In addition, this technique uses measured rigid joint states only and assumes vibration in the macromanipulator is large enough to create motion in the micromanipulator. In systems where the actuators are highly nonlinear or demonstrate a large amount of friction, such as hydraulic actuators, the base vibration will not be observable in the rigid robot joint motion. Finally, it also requires the full macro/micromanipulator model in order to determine the appropriate P-PED gains.

Vliet and Sharf [81] introduced another energy dissipation method entitled impedance matching (IM). First, they developed an expression for the power dissipated by the rigid robot, $\tau^*\dot{\theta}$, where τ represents joint actuation torques and $\dot{\theta}$ represents the rigid robot joint velocities. By assuming constant amplitude harmonic joint motion at a single frequency, an expression for the joint velocities can be found. Then, assuming the use of a rigid joint PD controller, an expression for the joint torques can be found and PD gains selected to maximize the power dissipated by the rigid robot. The same limitations apply as for the P-PED method, except no macromanipulator information is needed.

Vliet also discusses in his thesis limitations associated with the P-PED method, further discusses the coupling map described in section 2.4, and proposes some additional measures of coupling [80]. One is an accelerative damping measure based on the Euclidean norm of the eigenvalues of a matrix that consists of the rigid robot inertias and the macromanipulator stiffnesses. Another coupling measure he proposes is a modal inertia map, which is derived from the joint torques required to hold the rigid robot in place as the macromanipulator vibrates. He also presents in his thesis and in [81] experimental work comparing the effectiveness of both the P-PED and IM methods in damping vibration in a single flexible link using a three degree of freedom rigid manipulator.

The P-PED and IM methods both assume the robot is first moved into place and then the gains are switched to the vibration control gains. Thus, energy is dissipated from the flexible manipulator only when the vibration control gains are used. They also rely on the assumption that coupling effects between the rigid and flexible manipulator are large enough to produce significant micromanipulator joint motion.

2.5.2 Inertial Damping Control

These schemes use sensory feedback of the base vibration to command the rigid manipulator to create the appropriate inertial interactions to actively control the base vibration. Lee and Book [11,33] developed a dual position and vibration damping controller for a macro/micromanipulator and proved its stability. They considered the rigid robot from the perspective that it has the ability to apply "inertial damping forces" onto the tip of the flexible robot. Dynamics were split into slow/fast submodels. A slow controller was used to handle the rigid joint positions while a fast controller was used for vibration suppression. The rigid control gain matrices were carefully chosen to keep time scale separation between the controller and the flexible modes of vibration. In this case, the rigid controller was critically damped and the position controller chosen to be approximately four times slower than the fundamental frequency of the flexible manipulator. The fast controller was based on strain rate feedback of the measured vibration. It was concluded that damping control was best because it is effective and easier to implement than a full state feedback law.

The scheme was experimentally verified for planar vibration on a two link flexible robot, RALF, with a three degree of freedom rigid robot, SAM (Small Articulated Manipulator) mounted on its tip. Two links of SAM were used to damp the vibration in a single fixed configuration selected to provide effective inertial interaction forces. Several

items were pointed out that still needed to be addressed to extend the general applicability of the technique. These included limits on joint torques (actuator saturation), required joint travel, limits on actuator bandwidth, and time scale separation between the joint controller and unmodeled flexible dynamics.

Sharf [63] recognized the interaction forces as the control variables of interest. The basic idea was that, given the relationship between the rigid robot joint accelerations and the interaction forces, the appropriate rigid body motion could be commanded to modify the dynamics of the flexible robot as desired. She showed in simulation the effectiveness of the method by commanding the desired interaction forces to be:

$$M_b \ddot{\mathbf{x}} + C_b \dot{\mathbf{x}} + K_b \mathbf{x} = \mathbf{F}_{IF} = -(G_p \mathbf{x} + G_d \dot{\mathbf{x}})$$
 (2-4)

 M_b , C_b , and K_b are the macromanipulator properties, \mathbf{x} represents the flexible robot generalized coordinates, and \mathbf{F}_{IF} are the interaction forces applied by the micromanipulator. G_p and G_d are the flexible motion feedback gains. This scheme was designed only to damp the macromanipulator vibration and would need to be followed by a joint PD controller to dissipate any remaining energy in the system and for rigid robot control.

Lew and Trudnowski [39] along with Evans and Bennett [40] added a flexible motion compensator based on strain rate feedback of the flexible system motion in parallel with an existing rigid joint PD controller. The assumption of small motion of the system allowed linearization about an operating point. Since the micromanipulator moves

relatively slowly compared to the fundamental frequency of the macromanipulator arm, the flexible dynamics were assumed negligible during commanded joint motion. The joint control loop was first closed and the flexible controller designed from the closed loop transfer function of the system. It was shown that, as long as the flexible motion controller is designed to be stable, the joint controller would also be stable. The vibration compensator was designed to add damping to the first mode while limiting the bandwidth to avoid exciting higher modes. The resulting flexible motion compensator takes the form:

$$C_f(s) = \left(\frac{T_1 s}{1 + T_1 s}\right) \left(\frac{k}{1 + T_2 s}\right) \cdots$$
 (2-5)

where T_1 and T_2 are time constants used to remove steady-state offsets and decrease high frequency gain, respectively. Additional lead-lag blocks were also needed for proper phase compensation. This signal was then added to the joint PD controller.

Raab and Trudnowski [58] considered an active damping technique using inertial torques generated by torque wheels mounted at the end of a single flexible link. They studied the flexible mode suppression only. They were able to demonstrate two degrees of freedom of vibration damping under varying payload masses. The vibration was sensed using strain gage pairs near the hub of the link. The resulting flexible motion compensator took the form:

$$C_f(s) = \frac{Ks}{s+p} \tag{2-6}$$

where p was chosen to provide optimum phase compensation at the mid-loading point.

Both of these techniques showed promising results for vibration control in two degrees of freedom under certain conditions.

Cannon [15] furthered the concept of inertial damping to include an inverse dynamics model, helping reduce the variation in performance throughout micromanipulator's workspace. He developed and demonstrated the effectiveness of the combined position and vibration controller in one degree of freedom on a flexible link with a single link rigid robot mounted to its tip to provide the vibration damping. The rigid position control scheme was chosen with stiff PD gains so the closed loop natural frequency of the system was approximately ten times the frequency of vibration to be controlled. Acceleration measured at the tip of the flexible link was used for feedback of the base vibration. In this case, the resulting vibration controller took the form:

$$\tau_f = \frac{K\ddot{x}}{-296 + 2.6378\sin\theta} \tag{2-7}$$

where \ddot{x} represents the measured base vibration in a single degree of freedom, θ is the position of the single flexible link rigid robot, and the denominator represents the rigid robot dynamics. This control torque is then added to the total PD joint control torque.

Cannon noted three disadvantages of using this method alone: it does not reduce the maximum amplitude of the vibration or the control effort needed, and can increase the settling time of the joint angle response. He also noted decreased improvement in damping as the joint PD gains are increased. He also combined the inertial damping method with command shaping techniques to show that the combination could provide

both vibration damping and amplitude reduction. The conclusion was that the use of the inertial damping technique does not preclude the use of another control technique if an additional performance measure, such as vibration amplitude, is a concern. These techniques were also later applied to a macro/micromanipulator at Pacific Northwest Laboratory [16] and showed similar improvements in performance.

Loper and Book [12,42] extended the inertial damping scheme to two degrees of freedom of vibration. They used the same control technique as Cannon except accelerations were measured in two directions and two links of a three degree of freedom robot were used. The controller took the form of equation 2-7, except accelerations in two directions were used and the rigid robot dynamics were modeled using two links of the robot. This technique was shown experimentally to be effective for planar vibration, again under certain conditions.

Lew and Moon [35-38] have recently considered the more general case of a robot attached to a passive compliant base, but only allow three degrees of freedom of base translation. The scheme compensates for base vibration while following a desired position. Real-time estimates of the nonlinear rigid body dynamics are computed from joint accelerations calculated from measured optical encoder position data. The coupled rigid body equation of motion (last row of equation 2-3) can be written as:

$$B_{\tau}(\mathbf{\theta})\ddot{\mathbf{\theta}} + N(\mathbf{\theta}, \dot{\mathbf{\theta}}, \mathbf{q}, \dot{\mathbf{q}}) = \mathbf{\tau}$$
 (2-8)

Again, instead of the notation used in his paper, notation used here is consistent with the notation introduced in equations 2-1 and 2-2. N represents the rigid robot nonlinear, gravitational, and coupling terms. The new rigid robot command torque becomes:

$$\boldsymbol{\tau} = \boldsymbol{\tau}_{p} - \hat{B}_{\tau}(\boldsymbol{\theta})\ddot{\boldsymbol{\theta}} + u \tag{2-9}$$

where τ_p represents the previously commanded joint torques, \hat{B}_{τ} is the estimated rigid robot inertia matrix, and u is the new rigid robot control input. Using Equation 2-9 in 2-8 and τ_p to estimate the nonlinear terms, the new equations of motion (equation 2-3 rearranged) become:

$$\begin{bmatrix} M_b + M_{b/r}(\mathbf{q}, \boldsymbol{\theta}) & M_{br}(\mathbf{q}, \boldsymbol{\theta}) \\ 0 & B_r(\boldsymbol{\theta}) \end{bmatrix} \begin{bmatrix} \ddot{\mathbf{x}}_f \\ \ddot{\boldsymbol{\theta}} \end{bmatrix} + \begin{bmatrix} C_b \dot{\mathbf{x}}_f + C_{br}(\dot{\mathbf{q}}, \mathbf{q}, \dot{\boldsymbol{\theta}}, \boldsymbol{\theta}) \\ 0 \end{bmatrix} + \begin{bmatrix} K_b & 0 \\ 0 & 0 \end{bmatrix} \begin{bmatrix} \mathbf{x}_f \\ \boldsymbol{\theta} \end{bmatrix} = \begin{bmatrix} 0 \\ u \end{bmatrix}$$
(2-10)

A two-time scale controller is then applied to the partially decoupled models with a fast controller for rigid link position and a slow controller for the vibration controller. The new rigid robot control input, u, is commanded so the joint accelerations are proportional to the flexible base velocity and damping is added to the system. Note to find the required joint control input, u, according to equation 2-9, requires the joint accelerations, which may be noisy and difficult to acquire real-time if only joint position measurements are available.

Of course, another area that is only briefly mentioned here is hardware modifications such as smart structures or passive damping, which may be the only solution to certain

problems. One example may be if the controlled motion is fully prescribed and no deviation is allowed for path modifications or to damp the vibration. Another example would be if the vibration is not controllable at the point of interface with the rigid robot or if the vibration is not observable (the micromanipulator or sensors can only be placed at a node point). Other cases could occur when the vibration controller is designed based on a reduced order model and fails to compensate for excitation of higher modes in the system. In these cases, another option may be to introduce a dissipation mechanism to enhance damping rather than modify the control loop [9,10].

2.6 Limitations of Previous Research

Control of macro/micromanipulators has been investigated using many different techniques. As noted previously, inertial damping schemes using the micromanipulator to damp the vibration is an attractive compromise between control system complexity and system performance. These schemes have been developed and demonstrated for a very specialized class of systems in unique configurations. Some of the limitations of the research performed so far in this area are:

1. Full macromanipulator flexibility (translational and rotational) has not been considered. Lew and Moon [35-38] have taken the more general approach of considering the macromanipulator as a compliant base, but limit the motion to only translational motion, which greatly simplifies the problem. The space robotics work by Yoshida et al [92,93] considers the case of a robot mounted on a floating base and has lent some valuable theoretical work to this area, but detailed work is yet to be seen.

- 2. The variation in performance throughout the workspace has not been fully addressed. In particular, there are locations in the workspace where the ability of the manipulator to generate effective interaction forces and torques is diminished. There has been some work in space robotics by Torres et al [77,78] and Vliet [80] that begins to address this issue. A rigorous investigation of these singularities, similar to the work done by Papadopoulos and Dubowsky [56] for space dynamic singularities, is lacking. In addition, there has not been a method proposed to address how to use the variation in performance to improve the effectiveness of the damping scheme.
- 3. Most of the above schemes have assumed ideal system modeling for development of the vibration control scheme. Lew and Moon [35-38] looked at estimating nonlinear and coupling effects but practical implementation of this method could become challenging. There still needs to be a detailed investigation of the coupled system model as well as an evaluation of the robustness of the control scheme to modeling errors.
- 4. Few hardware demonstrations have been performed on realistic macro/micromanipulators. Those that have been were on robots in specific configurations and with only one or two vibrational degrees of freedom. In addition, the only two degree of freedom demonstrations have been on robots that have naturally decoupled inertial damping performance. The effects of (1-3) may become even more important with additional degrees of freedom.
- 5. Methods to maximize the amount of damping provided by the vibration controller have not been addressed. In addition, practical limitations such as actuator saturation and limits on joint travel have not been addressed. In fact, very little guidance is available on

choosing the vibration control gains or establishing limits on gains that consider these factors.

6. The impact of the vibration damping controller on the position controller has not been systematically analyzed. Some researchers have chosen to consider the vibration problem separately [12,15,63,81,93] while others have carefully chosen the position control and vibration control loops to have time scale separation [11,33,35].

Of course, there is plenty of room for additional work in this area. This dissertation seeks to address some of the major issues remaining in the field. In particular, this research includes:

- 1. Consideration of the multi-degree of freedom (DOF) macro/micromanipulator control problem by studying the analogous problem of a rigid robot mounted on a flexible base.
- 2. Investigation of the variation in performance throughout the workspace and inertial singularities, or locations in the workspace where the rigid robot loses its ability to create effective interactions in one or more degrees of freedom.
- 3. Development of a control scheme that provides active base vibration damping in parallel with position control and establishment of appropriate vibration control gain limits.
- 4. Simulation and experimental work on a realistic multi-degree of freedom macro/micromanipulator.

CHAPTER III

FLEXIBLE BASE MANIPULATOR MODELING

3.1 Introduction

This chapter describes modeling of a rigid robot mounted on a flexible base. The flexible base represents a multi-link macromanipulator with locked joints. The rigid robot will provide the fine-tuned end point position control. In this research, it is also used to damp vibration in the flexible base. Thus, it is especially important to characterize the dynamic interactions between the macro and micromanipulator and in order to do this the system needs to be modeled.

First, a recursive Lagrangian approach is described which is used to model the macromanipulator. This approach is commonly used in flexible robot modeling and hence is only briefly reviewed here. Next, the micromanipulator model is developed using a recursive Newton-Euler algorithm. The important dynamic effects that need to be characterized are the required joint torques to operate the robot and the interaction forces and torques acting at the base of the robot. The joint torque equations are the same form as those for a fixed base rigid robot with additional coupling terms due to the base motion. The interaction forces and torques are explicitly solved for and are the subject of

further investigation in Chapter 4. Chapter 5 then investigates how to control these interactions to damp the base vibration.

3.2 Flexible Base Model

The flexible base represents a multi-link flexible manipulator with locked joints. The method chosen here is a recursive Lagrangian formulation using a finite number of assumed modes, which is applicable to an n-DOF flexible link manipulator. The advantage of this method is its ability to include flexible link deformation. This method is well documented and more detailed descriptions may be found in the paper by Book [8] and others who have used this method to model flexible manipulators [15,32,34,42, 52,53,62,72]. However, other methods may be used provided they yield inertia and stiffness properties and adequately capture the significant dynamics of the macromanipulator. Modal damping estimates are also often added and could be based on experimental results or estimated from material properties.

The key difference between a flexible and rigid robot is its continuous nature. Both rigid joint motion and elastic deflections govern the motion of a flexible robot, so it theoretically has an infinite number of degrees of freedom. However, it is necessary to develop a more manageable model that approximates the system, yet adequately captures the significant dynamics. The approach described here begins with assuming an appropriate number of modes to model the flexibility in each link for each degree of freedom. The position of an arbitrary point on each link is composed of summations of the assumed mode shapes multiplied by the generalized coordinates. These are used to

form the kinetic and potential energy of the system and with Lagrange's equations yield the equations of motion of the system. It is assumed for this work the resulting macromanipulator model can be linearized about an operating point, i.e. at a fixed joint configuration and neglecting the flexible generalized coordinates in the inertia, stiffness, and damping matrices. It is further assumed the flex model is developed referenced to an inertial coordinate frame coincident with its last link, or at the base of the micromanipulator. The resulting matrices, although constant at a given locked joint configuration, will generally be fully coupled and the generalized coordinates will only include the flexible states.

It is assumed each link could have two degrees of freedom of transverse vibration plus torsion about the z-axis (Figure 3-1) and that axial vibration is negligible. Thus, there will be a total of $\sum_{i=1}^{n} \sum_{k=1}^{3} m_{ik}$ equations of motion and generalized coordinates, where n is the number of macromanipulator links, k represents vibration in the x, y, or θ_z direction, and m_{ik} is the number of assumed modes for the k^{th} direction of vibration of the i^{th} link.

3.2.1 Assumed Modes

The first task is to assume an appropriate set of modes for each degree of freedom. The mode shapes could be based on many methods, such as Ritz series, finite element models, or analytical results for continuous systems [24]. The chosen set of modes only needs to be linearly independent and satisfy the system geometric boundary conditions

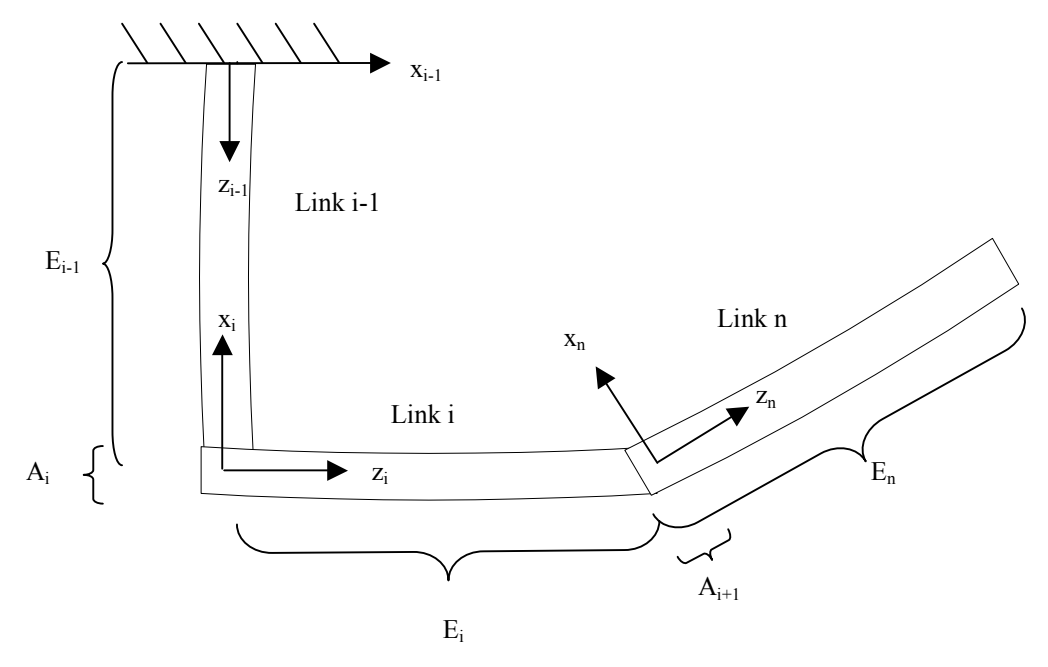


Figure 3-1 Flexible Link Model Notation

[13]. A reasonable method of estimating assumed modes for flexible manipulators is based on Euler-Bernoulli, or classical beam theory. In order for this to apply, the centroids of each link must lie along the z-axis in the undeformed state. In addition, the cross-sectional dimensions must be small relative to the length of the link and the cross sectional shape should vary little along the z direction [24]. These are often reasonable assumptions for a macromanipulator, which is characterized by its long, lightweight links. Transverse and torsional vibration mode shapes for flexible beams subject to common boundary conditions may be found in many references, including Ginsberg [24], Meirovitch [49], Rao [59], and Weaver, Timoshenko, and Young [83].

The governing differential equation of motion for transverse vibration of a uniform beam [83] is:

$$EI\frac{\partial^4 u(z,t)}{\partial z^4} + \rho A \frac{\partial^2 u(z,t)}{\partial z^2} = 0$$
 (3-1)

u(z,t) describes the resulting vibration in the x direction (or v(z,t) in the y direction), as defined in Figure 3-1, for the i^{th} link. E is modulus of elasticity, ρ is mass density, A is the cross-sectional area and I is the moment of inertia of the link about the x or y axis (all assumed constant). Using separation of variables,

$$u(z,t) = \sum_{i=1}^{m_{ik}} \phi_j(z) T(t)$$
 (3-2)

a basis set of mode shape functions can be found of the form:

$$\phi_i = C_{i1}\sin(\beta_i z) + C_{i2}\cos(\beta_i z) + C_{i3}\sinh(\beta_i z) + C_{i4}\cosh(\beta_i z)$$
(3-3)

 C_j s and β_j s are determined from the eigenvalue problem appropriate for the system's boundary conditions. m_{ik} should be truncated to a reasonable number of modes to adequately model the flexible dynamics without unnecessarily increasing model size and complexity. Some researchers have found that two or three modes suffice to represent flexible dynamics on relatively uncomplicated systems [13], based on the low amplitude of the higher frequency modes.

Common boundary conditions used for modeling flexible manipulators are fixed/free or pinned-pinned, but other boundary conditions may be more applicable depending on the specific application. For example, fixed/free boundary conditions are:

$$\phi_{j}(0) = 0 \text{ (no motion at attach point)}$$

$$\frac{d\phi_{j}(0)}{dz} = 0 \text{ (zero velocity at attach point)}$$

$$\frac{d^{2}\phi_{j}(0)}{dz^{2}} = 0 \text{ (no bending moment at attach point)}$$

$$\frac{d^{3}\phi_{j}(0)}{dz^{3}} = 0 \text{ (no shear force at attach point)}$$
(3-4)

Using these boundary conditions in equation 3-3 results in a set of 4x4 equations that yield the following eigenfunctions, or assumed modes:

$$\phi_{j} = C_{j} \left\{ \sin(\beta_{j}z) - \sinh(\beta_{j}z) + \frac{\cos(\beta_{j}L) + \cosh(\beta_{j}L)}{\sin(\beta_{j}L) + \sinh(\beta_{j}L)} \left[\cos(\beta_{j}z) - \cosh(\beta_{j}z) \right] \right\}$$

$$C_{j} \text{ are chosen such that } \phi_{j} = 1 \text{ at } z = L \text{ (link length)}$$
(3-5)

The first four natural frequencies for transverse vibration of a beam with fixed-free boundary conditions are [83]:

$$\beta_1 L = 1.875104$$
 $\beta_2 L = 4.694091$
 $\beta_3 L = 7.854757$
 $\beta_4 L = 10.995541$ (3-6)

The other issue that could be important for flexible manipulators is torsional beam vibration. Assuming a uniform shaft with uniform cross section, the free vibration is governed by [49]:

$$\frac{G}{\rho} \frac{\partial^2 \theta_z(z,t)}{\partial z^2} = \frac{\partial^2 \theta_z(z,t)}{\partial t^2}$$
 (3-7)

where G is the shear modulus of elasticity (assumed constant) and θ_z describes the rotation of the flexible link about the z-axis. Again, separation of variables allows solving for the mode shapes, which take the form:

$$\chi_{j}(z) = A_{j} \cos \frac{\omega_{j} z}{c} + B_{j} \sin \frac{\omega_{j} z}{c}$$

$$c = \sqrt{\frac{G}{\rho}}$$
(3-8)

The frequencies again depend on the boundary conditions and for fixed/free boundary conditions, the mode shapes take the form:

$$\chi_{j}(z) = C_{j} \sin(\frac{(2j+1)\pi}{2L}z)$$
 (3-9)

The motion of the ith link can now be described as a summation of the assumed modes and associated generalized coordinates.

$$u_{i}(z_{i},t) = \sum_{j=1}^{m_{ik}} \phi_{ij}(z_{i}) p_{ij}(t)$$

$$v_{i}(z_{i},t) = \sum_{j=1}^{m_{ik}} \psi_{ij}(z_{i}) q_{ij}(t)$$

$$\theta_{zi}(z_{i},t) = \sum_{i=1}^{m_{ik}} \chi_{i}(z_{i}) s_{ij}(t)$$
(3-10)

 u_i and v_i are the resulting i^{th} link deflection in the x and y directions and θ_{zi} the torsional rotation about the z-axis. p_{ij} , q_{ij} , and s_{ij} are the time-varying amplitudes of mode j of link i in the x, y, and θ_z directions.

3.2.2 Kinetic and Potential Energy

Next Lagrange's equations will be used to extract the inertia and stiffness properties of the macromanipulator. First, kinetic and potential energy expressions need to be formed for each flexible link. The kinetic energy terms represent distributed translational and rotational energy, while the potential energy terms represent elastic bending effects and gravity.

First, an arbitrary position on the macromanipulator needs to be described relative to the fixed inertial coordinate system x_{i-1} , y_{i-1} , z_{i-1} in Figure 3-1. The coordinate transformation between links involves both the rigid joint transformations (A_i) as well as link deflection transformations (E_i). Book [8] described a practical means of doing this by using 4x4 homogeneous transformation matrices to describe the position and orientation of one coordinate frame with respect to another.

Using the notation introduced in his paper and referenced to the fixed inertial coordinates at the base of the macromanipulator, the position of a point on link i can be written as:

$$\mathbf{h}_{i} = W_{i} \mathbf{h}_{i}^{i}$$

$$\mathbf{h}_{i} = \text{point referenced to fixed frame} = \begin{bmatrix} \mathbf{r}_{i} \\ 1 \end{bmatrix}$$

$$\mathbf{h}_{i}^{i} = \text{point referenced to link i frame} = \begin{bmatrix} u_{i} \\ v_{i} \\ z_{i} \\ 1 \end{bmatrix}$$
(3-11)

 u_i and v_i are as defined in equation 3-10 and z_i is the distance along link i. The transformation W_i can be split into rigid and flexible components, as defined in Figure 3-1, or:

$$W_i = W_{i-1} E_{i-1} A_i (3-12)$$

For this research, A_i is assumed fixed at a specific macromanipulator joint configuration. E_i , however, must include both link deflections as well as rotations. The rotation that occurs between i and i-1 is due to the small rotations at the tip caused by the transverse vibration as well as the torsional vibration.

Assuming small rotation angles, the direction cosine matrix simplifies and the complete link transformation matrix can be written as:

$$E_{i} = \begin{bmatrix} 1 & 0 & 0 & 0 \\ 0 & 1 & 0 & 0 \\ 0 & 0 & 1 & l_{i} \\ 0 & 0 & 0 & 1 \end{bmatrix} + \begin{bmatrix} 0 & \theta_{zi} & \theta_{yi} & u_{i} \\ \theta_{zi} & 0 & -\theta_{xi} & v_{i} \\ -\theta_{yi} & \theta_{xi} & 0 & 0 \\ 0 & 0 & 0 & 0 \end{bmatrix}_{z=L}$$

$$(3-13)$$

where L_i is the length of link i. The assumption of small rotations gives:

$$\theta_{xi}(z_i, t) \approx \sum_{j=1}^{m_i} \frac{\partial \psi_{ij}(z_i)}{\partial z_i} q_{ij}(t)$$

$$\theta_{yi}(z_i, t) \approx \sum_{j=1}^{m_i} \frac{\partial \phi_{ij}(z_i)}{\partial z_i} p_{ij}(t)$$
(3-14)

However, if the macromanipulator has multiple links, it will be more useful to write the position vector referenced to a fixed coordinate system coincident with the last link of the macromanipulator (x_n, y_n, z_n) in its equilibrium position (E=I). Thus, the position vector can be found from:

$$\mathbf{h}_{i} = A_{i}^{-1} W_{i} \mathbf{h}_{i}^{i} = \begin{bmatrix} \mathbf{r}_{i} \\ 1 \end{bmatrix}$$
 (3-15)

 $\boldsymbol{\theta}$ is found the same way except using the rotational terms only in E_i (3x3s). The potential and kinetic energy of the system can now be written as:

$$T = \sum_{i=1}^{n} \left[\frac{1}{2} \rho_{i} A_{i} \int_{0}^{L_{i}} \dot{\mathbf{r}}_{i}^{T} \dot{\mathbf{r}}_{i} dz_{i} \right] + \sum_{i=1}^{n} \left[\frac{1}{2} I_{i} \int_{0}^{L_{i}} \dot{\boldsymbol{\theta}}_{i}^{T} \dot{\boldsymbol{\theta}}_{i} dz_{i} \right]$$

$$V = \sum_{i=1}^{n} \frac{1}{2} E_{i} I_{xi} \int_{0}^{L_{i}} \left(\frac{\partial \theta_{xi}}{\partial z_{i}} \right)^{2} dz_{i} + \sum_{i=1}^{n} \frac{1}{2} E_{i} I_{yi} \int_{0}^{L_{i}} \left(\frac{\partial \theta_{yi}}{\partial z_{i}} \right)^{2} dz_{i} + \sum_{i=1}^{n} \frac{1}{2} G_{i} J_{i} \int_{0}^{L_{i}} \left(\frac{\partial \theta_{zi}}{\partial z_{i}} \right)^{2} dz_{i}$$
(3-16)

where:

 ρ = mass density

A = cross-sectional area

E = modulus of elasticity

 I_x, I_y = area moment of inertia of the cross sectional area computed about the x or y axis

G = modulus of rigidity

J = polar area moment of the cross sectional area computed about the neutral axis

One of the benefits of this method is that as much detail can be included in the equations of motion as desired. Here many of the assumptions that have been used and justified by other researchers have been used to pare the equations of motion down to the most significant contributions [8,24,34,46,52,72,83].

Now Lagrange's equations can be used to derive the equations of motion.

$$\frac{d}{dt} \left(\frac{\partial T}{\partial \dot{q}_i} \right) - \frac{\partial T}{\partial q_i} + \frac{\partial V}{\partial q_i} = \mathbf{Q}_i$$
 (3-17)

 \mathbf{Q}_i are the nonconservative generalized forces applied to the macromanipulator corresponding to the generalized coordinate \mathbf{q}_i . In this research, these are the interaction forces and torques created by the micromanipulator. The generalized forces are determined from the virtual work done by the micromanipulator, or

$$\delta Work = \mathbf{F}_{\scriptscriptstyle H} \delta r + \mathbf{\tau}_{\scriptscriptstyle H} \delta \theta \tag{3-18}$$

The infinitesimal displacements and rotations at the tip of the macromanipulator are given by equation 3-15 evaluated at z_i = L_i . The partial derivatives of the resulting infinitesimal displacements and rotations are taken with respect to each generalized coordinate to find the generalized forces.

The final equations of motion take the form:

$$M(\tilde{\mathbf{q}})\ddot{\mathbf{q}} + C(\tilde{\mathbf{q}})\dot{\mathbf{q}} + K(\tilde{\mathbf{q}})\mathbf{q} = \mathbf{Q}$$
(3-19)

where it is assumed the mass, stiffness, and damping matrices can be linearized about a nominal operating point. Since the joints of the macromanipulator are locked, \mathbf{q} represents the flexible states and consists of a finite number of modes of interest. The mass, stiffness, and damping matrices can be linearized and assumed approximately constant about an operating point, $\tilde{\mathbf{q}}$.

3.3 Flexible Base Rigid Manipulator Model

In order to better understand and analyze the coupling effects between a rigid manipulator and flexible macromanipulator, the problem was generalized into a rigid manipulator mounted on a flexible base (Figure 3-2). The base represents inertia, stiffness, and damping properties of a distributed parameter system, modeled as discussed in section 3.2. There are two goals of this portion of the work. The first goal is to develop the equations of motion in order to model and simulate the interactions between the robot and its flexible base. The second is to investigate these effects in order to determine which are most significant. The analysis of the interaction forces and torques is discussed in Chapter 4.

A recursive Newton-Euler method, commonly used to develop joint torque equations for rigid robots [18,48,61], was used to find the interaction forces and torques. Other methods are also valid if they allow solving for the interaction forces and torques that act at the base of the micromanipulator. It is assumed that the origin of an inertial coordinate

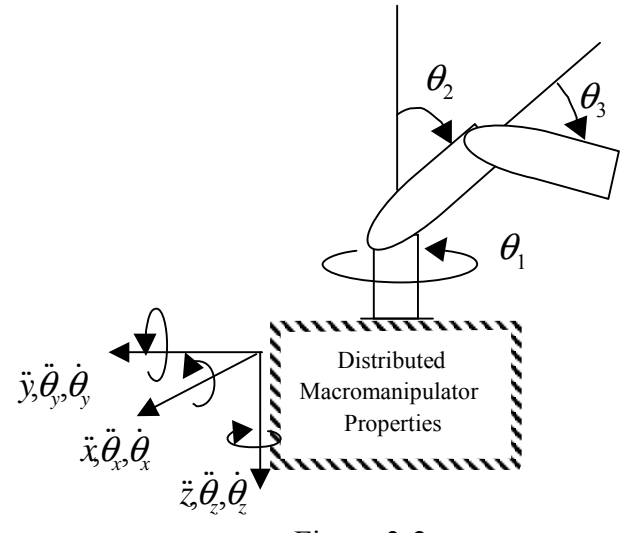


Figure 3-2 Flexible Base Rigid Robot

system is located at the base of the rigid robot, or at the tip of the undeformed macromanipulator. The elastic states of the macromanipulator affect the rigid robot by moving its base in Cartesian space (Figure 3-2). In developing the equations of motion, these become boundary conditions on the rotational velocities and translational and rotational accelerations of the first link and are then propagated forward to the other links. Then, a backward recursion is used to solve for the forces and torques acting on each link, with the final set giving the forces and torques acting between the rigid robot and the macromanipulator.

The assumptions made in the development of these ideal equations of motion are:

- 1) No contact forces or moments are applied to the tip of the micromanipulator
- 2) Off-diagonal products of inertia are negligible
- 3) Position vectors for off-axis distances to link centers of gravity (CGs) are negligible

- 4) Friction effects and other nonlinearities are not modeled
- 5) Rotor inertia effects are not included.

If actuator dynamics dominate the rigid robot performance, an alternate form of the rigid robot model may apply. However, the interaction forces and torques described by this model will still be valid.

First, consider for the moment a single link rigid robot mounted to a flexible base. The base is free to move in any direction. The arm rotates about the x-axis as defined in Figure 3-3 (out of the page).

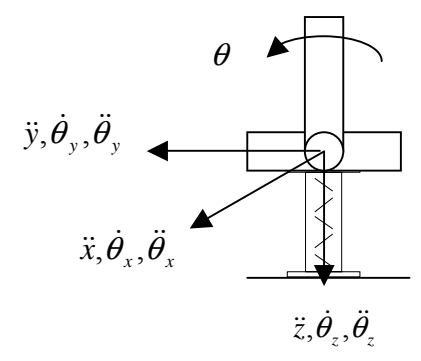


Figure 3-3 Flexible Base Single Link Rigid Robot

The acceleration of the center of gravity of the link is given by:

$$\mathbf{a}_{G} = \mathbf{a}_{0} + \boldsymbol{\alpha} \times \mathbf{r}_{CG} + \boldsymbol{\omega} \times (\boldsymbol{\omega} \times \mathbf{r}_{CG})$$
where:
$$\mathbf{a}_{0} = \ddot{x}\hat{i} + \ddot{y}\hat{j} + (\ddot{z} + g)\hat{k}$$

$$\boldsymbol{\omega} = (\dot{\theta}_{x} + \dot{\theta})\hat{i} + \dot{\theta}_{y}\hat{j} + \dot{\theta}_{z}\hat{k}$$

$$\boldsymbol{\alpha} = (\ddot{\theta}_{x} + \ddot{\theta})\hat{i} + \ddot{\theta}_{y}\hat{j} + \ddot{\theta}_{z}\hat{k}$$
(3-20)

where:

 \mathbf{a}_{G} = acceleration of the center of gravity of the rigid link

 \mathbf{a}_0 = acceleration of the base

g = gravitational constant

 ω = angular velocity of the link

 α = angular acceleration of the link

 \mathbf{r}_{CG} = position vector from the base to the center of gravity of the link

Now the interaction forces and torques at the base of the link can be solved for:

$$\mathbf{F}_{IF} = m \, \mathbf{a}_{G}$$

$$\mathbf{\tau}_{IF} = -\mathbf{r}_{CG} \times \mathbf{F}_{IF} + \begin{bmatrix} I_{xx} (\ddot{\theta}_{x} + \ddot{\theta}) \\ I_{yy} \ddot{\theta}_{y} \\ I_{zz} \ddot{\theta}_{z} \end{bmatrix}$$
(3-21)

where m is the mass of the robot arm and I_{xx} , I_{yy} , and I_{zz} are moments of inertia of the link about the respective axes. Just for this one link case, the interaction forces take the form:

$$\begin{bmatrix} F_{IFx} \\ F_{IFy} \\ F_{IFz} \end{bmatrix} = m \begin{cases} \begin{bmatrix} 1 & 0 & 0 \\ 0 & 1 & 0 \\ 0 & 0 & 1 \end{bmatrix} \begin{bmatrix} \ddot{x} \\ \ddot{y} \\ \ddot{z} \end{bmatrix} + \begin{bmatrix} 0 \\ rc\theta \\ rs\theta \end{bmatrix} \ddot{\theta} + \begin{bmatrix} 0 & -rc\theta & -rs\theta \\ rc\theta & 0 & 0 \\ rs\theta & 0 & 0 \end{bmatrix} \begin{bmatrix} \ddot{\theta}_x \\ \ddot{\theta}_y \\ \ddot{\theta}_z \end{bmatrix} + \begin{bmatrix} 0 & 0 & 0 & 0 \\ -rs\theta & 0 & -rs\theta \\ rc\theta & rc\theta & 0 \end{bmatrix} \begin{bmatrix} \dot{\theta}_x^2 \\ \dot{\theta}_y^2 \\ \dot{\theta}_z^2 \end{bmatrix} \\ + \begin{bmatrix} rs\theta & -rc\theta & 0 \\ 0 & 0 & -rc\theta \\ 0 & 0 & rs\theta \end{bmatrix} \begin{bmatrix} \dot{\theta}_x \dot{\theta}_y \\ \dot{\theta}_x \dot{\theta}_z \\ \dot{\theta}_y \dot{\theta}_z \end{bmatrix} + \begin{bmatrix} 0 & rs\theta & -rc\theta \\ -2rs\theta & 0 & 0 \\ 2rc\theta & 0 & 0 \end{bmatrix} \begin{bmatrix} \dot{\theta}_x \dot{\theta} \\ \dot{\theta}_y \dot{\theta} \\ \dot{\theta}_z \dot{\theta} \end{bmatrix} + \begin{bmatrix} 0 \\ 0 \\ \dot{\theta}_z \dot{\theta} \end{bmatrix} \end{cases}$$
(3-22)

Here the abbreviated form for the trigonometric functions, $c\theta$ and $s\theta$, are used to represent $\cos\theta$ and $\sin\theta$, as will be the case for the remainder of this document. Using the notation for the macromanipulator in the previous section and equations 3-10 and 3-14, the displacements and rotations at the tip of the macromanipulator can be written in terms

of the generalized coordinates, **q**. Thus, these equations can be written in more compact form as:

$$\begin{bmatrix} F_{IF} \\ \tau_{IF} \end{bmatrix} = \begin{bmatrix} C_f(\theta) & B_f(\theta) \\ C_{\tau_0}(\theta) & B_{\tau_0}(\theta) \end{bmatrix} \begin{bmatrix} \ddot{\mathbf{q}} \\ \ddot{\theta} \end{bmatrix} + \begin{bmatrix} N_f(\theta) \\ N_{\tau_0}(\theta) \end{bmatrix} \dot{\theta}^2 + \begin{bmatrix} N_{fc1}(\theta) \\ N_{\tau_{0c1}}(\theta) \end{bmatrix} \dot{\mathbf{q}}^2 + \begin{bmatrix} N_{fc2}(\theta, \dot{\theta}) \\ N_{\tau_{0c2}}(\theta, \dot{\theta}) \end{bmatrix} \dot{\mathbf{q}} + \begin{bmatrix} G_f(\theta) \\ G_{\tau_0}(\theta) \end{bmatrix} \tag{3-23}$$

The goal of the control scheme is to control the interaction forces and torques via the rigid robot to damp vibration in the macromanipulator. From the above reduced equations of motion, it is apparent the effects that directly influence the interaction forces and torques are given by:

$$\begin{bmatrix} F_{IF} \\ \tau_{IF} \end{bmatrix} = \begin{bmatrix} B_f(\theta) \\ B_{\tau 0}(\theta) \end{bmatrix} \ddot{\theta} + \begin{bmatrix} N_f(\theta) \\ N_{\tau 0}(\theta) \end{bmatrix} \dot{\theta}^2$$
(3-24)

The generic algorithm is similar to the well-documented Newton-Euler method for deriving the equations of motion for a rigid robot, except in this case the interaction forces and torques are required in addition to the joint torque equations. The notation used below is consistent with that found in Sciavicco and Siciliano [61] where the more efficient method of referring the vectors to the current frame associated with link i is used. The algorithm uses forward recursions, which propagate the velocities and accelerations of each link forward to the next link. This is followed by backward recursions, which solve for the forces and torques acting on each link starting with the force and moment applied to the end effector (assumed zero for this work).

Using parameters as defined in Figure 3-4, the forward recursions take the form:

$$\boldsymbol{\omega}_{i}^{i} = \begin{cases} (R_{i}^{i-1})^{T} [\boldsymbol{\omega}_{i-1}^{i-1} + \dot{\theta}_{i} z_{0}] & \text{revolute} \\ (R_{i}^{i-1})^{T} \boldsymbol{\omega}_{i-1}^{i-1} & \text{prismatic} \end{cases}$$

$$\dot{\boldsymbol{\omega}}_{i}^{i} = \begin{cases} (R_{i}^{i-1})^{T} [\dot{\boldsymbol{\omega}}_{i-1}^{i-1} + \ddot{\boldsymbol{\theta}}_{i} z_{0} + \dot{\boldsymbol{\theta}}_{i} \boldsymbol{\omega}_{i-1}^{i-1} \times z_{0}] & \text{revolute} \\ (R_{i}^{i-1})^{T} \dot{\boldsymbol{\omega}}_{i-1}^{i-1} & \text{prismatic} \end{cases}$$

$$\ddot{\boldsymbol{p}}_{i}^{i} = \begin{cases} (R_{i}^{i-1})^{T} \ddot{\boldsymbol{p}}_{i-1}^{i-1} + \dot{\boldsymbol{\omega}}_{i}^{i} \times r_{i-1}^{i} + \boldsymbol{\omega}_{i}^{i} \times r_{i-1}^{i} + \boldsymbol{\omega}_{i}^{i} \times r_{i-1}^{i}) & \text{revolute} \\ (R_{i}^{i-1})^{T} (\ddot{\boldsymbol{p}}_{i-1}^{i-1} + \dot{\boldsymbol{d}}_{i} z_{0}) + 2\dot{\boldsymbol{d}}_{i} \boldsymbol{\omega}_{i}^{i} \times (R_{i}^{i-1})^{T} z_{0} + \dot{\boldsymbol{\omega}}_{i}^{i} \times r_{i-1}^{i} + \boldsymbol{\omega}_{i}^{i} \times (\boldsymbol{\omega}_{i}^{i} \times r_{i-1}^{i}) & \text{prismatic} \end{cases}$$

$$\ddot{\boldsymbol{p}}_{ci}^{i} = \ddot{\boldsymbol{p}}_{i}^{i} + \dot{\boldsymbol{\omega}}_{i}^{i} \times rc_{i}^{i} + \boldsymbol{\omega}_{i}^{i} \times (\boldsymbol{\omega}_{i}^{i} \times rc_{i}^{i}) \qquad (3-25)$$

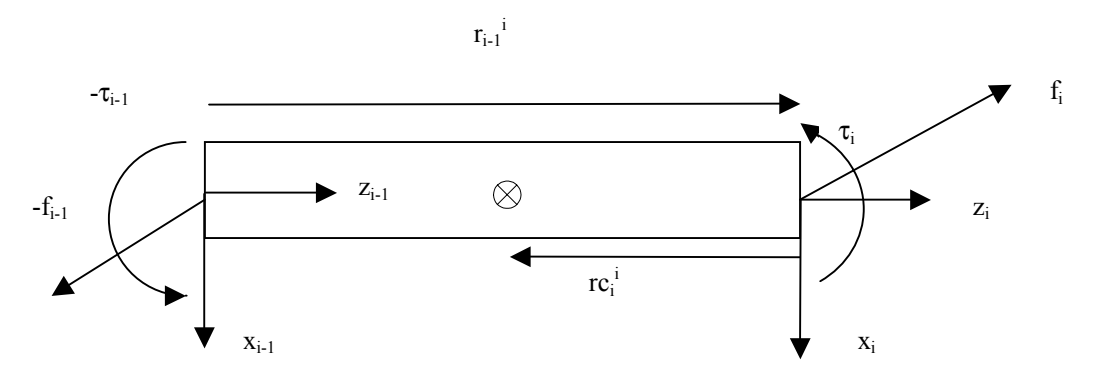


Figure 3-4
Notation Used for Recursive Newton-Euler Algorithm

where:

$$z_0 = \text{unit vector of joint 0 axis} = \begin{bmatrix} 0 \\ 0 \\ 1 \end{bmatrix}$$

 ω_i^i = angular velocity of link i

 $\dot{\omega}_{i}^{i}$ = angular acceleration of link i

 \ddot{p}_{i}^{i} = linear acceleration of the origin of frame i

 \ddot{p}_{ci}^{i} = linear acceleration of the center of mass of link i

The backward recursions take the form:

$$f_{i} = R_{i+i}^{i} f_{i+1} + m_{i} \ddot{p}_{ci}^{i}$$

$$\tau_{IFi} = R_{i+i}^{i} \tau_{IFi+1} + R_{i+i}^{i} f_{i+1} \times rc_{i}^{i} - f_{i} \times rc_{i}^{i} + I_{i} \dot{\omega}_{i}^{i} + \omega_{i}^{i} \times I_{i} \omega_{i}^{i}$$

$$\tau_{i} = \begin{cases} \tau_{IFi}^{T} (R_{i}^{i-1})^{T} z_{0} & \text{revolute} \\ f_{I}^{T} (R_{i}^{i-1})^{T} z_{0} & \text{prismatic} \end{cases}$$

$$f_{i} = \text{interaction force between links i and i-1}$$

$$\tau_{IFi} = \text{interaction torque between links i and i-1}$$

$$\tau_{i} = \text{generalized joint actuation torque for link i}$$

$$(3-26)$$

Boundary conditions of the tip velocities and accelerations of the macromanipulator are applied to the first link and propagated through the forward recursions. It is assumed that the micromanipulator is not in contact with any object so the forces and torques applied to the tip of its last link are zero.

The equations of motion take the general form:

$$\begin{aligned} \mathbf{F}_{IF} &= B_f(\boldsymbol{\theta}) \ddot{\boldsymbol{\theta}} + N_f(\boldsymbol{\theta}, \dot{\boldsymbol{\theta}}_i \dot{\boldsymbol{\theta}}_j) + C_f(\boldsymbol{\theta}) \ddot{\mathbf{q}} + N_{fc}(\mathbf{q}, \dot{\mathbf{q}}, \boldsymbol{\theta}, \dot{\boldsymbol{\theta}}) \\ \boldsymbol{\tau}_{IF} &= B_{r0}(\boldsymbol{\theta}) \ddot{\boldsymbol{\theta}} + N_{r0}(\boldsymbol{\theta}, \dot{\boldsymbol{\theta}}_i \dot{\boldsymbol{\theta}}_j) + C_{r0}(\boldsymbol{\theta}) \ddot{\mathbf{q}} + N_{r0c}(\mathbf{q}, \dot{\mathbf{q}}, \boldsymbol{\theta}, \dot{\boldsymbol{\theta}}) \\ \boldsymbol{\tau} &= B_r(\boldsymbol{\theta}) \ddot{\boldsymbol{\theta}} + N_r(\boldsymbol{\theta}, \dot{\boldsymbol{\theta}}_i \dot{\boldsymbol{\theta}}_j) + C_r(\boldsymbol{\theta}) \ddot{\mathbf{q}} + N_{rc}(\mathbf{q}, \dot{\mathbf{q}}, \boldsymbol{\theta}, \dot{\boldsymbol{\theta}}) \end{aligned}$$
(3-27)

 θ represents the rigid robot joint variables and \mathbf{q} represents the flexible base generalized coordinates. B_f , $B_{\tau 0}$, C_f , and $C_{\tau 0}$ represent inertia effects of the micro and macro manipulators, respectively. B_f and $B_{\tau 0}$ are particularly important because they represent the controllable rigid robot inertia effects. These matrices are, in general, not symmetric, or positive definite (but the inertia matrix for the complete coupled system is, of course). The remaining terms in 3-27 represent nonlinear and gravitational effects. The third equation is the typical joint torque equation with extra coupling terms. Often actuator dynamics or other effects dominate the robot performance, so this equation could take

other forms. However, for this work it is assumed the relationship between the joint actuation torques and joint positions is known and controllable.

These equations were written in symbolic form in Matlab [21]. The macromanipulator tip angular velocities, angular accelerations, and translational accelerations are the boundary conditions and are given by:

$$\boldsymbol{\omega}_{0}^{0} = \begin{bmatrix} \boldsymbol{\omega}_{x} \\ \boldsymbol{\omega}_{y} \\ \boldsymbol{\omega}_{z} \end{bmatrix}, \dot{\boldsymbol{\omega}}_{0}^{0} = \begin{bmatrix} \dot{\boldsymbol{\omega}}_{x} \\ \dot{\boldsymbol{\omega}}_{y} \\ \dot{\boldsymbol{\omega}}_{z} \end{bmatrix}, \ddot{\boldsymbol{p}}_{0}^{0} = \begin{bmatrix} \ddot{x} \\ \ddot{y} \\ g + \ddot{z} \end{bmatrix}$$
(3-28)

These were used in equation 3-25 and propagated forward to each link, and then equations 3-26 were used to find the interaction forces and torques and joint actuation torques. These equations were developed for anthropomorphic, spherical, wrist, and anthropomorphic/wrist robot configurations and many are included in Appendix A. The ability of this method to predict the interaction forces and torques was verified experimentally with a six-degree-of freedom force/torque sensor mounted at the base of a three DOF anthropomorphic rigid robot.

3.4 Coupled Macro/Micromanipulator Model

The micromanipulator is considered in this work to apply the interaction forces and torques to the flexible base. The flexible manipulator, given by equation 3-19, is now written with translational and rotational effects considered separately. The generalized forces applied by the micromanipulator are given by 3-18. Here, for the sake of generality, the interactions are assumed applied directly to the flexible base. In this case, the flexible manipulator equations of motion become:

$$\begin{bmatrix} M & 0 \\ 0 & J \end{bmatrix} \begin{bmatrix} \ddot{\mathbf{x}}_f \\ \ddot{\boldsymbol{\theta}}_f \end{bmatrix} + \begin{bmatrix} C & 0 \\ 0 & C_r \end{bmatrix} \begin{bmatrix} \dot{\mathbf{x}}_f \\ \dot{\boldsymbol{\theta}}_f \end{bmatrix} + \begin{bmatrix} K & 0 \\ 0 & K_r \end{bmatrix} \begin{bmatrix} \mathbf{x}_f \\ \boldsymbol{\theta}_f \end{bmatrix} = -\begin{bmatrix} \mathbf{F}_{IF} \\ \boldsymbol{\tau}_{IF} \end{bmatrix}$$
(3-29)

where \mathbf{x}_f represents the coordinates governing the translational motion of the flexible base and $\boldsymbol{\theta}_f$ represents the coordinates governing the rotational motion of the base. The interactions commanded by the rigid robot motion are given by equations 3-27.

These are rewritten here to explicitly to identify a few key terms:

$$\begin{split} \mathbf{F}_{IF} &= B_{f}(\boldsymbol{\theta}) \ddot{\boldsymbol{\theta}} + N_{f}(\boldsymbol{\theta}, \dot{\boldsymbol{\theta}}_{i} \dot{\boldsymbol{\theta}}_{j}) + A_{f}(\boldsymbol{\theta}) \ddot{\mathbf{x}}_{f} + B_{wf}(\boldsymbol{\theta}) \ddot{\boldsymbol{\theta}}_{f} + N_{fc}(\mathbf{x}_{f}, \dot{\mathbf{x}}_{f}, \boldsymbol{\theta}_{f}, \dot{\boldsymbol{\theta}}_{f}, \boldsymbol{\theta}, \dot{\boldsymbol{\theta}}) \\ \boldsymbol{\tau}_{IF} &= B_{\tau 0}(\boldsymbol{\theta}) \ddot{\boldsymbol{\theta}} + N_{\tau 0}(\boldsymbol{\theta}, \dot{\boldsymbol{\theta}}_{i} \dot{\boldsymbol{\theta}}_{j}) + A_{\tau 0}(\boldsymbol{\theta}) \ddot{\mathbf{x}}_{f} + B_{w\tau 0}(\boldsymbol{\theta}) \ddot{\boldsymbol{\theta}}_{f} + N_{f\tau 0}(\mathbf{x}_{f}, \dot{\mathbf{x}}_{f}, \boldsymbol{\theta}_{f}, \dot{\boldsymbol{\theta}}_{f}, \boldsymbol{\theta}, \dot{\boldsymbol{\theta}}) \\ \boldsymbol{\tau} &= B_{\tau}(\boldsymbol{\theta}) \ddot{\boldsymbol{\theta}} + N_{\tau}(\boldsymbol{\theta}, \dot{\boldsymbol{\theta}}_{i} \dot{\boldsymbol{\theta}}_{j}) + B_{f}^{\tau}(\boldsymbol{\theta}) \ddot{\mathbf{x}}_{f} + B_{\tau 0}^{T}(\boldsymbol{\theta}) \ddot{\boldsymbol{\theta}}_{f} + N_{\tau c}(\mathbf{x}_{f}, \dot{\mathbf{x}}_{f}, \boldsymbol{\theta}_{f}, \dot{\boldsymbol{\theta}}_{f}, \boldsymbol{\theta}, \dot{\boldsymbol{\theta}}) \end{split} \tag{3-30}$$

Substituting 3-30 into 3-29 and rearranging yields the coupled equations of motion:

$$\begin{bmatrix} M + A_{f}(\boldsymbol{\theta}) & B_{wf}(\boldsymbol{\theta}) & B_{f}(\boldsymbol{\theta}) \\ A_{r0}(\boldsymbol{\theta}) & J + B_{wr0}(\boldsymbol{\theta}) & B_{r0}(\boldsymbol{\theta}) \\ B_{f}^{T}(\boldsymbol{\theta}) & B_{r0}^{T}(\boldsymbol{\theta}) & B_{r}(\boldsymbol{\theta}) \end{bmatrix} \begin{bmatrix} \ddot{\mathbf{x}}_{f} \\ \ddot{\boldsymbol{\theta}}_{f} \\ \ddot{\boldsymbol{\theta}} \end{bmatrix} + \begin{bmatrix} C & 0 & 0 \\ 0 & C_{r} & 0 \\ 0 & 0 & 0 \end{bmatrix} \begin{bmatrix} \dot{\mathbf{x}}_{f} \\ \dot{\boldsymbol{\theta}}_{f} \end{bmatrix} + \begin{bmatrix} K & 0 & 0 \\ 0 & K_{r} & 0 \\ 0 & 0 & 0 \end{bmatrix} \begin{bmatrix} \mathbf{x}_{f} \\ \mathbf{\theta}_{f} \end{bmatrix} + \begin{bmatrix} K_{r} & 0 & 0 \\ 0 & K_{r} & 0 \\ 0 & 0 & 0 \end{bmatrix} \begin{bmatrix} \mathbf{x}_{f} \\ \mathbf{\theta}_{f} \end{bmatrix} + \begin{bmatrix} K_{r} & 0 & 0 \\ 0 & K_{r} & 0 \\ 0 & 0 & 0 \end{bmatrix} \begin{bmatrix} \mathbf{x}_{f} \\ \mathbf{\theta}_{f} \end{bmatrix} + \begin{bmatrix} K_{r} & 0 & 0 \\ 0 & K_{r} & 0 \\ 0 & 0 & 0 \end{bmatrix} \begin{bmatrix} \mathbf{x}_{f} \\ \mathbf{\theta}_{f} \end{bmatrix} + \begin{bmatrix} K_{r} & 0 & 0 \\ 0 & K_{r} & 0 \\ 0 & 0 & 0 \end{bmatrix} \begin{bmatrix} \mathbf{x}_{f} \\ \mathbf{\theta}_{f} \end{bmatrix} + \begin{bmatrix} K_{r} & 0 & 0 \\ 0 & K_{r} & 0 \\ 0 & 0 & 0 \end{bmatrix} \begin{bmatrix} \mathbf{x}_{f} \\ \mathbf{\theta}_{f} \end{bmatrix} + \begin{bmatrix} K_{r} & 0 & 0 \\ 0 & K_{r} & 0 \\ 0 & 0 & 0 \end{bmatrix} \begin{bmatrix} \mathbf{x}_{f} \\ \mathbf{\theta}_{f} \end{bmatrix} + \begin{bmatrix} K_{r} & 0 & 0 \\ 0 & K_{r} & 0 \\ 0 & 0 & 0 \end{bmatrix} \begin{bmatrix} \mathbf{x}_{f} \\ \mathbf{\theta}_{f} \end{bmatrix} + \begin{bmatrix} K_{r} & 0 & 0 \\ 0 & K_{r} & 0 \\ 0 & 0 & 0 \end{bmatrix} \begin{bmatrix} \mathbf{x}_{f} \\ \mathbf{\theta}_{f} \end{bmatrix} + \begin{bmatrix} K_{r} & 0 & 0 \\ 0 & K_{r} & 0 \\ 0 & 0 & 0 \end{bmatrix} \begin{bmatrix} \mathbf{x}_{f} \\ \mathbf{\theta}_{f} \end{bmatrix} + \begin{bmatrix} K_{r} & 0 & 0 \\ 0 & K_{r} & 0 \\ 0 & 0 & 0 \end{bmatrix} \begin{bmatrix} \mathbf{x}_{f} \\ \mathbf{\theta}_{f} \end{bmatrix} + \begin{bmatrix} K_{r} & 0 & 0 \\ 0 & K_{r} & 0 \\ 0 & 0 & 0 \end{bmatrix} \begin{bmatrix} \mathbf{x}_{f} \\ \mathbf{\theta}_{f} \end{bmatrix} + \begin{bmatrix} K_{r} & 0 & 0 \\ 0 & K_{r} & 0 \\ 0 & 0 & 0 \end{bmatrix} \begin{bmatrix} \mathbf{x}_{f} \\ \mathbf{\theta}_{f} \end{bmatrix} + \begin{bmatrix} K_{r} & 0 & 0 \\ 0 & K_{r} & 0 \\ 0 & 0 & 0 \end{bmatrix} \begin{bmatrix} \mathbf{x}_{f} \\ \mathbf{\theta}_{f} \end{bmatrix} + \begin{bmatrix} K_{r} & 0 & 0 \\ 0 & K_{r} & 0 \\ 0 & 0 & 0 \end{bmatrix} \begin{bmatrix} \mathbf{x}_{f} \\ \mathbf{\theta}_{f} \end{bmatrix} + \begin{bmatrix} K_{r} & 0 & 0 \\ 0 & K_{r} & 0 \\ 0 & 0 & 0 \end{bmatrix} \begin{bmatrix} \mathbf{x}_{f} \\ \mathbf{\theta}_{f} \end{bmatrix} + \begin{bmatrix} K_{r} & 0 & 0 \\ 0 & 0 & 0 \end{bmatrix} \begin{bmatrix} \mathbf{x}_{f} \\ \mathbf{\theta}_{f} \end{bmatrix} + \begin{bmatrix} K_{r} & 0 & 0 \\ 0 & 0 & 0 \end{bmatrix} \begin{bmatrix} K_{r} \\ \mathbf{\theta}_{f} \end{bmatrix} + \begin{bmatrix} K_{r} & 0 & 0 \\ 0 & 0 & 0 \end{bmatrix} \begin{bmatrix} K_{r} \\ \mathbf{\theta}_{f} \end{bmatrix} + \begin{bmatrix} K_{r} & 0 & 0 \\ 0 & 0 & 0 \end{bmatrix} \begin{bmatrix} K_{r} \\ \mathbf{\theta}_{f} \end{bmatrix} + \begin{bmatrix} K_{r} & 0 & 0 \\ 0 & 0 & 0 \end{bmatrix} \begin{bmatrix} K_{r} \\ \mathbf{\theta}_{f} \end{bmatrix} + \begin{bmatrix} K_{r} & 0 & 0 \\ 0 & 0 & 0 \end{bmatrix} \begin{bmatrix} K_{r} \\ \mathbf{\theta}_{f} \end{bmatrix} + \begin{bmatrix} K_{r} & 0 & 0 \\ 0 & 0 & 0 \end{bmatrix} \begin{bmatrix} K_{r} \\ \mathbf{\theta}_{f} \end{bmatrix} + \begin{bmatrix} K_{r} & 0 & 0 \\ 0 & 0 & 0 \end{bmatrix} \begin{bmatrix} K_{r} \\ \mathbf{\theta}_{f} \end{bmatrix} + \begin{bmatrix} K_{r} & 0 & 0 \\ 0 & 0 & 0 \end{bmatrix} \begin{bmatrix} K_{r} \\ \mathbf{\theta}_{f} \end{bmatrix} + \begin{bmatrix} K_{r} & 0 & 0 \\ 0 & 0 & 0 \end{bmatrix} \begin{bmatrix} K_{r} \\ \mathbf{\theta}_{f} \end{bmatrix} + \begin{bmatrix} K_{r} & 0 & 0 \\ 0 & 0 & 0 \end{bmatrix} \begin{bmatrix} K_{r} \\ \mathbf{\theta}_{f} \end{bmatrix} + \begin{bmatrix} K_{r} & 0 & 0 \\ 0 & 0 & 0 \end{bmatrix} \begin{bmatrix} K_{r} \\ \mathbf{\theta}$$

The goal of the next chapter is to investigate these equations of motion more thoroughly and, in particular, study the interactions directly controllable by the rigid robot.

CHAPTER IV

INTERACTION FORCES AND TORQUES AND INERTIAL SINGULARITIES

4.1 Introduction

This chapter addresses the interaction forces and torques acting between the rigid robot and its flexible base. Recall these are given by:

$$\mathbf{F}_{IF} = B_f(\mathbf{\theta})\ddot{\mathbf{\theta}} + N_f(\mathbf{\theta}, \dot{\mathbf{\theta}}_i \dot{\mathbf{\theta}}_j) + C_f(\mathbf{\theta})\ddot{\mathbf{q}} + N_{fc}(\mathbf{q}, \dot{\mathbf{q}}, \mathbf{\theta}, \dot{\mathbf{\theta}})$$

$$\mathbf{\tau}_{IF} = B_{\tau 0}(\mathbf{\theta})\ddot{\mathbf{\theta}} + N_{\tau 0}(\mathbf{\theta}, \dot{\mathbf{\theta}}_i \dot{\mathbf{\theta}}_j) + C_{\tau 0}(\mathbf{\theta})\ddot{\mathbf{q}} + N_{\tau 0c}(\mathbf{q}, \dot{\mathbf{q}}, \mathbf{\theta}, \dot{\mathbf{\theta}})$$
(4-1)

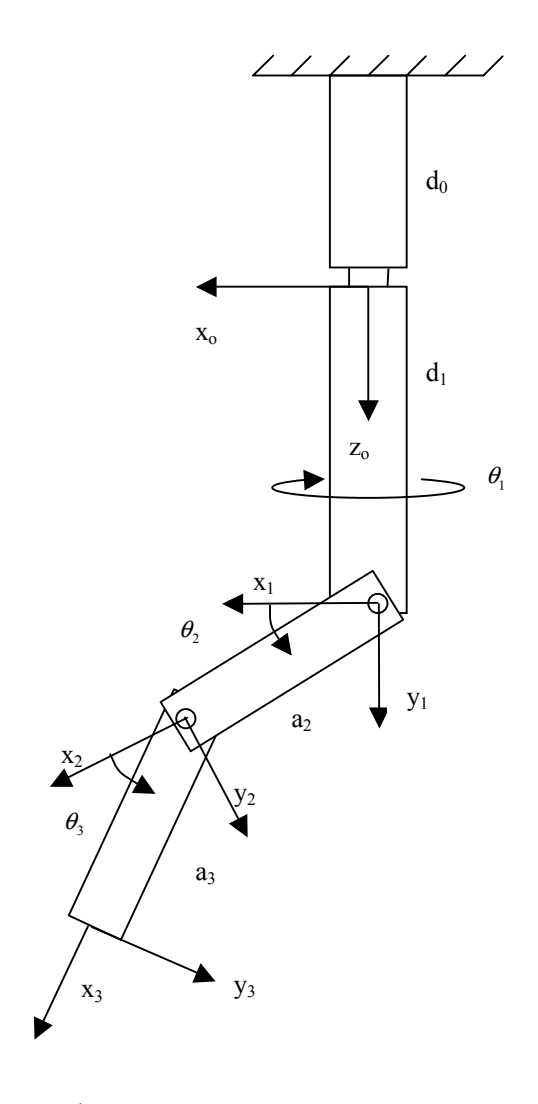
The focus of this chapter is the directly controllable rigid robot effects, or those terms that are only functions of $\boldsymbol{\theta}$ (the first two terms in each equation). For completeness, the more detailed equations of motion for each robot may be found in Appendix A (anthropomorphic, spherical, wrist, and anthropomorphic/wrist robots). The notation and coordinate systems used are shown in Figures 4-1 through 4-4. The robot configurations are defined consistent with those described in Sciavicco and Siciliano [61] for anthropomorphic and spherical arm robots and spherical wrist robots, with one exception noted in Figure 4-1. In addition, terminology consistent with McGill/King [47] will be used where centripetal refers to accelerations and centrifugal refers to forces.

First, the inertia forces and torques are discussed, or those generated by accelerating the links of the rigid robot. An important part of this work involved investigating "inertial singularities," or regions in the workspace where the robot loses its ability to create inertia interactions in one or more degrees of freedom. These are important because the control scheme inverts the inertia matrix, which presents a problem when these matrices become singular. However, these singularities also represent physical limitations, so it is important to understand where and why they occur and, if possible, devise ways of avoiding operation in or near these regions.

Next, the nonlinear centrifugal and coriolis forces and torques are discussed. There are regions in the workspace where these can become large during multi-DOF actuation of the joints. These effects are driven by the joint space configuration of the robot and the joint velocities. In most configurations, the ratio of inertia to nonlinear effects is large. However, in some configurations the nonlinear effects can interfere with the inertia effects. If the amplitude of joint motion is limited appropriately, this ratio can be improved. The remainder of the interaction terms involve combined rigid robot and flexible base coordinates and are not discussed further here other than to note they are important for accurate modeling. Finally, the interaction forces and torques were developed using the Newton-Euler method described in chapter 3. However, a more efficient approach to find the inertia and nonlinear rigid force effects is presented here.

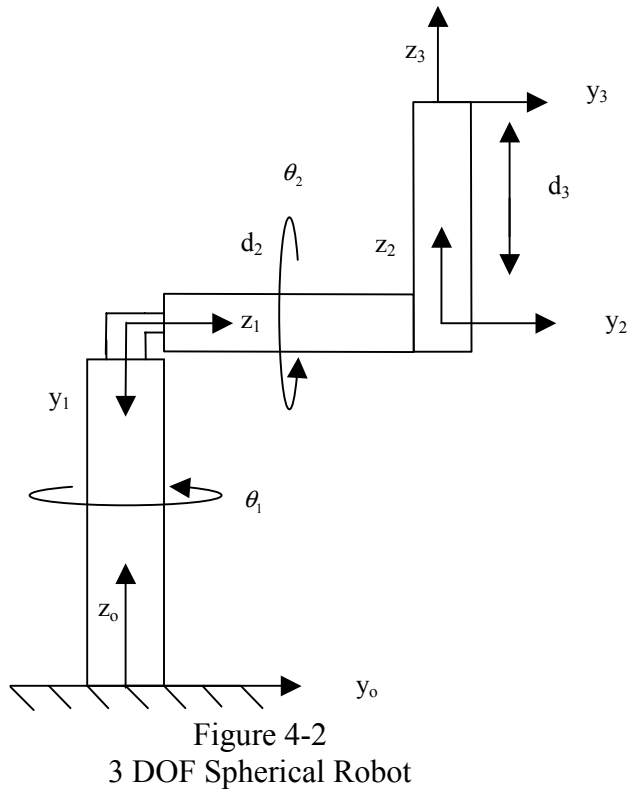
The work presented in this chapter leads to two important conclusions, which will be used in the development of the control scheme. First, since the inertia effects are functions of the joint configuration, this variation in performance may be used to ensure the robot operates in joint space configurations better suited for inertial damping. This is possible because there are normally multiple inverse kinematic solutions corresponding

to a given end point position (provided the robot is not operating at a kinematic singularity). A performance measure to predict the rigid robot's ability to create effective multi-DOF inertia interactions is introduced here. It can be used to choose better inverse kinematic solutions for inertial damping and will become an important part of the performance index discussed in Chapter 5. Second, if the joint amplitudes are limited appropriately, the ratio of inertia/nonlinear effects can be improved. The amplitude of motion can be controlled by establishing proper limits on the vibration control feedback gains. The control scheme and feedback gains will be discussed in Chapter 5. The adequacy of these models in predicting the interactions was tested on a three DOF anthropomorphic robot with a six-axis ATI force/torque sensor mounted to its base.



* note unconventional definition of θ_2

Figure 4-1
3 DOF Anthropomorphic Robot



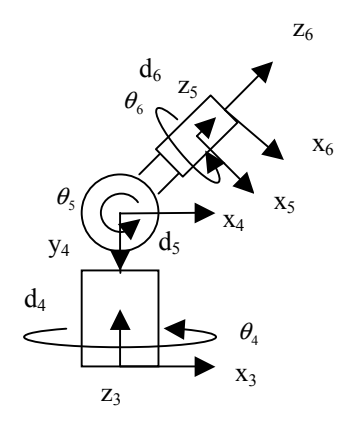


Figure 4-3 3 DOF Wrist Robot

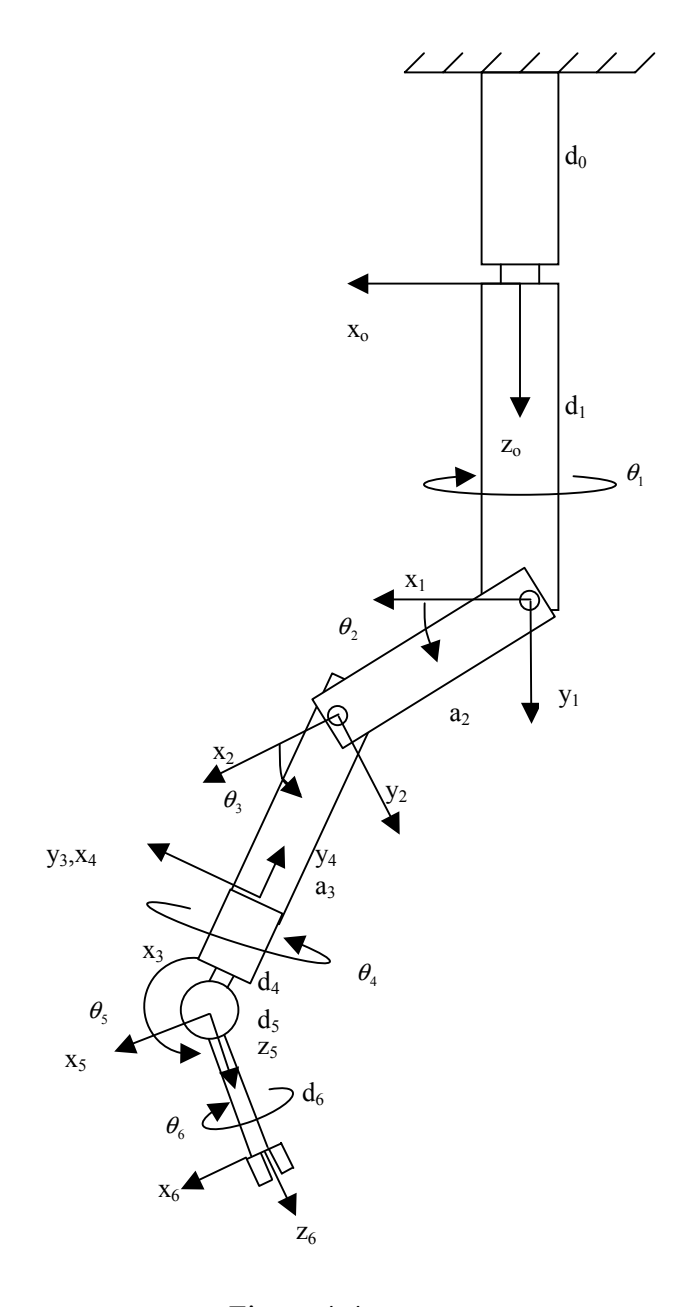


Figure 4-4
6 DOF Anthropomorphic Robot with Wrist

4.2 Inertia Forces and Torques and Inertial Singularities

The inertia forces and torques are functions of the joint configuration of the robot and joint accelerations. The ability of three typical robots to generate interactions is examined in three degrees of freedom since this is easily visualized. Using the notation defined in equation 4-1, B_f and $B_{\tau 0}$ are inertia-like matrices but they are, in general, not square, symmetric, or positive definite (the inertia matrix for the coupled system, B_{τ} from equation 3-27, is). These matrices are particularly important for two reasons. First, the rigid robot needs to have enough inertia to apply effective interaction forces and torques to the macromanipulator. The ratio of the rigid inertia to flexible inertia effects becomes an important part of the performance index. Second, there are locations in the workspace where these matrices become singular, which presents a problem since they are inverted in the control scheme. However, the more important consideration is that these "inertial singularities" represent *physical* limitations in that an inertia force or torque cannot be created in one or more degrees of freedom.

4.2.1 Performance Measure for Inertial Damping

The following performance measure provides a quick and accurate measure of the ability of the rigid robot in generating effective interaction forces and torques and assesses its variation throughout the workspace:

$$\left| B_f^T(\mathbf{\theta}) B_f(\mathbf{\theta}) \right|, \left| B_{\tau 0}^T(\mathbf{\theta}) B_{\tau 0}(\mathbf{\theta}) \right| \tag{4-2}$$

Alternately the combined ability of the robot to generate interaction forces and torques may be evaluated by assessing:

$$\begin{vmatrix} B^{T}(\mathbf{\theta})B(\mathbf{\theta}) \\ B = \begin{bmatrix} B_{f}(\mathbf{\theta}) \\ B_{\tau 0}(\mathbf{\theta}) \end{bmatrix}$$
(4-3)

First, it is important to note a few points about these matrices. They are real but not, in general, square, or symmetric and thus will not have real eigenvalues [73]. However, B^TB will always be symmetric and its determinant will be positive. Singular value decomposition is a related technique noted for its usefulness in determining how near a matrix comes to becoming singular. It has also been noted that the use of only the minimum and maximum singular values is overconservative [23]. Thus, the determinant of B^TB, which is the product of the singular values, was chosen for the performance measure. In addition, although this dissertation does not specifically address cases of underactuation or redundancy, the proposed measure may be extended to those cases since there is no requirement that the matrices be square. Finally, the determinant of a matrix can much more easily be evaluated than eigenvalues or singular values, which is particularly important if the performance measure will be used in real-time. measure not only provides an indication of how these effects vary throughout the workspace, but also shows regions where full multi-DOF inertial damping capability is not possible. The goal here is to use this performance measure to choose robot joint space locations where the inertia effects are large, whenever possible.

4.2.2 Interaction Force Performance

Consider the three degree of freedom anthropomorphic robot shown in Figure 4-1. Note this is a special case where three joints create interactions in three degrees of freedom. Hence the inertia force matrix is square and given by:

$$B_{f} = \begin{bmatrix} -s_{1}(Ac_{2} + Bc_{23}) & -c_{1}(As_{2} + Bs_{23}) & -Bc_{1}s_{23} \\ c_{1}(Ac_{2} + Bc_{23}) & -s_{1}(As_{2} + Bs_{23}) & -Bs_{1}s_{23} \\ 0 & Ac_{2} + Bc_{23} & Bc_{23} \end{bmatrix}$$
(4-4)

where:

 $A=m_2r_2+m_3a_2 \\ B=m_3r_3 \\ m_i=mass of link i \\ a_i=length of link i \\ r_i=distance to the center of gravity (CG) of link i$

The determinant allows an evaluation of the singularity points and is given by:

$$\left| B_f \right| = -ABs_3(Ac_2 + Bc_{23}) \tag{4-5}$$

The matrix becomes singular whenever $s_3=0$ or $Ac_2+Bc_{23}=0$.

The variation in force performance, as quantified by the performance measure in equation 4-2, is shown in Figure 4-5 over a reduced range of joint motion in order to help clarify the presentation. Cases 1 and 2 refer to specific regions in the workspace that will be referred to later.

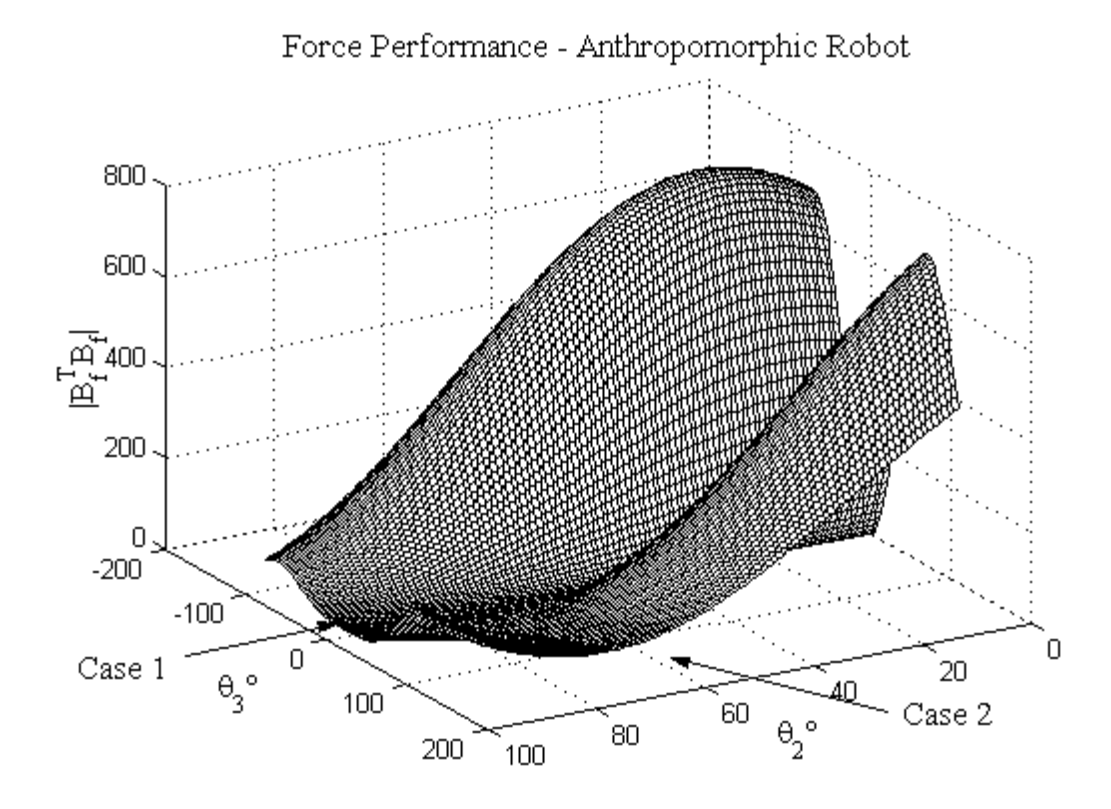


Figure 4-5
Force Performance – 3 DOF Anthropomorphic Robot

The inertia matrix for the spherical robot and its determinant are given by:

$$B_{f} = \begin{bmatrix} -A_{s}c_{1} - B_{s}s_{1}s_{2} & B_{s}c_{1}c_{2} & m_{3}c_{1}s_{2} \\ -A_{s}s_{1} + B_{s}c_{1}s_{2} & B_{s}s_{1}c_{2} & m_{3}s_{1}s_{2} \\ 0 & -B_{s}s_{2} & m_{3}c_{2} \end{bmatrix}$$

$$|B_{f}| = -m_{3}^{3}s_{2}r_{3}^{2}$$

$$(4-6)$$

where:

 $A_s=m_2r_2+m_3d_2$ $B_s=m_3r_3$ (note r_3 is not constant) $d_i=$ length of link i Its variation in performance is shown in Figure 4-6.

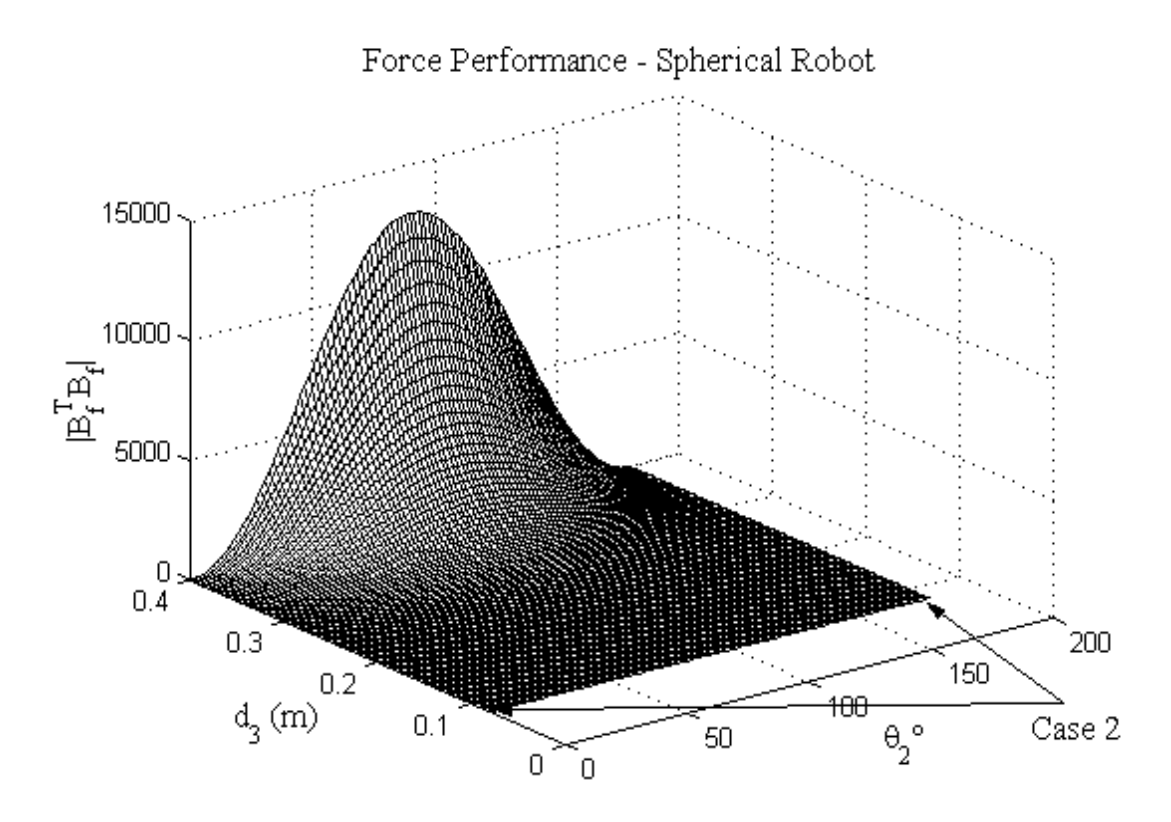


Figure 4-6
Force Performance – 3 DOF Spherical Robot

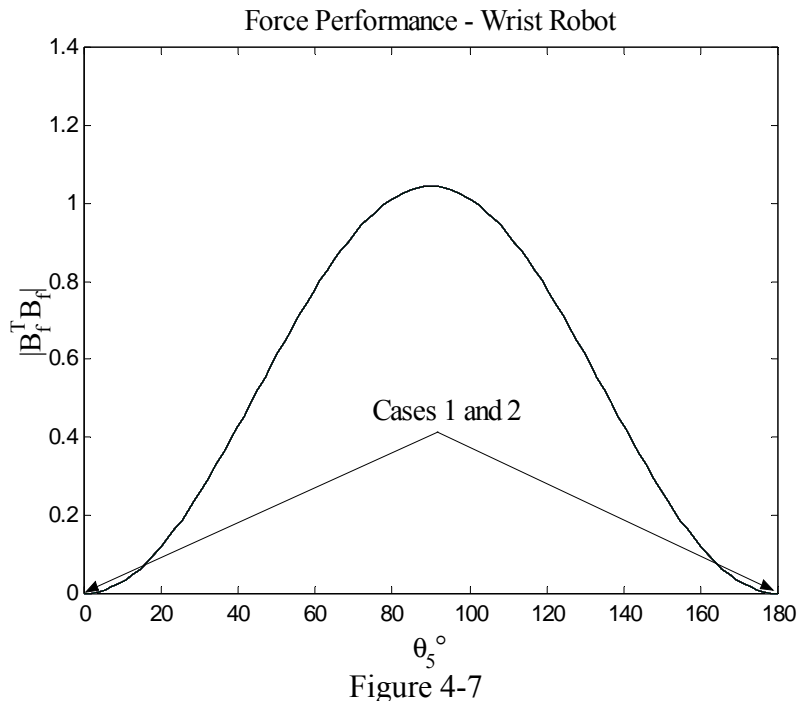
The equivalent matrix for the three DOF wrist is given by:

$$B_{f} = \begin{bmatrix} -A_{w}s_{4}s_{5} & A_{w}c_{4}c_{5} & 0\\ A_{w}c_{4}s_{5} & A_{w}s_{4}c_{5} & 0\\ 0 & -A_{w}s_{5} & 0 \end{bmatrix}$$
(4-7)

where:

 $A_w = m_5 r_5 + (d_5 + r_6) m_6$

Its variation in performance is shown in Figure 4-7.



Force Performance – 3 DOF Wrist Robot

The regions with very low values represent locations in the workspace where the robot cannot produce inertia forces in one or more degrees of freedom. These will be termed "inertial singularities." These singularities consist of some of the kinematic singularities plus additional dynamically singular configurations. The two general cases are annotated on Figures 4-5 through 4-7. The singularities are driven by the columns of B_f when the matrix contains:

1) Linearly dependent columns, which indicate that the inertia forces created by two or more links are parallel. For example, this singularity occurs for the anthropomorphic robot when the last two links are aligned. This also corresponds to a kinematic singularity, when the velocities generated by the two links are parallel. For the

spherical robot, this occurs when joint 2 is at 0° or 180°, when both links 1 and 2 create velocities (and inertia forces) in the horizontal direction. All of the three DOF spherical robot singularities are the same as the kinematic singularities.

2) A column of zeros, which indicates a location in the workspace where the motion of a joint cannot create any inertia interaction forces. This singularity occurs when the CG of the robot is aligned along an axis of rotation. For the anthropomorphic robot, this occurs when the system CG is aligned along the z-axis, so link 1 can produce no interaction inertia forces. In the spherical robot, this will occur if link 3 is aligned along the axis of joint 2, which renders a middle column of zeros. This singularity can be avoided by requiring some minimum length to link three. These are, in general, different from the kinematic singularities. The inertial singularities depend on the location of the CG of the system. If it is known where these occur, they can be avoided by not operating in those joint space configurations.

In the case of the anthropomorphic and spherical robots, link 1 has no effect on the inertia force performance because it cannot affect the CG of the system.

Given the configuration shown in Figure 4-3, the wrist is always singular in three degrees of freedom. Its last link cannot create any inertia interaction forces since its axis of rotation is along the main link of the robot. In addition, only the orientation of joint 5 affects the inertia forces since it is the only joint that affects the CG of the system. It is also interesting to note the wrist singularities occur when the arm is straight down or straight up (θ_5 =0° or 180°). This is a combination of cases 1 and 2 since these are kinematic singularities and the CG is aligned along joint 1. Note the extremely small

force magnitudes generated by the wrist, indicating its use alone would not be very effective at creating interactions.

It is also worth mentioning another type of singularity, which corresponds to a row of zeros in the matrix or two parallel rows. This singularity occurs in conjunction with one of the other singularity configurations discussed above. For example, if the CG of the anthropomorphic robot is oriented along the axis of rotation of joint 1 (case 2), an inertia force cannot be produced in the out-of-plane direction. In this case, two of the rows can become parallel or one can become a row of zeros, depending on θ_1 . Two other types of row singularities can occur in conjunction with the kinematic singularity at θ_3 =0° (case 1). When joint 2 is at 90° (straight down) and joint 3 is at 0°, no inertia forces can be produced in the z direction and the third row becomes a row of zeros. Finally the orientation at θ_2 =0°, θ_3 =0° can result in a row of zeros in either the x or y direction, depending on θ_1 . These are easily identified using the proposed performance measure defined in equation 4-2 and serve to further verify the singularities are driven by the columns of the inertia matrices.

4.2.3 Interaction Torque Performance

The interaction torque matrices are given by equations 4-8 through 4-10:

Anthropomorphic Robot:

$$\begin{split} &B_{\tau 0}(1,1) = c_1 \{ -2c_2 s_{23} [c_3 (E+J) + Ba_2] + (E+J) (s_2 c_2 + s_3 c_3) + B(a_2 s_3 - Dc_{23}) + (G-K) s_2 c_2 - ADc_2 \} \\ &B_{\tau 0}(1,2) = s_1 \{ B(2a_2 c_3 + Ds_{23}) + ADs_2 + (E+H+K) \} \\ &B_{\tau 0}(1,3) = s_1 \{ B(a_2 c_3 + Ds_{23}) + E + I_{3zz} \} \\ &B_{\tau 0}(2,1) = s_1 \{ -2c_2 s_{23} [c_3 (E+J) + Ba_2] + (E+J) (s_2 c_2 + s_3 c_3) + B(a_2 s_3 - Dc_{23}) + (G-K) s_2 c_2 - ADc_2 \} \\ &B_{\tau 0}(2,2) = -c_1 \{ B(2a_2 c_3 + Ds_{23}) + ADs_2 + (E+H+K) \} \\ &B_{\tau 0}(2,3) = -c_1 \{ B(a_2 c_3 + Ds_{23}) + (E+I_{3zz}) \} \\ &B_{\tau 0}(3,1) = 2c_2 c_{23} [c_3 (E+J) + Ba_2] - (E+J) (c_2^2 + c_3^2) + (K-G) c_2^2 + E+L \\ &B_{\tau 0}(3,2) = B_{\tau 0}(3,3) = 0 \end{split} \tag{4-8}$$

where:

$$\begin{array}{l} D=d_0+d_1\\ E=m_3r_3^2\\ G=I_{2xx}-I_{2yy}\\ H=I_{2zz}+I_{3zz}\\ J=-(I_{3xx}-I_{3yy})\\ K=m_2r_2^2+m_3a_2^2\\ L=I_{1yy}+I_{2xx}+I_{3yy}\\ d_0=length\ of\ link\ 0\ (inert\ link)\\ I_{jkk}=moment\ of\ inertia\ of\ link\ j\ about\ the\ k\ axis \end{array}$$

Spherical Robot:

$$B_{\tau 0}(1,1) = (H_s - E_s - G_s)c_1c_2s_2 + B_s(a_1c_1s_2 + a_2s_1c_2) - A_sa_1s_1$$

$$B_{\tau 0}(1,2) = -(E_s + F_s)s_1 + B_s(a_1s_1c_2 - a_2c_1s_2)$$

$$B_{\tau 0}(1,3) = m_3(a_1s_1s_2 + a_2c_1c_2)$$

$$B_{\tau 0}(2,1) = (H_s - E_s - G_s)s_1s_2c_2 + B_s(a_1s_1s_2 - a_2c_1c_2) + A_sa_1c_1$$

$$B_{\tau 0}(2,2) = (E_s + F_s)c_1 - B_s(a_1c_1c_2 + a_2s_1s_2)$$

$$B_{\tau 0}(2,3) = -m_3(a_1c_1s_2 - a_2s_1c_2)$$

$$B_{\tau 0}(3,1) = E_s + I_{1yy} + G_s + K_s + (H_s - E_s - G_s)c_2^2$$

$$B_{\tau 0}(3,2) = -B_sa_2c_2$$

$$B_{\tau 0}(3,3) = -m_3a_2s_2$$

$$(4-9)$$

where:

$$E_s = m_3 r_3^2$$

 $F_s = I_{2yy} + I_{3yy}$
 $G_s = I_{2xx} + I_{3xx}$
 $H_s = I_{3zz} + I_{2zz}$
 $K_s = m_3 a_2^2 + m_2 r_2^2$

Wrist Robot:

$$B_{\tau 0}(1,1) = -s_{5} \left\{ (K_{w} + E_{w} + L_{w})c_{4}c_{5} + A_{w}d_{4}c_{4} + J_{w}c_{6}(s_{4}s_{6} - c_{4}c_{5}c_{6}) \right\}$$

$$B_{\tau 0}(1,2) = -(M_{w} + E_{w} + L_{w})s_{4} - A_{w}d_{4}s_{4}c_{5} - J_{w}c_{6}(s_{4}c_{6} + c_{4}c_{5}s_{6})$$

$$B_{\tau 0}(1,3) = I_{6zz}c_{4}s_{5}$$

$$B_{\tau 0}(2,1) = s_{5} \left\{ -(K_{w} + E_{w} + L_{w})s_{4}c_{5} - A_{w}d_{4}s_{4} + J_{w}c_{6}(c_{4}s_{6} - s_{4}c_{5}c_{6}) \right\}$$

$$B_{\tau 0}(2,2) = (M_{w} + E_{w} + L_{w})c_{4} + A_{w}d_{4}c_{4}c_{5} + J_{w}c_{6}(c_{4}c_{6} - s_{4}c_{5}s_{6})$$

$$B_{\tau 0}(2,3) = I_{6zz}s_{4}s_{5}$$

$$B_{\tau 0}(3,1) = -s_{5}^{2}(K_{w} + E_{w} + L_{w}) - J_{w}s_{5}^{2}c_{6}^{2}$$

$$B_{\tau 0}(3,2) = J_{w}s_{5}s_{6}c_{6}$$

$$B_{\tau 0}(3,3) = I_{6zz}c_{5}$$

$$(4-10)$$

where:

$$\begin{split} E_w &= m_6 r_6^2 \\ J_w &= I_{6yy} - I_{6xx} \\ K_w &= m_5 r_5^2 + m_6 d_5^2 \\ L_w &= I_{5xx} - I_{5zz} + I_{6yy} - I_{6zz} + 2m_6 r_6 d_5 \\ M_w &= I_{5yy} + I_{6xx} + 2m_6 r_6 d_5 \\ N_w &= I_{4yy} + I_{5xx} + I_{6yy} + 2m_6 r_6 d_5 \end{split}$$

The inertia torque performance of the three DOF anthropomorphic robot can be seen in Figure 4-8 by evaluating the torque performance measure defined in equation 4-2. However, the inertia torques created by accelerating joints 2 and 3 are always parallel so this evaluation was made for joints 1 and 2 only (first two columns of the matrix). This highlights one advantage of using this performance measure instead of the determinant of the matrix, because performance of the robot in reduced degrees of freedom can still be

evaluated. The inertia torque performance for the spherical robot is shown in Figure 4-9 and the wrist torque performance is shown in Figure 4-10.

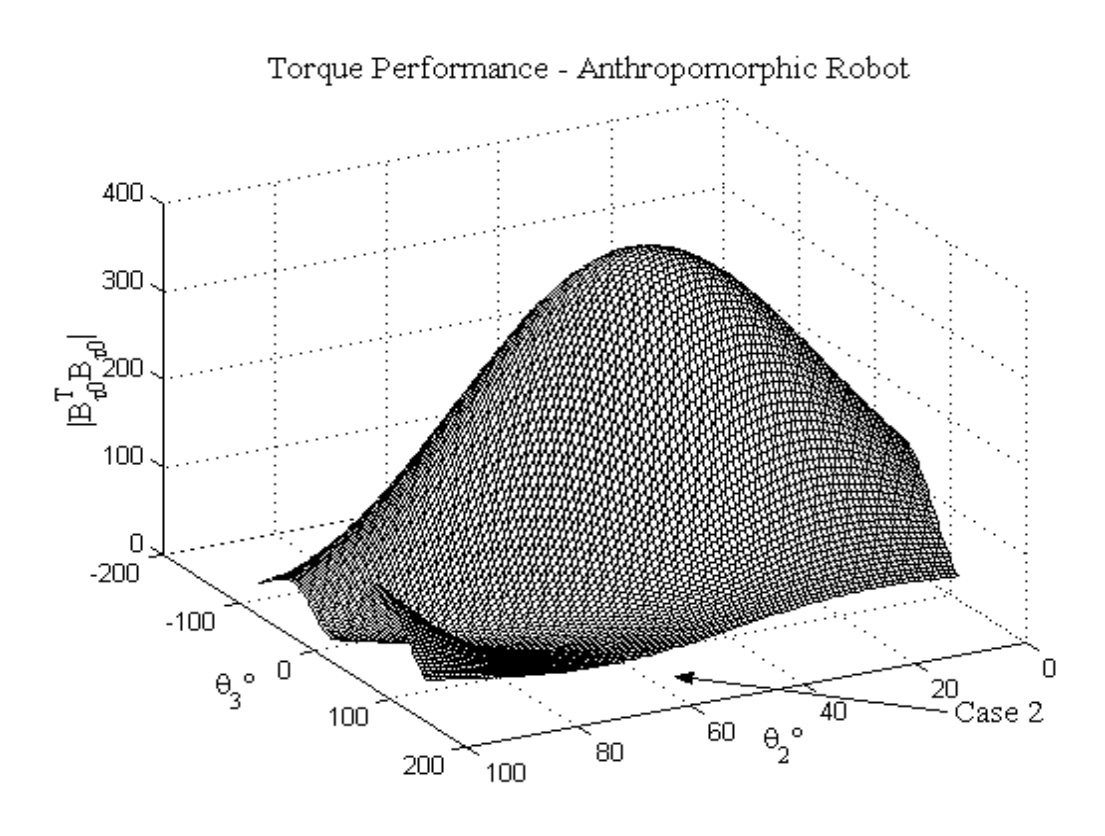


Figure 4-8
Torque Performance – 2 DOF Anthropomorphic Robot

The torque singularities are much less intuitive than the force singularities. This is further complicated by the complexity of the interaction torque equations, even when simplified as much as possible (nor does the determinant simplify into a nice form). However, they still occur in the same two general cases: either when one or more columns becomes parallel (case 1) or one or more columns of zeros occur in the $B_{\tau 0}$ matrix (case 2). For the anthropomorphic robot, the torque singularities occur near the

same regions as the case 2 force singularities. However, in this case the torques created by accelerating the CG of the robot are cancelled by accelerating the inertia of a link, which results in a column of zeros. The spherical torque singularities occur when the torques created by all three links become parallel.

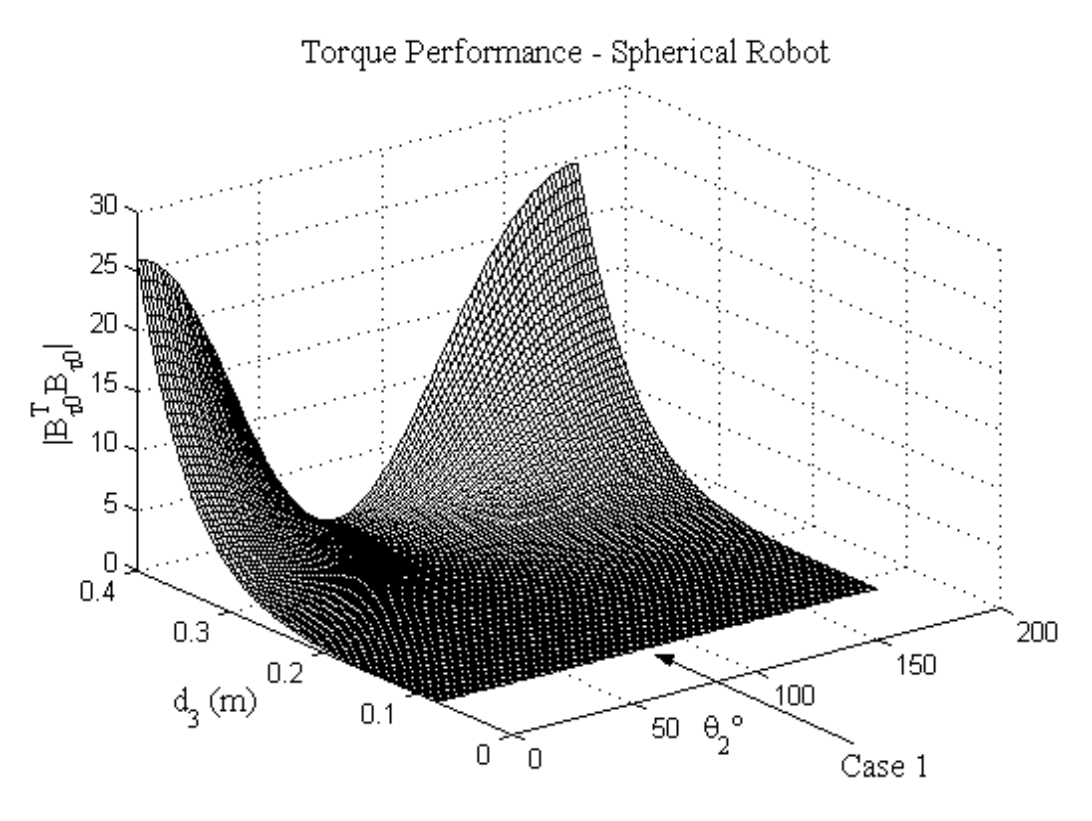
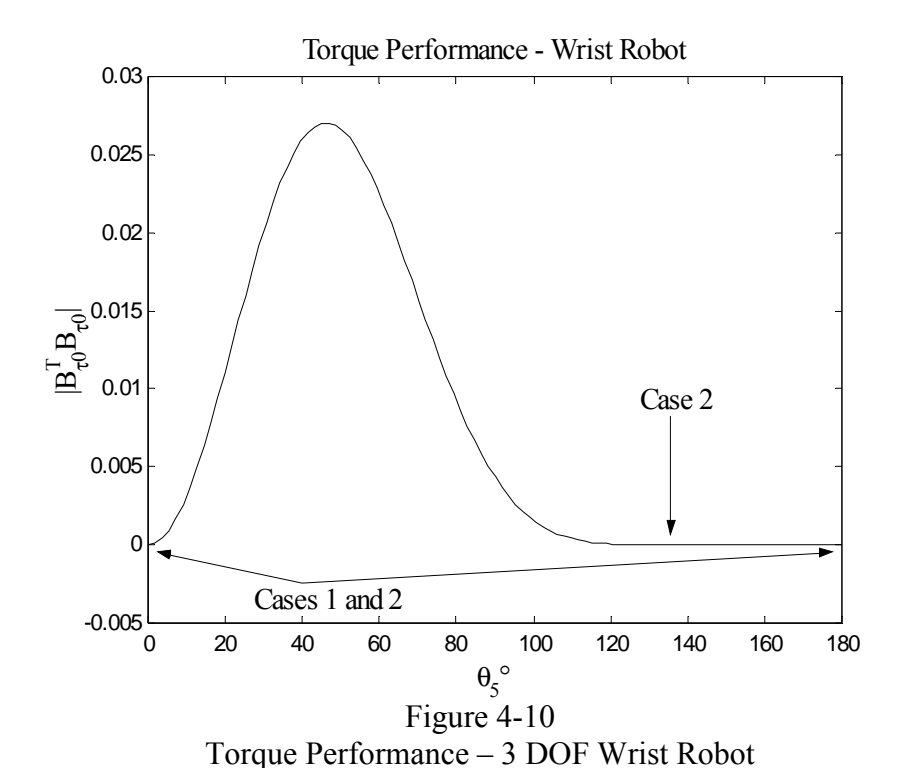


Figure 4-9
Torque Performance – 3 DOF Spherical Robot



The wrist torque performance is again only a function of θ_5 and of relatively small magnitude, reiterating the assertion that it is unlikely to be useful alone in creating effective interactions. It also has a large region of very small torque performance from $100^{\circ}<\theta_5<180^{\circ}$. This occurs because the last link is oriented up towards the first link, which reduces the effective inertia of links 1 and 3. However, the wrist can be useful when added to the last link of an existing robot. First, the full inertia matrix, B(θ),

becomes 6 x 6 and could then be directly inverted in the control scheme to provide full

six degree of freedom inertial damping capability. Another option is to use the additional

inertia of the wrist to increase the damping effectiveness of the base robot. The wrist

4.2.4 Combined Performance

The combined force and torque performance of the robots can be evaluated by using equation 4-3. It is important to note that, even if the interaction forces or torques are prescribed independently, commanding one will always command the other. Thus, it becomes important to be able to evaluate the combined force and torque performance of the robot. The combined performance plots for the anthropomorphic and spherical robots are shown in Figures 4-11 and 4-12. In these cases, the interaction inertia matrix becomes 6x3, but the proposed performance measure still allows evaluation of the combined force and torque performance.

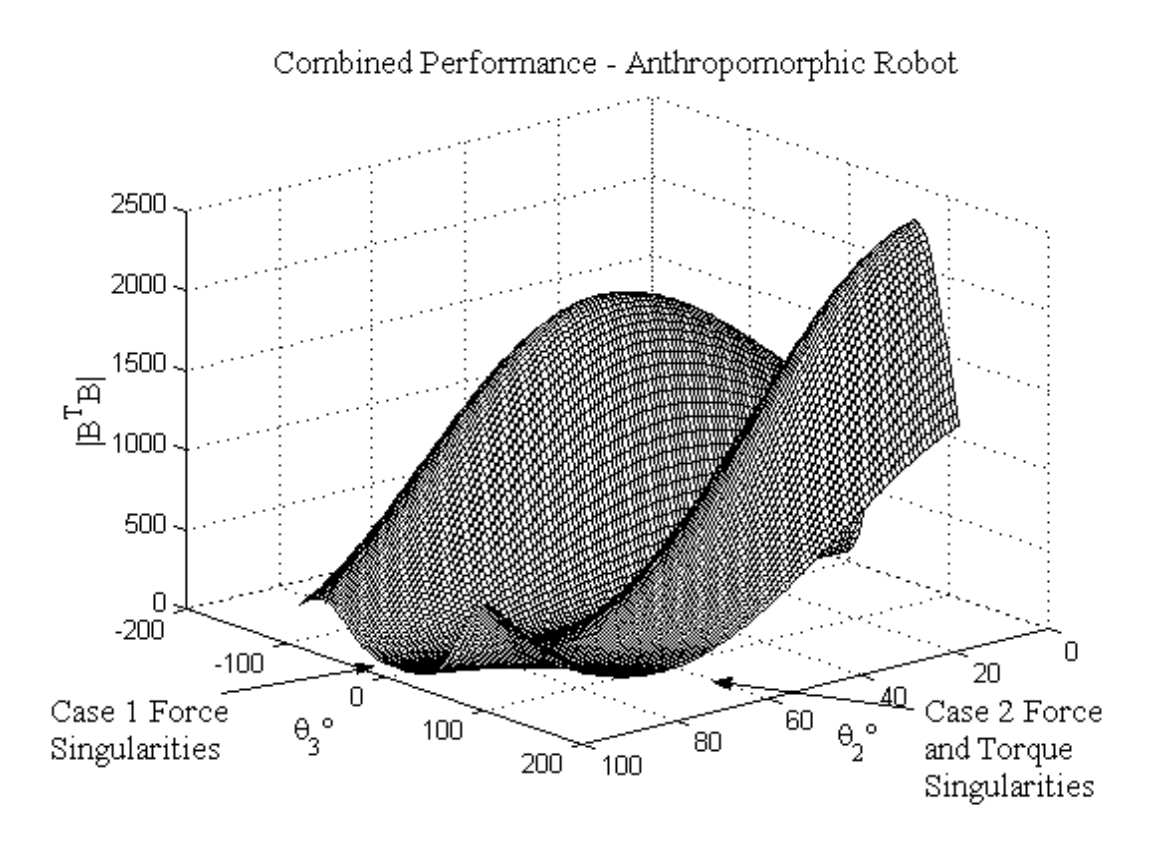


Figure 4-11
Combined Force and Torque Performance – 3 DOF Anthropomorphic Robot

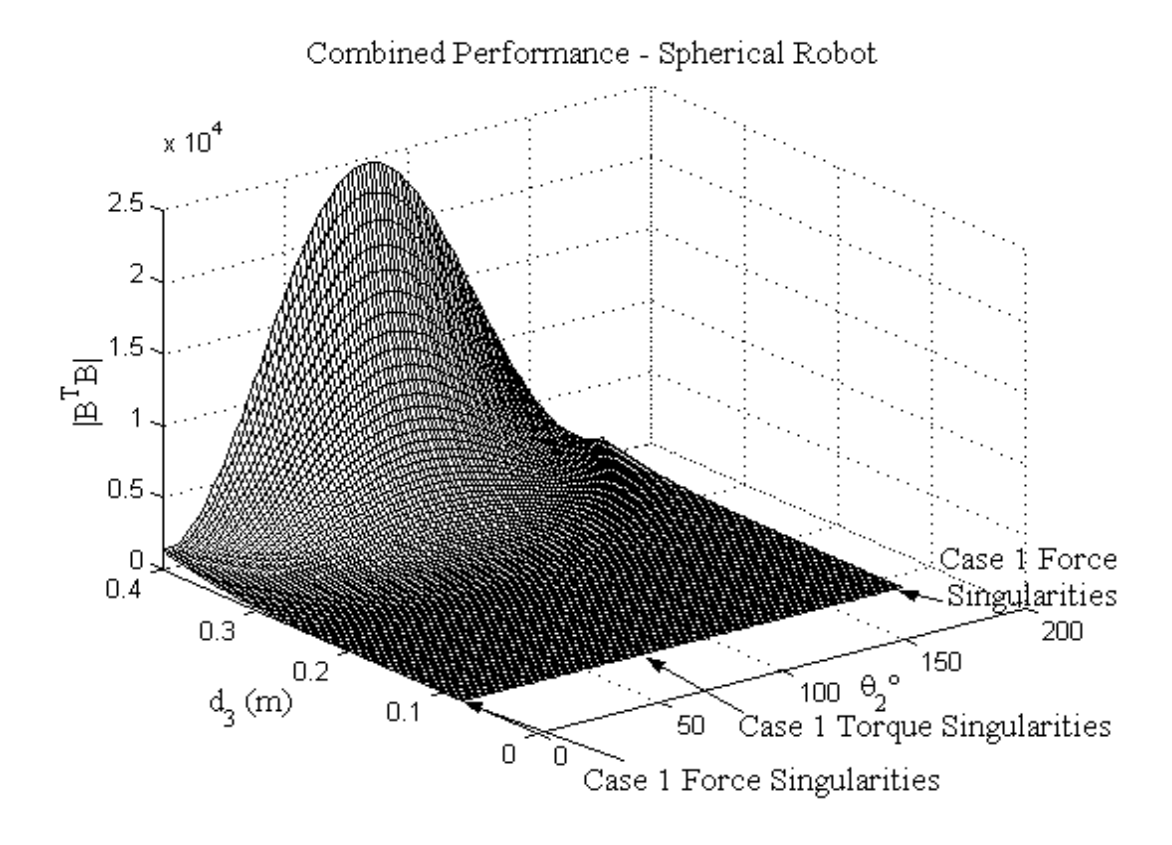


Figure 4-12 Combined Force and Torque Performance – 3 DOF Spherical Robot

For the two robot configurations shown here, the addition of the torque effects makes little difference in the overall performance. As can be seen in Figure 4-11, the anthropomorphic robot inertial force singularities are still clearly apparent and the overall shape of the performance measure remains the same. For the spherical robot, the inertia forces are even more dominant and the torque singularities are practically eliminated from the plot. The torque effects also slightly improve the performance around the case 1 force singularities. The ideal situation would be to fully prescribe both forces and torques for six DOF base vibration damping. However, these plots indicate that if only

the forces or torques are to be prescribed it is more important to consider the interaction forces.

4.3 Nonlinear Rigid Interaction Force and Torque Effects

This section investigates the nonlinear interaction forces and torques expecting during *multi-degree of freedom* inertial damping. Inertial damping has been shown previously in limited degrees of freedom and with robots oriented in specific configurations. The single link case is relatively straightforward since the acceleration of the CG of the link and centripetal acceleration will be perpendicular for rotational joint motion [47]. This will not be the case with multiple joint actuation, so it becomes more important to address these.

The interaction forces and torques directly controllable by the rigid micromanipulator are given by:

$$\mathbf{F}_{IF} = B_{f}(\mathbf{\theta}) \begin{bmatrix} \ddot{\theta}_{1} \\ \ddot{\theta}_{2} \\ \ddot{\theta}_{3} \end{bmatrix} + N_{Rf}(\mathbf{\theta}) \begin{bmatrix} \dot{\theta}_{1} \dot{\theta}_{2} \\ \dot{\theta}_{1} \dot{\theta}_{3} \\ \dot{\theta}_{2} \dot{\theta}_{3} \end{bmatrix} + N_{Cf}(\mathbf{\theta}) \begin{bmatrix} \dot{\theta}_{1}^{2} \\ \dot{\theta}_{2}^{2} \\ \dot{\theta}_{3}^{2} \end{bmatrix} + G_{f}(\mathbf{\theta})$$

$$\mathbf{\tau}_{IF} = B_{\tau 0}(\mathbf{\theta}) \begin{bmatrix} \ddot{\theta}_{1} \\ \ddot{\theta}_{2} \\ \ddot{\theta}_{3} \end{bmatrix} + N_{R\tau 0}(\mathbf{\theta}) \begin{bmatrix} \dot{\theta}_{1} \dot{\theta}_{2} \\ \dot{\theta}_{1} \dot{\theta}_{3} \\ \dot{\theta}_{2} \dot{\theta}_{3} \end{bmatrix} + N_{C\tau 0}(\mathbf{\theta}) \begin{bmatrix} \dot{\theta}_{1}^{2} \\ \dot{\theta}_{2}^{2} \\ \dot{\theta}_{3}^{2} \end{bmatrix} + G_{\tau 0}(\mathbf{\theta})$$

$$(4-11)$$

Here coriolis and centrifugal effects have been written separately. Gravity effects are not further discussed here since they are not dynamic effects. In addition, in Chapter 5 rationale will be presented which allows the assumption to be made that the matrices governing the interactions may be linearized about an operating point.

The nonlinear rigid effects are functions of the manipulator position and joint velocities. The anthropomorphic rigid coriolis force matrix is given by:

$$N_{Rf} = \begin{bmatrix} 2s_1(As_2 + Bs_{23}) & 2Bs_1s_{23} & -2Bc_1c_{23} \\ -2c_1(As_2 + 2Bs_{23}) & -2Bc_1s_{23} & -2Bs_1c_{23} \\ 0 & 0 & -2Bs_{23} \end{bmatrix}$$
(4-12)

The anthropomorphic rigid centrifugal force matrix is given by:

$$N_{Cf} = \begin{bmatrix} -c_1(Ac_2 + Bc_{23}) & -c_1(Ac_2 + Bc_{23}) & -Bc_1c_{23} \\ -s_1(Ac_2 + Bc_{23}) & -s_1(Ac_2 + Bc_{23}) & -Bs_1c_{23} \\ 0 & -(As_2 + Bs_{23}) & -Bs_{23} \end{bmatrix}$$
(4-13)

First, the variation in the nonlinear effects due to joint position is investigated. Next, the effect of joint amplitudes on these effects will be discussed.

Assuming harmonic base vibration of mode i of the flexible base, the base motion and prescribed interaction forces and/or torques will be harmonic and take the form (justification for this will be shown in Chapter 5):

$$x_{i} = X_{i} \sin \omega_{i} t$$

$$F_{IF} / T_{IF} = -K_{i} X_{i} \omega_{i} \cos \omega_{i} t$$
(4-14)

K_i can be used to adjust the amount of damping added to the system. From equation 4-11, the interaction effects are controlled by joint postions, velocities, and accelerations. If any one of these are commanded harmonically, the others will also be commanded harmonically.

First, consider the nonlinear forces generated by the anthropomorphic robot during multi-degree of freedom harmonic joint motion (Figures 4-13 and 4-14). These plots

were generated assuming all joints are actuating simultaneously and at constant amplitudes given by:

$$\theta = 15^{\circ} \left(\frac{\pi}{180^{\circ}}\right) \cos(1.4 * 2\pi t)$$

$$\dot{\theta} = -2.3 \sin(1.4 * 2\pi t)$$

$$\ddot{\theta} = -20 \cos(1.4 * 2\pi t)$$
(4-15)

Harmonic motion at 1.4 Hz was chosen because it is the fundamental mode of vibration of a long, flexible link. This is representative of a fundamental mode of a flexible macromanipulator, i.e. lightly damped, low frequency harmonic vibration. The inertia forces generated under these same circumstances can be seen in Figure 4-15. Note these are *not* the same comparisons as the figures in Section 4.2.

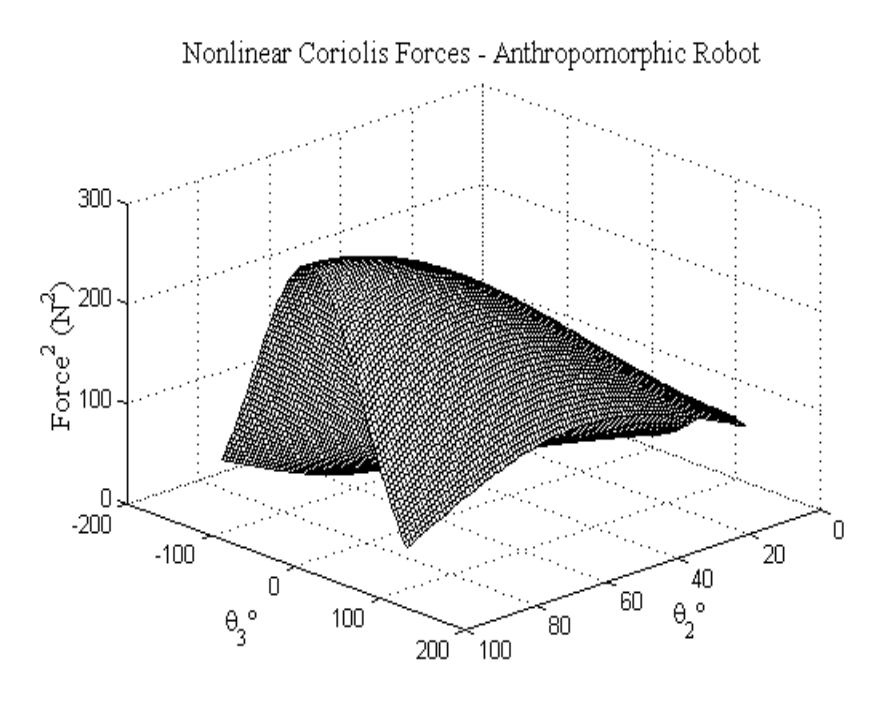


Figure 4-13
Anthropomorphic Robot Coriolis Forces

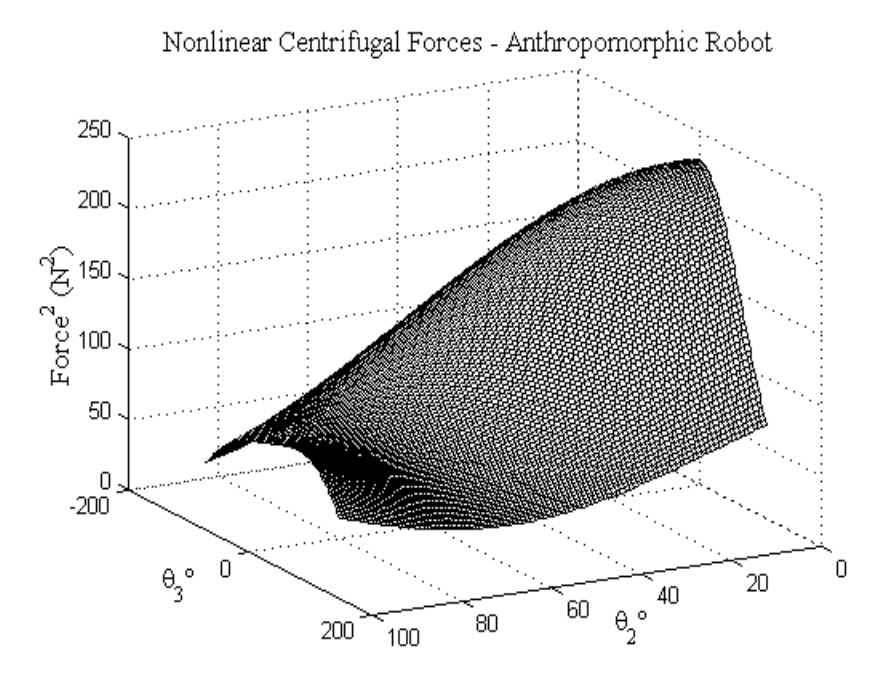


Figure 4-14 Anthropomorphic Robot Centrifugal Forces

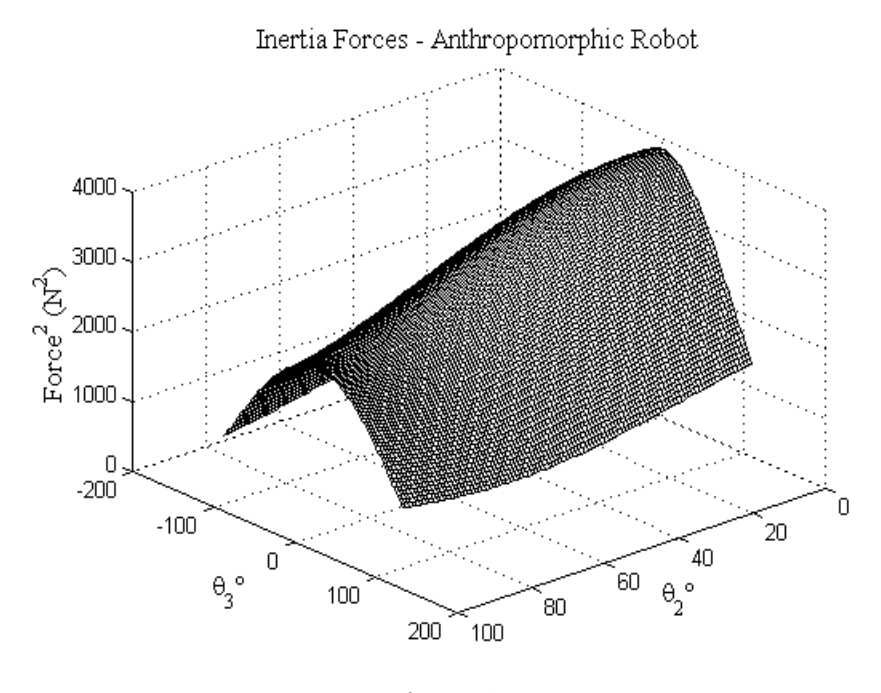


Figure 4-15 Anthropomorphic Robot Inertia Forces

Although this initial analysis may be overconservative since it does not consider the effect of decaying amplitudes or phasing, it does bring to light several important considerations. First, the magnitude of the inertia forces is much larger than the nonlinear forces. Second, *coriolis forces* are largest in near-singularity regions (case 2 in Figure 4-5). Thus, the coriolis forces are not a great concern because operation in these regions will be avoided by using the performance index. However, the *centrifugal forces* are largest around the kinematic singularities (case 1 in Figure 4-5) and where the inertia forces are largest, as shown in Figure 4-15. In fact, the centrifugal forces are maximum at the singularity point θ_2 =0°, θ_3 =0°. Operation exactly at the singularity points will be avoided, but operation around them may be required, especially if large inertia forces are desired.

Since the anthropomorphic robot is always singular in three DOF inertia torque performance, the spherical robot was chosen to study the nonlinear torque effects. The spherical robot coriolis and centrifugal torque matrices are given by equations A-37 and A-38 in Appendix A. Note the third link is prismatic, so r_3 is a variable. Figures 4-16 and 4-17 show the variation in nonlinear torque performance throughout the joint workspace and Figure 4-18 shows the inertia torques. These plots indicate that the coriolis torques are greatest in joint configurations where the inertia torque effects are largest. The centrifugal torques are largest in regions where the inertia torques are small, indicating they will interfere less with the inertia torques. Again, the magnitude of the inertia torques is greater than the nonlinear torques, but not to the same extent seen for the anthropomorphic robot forces. Although these results are not presented here, the

anthropomorphic robot also has a much larger ratio of inertia/nonlinear torques than the spherical and wrist robots. This occurs primarily because the last link of the spherical robot is prismatic and accelerating it does not provide the additional rotational inertia effects. In general, for both robots the centrifugal torques become large near the inertial singularity torque regions, while the coriolis torques become more of a concern in regions where the inertia torques are large.

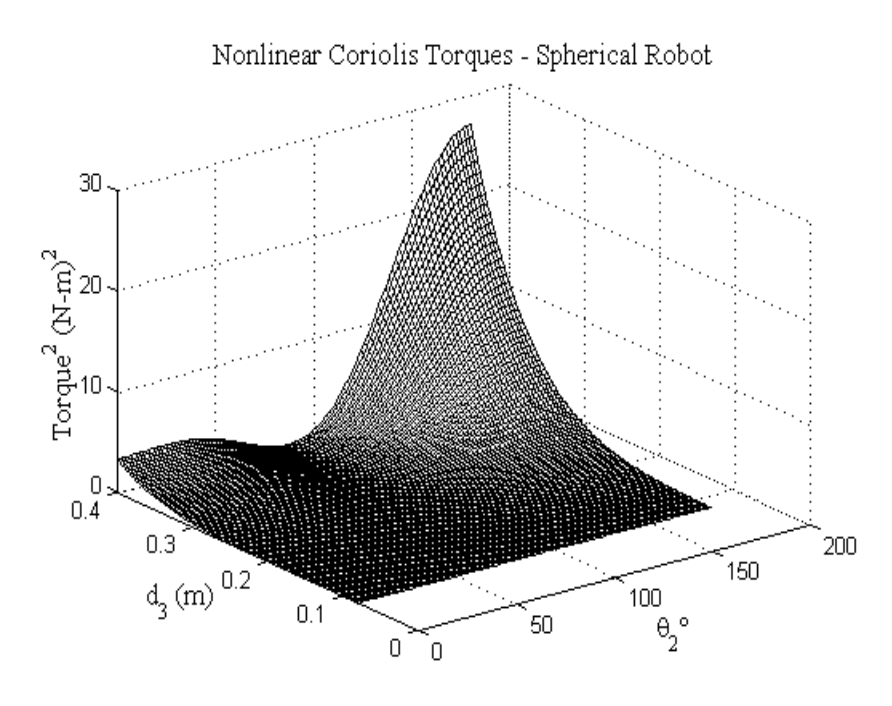


Figure 4-16 Spherical Robot Coriolis Torques

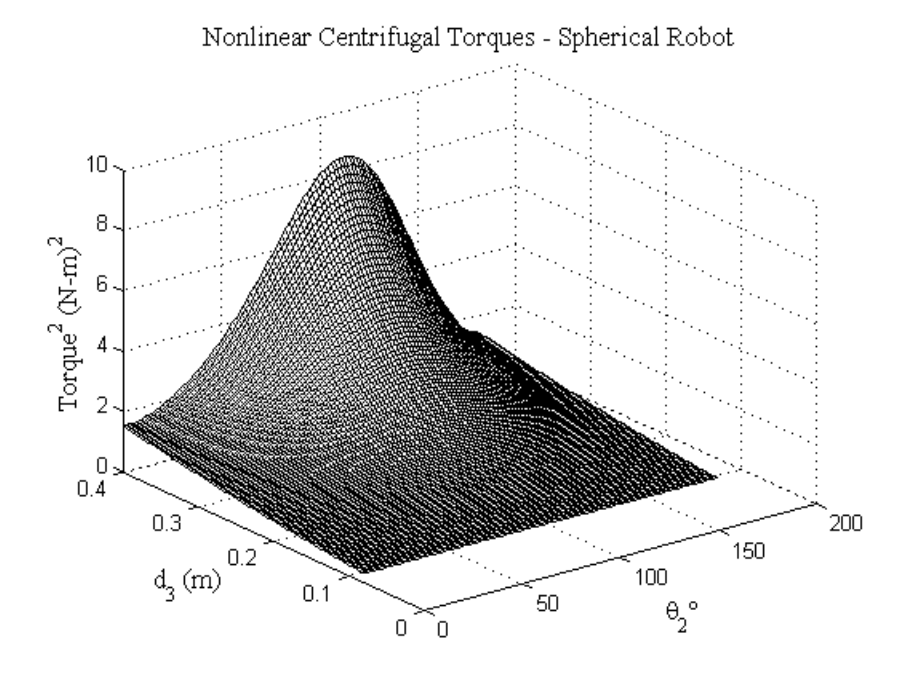


Figure 4-17 Spherical Robot Centrifugal Torques

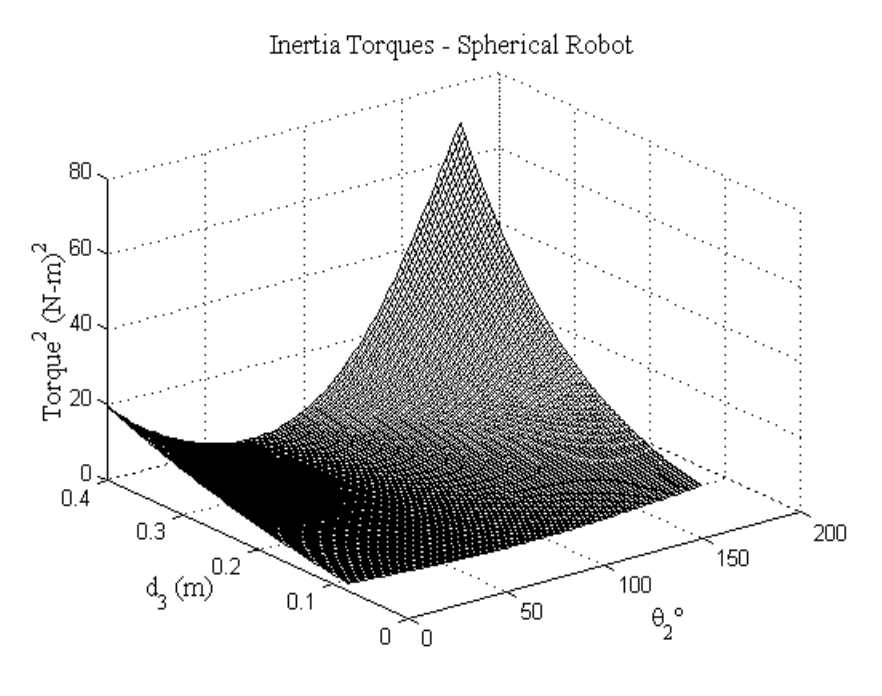


Figure 4-18 Spherical Robot Inertia Torques

From these initial studies, Matlab simulations were built for the anthropomorphic robot to further investigate the relative magnitudes of the force and torque effects. These were simulated by commanding the joint accelerations proportional to the velocities calculated from assumed harmonic motion of the base in three degrees of freedom. For example, the anthropomorphic robot was tested in a configuration expected to provide a large inertia/nonlinear force ratio, as predicted by Figures 4-5, 4-13, and 4-14 (0°, 20°, 70°). The ratio of the inertia to nonlinear effects is large, as can be seen in Figure 4-19 (in these plots, the inertia and total force traces nearly overlay and are indistinguishable).

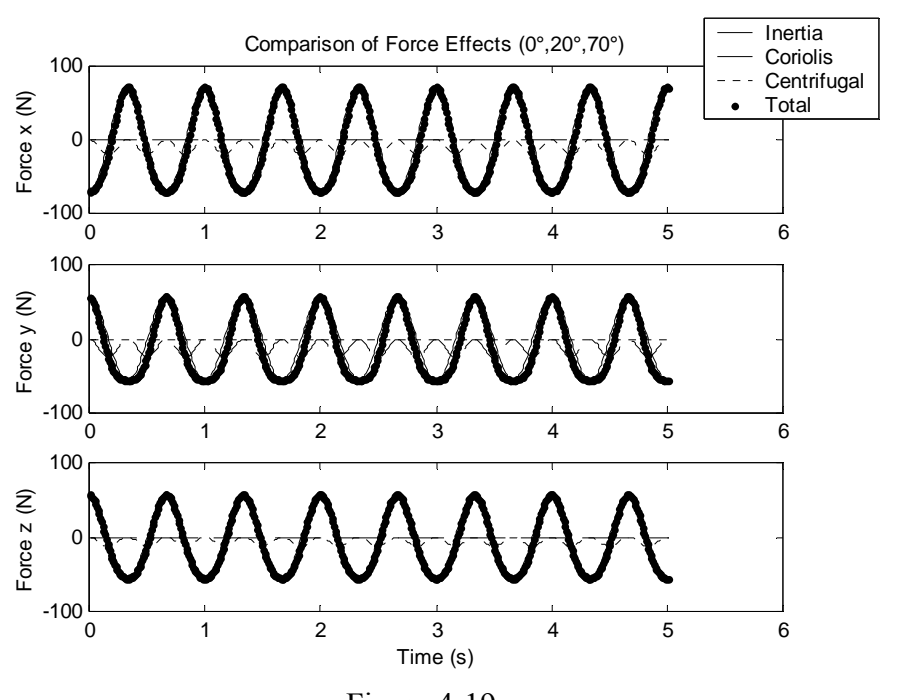


Figure 4-19
Anthropomorophic Interaction Forces, Large Inertia Effects

The same comparison is shown in Figure 4-20 with the robot in the configuration [0°, 85°, 10°], which is a region where the coriolis forces are expected to be large as well as

near a case 2 inertial singularity. The reduced ability of the robot to produce inertia forces is seen in the y direction as well as the increased coriolis effects (coriolis and total traces are nearly overlaid in the second subplot). Also, note the increased centrifugal forces in the z direction (centrifugal and total traces are overlaid in the third subplot). Since both joints are nearly straight out, the centrifugal forces due to joints 2 and 3 act primarily in the z direction. This scenario is near an inertial singularity region, which will be avoided if possible. The nonlinear effects give even more reason to avoid these joint space configurations.

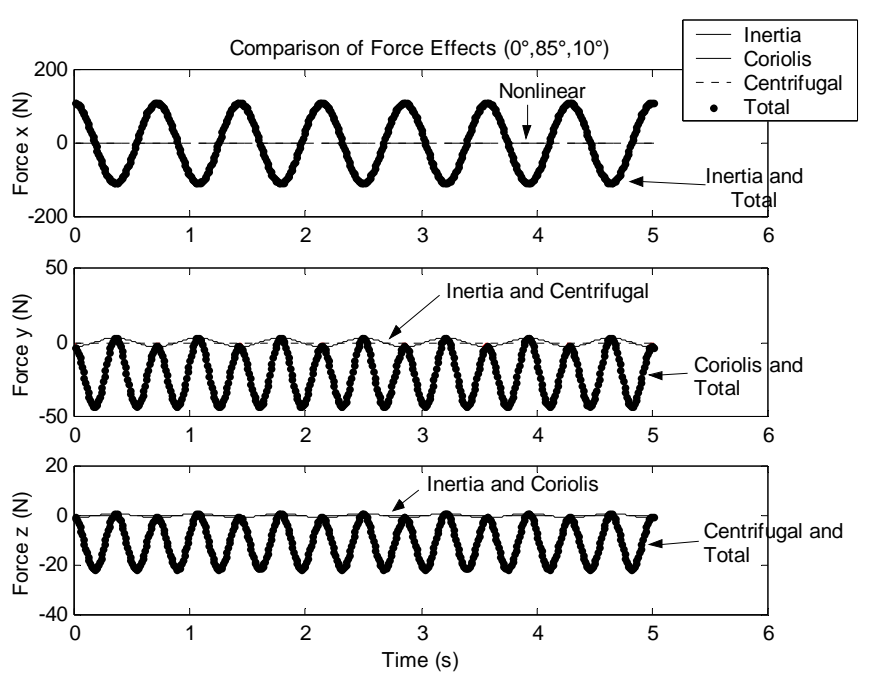


Figure 4-20 Anthropomorphic Interaction Forces, Near Singularity Case 2

Figure 4-14 predicted large centrifugal forces in a region with expected large inertia forces. The same comparison is shown in Figure 4-21 in the configuration [0°,20°,-10°], shown in Figure 4-22. In this case, the inertia forces act primarily in the y direction, while the nonlinear centrifugal forces all align primarily along the x-axis. The ratio of the inertia to nonlinear forces becomes smaller in the x direction, which results in more nonlinear effects in the total force trace. This is clearly seen in the top figure where the centrifugal (dashed line) effects are picked up in the total force trace.

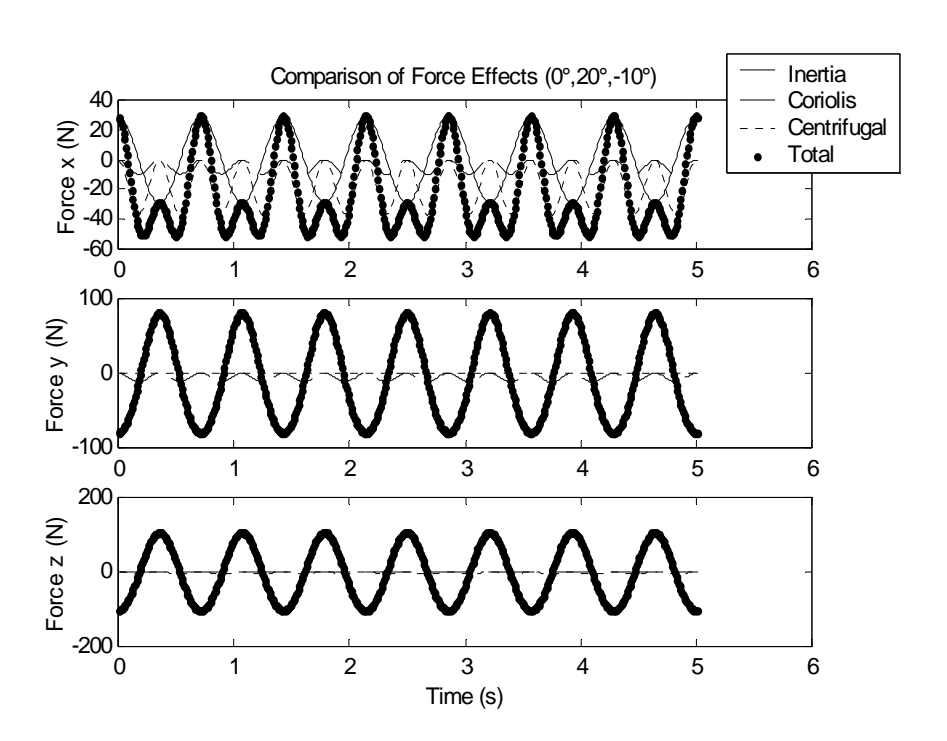


Figure 4-21 Anthropomorphic Interaction Forces, Large Centrifugal Effects

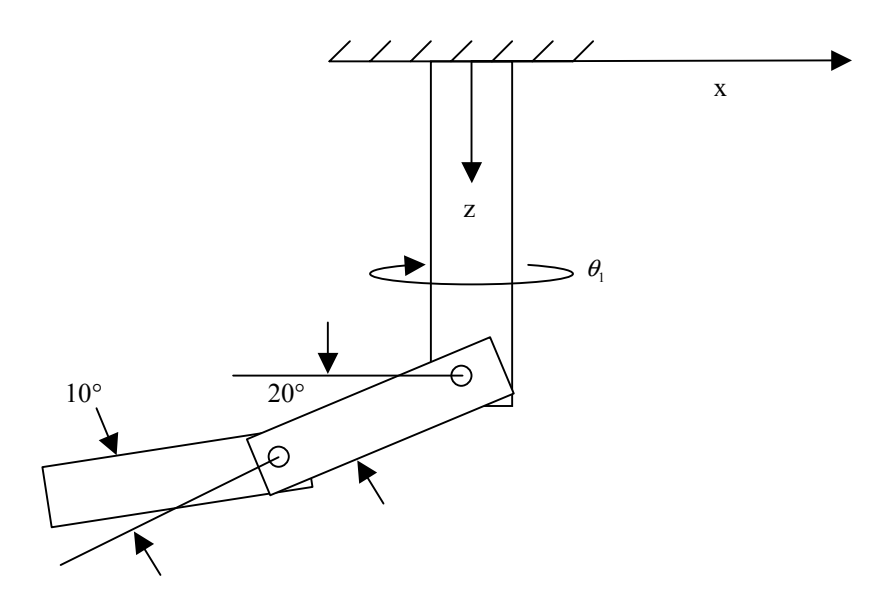


Figure 4-22 Anthropomorphic Configuration with Large Nonlinear Forces

4.3.1 Amplitude Effects

During active damping (this will be discussed more in Chapter 5), the joints will be actuating harmonically to damp the base vibration. The effect of the amplitude of the harmonic joint motion has not yet been considered. As an example, consider prescribing harmonic joint accelerations:

$$\ddot{\theta} = A\cos\omega t \tag{4-16}$$

The joint velocities will be:

$$\dot{\theta} = \frac{A}{\omega} \sin \omega t \tag{4-17}$$

The ratio of the joint accelerations, which directly affect the inertia effects, to the square of the joint velocities, which directly affect the centrifugal effects and occur at the first harmonic of the fundamental frequency, is given by:

$$\frac{\ddot{\theta}}{\dot{\theta}^2} = \frac{A\cos\omega t}{(\frac{A^2}{\omega^2})\sin^2\omega t} \tag{4-18}$$

The ratio of their amplitudes becomes:

$$\frac{\left|\ddot{\theta}\right|}{\left|\dot{\theta}^2\right|} = \frac{\omega^2}{A} \tag{4-19}$$

Alternately, if two joints are actuating, the link accelerations and velocities are given by:

$$\ddot{\theta}_{1} = A_{1} \cos \omega_{1} t \quad \ddot{\theta}_{2} = A_{2} \cos \omega_{2} t$$

$$\dot{\theta}_{1} = \frac{A_{1}}{\omega_{1}} \sin \omega_{1} t \quad \dot{\theta}_{2} = \frac{A_{2}}{\omega_{2}} \sin \omega_{2} t \tag{4-20}$$

The ratio of the joint accelerations, which drive the inertia effects, to the product of joint velocities, which drive the coriolis effects, becomes:

$$\frac{\left|\ddot{\theta}_{1}\right|}{\left|\dot{\theta}_{1}\dot{\theta}_{2}\right|} = \frac{\omega_{1}\omega_{2}}{A_{2}} \tag{4-21}$$

The frequencies of actuation will be driven by the natural frequencies of the macromanipulator, which are not controllable. However, the ratio is also inversely proportional to the amplitude of motion, which is controllable. This issue is addressed more rigorously in Chapter 5, where the joint amplitudes are related to the feedback gains and appropriate gain limits established. By limiting the amplitude of motion of each joint, both of the nonlinear effects will be reduced.

For example, consider the anthropomorphic robot in a configuration of [0°, 75°, 10°]. The second link is moved slightly from the configuration used in Figure 4-20 so the robot is not as near the inertial singularity region. The inertia, coriolis, centrifugal, and total forces are shown in Figure 4-23. The top two plots show the interactions due to all three joints actuating with constant amplitudes of approximately 23°. The bottom two plots show the forces when the joint amplitudes are reduced in half. While this results in lower inertia forces, it also has the effect of improving the ratio of the inertia/nonlinear effects.

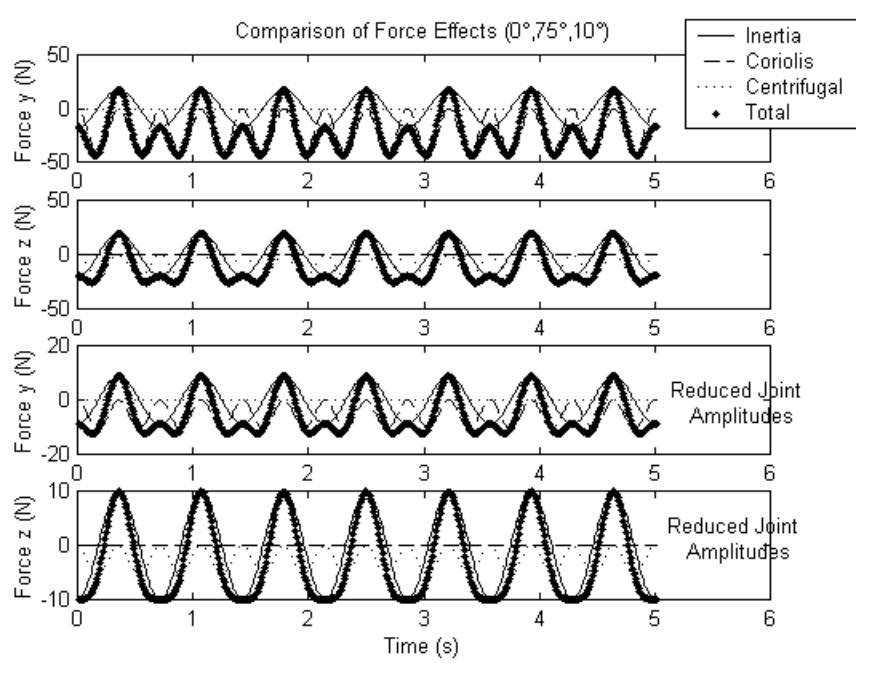


Figure 4-23
Effect of Reducing Joint Amplitudes on Nonlinear Effects

4.4 CG Method to Identify Critical Interaction Force Effects

This chapter concentrated on the interaction effects directly controllable by the rigid robot, which are the inertia and nonlinear rigid effects. The method originally used to develop the force equations is the Newton-Euler method described in Section 3.3. However, a much more efficient method may be used to develop the interaction forces directly controllable by the rigid robot. This made developing the six DOF anthropomorphic/wrist force equations manageable and was the method used to derive equations A-48 through A-50 in Appendix A.

The micromanipulator does not have a fixed point, so the interaction forces acting between each link are found by summing the moments about the CG of each link. Alternatively, the moments may be summed about the CG of the overall robot. The position vectors to the CG of each robot are given in Appendix A. Let:

$$\dot{\mathbf{r}}_{CG} = J_{CG}\dot{\mathbf{\theta}} \tag{4-22}$$

The interaction forces are given by:

$$\mathbf{F}_{IF} = \frac{d}{dt} M(J_{CG} \dot{\mathbf{\theta}}) \tag{4-23}$$

where M is the total mass of the rigid robot. The inertia and nonlinear rigid effects, defined in Equation 4-1, are given by:

$$B_f = MJ_{CG}$$

$$N_f = M\dot{J}_{CG}\dot{\theta}_i$$
(4-24)

where N_f represents combined coriolis and centrifugal forces. If desired, the macromanipulator inertia effects may be added by including the base direction cosine matrix, which is defined and discussed in Book [8], Lew [34], and Senda [62].

$$\mathbf{r}_{CG} = \mathbf{r}_{CGr} + \begin{bmatrix} 1 & -\theta_z & \theta_y \\ \theta_z & 1 & \theta_x \\ -\theta_y & \theta_x & 1 \end{bmatrix} \mathbf{r}_{CGr}$$

$$B_f + A_f = J_{CG}$$
 (4-25)

where \mathbf{r}_{CGr} is the position vector (from the base) to the CG of the rigid robot and θ_x , θ_y , and θ_z are the small base rotations about the x, y, and z axis.

4.5 Conclusions

The interaction forces and torques will be used in the control scheme to add damping to the flexible base. At this point, some general conclusions should be made about the interaction effects, which will be used to develop the vibration controller and gain limits discussed in Chapter 5.

1) The nonlinear and inertia effects are driven by two factors: the configuration of the robot and joint accelerations and velocities. The inertia performance measure introduced in equations 4-2 and 4-3 and plotted in Figures 4-5 through 4-12 can be used to choose inverse kinematic solution(s) best suited for inertial damping. As an example, consider the anthropomorphic robot in the two configurations shown in Figure 4-24. The left configuration shows a very poor configuration for inertial damping (case 2 inertial singularity), while the alternate inverse kinematics solution shown on the right will provide much better inertia force performance.

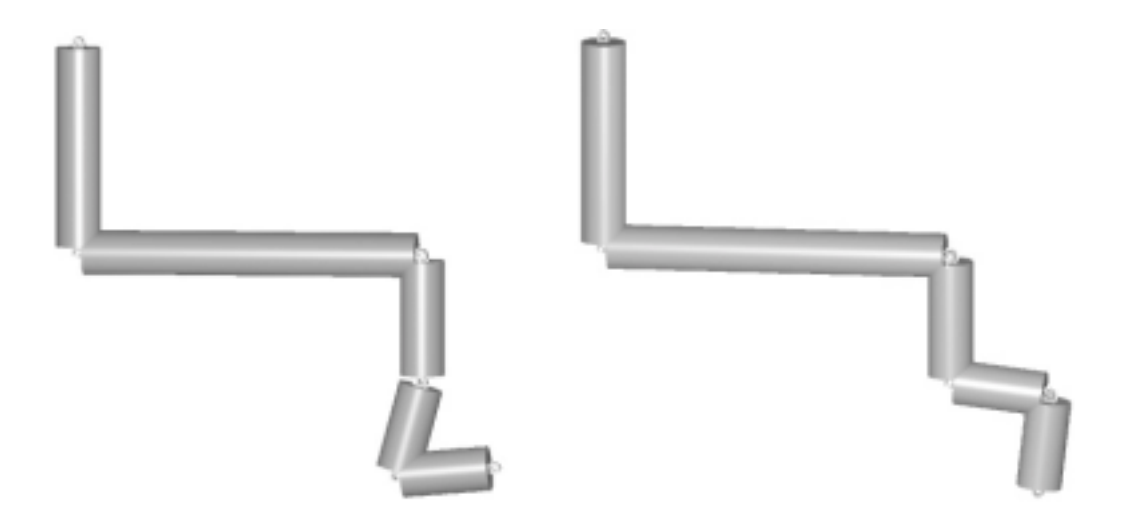


Figure 4-24 Alternate Inverse Kinematic Configurations for Anthropomorphic Robot

On the other hand, consider the configuration shown in Figure 4-22, which resulted in large centrifugal forces. The alternate inverse kinematics solution would not provide an improvement in performance in this case since the problem results from a combination of effects created by all of the joints, which would occur in either configuration.

- 2) In general, the coriolis forces are largest near inertial force singularity regions, while the centrifugal forces can become large in regions where inertia forces are large. The centrifugal torques are largest near inertial torque singularity regions, while the coriolis torques are more of the concern. There are configurations, however, where one or both can interfere with the ability of the robot to create effective inertia forces or torques.
- 3) The inertia effects are functions of the joint accelerations, while the nonlinear effects are functions of the joint velocities. The amplitude of joint motion directly influences the ratio of the inertia to nonlinear effects, as shown in equations 4-19, 4-21

and Figure 4-23. The relationship between the joint amplitudes and feedback gains will be developed in the next chapter, and gain limits established to ensure this ratio remains favorable for inertial damping.

When the performance index is used in conjunction with the limits on control gains, the most important dynamics of the coupled system (equation 3-31) take the form:

$$\begin{bmatrix} M_f + A_f(\boldsymbol{\theta}) & B_{wf}(\boldsymbol{\theta}) & B_f(\boldsymbol{\theta}) \\ A_{\tau 0}(\boldsymbol{\theta}) & J + B_{w\tau 0}(\boldsymbol{\theta}) & B_{\tau 0}(\boldsymbol{\theta}) \\ B_f^T(\boldsymbol{\theta}) & B_{\tau 0}^T(\boldsymbol{\theta}) & B_{\tau}(\boldsymbol{\theta}) \end{bmatrix} \begin{bmatrix} \ddot{\mathbf{x}}_f \\ \ddot{\boldsymbol{\theta}}_f \\ \ddot{\boldsymbol{\theta}} \end{bmatrix} + \begin{bmatrix} C & 0 & 0 \\ 0 & C_r & 0 \\ 0 & 0 & 0 \end{bmatrix} \begin{bmatrix} \dot{\mathbf{x}}_f \\ \dot{\boldsymbol{\theta}}_f \\ \dot{\boldsymbol{\theta}} \end{bmatrix} + \begin{bmatrix} K & 0 & 0 \\ 0 & K_r & 0 \\ 0 & 0 & 0 \end{bmatrix} \begin{bmatrix} \mathbf{x}_f \\ \boldsymbol{\theta}_f \\ \boldsymbol{\theta}_r \end{bmatrix} = \begin{bmatrix} 0 \\ 0 \\ \boldsymbol{\tau} \end{bmatrix} (4 - 26)$$

This also assumes the elastic deflections and rates are relatively small compared to the acceleration effects.

CHAPTER V

CONTROL SCHEME

5.1 Introduction

This chapter discusses the control scheme that will be used to provide position and base vibration control of a flexible base manipulator. The goal of the control scheme is to add to an existing position controller vibration damping capability. The rigid robot will be commanded to provide the interaction forces and torques to damp the vibration. An overview of the control scheme is shown in Figure 5-1. It is assumed the PID position controller is designed separately for rigid robot control. The rigid robot model is given by the third row of equation 3-27. The coupled rigid/flex dynamics are given by the first two rows of equation 3-27, and the flexible manipulator is modeled by equation 3-19. The reason this form was chosen for the controller is discussed in Section 5.4.3.

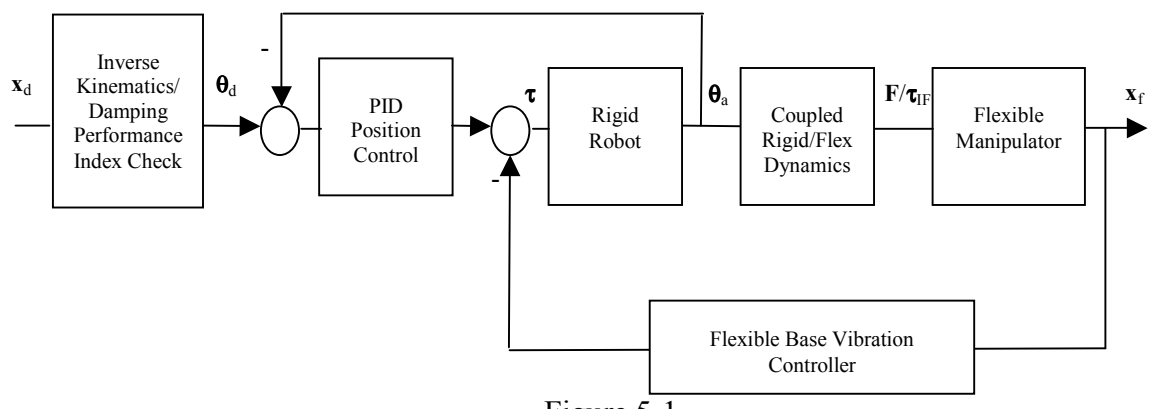


Figure 5-1
Combined Position and Base Vibration Control Scheme

First, the inverse kinematics/damping performance index check really consists of two parts. The complete performance index will predict the overall ability of the control scheme to be effective. This includes a comparison of the micromanipulator and macromanipulator inertia properties as well as weighting matrices to include other effects. The rigid robot performance measure that was introduced in equations 4-2 and 4-3 will be used in the weighting matrix for the rigid robot and can be used to choose the best inverse kinematics solutions for inertial damping.

Next, the vibration controller is introduced. One important goal of this section is to establish a range of vibration control feedback gains to ensure vibration energy is removed from the system. This involves establishing an upper limit that will limit the joint amplitudes such that the interaction effects due to the joint accelerations are greater than those due to the joint velocities, hence limiting the significance of the nonlinear effects. In addition, a lower limit is established to ensure higher system modes will be damped. Based on the results from Chapter 4, when the performance index is used along with these control gains, the most important dynamics take the form of equation 4-26. In order to add damping to the system, the joint accelerations will be commanded out of phase with the flexible base velocity.

The control scheme takes advantage of the fact that the base vibrations are of relatively high frequency compared to the rigid robot motion required to perform a task. The separation of bandwidths, or time constants, between the position and vibration control loops allows them to be considered separately. This is not addressed further here,

but more detail can be found in references [11], [33], and [35]. However, it is important to check the validity of this assumption for the specific application.

It may be desirable in some cases to provide feedback proportional to the velocity and position, akin to an ideal vibration absorber. This can give more flexibility in improving system damping but requires additional measurements or manipulation of the measured vibration data. However, the general form of the controller as well as guidelines for choosing feedback gains will remain the same for either form.

Finally, the control performance of the linearized system will be discussed in the single degree of freedom case. Root locus plots based on the linearized models verify that, over a range of feedback gains, damping can be added to the flexible system. For these studies, it has been assumed the rigid robot model takes the form of the third row in equation 3-27. The hardware on which this control scheme was implemented was a hydraulically operated robot. The actuator dynamics dominated the performance of the experimental robot, so this effect is also discussed in Section 5.4.5.

5.2 Performance Index

The performance index may be used for two tasks. First, it may be used to predict the expected effectiveness of the inertial damping control scheme. This needs to include a check for inertial singularity points and include other effects, such as the macromanipulator inertia and limits on allowable joint motion.

The following performance index will provide this measure:

$$PI = \left[\ddot{\mathbf{x}}_{m}^{T} M \left(\tilde{\mathbf{\theta}} \right)^{T} W_{f} M \left(\tilde{\mathbf{\theta}} \right) \ddot{\mathbf{x}}_{m} \right]^{-1} \left[\ddot{\mathbf{\theta}}_{m}^{T} B \left(\tilde{\mathbf{\theta}} \right)^{T} W_{r} B \left(\tilde{\mathbf{\theta}} \right) \ddot{\mathbf{\theta}}_{m} \right]$$
(5-1)

where:

$$\ddot{\mathbf{x}}_m = [\text{maximum flexible base accelerations}]$$

$$\ddot{\boldsymbol{\theta}}_m = [\text{maximum rigid robot joint accelerations}]$$
(5-2)

By including the maximum base accelerations and joint accelerations, a direct measure of the micromanipulator to macromanipulator interaction forces and torques can be made. In addition, different limits on joint accelerations can be accounted for via the maximum acceleration vectors. This could be important if the actuators of the rigid robot have bandwidth limitations or can saturate, which may impact the effectiveness of this technique. On the other hand, if the rigid robot can accelerate its links rapidy it will be more effective.

The micromanipulator and macromanipulator inertia properties are given by:

$$B = \begin{bmatrix} B_f(\tilde{\mathbf{\theta}}) \\ B_{\tau_0}(\tilde{\mathbf{\theta}}) \end{bmatrix}$$

$$M = \begin{bmatrix} M_f + A_f(\tilde{\mathbf{\theta}}) & B_{wf}(\tilde{\mathbf{\theta}}) \\ A_{\tau_0}(\tilde{\mathbf{\theta}}) & J + B_{w\tau_0}(\tilde{\mathbf{\theta}}) \end{bmatrix}$$
(5-3)

where these are the inertia effects from equation 4-26 linearized about an operating point. It is assumed the macromanipulator is in a fixed joint configuration so the macromanipulator properties are assumed approximately constant, but in reality they will vary with the configuration of the macromanipulator. Regardless, this performance measure will predict the expected performance based on the inertia properties of the macromanipulator in any configuration. The inertia matrices times the acceleration vectors provide the forces and torques due to the flexible and rigid manipulators in each direction. In the most general case, this results in two 6x1 vectors. The transpose of these vectors times the vectors of the forces and torques results in a constant equal to the sum of the square of the forces and torques. However, this measure alone does not indicate whether the rigid robot has the ability to generate these interactions in multi-degrees of freedom. Thus the weighting matrices need to be included.

The rigid robot weighting matrix is given by:

$$W_{r} = \frac{\left| B(\tilde{\boldsymbol{\theta}})^{T} B(\tilde{\boldsymbol{\theta}}) \right|}{\left| B(\tilde{\boldsymbol{\theta}})^{T} B(\tilde{\boldsymbol{\theta}}) \right|_{\text{max}}}$$
 (5-4)

This was partially discussed in Chapter 4 along with its usefulness in determining joint space configurations better suited for inertial damping. The only difference here is that it is normalized, essentially assigning a penalty as the rigid robot moves away from its best configuration. Another advantage of normalizing the performance measure is that the units of the resulting B^TB matrix do not matter.

Some authors have questioned the validity of eigenvalues and singular values for systems with physical inconsistencies, such as robots with mixed prismatic and revolute joints [20,60]. For example, the third link of the spherical robot is prismatic, so the B_f matrix in equation 4-6 has units of mass for the third column while the other columns

have units of mass times distance. This is not a problem if the determinant if B_f is taken, but using the determinant introduces many other disadvantages that were discussed in section 4.2.1. However, the weighting matrix is only intended to assign a penalty as the rigid robot moves nearer singularity regions. The units of the resulting system are not important since they are normalized, so the resulting weighting matrix is unitless. N is a 6x6 diagonal weighting matrix which is similar to the weighting functions used in optimal control [23]. Its purpose here is to scale the torques by a constant distance so the total forces and torques will have consistent units and may be added, although other considerations could be included if desired. The resulting performance measure for the rigid robot is given by:

$$PI_r = W_r * (\sum_{i=x,y,z} F_{i,\max}^2 + \frac{\tau_{i,\max}^2}{N})$$
 (5-5)

where $F_{i,max}$ and $\tau_{i,max}$ are the maximum interaction forces and torques that can be created by the rigid robot and $0 \le W_r \le 1$. The nearer the robot is to a singularity configuration, the smaller W_r will be.

The flexible base weighting matrix provides a scaling factor based on the inverse of the flexible base stiffnesses. It is also normalized based on the minimum stiffness in the system. This has the effect of reducing the weighting in stiffer directions or with higher frequency vibration. Assuming harmonic base vibration, the higher frequencies result in lower amplitude vibration and will damp more quickly than the lower frequencies. N is again a scaling factor to normalize the torques. The flexible weighting matrix is given by:

$$W_{f} = K_{\min} \begin{bmatrix} \frac{1}{K_{x}} & 0 & 0 & 0 & 0 & 0 \\ 0 & \frac{1}{K_{y}} & 0 & 0 & 0 & 0 \\ 0 & 0 & \frac{1}{K_{z}} & 0 & 0 & 0 \\ 0 & 0 & 0 & \frac{1}{N^{*}G_{x}} & 0 & 0 \\ 0 & 0 & 0 & 0 & \frac{1}{N^{*}G_{y}} & 0 \\ 0 & 0 & 0 & 0 & 0 & \frac{1}{N^{*}G_{z}} \end{bmatrix}$$

$$(5-6)$$

The resulting perfomance measure for the flexible base is given by:

$$PI_{f} = \sum_{i=x,y,z} F_{i,\max}^{2} \frac{K_{\min}}{K_{i}} + \sum_{i=\theta_{v},\theta_{v},\theta_{z}} \tau_{i,\max}^{2} \frac{G_{\min}}{NG_{i}}$$

$$(5-7)$$

where $F_{i,max}$ and $\tau_{i,max}$ are the maximum interaction forces and torques created at the base of the rigid robot due to the macromanipulator tip acceleration. The weighting matrix has the effect of reducing the magnitude of the interaction forces and torques due to the macromanipulator in stiff directions.

The overall performance measure compares the ratio of the performance measures (PI_r/PI_f) . Notice it will be larger if the macromanipulator has stiff directions that are of less concern for vibration. Also note it is immaterial whether the units are English or SI because the weighting matrices are normalized. The only requirement on units is that units used for the macromanipulator be consistent with those used for the micromanipulator. Finally, although it is not specifically addressed in this dissertation,

the measure may be extended to address cases of underactuation or redundancy, since there is no requirement for the B or M matrices to be square.

The measure discussed above will predict, in general, the ability of the inertial damping scheme to successfully damp vibration in the macromanipulator. It may be used in the control scheme, and for thoroughness, the full performance measure should be used if computational capability allows it. However, it may also create an unnecessary burden on the controller to carry out the calculations real-time. The reduced rigid robot performance measure introduced in equations 4-2 and 4-3 may provide a quicker and more easily implementable measure to use actively in the control scheme or in the development of pre-programmed trajectories. This reduced measure was used in Matlab simulations and experimental work discussed in Chapters 6 and 7 in order to reduce computation time and demonstrated its effectiveness.

5.3 Vibration Controller

In most workspace locations, the inertia effects dominate the controllable interaction forces and torques. The performance index discussed above may be used to choose workspace configurations where the inertia effects are large. In configurations where the nonlinear effects become large, the amplitude of joint motion can be limited to improve the ratio of inertia to nonlinear effects. When this is the case, the vibration controller will prescribe the joint accelerations out of phase with the base velocity as follows:

$$\ddot{\mathbf{\theta}} = -ID(\mathbf{\theta}, \dot{\mathbf{\theta}})K\dot{\mathbf{x}} \tag{5-8}$$

ID is an inverse dynamics function designed to cancel the significant rigid robot dynamics [4,19] and \mathbf{x} refers to the flexible base vibration (\mathbf{x}_f). K is a diagonal matrix of

gains K_i , where K_i is the gain for the i^{th} vibrational degree of freedom. With the limits on gains that will be developed in the next section, the inertia effects are expected to be most significant. Thus the prescribed joint accelerations will be:

$$\ddot{\mathbf{\theta}} = -B^{-1}(\mathbf{\theta})K\dot{\mathbf{x}} \tag{5-9}$$

However, the joint torques will need to be commanded so the final vibration controller takes the form:

$$\boldsymbol{\tau} = -B_{\tau}(\boldsymbol{\theta})B^{-1}(\boldsymbol{\theta})(K\dot{\mathbf{x}}) \tag{5-10}$$

 $B_{\tau}(\theta)$ is as defined in equation 3-27 and

$$B = \begin{bmatrix} B_f(\mathbf{\theta}) \\ B_{\tau_0}(\mathbf{\theta}) \end{bmatrix} \tag{5-11}$$

It is assumed the rigid robot joint positions, θ , are measured and available for use in the control scheme. There should be a minimum value established for the determinant of the inertia matrix to prevent it from being inverted when the robot is passing through a singularity configuration. Although these regions will be avoided for point-to-point motion and fixed configuration operation, it may be necessary to pass through the singularity regions. In this case, it will become necessary to limit the commanded output from the controller.

5.3.1 Vibration Control Gains

The goal of this section is to establish a range of vibration control feedback gains to ensure vibration energy is removed from the system. The upper limit is developed in order to limit the joint amplitudes such that the interaction effects due to joint accelerations (inertia effects) are greater than those due to the joint velocities, hence

limiting the significance of the nonlinear effects. In addition, a lower limit is established to ensure higher system modes will be damped.

5.3.1.1 Upper Limit

In order to establish an upper limit on the feedback gains, first assume harmonic base vibration of mode i. As discussed in Chapter 4, assuming harmonic motion of the rigid robot, the inertia effects will be functions of the joint accelerations and, with the proper limit on the amplitude of joint motion, will be greater than the nonlinear effects. Thus, the vibration controller will prescribe the joint accelerations out of phase with the base velocity in order to add damping to the flexible base.

The prescribed joint accelerations, velocities, and positions for the jth joint will be approximately harmonic and take the form:

$$x_{i} = X_{i} \sin \omega_{i} t$$

$$\ddot{\boldsymbol{\theta}}_{j} = -B^{-1}(\tilde{\boldsymbol{\theta}}) K_{i} X_{i} \omega_{i} \cos \omega_{i} t$$

$$\dot{\boldsymbol{\theta}}_{j} = -B^{-1}(\tilde{\boldsymbol{\theta}}) K_{i} X_{i} \sin \omega_{i} t$$

$$\boldsymbol{\theta}_{j} = \frac{B^{-1}(\tilde{\boldsymbol{\theta}}) K_{i} X_{i}}{\omega_{i}} \cos \omega_{i} t$$
(5-12)

Here is it assumed the inertia matrix, $B(\theta)$, can be linearized and is approximately constant about an operating point. The feedback gains will be selected to ensure this is a reasonable assumption and will be discussed in more detail later.

The maximum amplitude of the prescribed joint motion will occur during the first few cycles of vibration damping and for each joint can be written as:

$$\left|\theta_{j}\right| = \frac{K_{i}B^{-1}(\tilde{\boldsymbol{\theta}})X_{i}}{\omega_{i}} \equiv A \tag{5-13}$$

where A is defined as the amplitude of motion. It is clear that an upper limit on the feedback gains is necessary, if for no other reason than to ensure the joint motion remains inside the allowable workspace or to prevent actuator saturation. Another consideration is the ratio of the inertia effects (functions of the joint accelerations) to the nonlinear effects (functions of products of the joint velocities). This was discussed extensively in section 4.3.1, and Figure 4-23 showed that the ratio of inertia effects to nonlinear effects can be improved by reducing the amplitude of joint motion. Here, the centrifugal effects are considered, so these become functions of the square of the joint velocities:

$$\frac{\left|\frac{\ddot{\theta}_{j}}{\left|\dot{\theta}_{j}^{2}\right|} = \frac{-B^{-1}(\tilde{\mathbf{\theta}})K_{i}X_{i}\omega_{i}}{-B^{-2}(\tilde{\mathbf{\theta}})K_{i}^{2}X_{i}^{2}} = \frac{\omega_{i}B(\tilde{\mathbf{\theta}})}{K_{i}X_{i}}$$
(5-14)

Solving equation 5-13 for K_i and substituting into equation 5-14 yields:

$$\frac{\left|\ddot{\theta}_{j}\right|}{\left|\dot{\theta}_{j}^{2}\right|} = \frac{A\omega_{i}^{2}}{A^{2}\omega_{i}^{2}} = \frac{1}{A} \tag{5-15}$$

Likewise, the ratio of inertia to coriolis effects takes the form:

$$\frac{\left|\ddot{\theta}_{j}\right|}{\left|\dot{\theta}_{i}\dot{\theta}_{j}\right|} = \frac{\omega_{i}}{A_{j}\omega_{j}} \tag{5-16}$$

where ω_i and ω_i are two different frequencies of base vibration.

Notice by relating the feedback gains to the amplitude of joint motion, the ratios become inversely proportional to the amplitude of motion, A. Thus, A can be limited to ensure the joint acceleration effects remain larger than joint velocity effects. One upper limit is A<1 radian, although there may be more restrictive limits due to other considerations. The gains should be limited such that:

$$K_{i} < \frac{\omega_{i\min} B(\tilde{\mathbf{\theta}})_{\min}}{X_{i\max}} A \tag{5-17}$$

The true multi degree-of freedom case is more complex, of course. In addition, the selection of A and B_{min} will be specific to the macro/micromanipulator. The inertia and force effects also vary throughout the workspace, as discussed in Chapter 4. However, the above limit will help reduce the significance of the nonlinear effects, even when in workspace locations where they can become large. Also, note this ratio improves with decreasing amplitude, which increases the effectiveness of the scheme as the vibration is damped.

This limit also helps validate the assumption that the inertia matrix B can be linearized about an operating point. Consider the sensitivity of the inertia matrix to changes in the joint positions. In order to keep this argument general, these matrices consist of terms involving sines, cosines, and combinations of sines and cosines. This general argument is intended to provide an example representative of all of the rigid robot effects (inertia, nonlinear, and gravity matrices). In order to determine the error introduced by evaluating B at an operating point, expand B in a Taylor series [6]:

$$B(\mathbf{\theta}) \square B(\tilde{\mathbf{\theta}}) + \Delta \theta_i \left(\frac{\partial B(\mathbf{\theta})}{\partial \theta_i} \right)_{\mathbf{\theta} = \tilde{\mathbf{\theta}}}$$
 (5-18)

where $\Delta\theta_i$ is harmonic and given by the last equation in 5-12. The inertia matrix B as well as its first partial derivatives are bounded and continuous. The limits on joint amplitudes will ensure the variation term remains small. Also, note this assumption becomes more valid as energy is removed from the system because the joint amplitudes are reduced. This, in general, is applicable to all of the rigid robot effects.

5.3.1.2 Lower Limit

A lower limit also needs to be established to ensure higher flexible system modes, if excited, will be damped. The nonlinear effects will still be commanded along with the damping effects. Here a worst-case scenario is considered where the nonlinear effects excite a mode of the flexible system. The goal here is ensure net energy removal from the system.

Assume an initial impulse force δ (N) applied over a finite amount of time T excites a fundamental mode of the flexible system. The rate of change of energy added to the flexible base is:

$$\frac{dW}{dt} = \delta \dot{x}$$

$$= \delta X_i \omega_i \cos \omega_i t \quad \left(\frac{N-m}{s}\right)$$
(5-19)

where the base motion is given by the first equation in 5-12. The energy added to the flexible base is given by:

$$\Delta W = \int_0^T \delta \omega_i X_i \cos \omega_i t dt$$

$$= \delta X_i \sin \omega_i t \Big|_0^T$$

$$= \delta X_i \sin \omega_i T \text{ (N-m)}$$
(5-20)

The rate of change of energy dissipated by the damping controller is [59]:

$$\frac{dW}{dt} = -K_i \dot{x}^2 \tag{5-21}$$

Over one cycle of vibration, the net energy dissipated by the vibration controller is:

$$\Delta W = -K_i \omega_i^2 X_i^2 \int_0^{\frac{2\pi}{\omega_i}} \cos^2 \omega_i t dt$$

$$= -K_i \omega_i^2 X_i^2 \left[\frac{t}{2} + \frac{\sin 2\omega_i t}{4\omega_i} \right]_0^{\frac{2\pi}{\omega_i}}$$

$$= -K_i \omega_i X_i^2 \pi \tag{5-22}$$

This holds regardless of whether velocity feedback alone is used or if velocity and position feedback are used. This is the energy removed over each cycle of vibration, so as long as the disturbance is applied over a finite period, the vibration controller will remove energy from the system.

Based on linearizing the system and assuming harmonic motion over each cycle of vibration, the nonlinear centrifugal forces take the form (the same form applies to the nonlinear torques):

$$F_{Ni} = N_f(\tilde{\mathbf{\theta}})\dot{\mathbf{\theta}}_j^2$$

$$F_{Ni} = N_f(\tilde{\mathbf{\theta}})B^{-2}(\tilde{\mathbf{\theta}})K_i^2 X_i^2 \sin^2 \omega_i t$$

$$F_{Ni} = \frac{N_f(\tilde{\mathbf{\theta}})B^{-2}(\tilde{\mathbf{\theta}})K_i^2 X_i^2}{2} (1 - \cos 2\omega_i t)$$
(5-23)

where N_f represents N_{Cf} or N_{Ct0} given in equation 4-11 for forces and torques, respectively and $(\sin \omega_i t)^2$ was replaced by an equivalent trigonometric identity. Define Y as the amplitude of the nonlinear forces, or:

$$Y(\tilde{\mathbf{\theta}}) \equiv \frac{N_f(\tilde{\mathbf{\theta}})B^{-2}(\tilde{\mathbf{\theta}})K_i^2 X_i^2}{2}$$
(5-24)

Y may be assumed approximately constant since $N_{\rm f}$ and B may be assumed approximately constant about an operating point, as discussed in section 5.3.1.1. The

nonlinear force may be split into two terms, Y and $-Y\cos 2\omega_i t$. The rate of change of energy added to the system due to the first term is given by:

$$\frac{dW}{dt} = Y(\tilde{\mathbf{\Theta}}) X_i \omega_i \cos \omega_i t \tag{5-25}$$

Regardless of the mode or number of modes excited, if Y is approximately constant the net work over each cycle of vibration will be small since:

$$\Delta W_{in} = Y(\tilde{\boldsymbol{\theta}}) \int_{0}^{\frac{2\pi}{\omega_{i}}} X_{i} \omega_{i} \cos \omega_{i} t dt \approx 0$$
 (5-26)

and the vibration controller will remove any energy added.

The effect of the second term is more interesting. Define the first harmonic of the fundamental frequency as:

$$\overline{\omega}_i = 2\omega_i \tag{5-27}$$

Consider the flexible base as a damped system responding to a harmonic forcing, or

$$M\ddot{x}_2 + C\dot{x}_2 + Kx_2 = -Y(\tilde{\theta})\cos\bar{\omega}_i t$$
 (5-28)

where M, C, and K are inertia, damping, and stiffness properties of the macromanipulator and the natural frequency and damping ratio of the flexible base mode are given by ω_n and ζ , respectively. Assume the resulting vibration will take the form:

$$x_2 = X_2 \cos(\overline{\omega}_i t - \phi) \tag{5-29}$$

where X_2 is the amplitude of the vibration and ϕ the resulting phase shift.

Substituting 5-29 into 5-28 and solving for the resulting amplitude and phase shift yields:

$$X_{2} = \frac{-Y}{L}$$

$$L = \frac{1}{M} \sqrt{(\omega_{n}^{2} - \overline{\omega}_{i}^{2})^{2} + (2\zeta \overline{\omega}_{i} \omega_{n})^{2}}$$
(5-30)

$$\tan \phi = \frac{C\overline{\omega}_i}{K - M\overline{\omega}_i^2}$$

$$= \frac{2\zeta\omega_n\overline{\omega}_i}{\omega_n^2 - \overline{\omega}_i^2}$$
(5-31)

The rate of change of energy into the system and net energy added over one cycle of vibration becomes:

$$\frac{dW}{dt} = YX_{2}\overline{\omega}_{i}\cos\overline{\omega}_{i}t * \sin(\overline{\omega}_{i}t - \phi)$$

$$\Delta W_{in} = YX_{2}\overline{\omega}_{i}\cos\phi \int_{0}^{\frac{2\pi}{\overline{\omega}_{i}}}\cos\overline{\omega}_{i}t\sin\overline{\omega}_{i}tdt - YX_{2}\overline{\omega}_{i}\sin\phi \int_{0}^{\frac{2\pi}{\overline{\omega}_{i}}}\cos^{2}\overline{\omega}_{i}tdt$$

$$= -YX_{2}\pi\sin\phi \tag{5-32}$$

Substituting 5-30 into 5-32 gives the net energy added to the system over one cycle of vibration:

$$\Delta W_{in} = \frac{Y^2 \sin \phi \pi}{L} \tag{5-33}$$

The net energy dissipated by the vibration controller over one cycle of vibration is:

$$\Delta W_{out} = -K_i X_2^2 \overline{\omega}_i \pi = \frac{-K_i Y^2 \overline{\omega}_i \pi}{L^2}$$
 (5-34)

In order to ensure energy dissipation, the goal is to choose K_i such that $\Delta W_{out} + \Delta W_{in} < 0$. This relationship becomes:

$$-K_{i}\overline{\omega}_{i} + L\sin\phi < 0 \tag{5-35}$$

The worst-case scenario occurs when the nonlinear harmonics occur exactly at a natural frequency of the system, or when $\overline{\omega}_i = \omega_n$ and $\sin \phi = 1$ in which case:

$$L = \frac{1}{M} \sqrt{(2\zeta \overline{\omega}_i \omega_n)^2}$$

$$= \pm \frac{2\zeta \overline{\omega}_i \omega_n}{M}$$
(5-36)

Thus the lower limit on the control gain to ensure net energy dissipation becomes:

$$K_i > \pm \frac{2\zeta\omega_n}{M} \tag{5-37}$$

Consider the meaning of this lower limit. As long as the vibration control gains are selected such that the vibration controller adds no more energy to higher system modes than that which can be dissipated by the natural damping in the system, overall vibration energy will be removed from the system. However, this lower limit analysis only considers the higher system modes. In order to prevent excitation of them along with other negative consequences of using negative feedback gains, the lower limit is realistically chosen as zero. Using the upper limit established previously, limiting the gains to the range:

$$0 < K_i < \frac{\omega_{i,\min} B(\tilde{\boldsymbol{\theta}})_{\min}}{X_{i,\max}} A$$
 (5-38)

will ensure effects due to joint accelerations are larger than those due to joint velocities, hence the inertia effects will also be larger. It also ensures there is enough damping available to successfully remove vibration energy from higher modes of vibration (if a concern) if they are excited.

5.4 Controller Performance

This section investigates the control performance of the linearized system, for both ideal robot models as well as a hydraulically operated robot. Using the linearized model

shown in Figure 5-2, the controllability of the system is discussed. Next, the combined system controller is discussed. The theoretical development in previous sections is based on assuming increasing vibration control feedback gains results in a direct increase in flexible base damping. This section shows that this is achievable over a range of feedback gains and under what circumstances the position and vibration controllers interfere. This is only briefly discussed for the linearized system here. For more extensive analysis on methods to decouple the two controllers, the reader is referred to Book and Lee [11], Lee[32,33] and, more recently Lew [35–38].

In most workspace regions, the inertia effects dominate the interactions, as discussed in Chapter 4. The performance index will be used to ensure the robot operates in these joint workspace configurations, whenever possible. In other regions where nonlinear effects can become large, the joint amplitudes will be limited as discussed in section 5.3.1 to reduce the nonlinear effects.

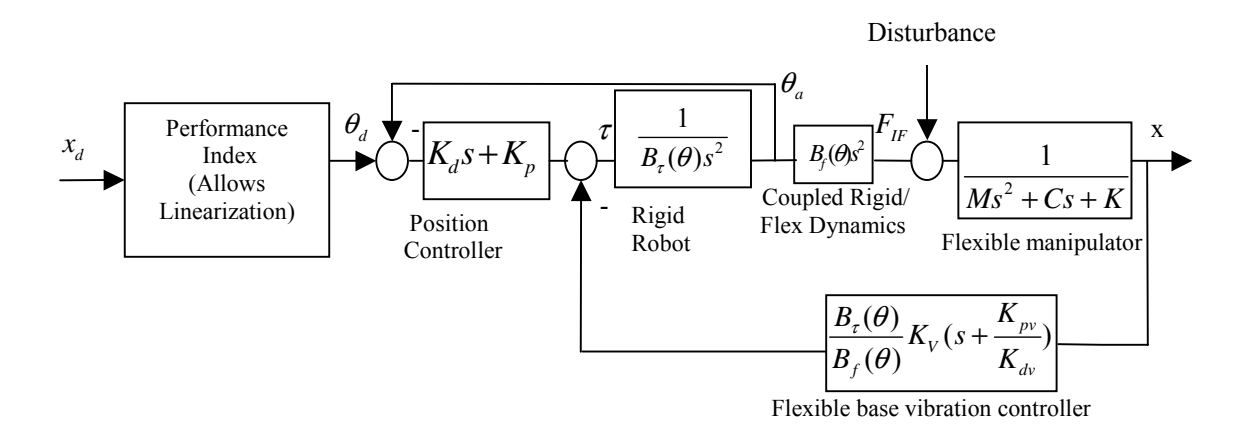


Figure 5-2 Linearized Single Degree of Freedom Control Scheme

When these conditions are met, the linearized equations of motion from equation 3-27 take the form:

$$\begin{split} F_{IF} &\cong B_f(\boldsymbol{\theta}) \ddot{\boldsymbol{\theta}} \\ \tau_{IF} &\cong B_{\tau 0}(\boldsymbol{\theta}) \ddot{\boldsymbol{\theta}} \\ \tau &\cong B_{\tau}(\boldsymbol{\theta}) \ddot{\boldsymbol{\theta}} \end{split} \tag{5-39}$$

The rigid robot control model does not include actuator dynamics, which would be a factor in most real robotics systems and is discussed in the next section. In order to shorten the notation in this section, \mathbf{F}_{IF} will refer to both interaction forces and torques.

5.4.1 Controllability

Controllability can be investigated for the linearized, single degree of freedom model.

The state space model takes the form:

$$\begin{bmatrix} \ddot{x} \\ \dot{x} \\ \ddot{\theta} \\ \dot{\theta} \end{bmatrix} = \begin{bmatrix} -C/M & -K/M & 0 & 0 \\ 1 & 0 & 0 & 0 \\ 0 & 0 & 0 & 0 \\ 0 & 0 & 1 & 0 \end{bmatrix} \begin{bmatrix} \dot{x} \\ x \\ \dot{\theta} \\ \theta \end{bmatrix} + \begin{bmatrix} B/(B_{\tau}M) \\ 0 \\ 1/B_{\tau} \\ 0 \end{bmatrix} \tau$$
 (5-40)

The controllability matrix [55] has a rank of four except when B=0 (B_{τ} is finite). The determinant of the controllability matrix is given by:

$$\det = \frac{B^2 K^2}{B_r^4 M^4} \tag{5-41}$$

Assuming the form of the controller given in equation 5-10, the system has full state controllability by the rigid robot joint torques, τ , except when B=0. Thus this is a sufficient but not necessary condition for controllability of the system since the states could still be controllable by some alternate controller form.

For the multi-degree of freedom case, this corresponds to an inertial singularity point discussed in Chapter 4. In these configurations, the rank of the controllability matrix reduces to two and, assuming the use of the controller in equation 5-10, the rigid robot inertia matrix is not invertible. Another problem situation occurs when the ratio of macromanipulator stiffness to inertia (K/M) becomes very small, which indicates an extremely flexible base or large macromanipulator. This would also present a problem since there will be no coupling between the rigid robot interactions and the mode of vibration. Note the performance index described in section 5.2 would also predict impacted performance in all of these scenarios.

5.4.2 Ideal Rigid Robot Model Control Performance

The general case of position and velocity feedback is investigated here (gain limits developed in Section 5.3.1 are applicable for either case). Simulations were built using velocity and position feedback as well as the more specific case of velocity feedback only. Experimental work used acceleration feedback with actuators that act as a velocity source.

The compensated closed loop transfer function is affected by both the joint controller and vibration controller and has a characteristic equation given by:

characteristic equation =
$$1 + \frac{PD_{pos}}{B_{\tau}s^{2}} + \frac{K_{v}(s + \frac{K_{pv}}{K_{dv}})}{Ms^{2} + Cs + K}$$
 (5-42)

 PD_{pos} represents a proportional-derivative position controller for the rigid robot. The last term is the vibration controller. The interaction forces and torques, are prescribed as:

$$F_{IF} / \tau_{IF} = -K_{\nu} (\dot{x} + \frac{K_{p\nu}}{K_{d\nu}} x)$$
 (5-43)

and are generated by accelerating the links of the rigid robot. The transfer function with the vibration controller feedback gain K_v as the multiplying factor takes the form [55]:

$$G(s)_{\text{vibration control}} = \frac{B_{\tau} s^{2} K_{\nu} (s + \frac{K_{p\nu}}{K_{d\nu}})}{(Ms^{2} + Cs + K) * (B_{\tau} s^{2} + K_{d} s + K_{p})}$$
(5 – 44)

Consider the typical case of a flexible base with a low fundamental mode (<2 Hz) and low damping. Under these circumstances the dominant flexible system poles are very close to the imaginary axis and at a value roughly equal to the first natural frequency of the system. Figure 5-3 shows a pole-zero map of equation 5-44, with lightly damped flexible poles near the j ω axis, critically damped rigid position control poles, and the placeable vibration control zero. To add damping directly to the system, the departure angle from the complex pole (the top one is considered here) would be approximately 225°, as shown in Figure 5-3:

$$180^{\circ} - 90^{\circ} + 180^{\circ} - 2 * \phi + \theta = 225^{\circ}$$
 (5-45)

where ϕ represents the angle of the vector from the rigid control poles to the flexible pole and θ the angle of the vector from the vibration control zero to the flexible pole.

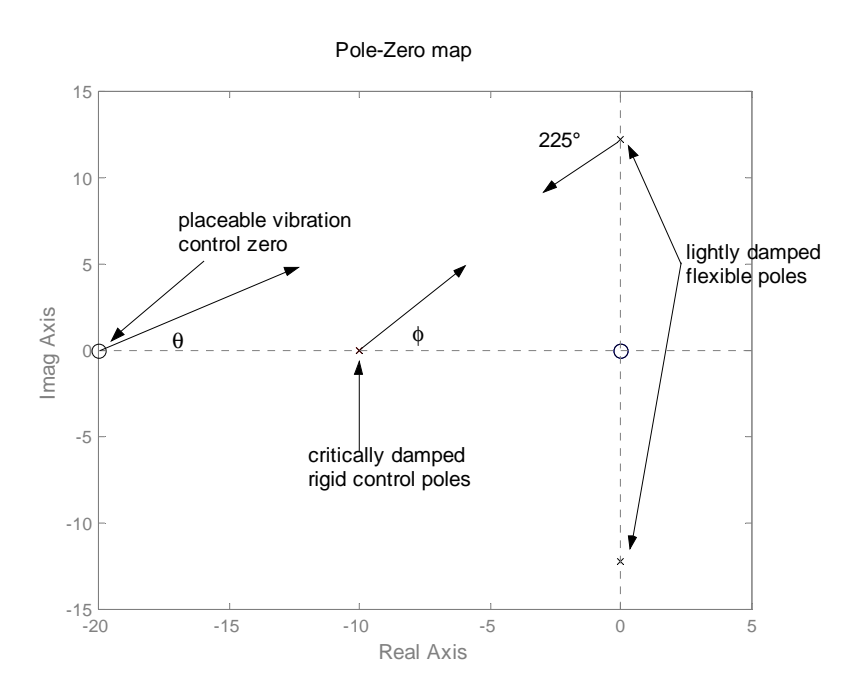


Figure 5-3
Pole-Zero Map of Closed Loop System

For critically damped performance and in order to limit the zero to the left half plane $(\theta>0^\circ)$, the lower limit for the rigid control poles is $\phi>22.5^\circ$. Note as ϕ increases the speed of the rigid controller decreases since the poles are moving closer to the imaginary axis. Thus, the tradeoff is a limit on position control bandwidth if optimal damping is desired, which corresponds to a limit of roughly 2.5 times the fundamental frequency. At the lower limit ($\phi=22.5^\circ$), the zero would need to be placed at an infinite distance along the negative real axis to achieve the best vibration control damping, which of course is unrealistic. However, it can be concluded that position plus velocity feedback of base vibration gives the best solution for combined position and base vibration control, in the case of an ideal rigid robot model.

For example, placing the poles at roughly twice the natural frequency of the flexible mode gives the best location for the zero at:

$$\theta = -45^{\circ} + 2 * \tan^{-1}(1/2)$$
 (5-46)

or at roughly 7 times the natural frequency of the flexible system. This results in the root locus plot shown in Figure 5-4 (again plotted for increasing vibration feedback gains). The resulting improvement in flexible pole damping is as desired, but the tradeoff is underdamped rigid robot position control performance. If the feedback gains are large enough to achieve critically damped rigid poles, the flexible system damping improvement is diminished. This suggests a lower allowance for the independently designed position control loop because the natural frequency of those poles increases when combined with an inertial damping controller.

The effect of the position control gains should also be considered. In this case, the open loop transfer function is given by:

$$G(s)_{position \ control} = \frac{(K_d s + K_p)(M s^2 + C s + K)}{B_{\tau} s^2 (M s^2 + C s + K + K_v (s + \frac{K_{pv}}{K_{dv}}))}$$
(5-47)

The root locus plot for increasing position control feedback gains is shown in Figure 5-5. The best flexible damping performance is achieved very quickly and at low gains for the position controller.

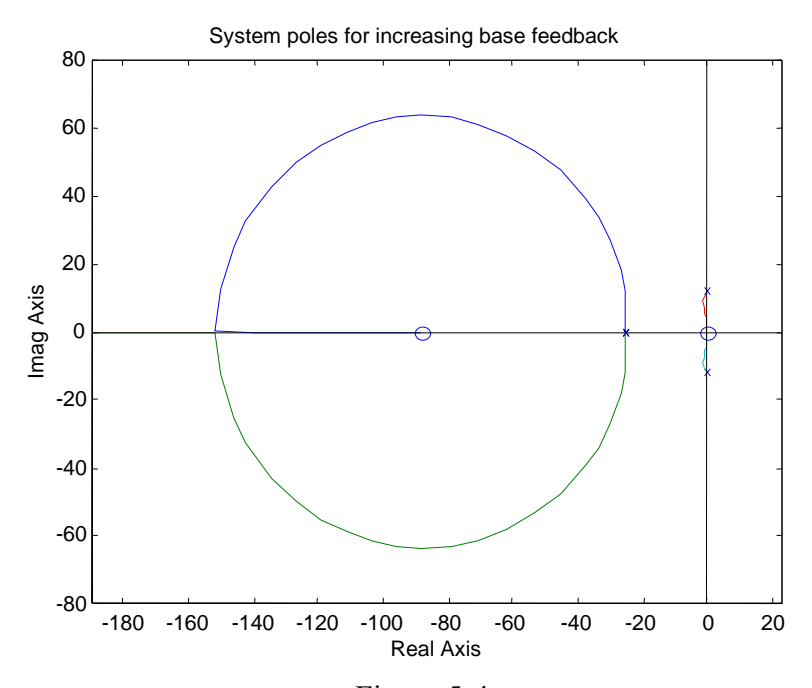


Figure 5-4
Root Locus for Increasing Vibration Control Feedback Gains

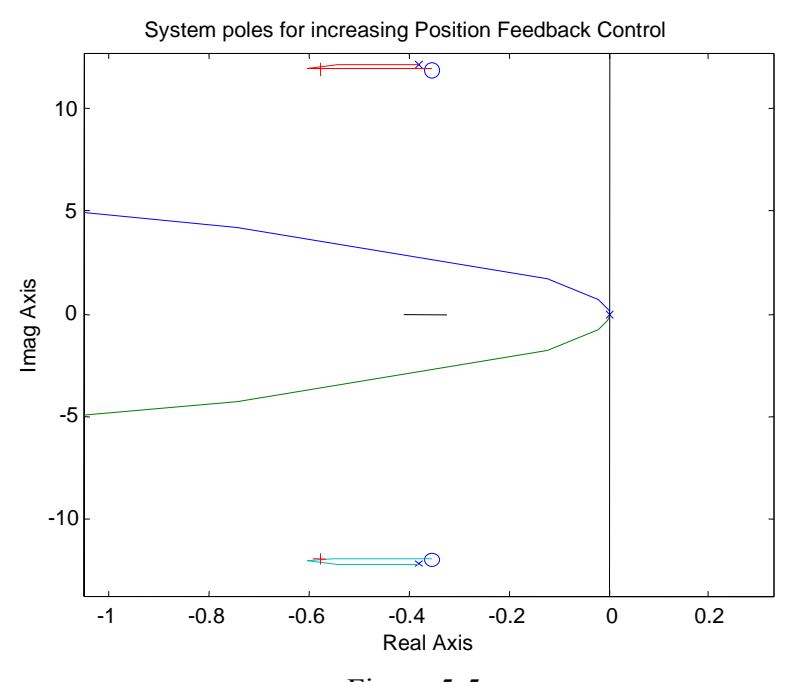


Figure 5-5
Root Locus for Increasing Position Control Feedback Gains

This can also be seen by considering the closed loop transfer function between the interaction forces and desired joint position:

$$\frac{F_{IF}(s)}{\theta_{d}(s)} = \frac{PD_{pos} \frac{B_{f}}{B_{\tau}}}{1 + \frac{PD_{pos}}{B_{\tau}s^{2}} + \frac{K_{v}(s + \frac{K_{pv}}{K_{dv}})}{Ms^{2} + Cs + K}}$$
(5-48)

Low position control gains also help reduce the interaction forces due to commanded movement, and hence unwanted vibration, induced by the rigid manipulator. Note using the scheme shown in Figure 5-1, the vibration control performance will not be affected. During active damping when the base vibration is significant, torque inputs required by the position controller are much smaller than those due to the vibration controller. When the base vibration subsides, the position controller will ensure the robot is in its correct position and with low PD gains any additional correctional movements will not induce vibration back into the system. On the other hand, very low gains are not desirable because it will lead to poor position control performance. A tradeoff is to ensure the rigid robot moves slowly enough that the interaction forces and torques generated are not significant. The interactions can also be reduced by combining the vibration control scheme with trajectories that help minimize inducing vibration (trapezoidal velocity profile or command shaping, for example) [15,61,68,70]. It should also be noted here that these results are based on the ideal rigid robot model; if nonlinearities or actuator dynamics dominate the system response these results are not necessarily applicable. One

representative case is discussed in Section 5.4.5 with a rigid robot dominated by hydraulic actuators.

This indicates it is important to maintain separation of the performance of the two control loops. The work shown here is a quick overview of the controller under typical operating conditions. However, the position controller can interfere with the vibration controller, as shown in Figure 5-6. In this case, the flexible system poles are drawn towards the real axis, as desired. However, the position control poles are drawn towards zero, which results in poor rigid robot control performance with increasing vibration control feedback gains.

When the critically damped rigid position control poles are chosen at the natural frequency of the flexible system and the zero chosen to cancel it, good performance results for both position and vibration control, as can be seen in Figure 5-7. With a given set of PD position control gains, the vibration control feedback gains can be selected to achieve the desired effect of increased damping of the lightly damped flexible poles while minimizing impact on the position control poles. In reality, perfect cancellation would not occur, but the impact is minimal and in the form of slightly reduced damping improvement or slight underdamped position control performance, as shown in Figures 5-8 and 5-9.

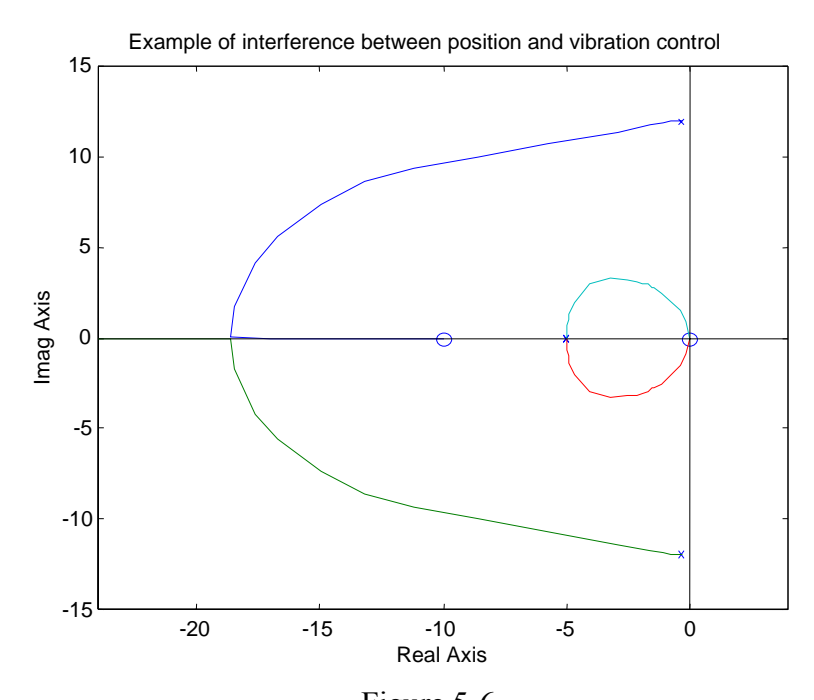


Figure 5-6
Root Locus with Poor Selection of Vibration and Rigid Position Controllers

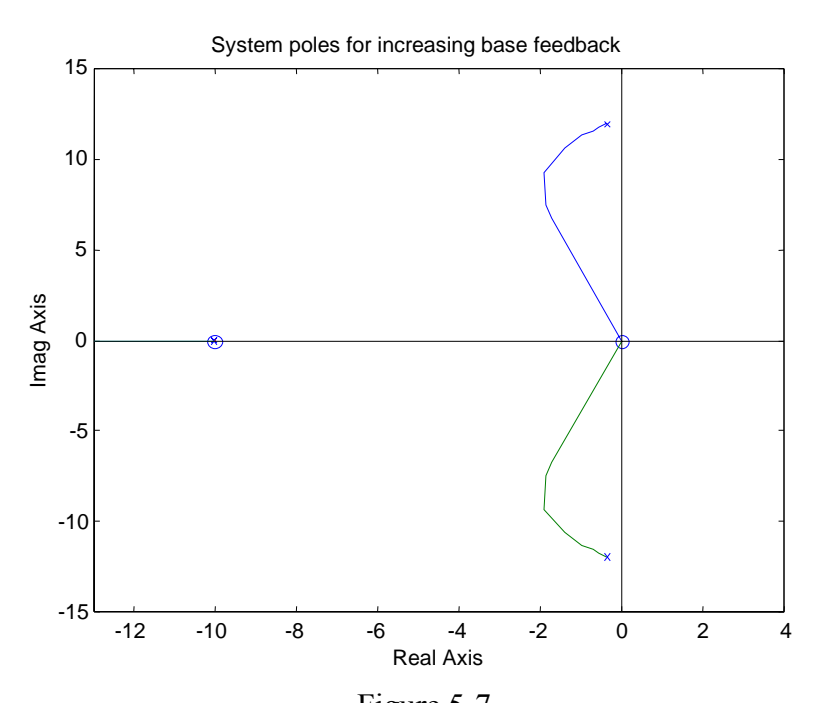


Figure 5-7
Root Locus with Better Selection of Vibration and Rigid Position Controllers

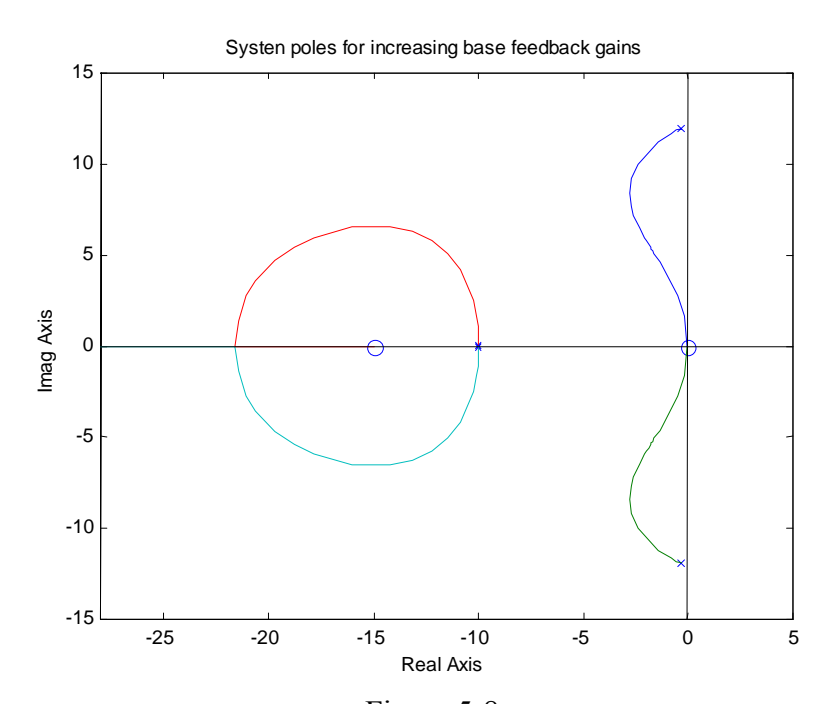


Figure 5-8
Effect of Choosing Vibration Control Zero too Large

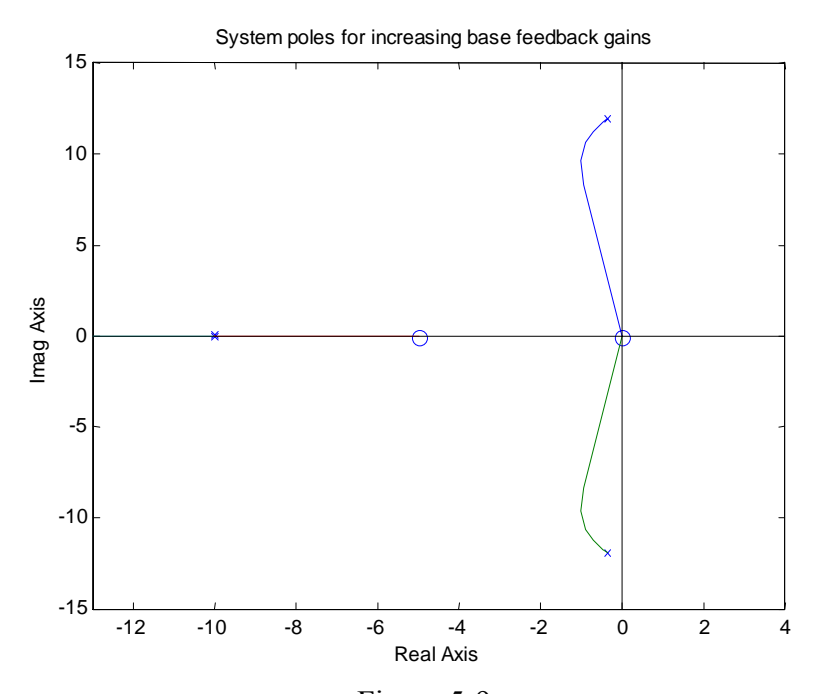


Figure 5-9
Effects of Choosing Vibration Control Zero too Small

When velocity feedback alone is used, improved damping is also achievable over a large range of gains K, as can be seen in Figure 5-10. For the flexible manipulator used to develop these plots, the natural frequency of the lightly damped poles is approximately 2 Hz. The maximum gain recommended by equation 5-38 (assumes B_{min}=A=1) is approximately K=12, while the maximum damping occurs at approximately K=440. The limits on gains will further help ensure the vibration controller remains in regions where increasing the gains directly increases damping.

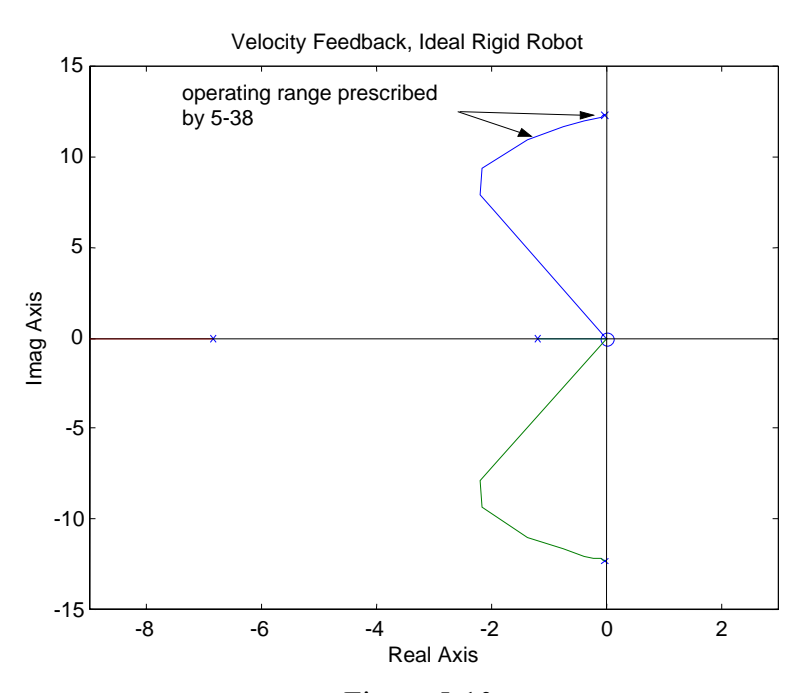
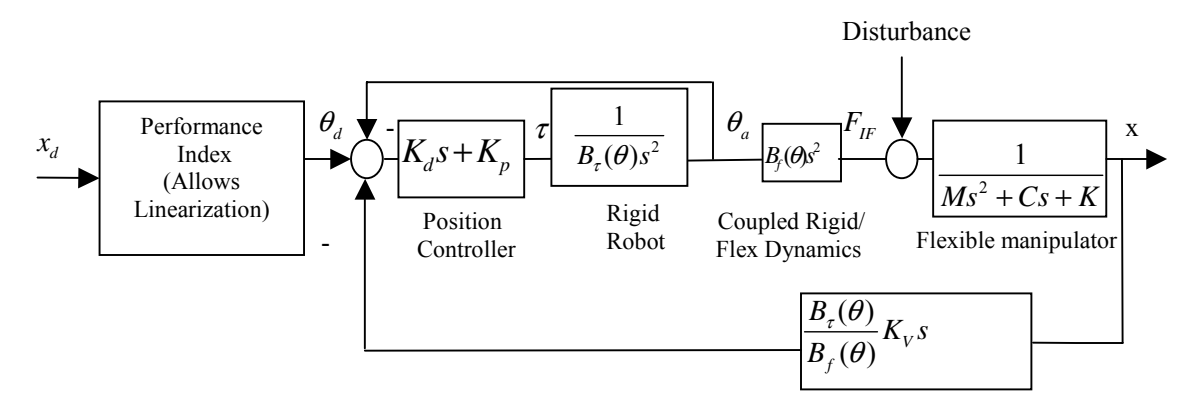


Figure 5-10 Root Locus for Velocity Feedback, Ideal Model

5.4.3 Alternate Contoller Form

One alternative to the controller shown in Figure 5-2 would be one that prescribes the vibration control via the desired joint positions, as shown in Figure 5-11.



Flexible base vibration controller

Figure 5-11 Alternate Form of Vibration Controller

Consider the poles of the closed loop system with the vibration control feedback gains as the multiplying factor (here velocity feedback is considered):

$$G(s)_{vibration \ control} = \frac{K_{v}(K_{d}s + K_{p})B_{\tau}s^{3}}{(Ms^{2} + Cs + K)(B_{\tau}s^{2} + K_{d}s + K_{p})}$$
(5-49)

The pole zero map of equation 5-49 is shown in Figure 5-12. Regardless of where the PD position control gains are chosen, one of the poles will tend to move toward the three zeros at the origin. This tends to interfere with the vibration damping of the lightly damped flexible poles and hence it becomes much more difficult to design the rigid position and vibration controllers independently. This increased interference between the controllers can also been seen by considering the poles of the closed loop system with the position control gains as the multiplying factor:

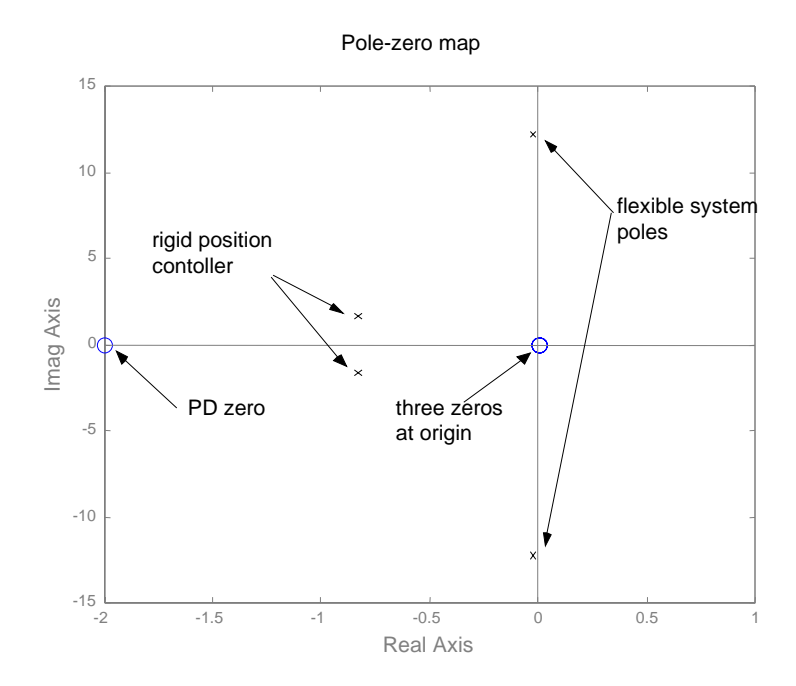


Figure 5-12 Pole-Zero Map of Alternate Controller

$$G(s)_{position\ control} = \frac{K_p(\frac{K_d}{K_p}s + 1)(Ms^2 + Cs + K + K_vB_{\tau}s^3)}{B_{\tau}s^2(Ms^2 + CS + K)}$$
(5-50)

The poles of the closed loop system will move toward the zero with increasing position control gains. Assuming a lightly damped flexible system, for example with M=20, C=1, and K=3000, in order to keep the zero driven by the vibration controller in the left half plane requires very small values of K_vB_τ (.0066). This reiterates the increased interference between the vibration and position controllers.

5.4.4 Simulations of Single Degree of Freedom Controller

The single degree of freedom control law was simulated in Matlab Simulink and takes the form shown in Figure 5-13:

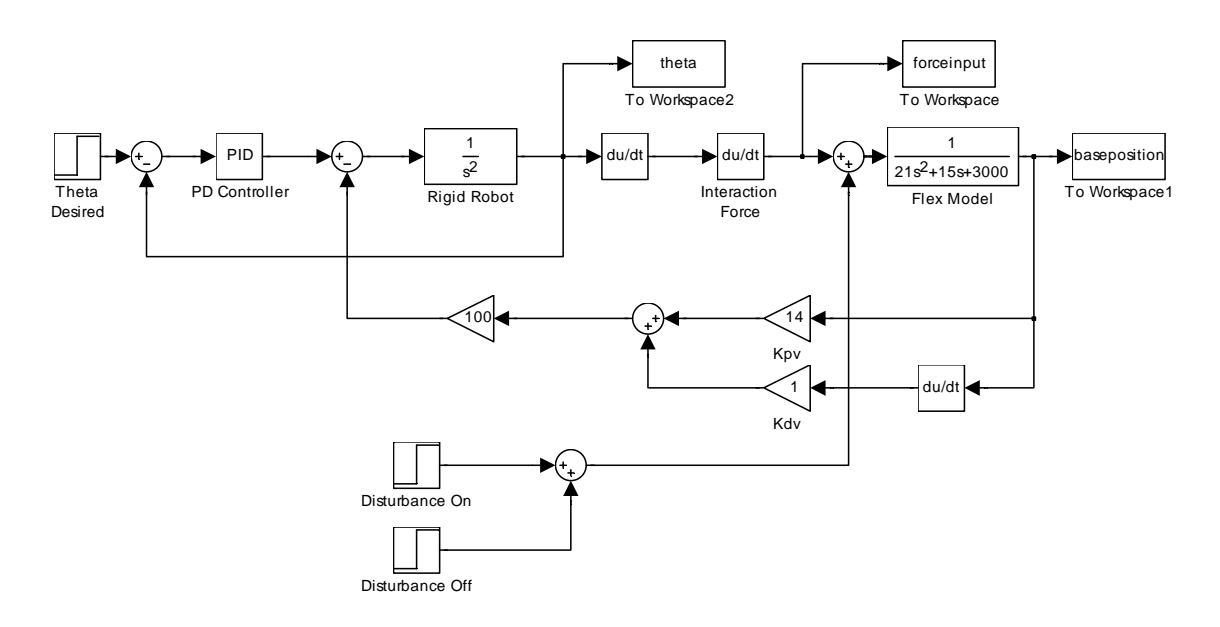


Figure 5-13 Single Degree of Freedom Matlab Simulation

This model simulates a single link rigid robot mounted on a flexible base, which here is simulated as a mass/spring/damper, as shown in Figure 5-14.

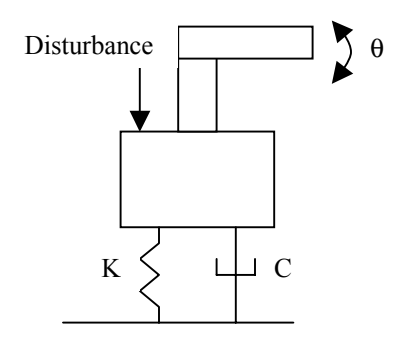


Figure 5-14
Single Degree of Freedom Flexible Base Manipulator

This simulates the last link of the robot shown in Figure 5-14 moving about an axis out of the page. This model allowed a quick evaluation of the control scheme and its ability to effectively damp vibration and maintain position control when a disturbance is applied to the system. The response to a disturbance is shown in Figures 5-15 and 5-16. Figure 5-15 shows much quicker damping with the inertial damping controller than without it. Figure 5-16 shows the joint motion that was used to damp the base vibration.

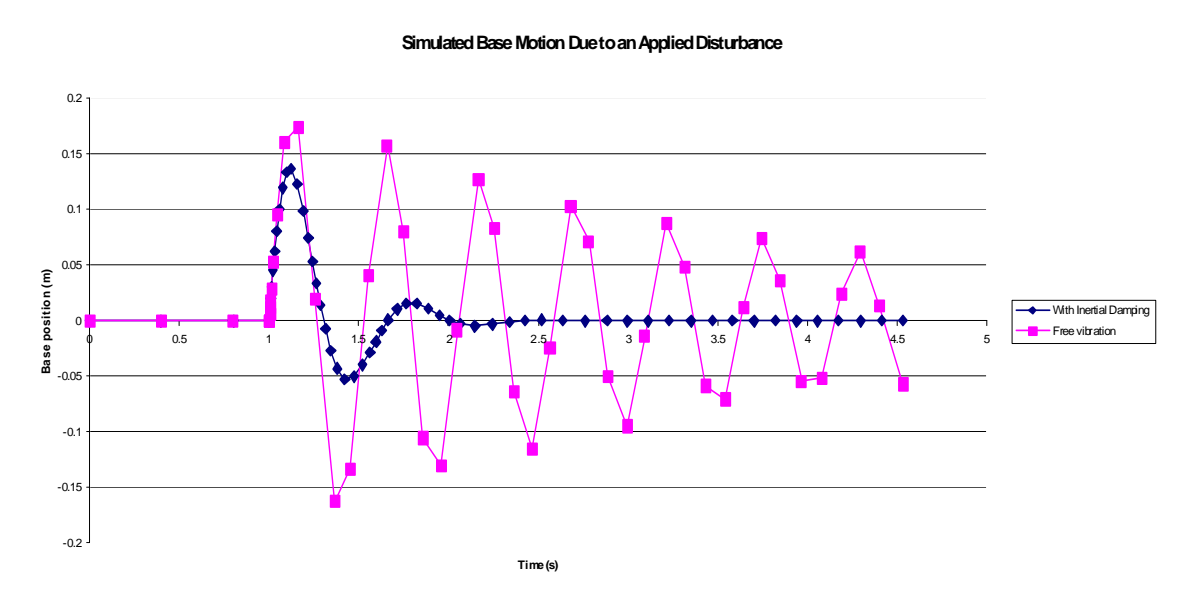


Figure 5-15 Simulated Base Motion Due to an Applied Disturbance

The scheme also allows the robot to move from one position to another and reduce induced vibration significantly. Figure 5-17 shows the joint actuating about its desired position in order to damp the vibration. The resulting base vibration is diminished with the use of the vibration controller, as shown in Figure 5-18.

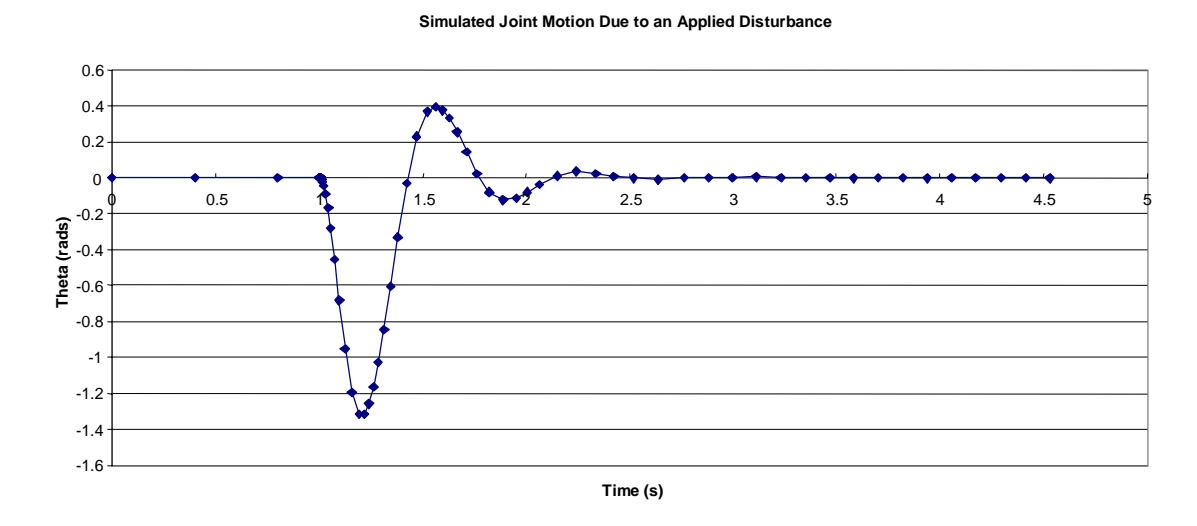


Figure 5-16 Simulated Joint Motion with Inertial Damping Due to an Applied Disturbance

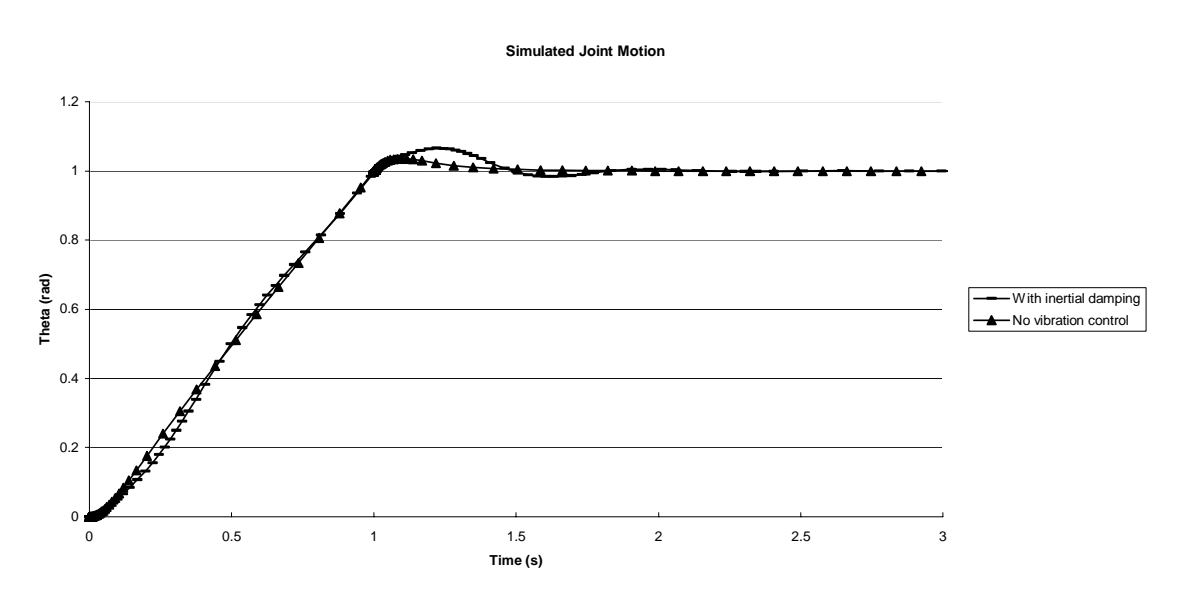


Figure 5-17 Simulated Commanded Joint Motion

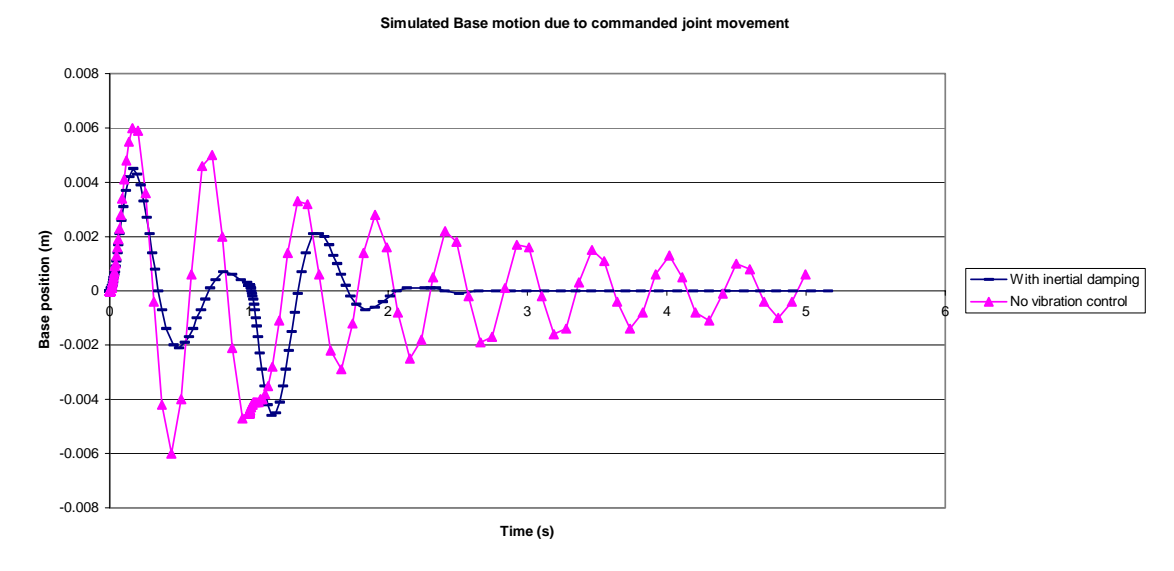


Figure 5-18
Simulated Base Vibration Due to Commanded Joint Motion

Base velocity feedback alone can also be used and can be seen to be effective at dampng vibration due to an applied disturbance, as shown in Figure 5-19.

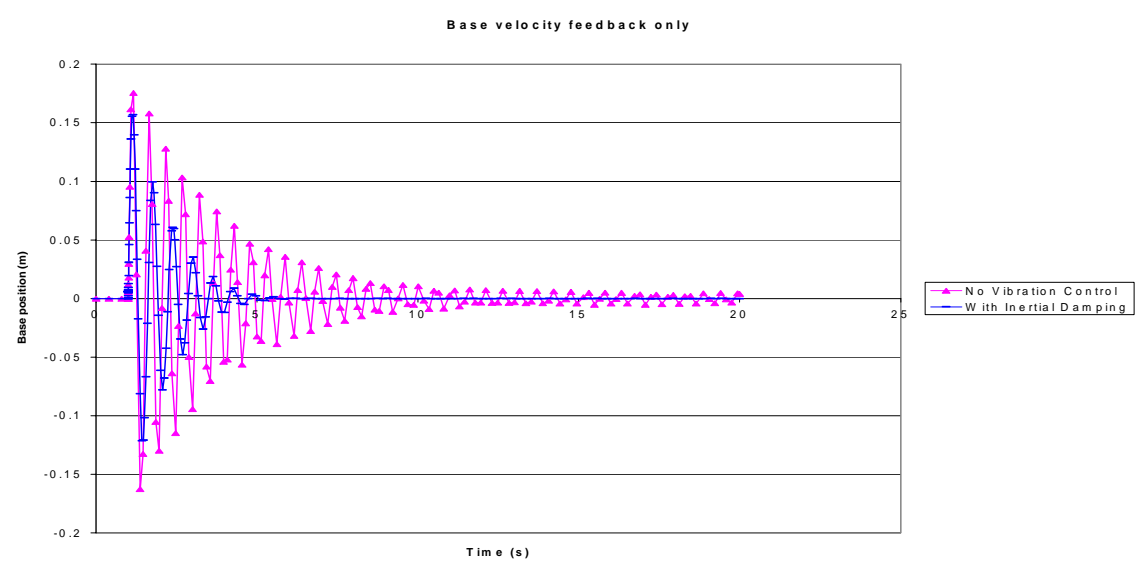


Figure 5-19
Simulated Inertial Damping Performance with Velocity Feedback

5.4.5 Hydraulics Dominated Rigid Robot Model Control Performance

This section extends the previous section to consider the case of a hydraulically dominated rigid robot model. More detail on the development of the model used may be found in Chapter 7. The control loop takes the form of Figure 5-20, again linearized using the equations in 5-39 with the exception of the third. Now the rigid robot is commanded as an approximate velocity source. The joint position controller is left in a general form here.

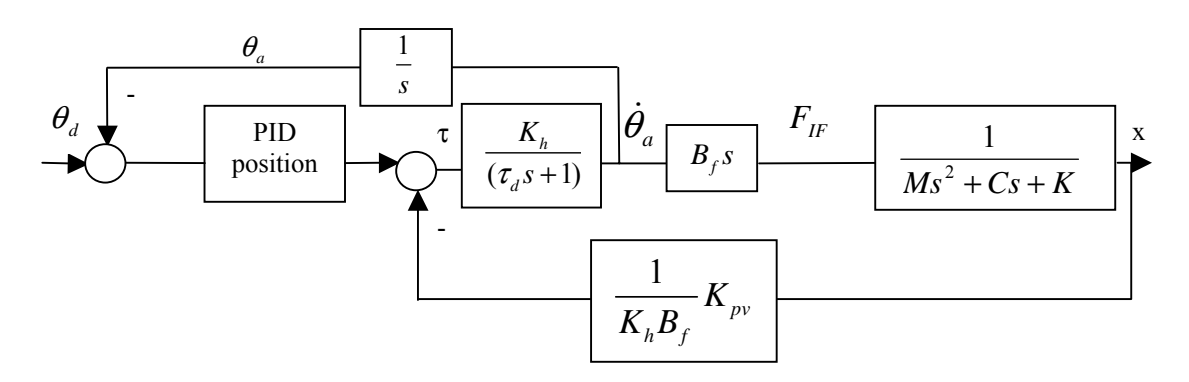


Figure 5-20 Actuator Dominated Linearized Rigid Robot Model

Now the characteristic equation takes the form:

$$characteristic\ equation = 1 + \frac{\text{PID}(s)*K_h}{s(\tau_d s + 1)} + \frac{K_{pv}s}{(\tau_d s + 1)(Ms^2 + Cs + K)}$$
 (5-51)

PID is the rigid robot proportional-integral-derivative position controller. In this case, if τ_d is small, the system can be considered an appoximate velocity source. The vibration controller and resulting interactions take the form shown in Figure 5-21 (not considering

the position controller for the moment). The rigid robot dynamics are shown on the top line with the resulting flexible system dynamics on the lower line.

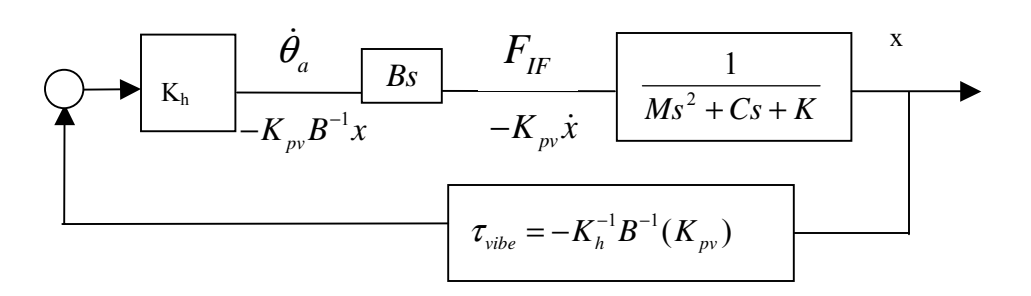


Figure 5-21 Form of Vibration Controller for Hydraulics Dominated Robot

The open loop transfer function with the vibration control gain as the multiplying factor is given by:

$$G(s)_{\text{vibration control}} = \frac{K_{pv}s^2}{(Ms^2 + Cs + K)[s(\tau_d s + 1) + K_h PID(s)]}$$
(5-52)

With increasing vibration position feedback gain, the closed loop poles vary as shown in Figure 5-22. Note increasing feedback gains K_{pv} leads to an increase in damping of the flexible poles over a relatively large range of gains. Also note the slight increase in natural frequency of those poles. This type of rigid robot can provide an advantage because often position measurements are more readily available than velocity measurements and can avoid the need for numerical manipulation of the measured vibration data.

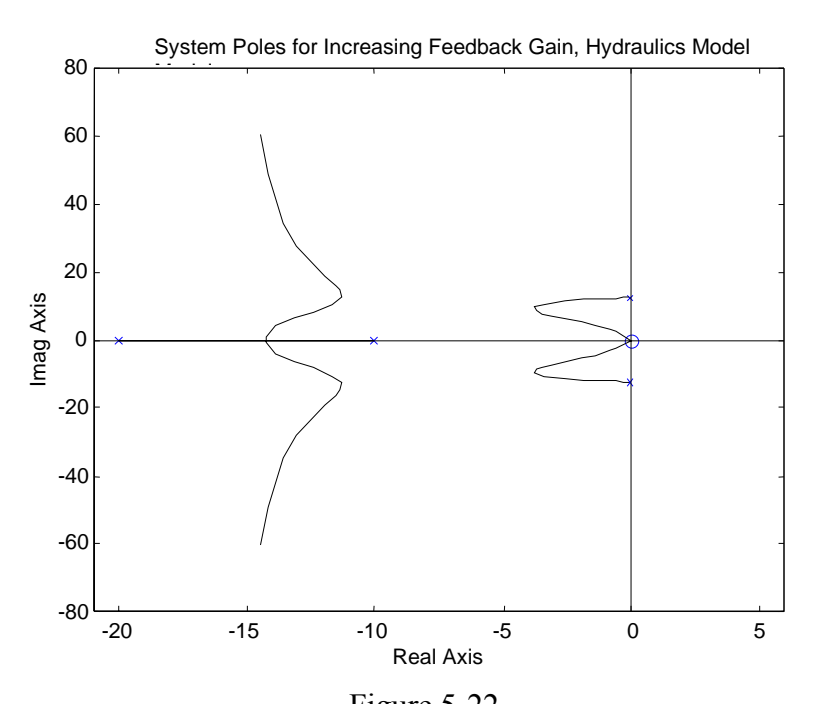


Figure 5-22 Root Locus for Increasing Vibration Control Gains, Hydraulics Model

The other advantage here is that, in this case, it is *beneficial* to have stiffer position control gains. In this case, the rigid robot position and vibration controllers can be designed more independently than in the ideal model case. This can also be seen by considering the poles of the characteristic equation in 5-51 with the position control gains as the multiplying factor. The root locus plot is shown in Figure 5-23. It can be seen that increasing position control gains has little effect on the lightly damped flexible system poles.

$$G(s)_{position\ control} = \frac{PID * K_h (Ms^2 + Cs + K)}{(Ms^2 + Cs + K)(\tau_d s^2 + s) + K_{pv} s^2}$$
(5-53)

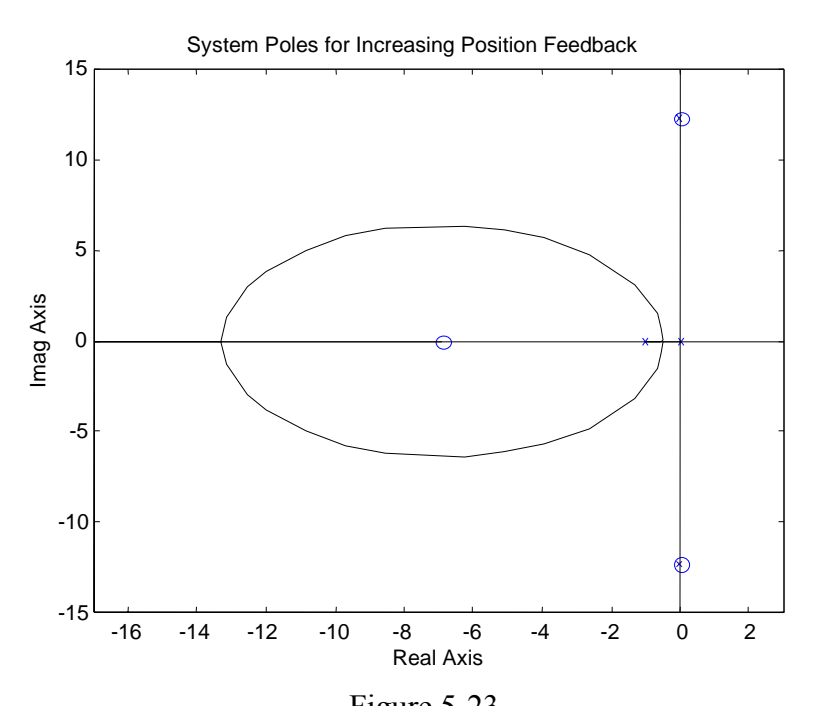


Figure 5-23 Root Locus for Increasing Position Control Gains, Hydraulics Model

Simulations demonstrating the controller performance in multi-degree of freedom operation will be discussed in Chapter 6.

CHAPTER VI

SIMULATIONS

6.1 Introduction

Simulations were built in Matlab to test the ability of the control scheme to damp vibration in multi-degrees of freedom. A macromanipulator was modeled assuming three degrees of freedom of vibration and using a recursive Lagrangian technique as described in Section 3.2. Two modes of transverse vibration were assumed in each planar direction. In order to add a sense of realism to the simulation, the third mode in the z direction was chosen based on assumed modes for torsional vibration. This was chosen since torsional vibration is common for flexible links and, although it is not a concern for single link macromanipulators, it will be a concern for multi-link manipulators. addition, since torsional vibration is at a higher frequency than transverse vibration, it allowed an early assessment of the ability of the scheme to operate over a wide range of frequencies. The resulting equations of motion for the flexible base take the form of equation 3-19 with constant matrices. A three degree of freedom rigid robot was used for damping and takes the form of the last equation in 3-27, while the interactions are given by equation 4-1. The purpose of these simulations was to test the controller and gain limits discussed in Chapter 5. In addition, the usefulness of the performance index

described in Section 5.2 was tested to determine joint configurations better suited for inertial damping.

The simulations were extended to the case of a two link flexible manipulator with a six degree of freedom anthropomorphic/wrist micromanipulator. The flexible base parameters were designed to give base motion similar to the two link experimental testbed, discussed in Chapter 7. The modes modeled in the first link were four transverse modes and one torsional mode, and one transverse mode was modeled in the second link. The complexity of this model made the simulation time extremely long. It was decided the three degree of freedom simulation with additional higher frequency modes added would suffice to study multi-degree of freedom vibration damping and sufficiently represented the testbed. Thus, the baseline simulations used primarily in this study had three degrees of freedom of base vibration and used a three degree of freedom rigid robot to provide the vibration damping.

Finally, an alternate configuration of a rigid robot with performance dominated by hydraulic actuators was studied. As discussed in Chapter 5, with a small change to the control scheme the controller performance is nearly identical to that of the ideal rigid robot performance. However, the effect of variation in actuator performance can add much more uncertainty to the system than the equivalent seen with the ideally modeled robot with nonlinearities. In particular, the effect of increasing the servovalve time constant and higher order dynamics were investigated in simulation, primarily prompted by issues that manifested during laboratory testing.

6.2 Single Flexible Link Macromanipulator with Anthropomorphic Rigid Robot

The overall schematic of the three degree of freedom simulation is shown in Figure 61. Starting at the left of the model, trajectory inputs in the form of desired joint trajectories are the inputs to the rigid robot. The trajectory inputs were either constant joint positions, used to test the response of the vibration controller to a disturbance input, or point-to-point trajectories. In order to test the use of the performance index in predicting inertial damping performance, point-to-point trajectories were generated from desired starting and end points. For each end point in the workspace, there are multiple joint space configurations that can be used to reach it (provided the robot is not operating at a kinematic singularity, which is assumed for this work). In each case, one of the joint configurations gives predicted better inertial damping performance than the other ones. Thus, two tracks were compared in these simulations; one is the track given by the beginning and end points in the better joint space configurations, and the other is the

The rigid robot model was written in the form of an s-function [21], which gives more flexibility in developing the system model and allows modeling nonlinearities. The inputs to the rigid robot are the controller torques, which consist of the PID position control torques plus the additional contribution due to the vibration controller. The total input to each joint is given by:

alternate joint space configuration track.

$$\tau = PID(\mathbf{\theta}_{d} - \mathbf{\theta}_{a}) - ID(\mathbf{\theta}_{a})K\dot{\mathbf{x}}$$
 (6-1)

where PID is an independent proportional-integral-derivative controller (or some variation such as PI or PD), ID is the inverse dynamics function defined in Equation 5-8,

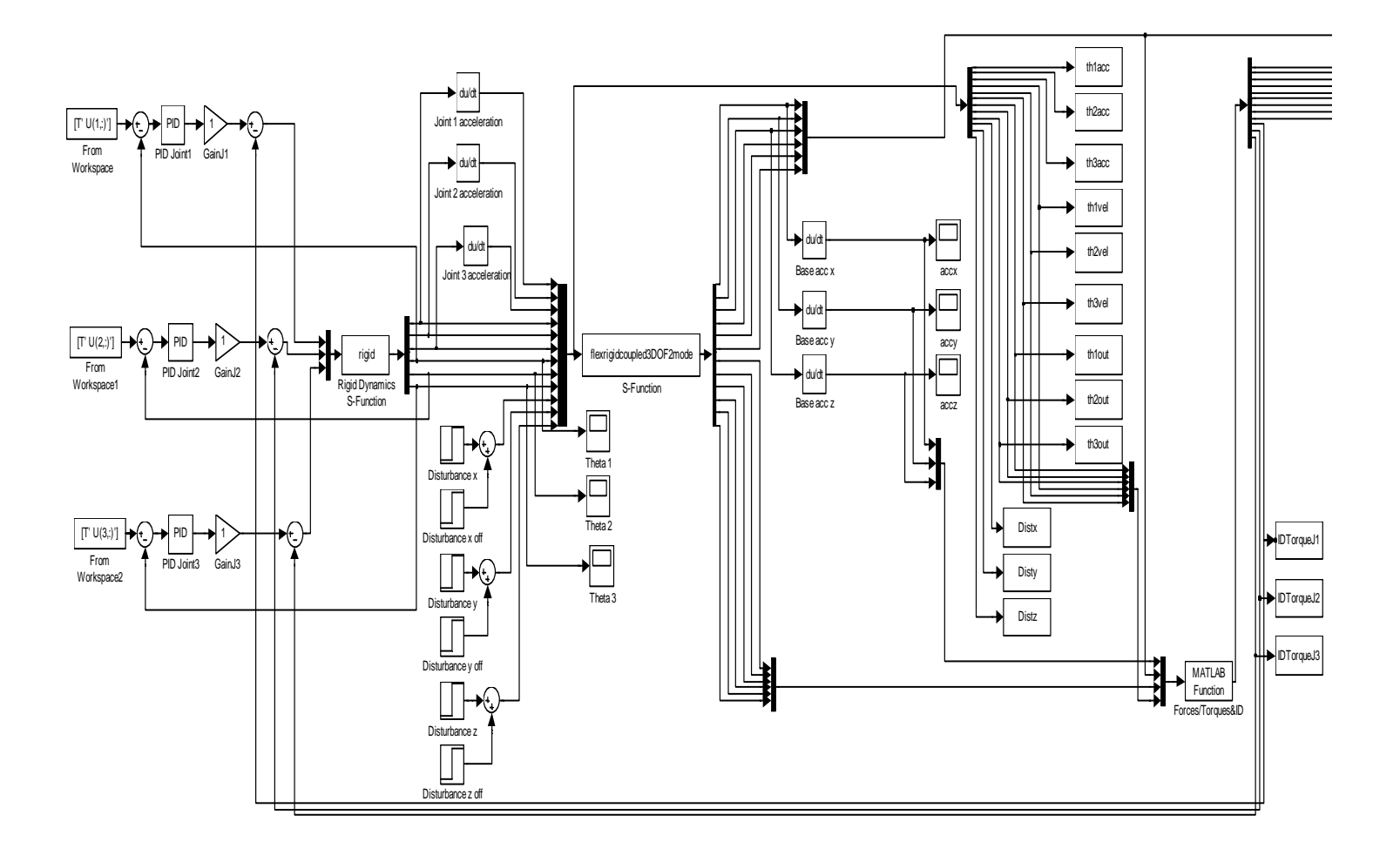


Figure 6-1 Matlab Simulation

and K is the vibration control feedback gains. For these simulations, a reduced inverse dynamics function consisting of only the interaction force effects was used, or

$$ID(\mathbf{\theta}) = B_{\tau}(\mathbf{\theta})B_f^{-1}(\mathbf{\theta}) \tag{6-2}$$

The output of the rigid dynamics s-function are the states of the rigid robot, which are the joint positions and velocities. The joint positions are fed back to the PID controller. The joint velocities are differentiated to yield the joint accelerations and used to calculate the interaction forces and torques, given by equation 4-1.

The flexible base is also modeled using equation 3-19 as an s-function, with inputs the interactions due to the rigid robot. There is also an option to apply a disturbance directly to the flexible base. Since the states of the flexible base are the generalized coordinates, the disturbances applied in each direction are applied to all of the states governing the motion in that direction. For example, an applied disturbance in the x direction is applied to all of the generalized coordinates that affect the motion in that direction. The states are the generalized coordinates and their rates, while the outputs are the overall base motion in the x, y and z directions and their derivatives. The applied distubances and interaction forces and torques are also output and recorded. All of the states and variables are sent to the workspace where they can be stored and analyzed later.

The mass, damping, and stiffness properties of the macromanipulator were determined as described in section 3.2 and are given by the 5x5 matrices M, C, and K from equation 3-19. The fully coupled system mass matrix representing the inertia properties of the coupled system is given by:

$$M_{T} = M + A_{f} + B_{f} B_{\tau}^{-1} A_{\tau} \tag{6-3}$$

where the coupling matrices are given by the appropriate equations in Appendix A. In order to form these equations in the typical state space form, the state matrix is defined as:

$$A = \begin{bmatrix} -M_T^{-1}C & -M_T^{-1}K \\ I & Z \end{bmatrix}$$
 (6-4)

where I is the 5x5 identity matrix and Z is a 5x5 matrix of zeros. The system states are given by:

$$\mathbf{x} = \left[\dot{p}_1 \ \dot{p}_2 \ \dot{q}_1 \ \dot{q}_2 \ \dot{s}_1 \ p_1 \ p_2 \ q_1 \ q_2 \ s_1 \right]^T \tag{6-5}$$

where p_1 and p_2 are generalized coordinates representing two transverse modes in the x direction, q_1 and q_2 represent two transverse modes in the y direction, and s_1 represents a torsional mode of vibration.

The input to the system is defined as:

$$Input = \begin{bmatrix} M_T^{-1} \mathbf{F} + M_T^{-1} \mathbf{D} \\ CZ \end{bmatrix}$$
 (6-6)

where CZ is a column of five zeros. **D** are disturbances that can be directly applied to the system generalized coordinates and **F** is the 5x1 set of interaction forces and torques. For most of the baseline simulations, only the interaction forces were calculated, but for some simulations both interaction forces and torques were included as discussed in Section 6.3.2. In the general case, **F** is given by:

$$\mathbf{F} = F_{IFi} + \frac{\partial \phi_{i}}{\partial \mathbf{z}} \bigg|_{\mathbf{z}=\mathbf{L}} (\tau_{IFi})$$
 (6-7)

where i represents the force or torque applied to the i^{th} generalized coordinate and ϕ represents the associated mode shape. The resulting base motion in each direction is given by:

$$x = p_1 + p_2$$

 $y = q_1 + q_2$ (6-8)
 $z = s_1$

6.3 Simulation Results

6.3.1 Disturbance Rejection

First, the performance of the controller was tested in three degrees of freedom with the inertia and nonlinear effects modeled, i.e. the terms in each of the three equations in 3-27 that contain base translational effects and rigid robot effects. This allowed an assessment of the performance of the controller and the gain limits discussed in section 5.3. In these simulations, velocity feedback of the base vibration was used. The performance of the vibration controller in a configuration of [45°,20°,-70°], the configuration shown in Figure 6-2, is shown in Figure 6-3. The controller gains were selected near the upper limit prescribed by equation 5-38 in order to provide maximum damping performance. The associated joint motion may be seen in Figure 6-4 and the total end point positions in the x, y, and z directions are shown in Figure 6-5. Each joint actuates about its operating point to provide the necessary interactions to damp the base motion. As can be seen, the scheme requires relatively small joint motions to damp the vibration.

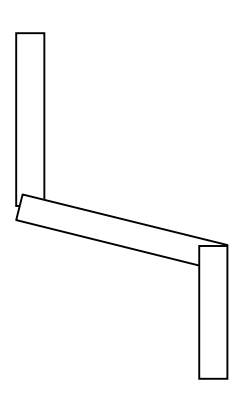


Figure 6-2 Anthropomorphic Robot Configuration [45°,20°,-70°]

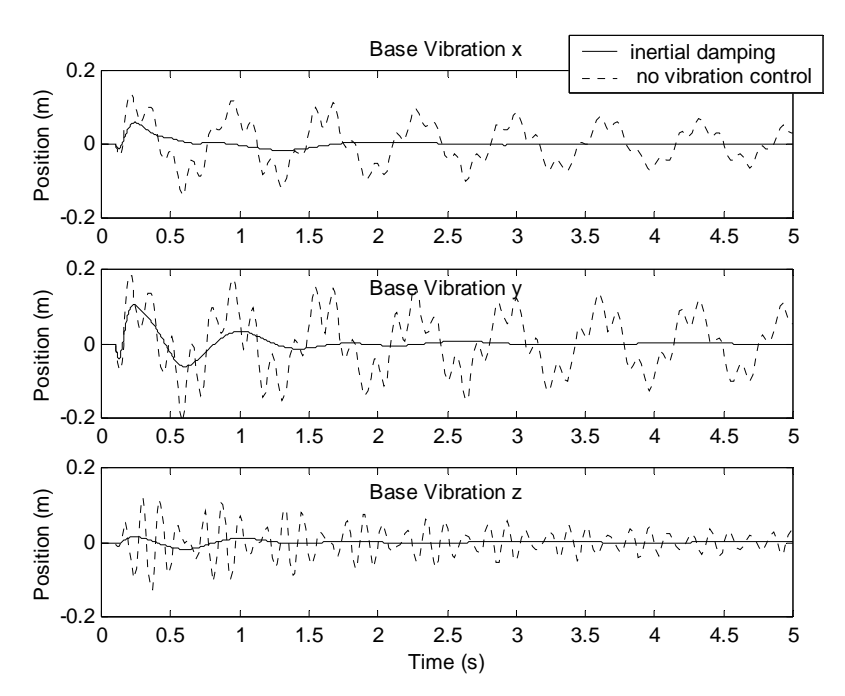


Figure 6-3 Simulated Base Vibration Due to an Applied Disturbance

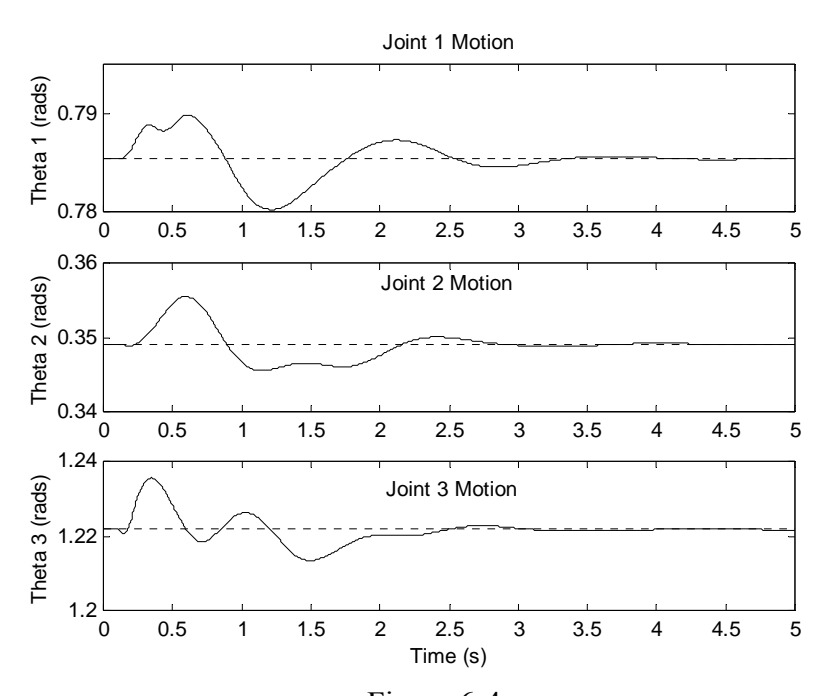


Figure 6-4
Simulated Joint Motion Due to an Applied Disturbance

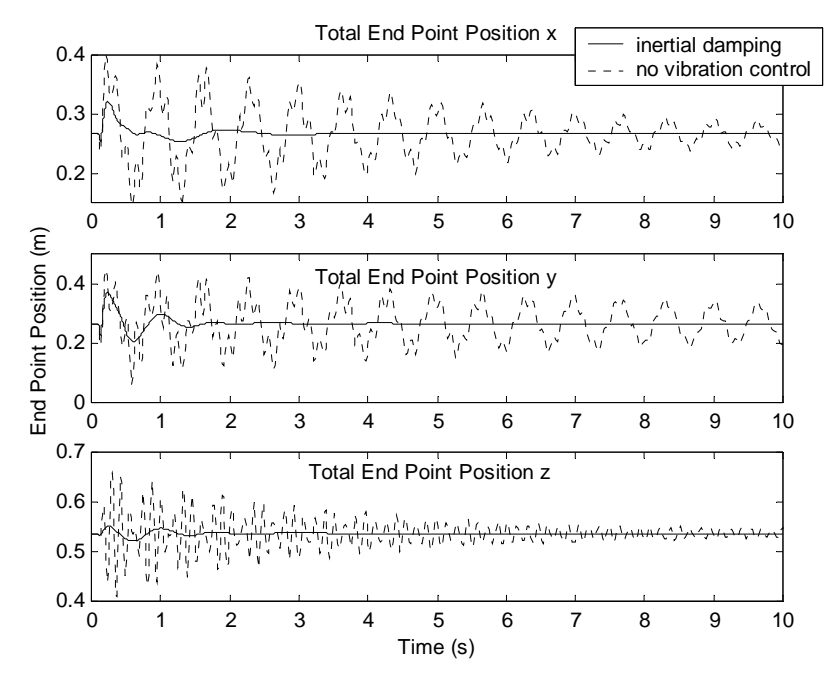
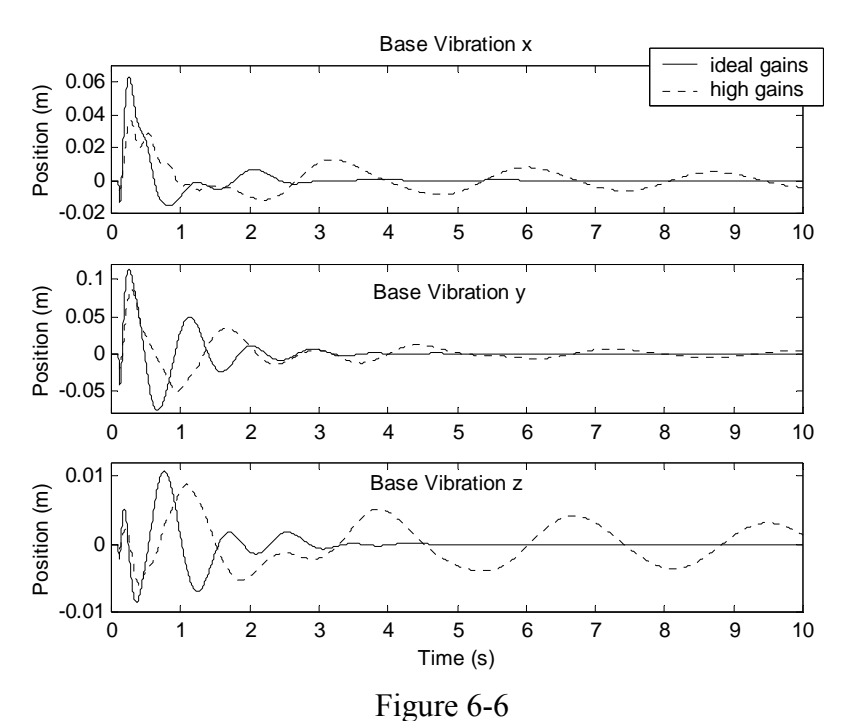
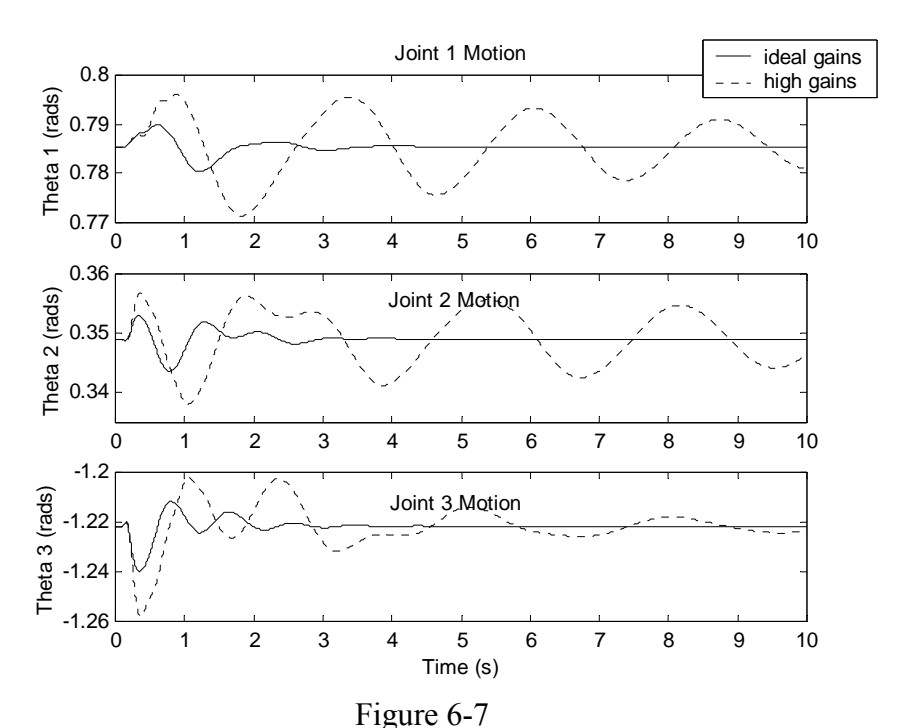


Figure 6-5
Simulated Total End Point Position Due to an Applied Disturbance

If the control gains are not chosen according to equation 5-38, the vibration controller will still remove the overall energy from the system but it is much less effective. As can be seen in Figures 6-6 and 6-7, when the control gains are chosen at three times the recommended limits, the joint amplitudes are much larger and the controller works less effectively. This also verifies the reduction in damping predicted in Figure 5-10 when the feedback gains are increased past a certain point. These results verify that there should be appropriate limits placed on the feedback gains for best vibration control performance. Note that the overall energy is still removed from the system, and relatively quickly compared to the free vibration case shown in Figure 6-3 (note the different y-axis scales between the two figures).



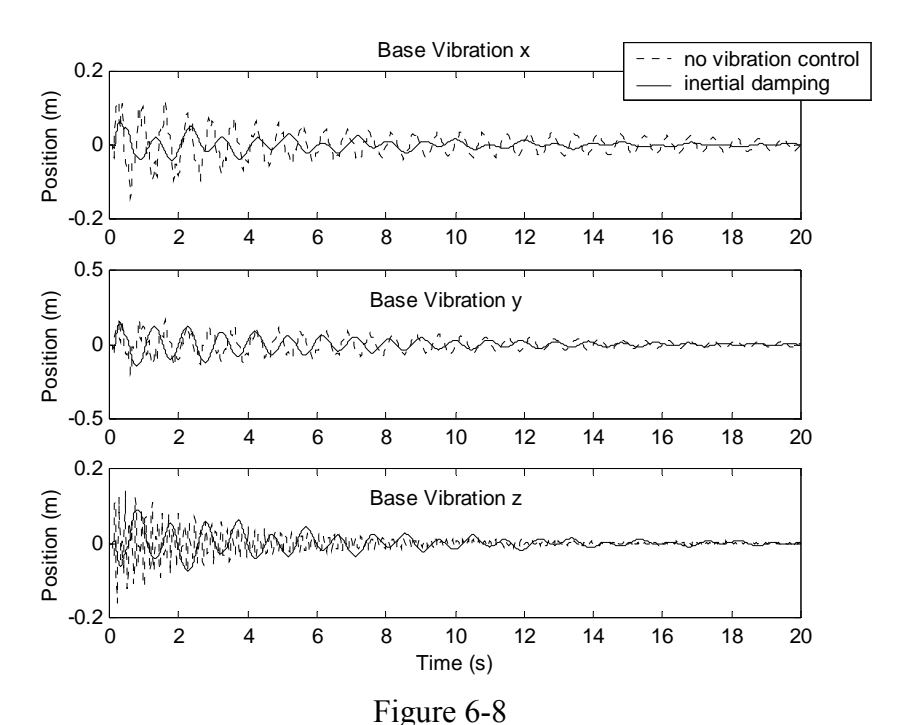
Simulated Base Vibration Due to an Applied Disturbance, Large Vibration Control Gains



Simulated Joint Motion Due to an Applied Disturbance, Large Vibration Control Gains

Next, the controller was tested in a worst-case configuration where the nonlinear effects are expected to be large compared to the inertia effects, as predicted by Figure 4-21. In a configuration of [45°,20°,-10°], which is the configuration shown in Figure 4-22, the resulting base vibration can be seen in Figure 6-8. The associated joint motion may be seen in Figure 6-9. Note the slight increased vibration in the z direction (third plot in Figure 6-8). This indicates that with the vibration controller in place motion by any of the joints creates interactions in all of the vibrational degrees of freedom of the base since the base model is fully coupled. Thus, all of the joints used for inertial damping must operate cooperatively to damp the overall vibration in the system. As expected, the vibration controller is less effective but still provides more damping than the undamped

case. This does indicate, however, that the control gains have to be carefully selected, especially in these regions, in order to ensure successful performance.



Simulated Base Vibration with Robot in a Region with Large Nonlinear Effects

6.3.2 Interaction Torque Effects

Interaction torque effects were originally included in simulations but later removed due to the time and complexity involved. In addition, implementation of the torque effects in the inverse dynamics would be extremely difficult to implement on the experimental system. The combined performance index measure of equation 4-3, shown in Figure 4-11, indicated the torque effects should be relatively small. However, anytime the interaction forces are prescribed, the interaction torques are also commanded. This section describes the effect of including these effects versus the interaction forces only.

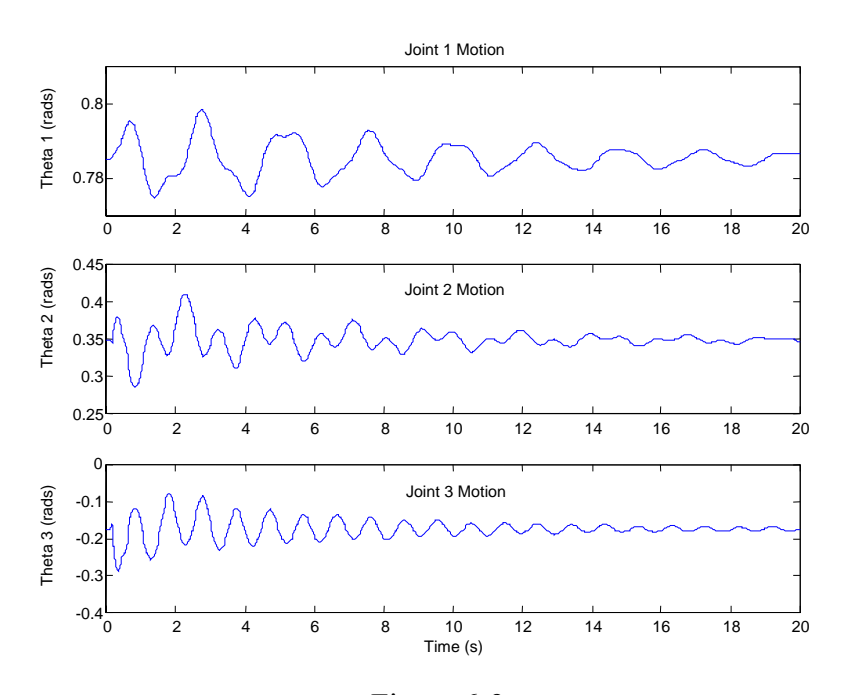


Figure 6-9
Simulated Joint Motion with Robot in a Region with Large Nonlinear Effects

As an example, consider the disturbance rejection capability of the control scheme in a configuration of [45°,45°,-70°]. This is similar to the configuration shown in Figure 6-2 except the second link is slightly further down. Both interaction force and torque effects (equations A-5 through A-7 and A-14 through A-16) are compared with performance when only the interaction force effects are considered. Both results may be seen in Figure 6-10. It can be seen that the vibration control performance is affected very little by considering the interaction force effects only. Thus it was considered a reasonable approximation in most workspace locations to model the full interaction forces only.

On the other hand, consider the robot in a configuration of [-90°,45°,-70°] (same configuration for the last two links, but now joint 1 is rotated 135°). The same

comparison is made and shown in Figure 6-11. The vibration controller still removes energy from the system in both cases, but the performance with and without the interaction torques is very different. An area of future research is recommended to investigate in more detail the interaction torques and determine appropriate simplifications to enable modeling them in a reasonable manner for simulation and experimental implementation. One possible reason for this change in performance is discussed in Section 7.5.3.

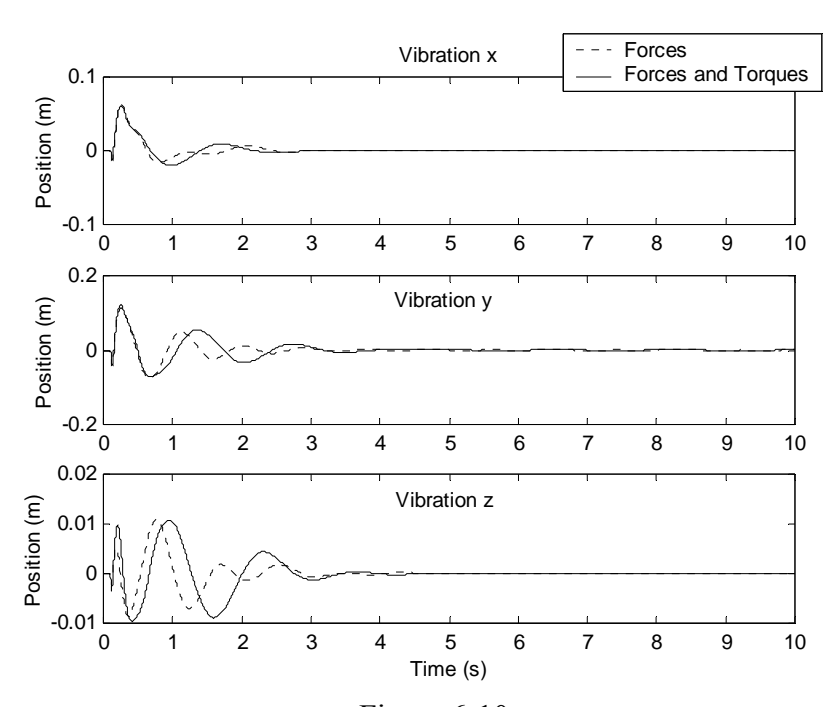


Figure 6-10 Simulated Base Vibration with Interaction Forces and Torques Modeled, Configuration [45°,45°,-70°]

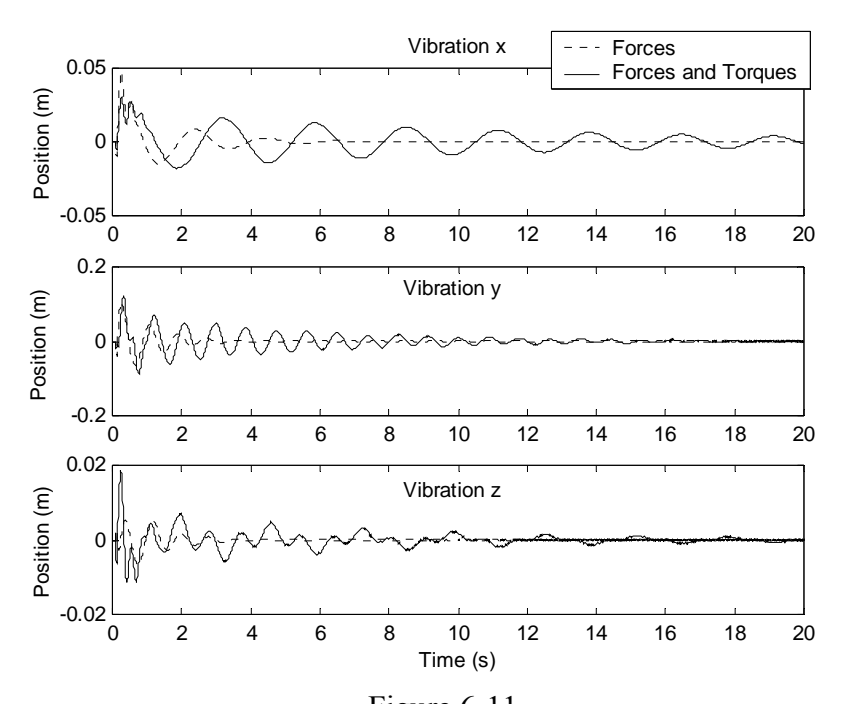


Figure 6-11
Simulated Base Vibration with Interaction Forces and Torques Modeled,
Configuration [-90°,45°,-70°]

6.3.3 Multi-Link Macromanipulator Simulations

Simulations were extended to a multi-link case with a macromanipulator model that consisted of twelve states. For the first link, three transverse modes were modeled in the x direction, one transverse y mode, and one torsional mode. One transverse mode was modeled for the second link. These were chosen to be similar to the modes seen on the actual testbed and will be discussed in Chapter 7. A six joint rigid micromanipulator was modeled, but only the first three links were used for active damping, again similar to the testbed. Due to the complexity and simulation time required, it was decided to use the single link model with additional higher modes of vibration added.

6.3.4 Combined Position and Vibration Control Performance

The second goal was to test the ability of the performance index to predict damping performance. In this case, point-to-point rigid robot motion was commanded to simulate the robot end effector moving from point-to-point in the joint workspace. The performance index was used to choose the best inverse kinematics track for inertial damping. The preferred track (trajectory 1) along with the alternate inverse kinematics track (trajectory 2) are shown in Table 6-1. Note the other two inverse kinematic solutions yield identical results since for the anthropomorphic robot the damping performance only varies with the configuration of joints 2 and 3. Also, note these simulations involve commanded *rigid robot motion only*, while the macromanipulator joints are assumed fixed. Thus, the induced vibrations are due to the motion of the rigid robot only. In reality, vibration would also be induced by macromanipulator motions, which would create larger amplitude initial disturbances similar to those discussed in section 6.3.1. However, this research considers the flexible base to be unactuated, which is a limited case of the general macro/micromanipulator problem.

The resulting base vibration can be seen in Figures 6-12 through 6-14. In each case, the bottom plot shows the base vibration due to point-to-point motion of the robot following trajectory 2 in Table 6.1 without vibration control. The third plot shows the same trajectory except with the vibration controller. The second plot in each figure shows no vibration control with the robot following Trajectory 1, and the top plot shows the robot following trajectory 1 with the vibration controller.

Table 6-1 Simulated Point-to-Point Motion

| E 1D : (| 4 | | 2 | | 4 |
|--------------|------|------|-------|-------------|-------|
| End Point | .4 | 2 | 2 | .4 | .4 |
| | | | | | |
| (m) | .4 | .4 | 2 | 2 | .4 |
| (111) | .т | .т | 2 | 2 | .т |
| | | | | | |
| | .4 | .4 | .4 | .4 | .4 |
| | | | | | |
| Trajectory 1 | 150 | 1170 | 1250 | 270 | 150 |
| Trajectory 1 | 45° | 117° | -135° | -27° | 45° |
| | | | | | |
| | 5° | 0° | 2° | 0° | 5° |
| | 5 | V | _ | V | |
| | | | | | |
| | 60° | 83° | 104° | 83° | 60° |
| | | | | | |
| T | 4.50 | 1170 | 1250 | 270 | 4.50 |
| Trajectory 2 | 45° | 117° | -135° | -27° | 45° |
| | | | | | |
| | 65° | 83° | 107° | 83° | 65° |
| | 0.5 | 0.5 | 107 | 0.5 | 0.5 |
| | | | | | |
| | -60° | -83° | -105° | -83° | -60° |
| | - • | | | | |
| m; () | 0.1 | 5.01 | 05.41 | 45.61 | 65.00 |
| Time (s) | 0-1 | 5-21 | 25-41 | 45-61 | 65-80 |
| | | | | | |
| | | | | | |

The associated joint motion of the first link can be seen in Figure 6-15 during the first leg of motion (movement from 45° to 117°). Plots of all of the joints for all of the cases may be seen in Figure 6-16 (trajectory 1 is labeled with "PI"). One clear tradeoff is that the joint position is affected when under inertial damping control. This is especially pronounced at the beginning and end of each leg, and is especially noticeable between 5 and 10 seconds in Figure 6-15. This is expected since the joint accelerations are largest when the robot starts and stops. The motion, however, is used to quickly damp the vibration, as shown in the top plot in each of Figure 6-12 through 6-14. The other tradeoff is the increased amplitude of vibration induced by moving into the better joint

configurations. This is expected since these regions allow more coupling, which also allows the robot to create larger disturbances. However, these regions also allow more effective coupling to damp the vibration more quickly, while the robot in the alternate track is much less effective at vibration damping. The conclusion is that the robot modeled by equation 3-27, even with nonlinear effects included, works effectively at damping vibration throughout the workspace provided the robot is able to operate in joint space configurations better suited for inertial damping.

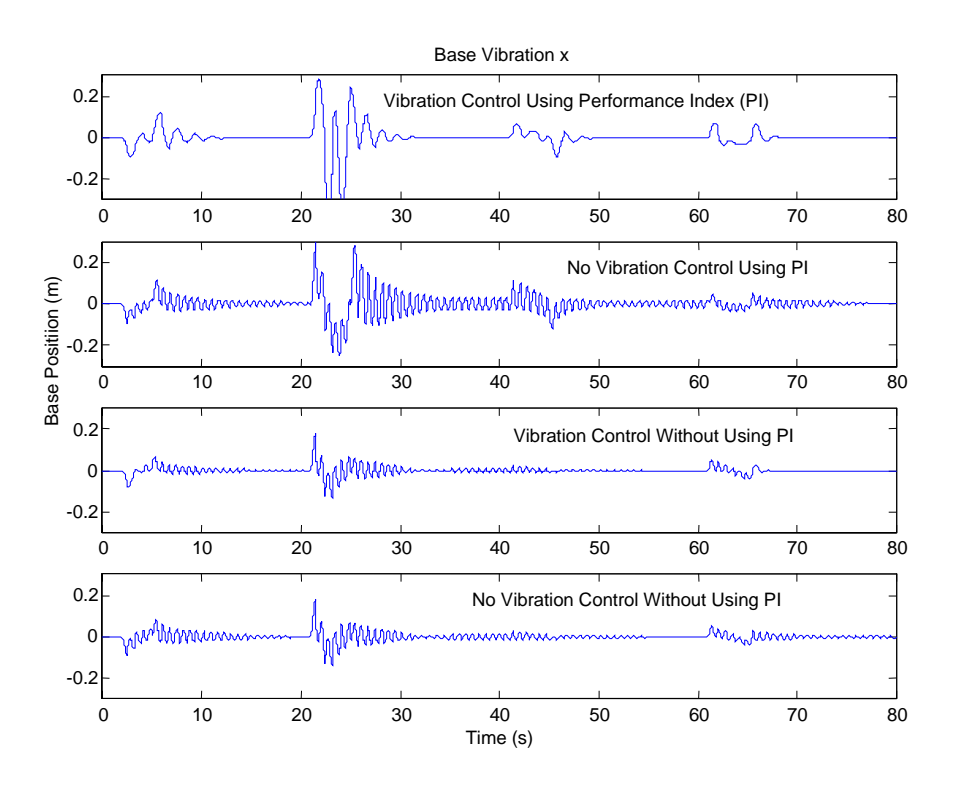


Figure 6-12 Simulated Base Vibration x Due to Point-to-Point Motion

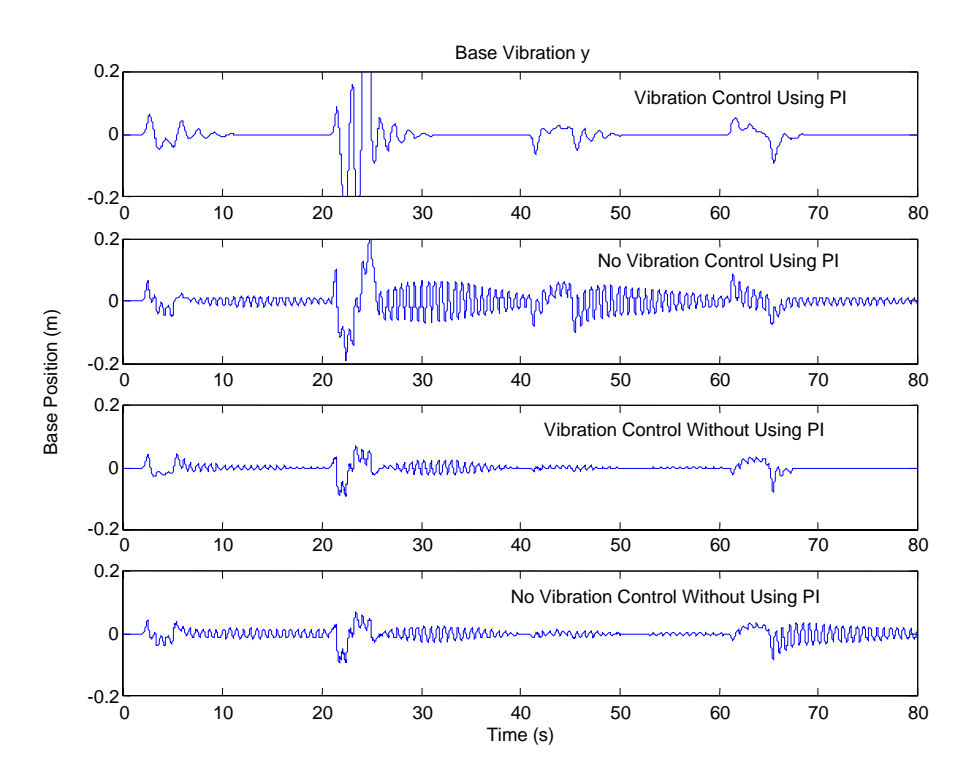


Figure 6-13 Simulated Base Vibration y Due to Point-to-Point Motion

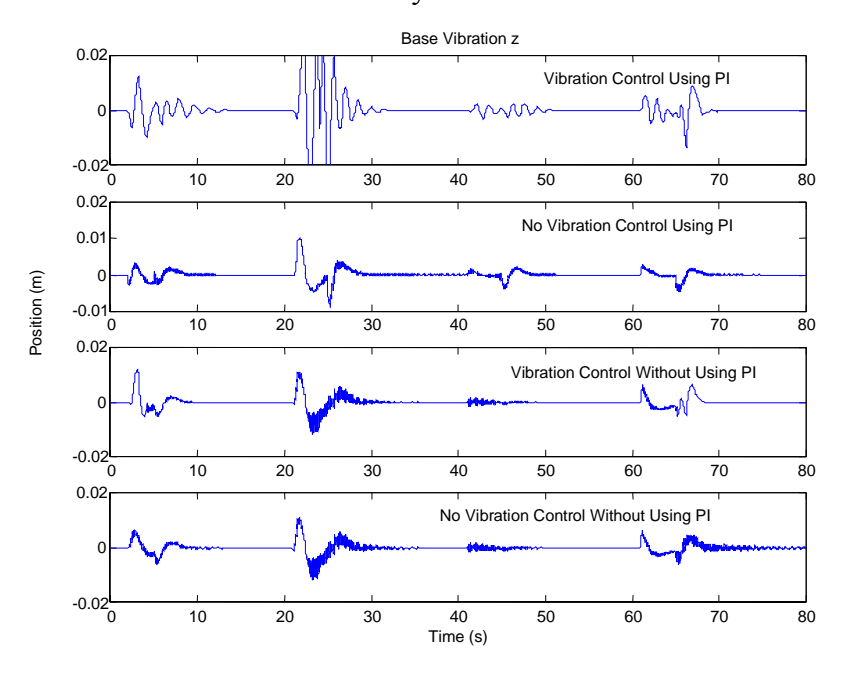


Figure 6-14 Simulated Base Vibration z Due to Point-to-Point Motion

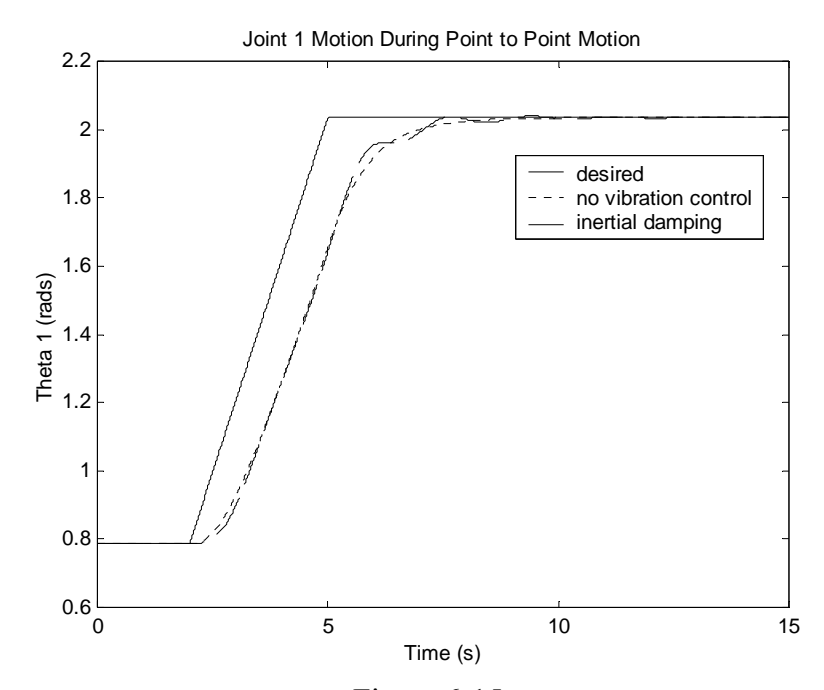
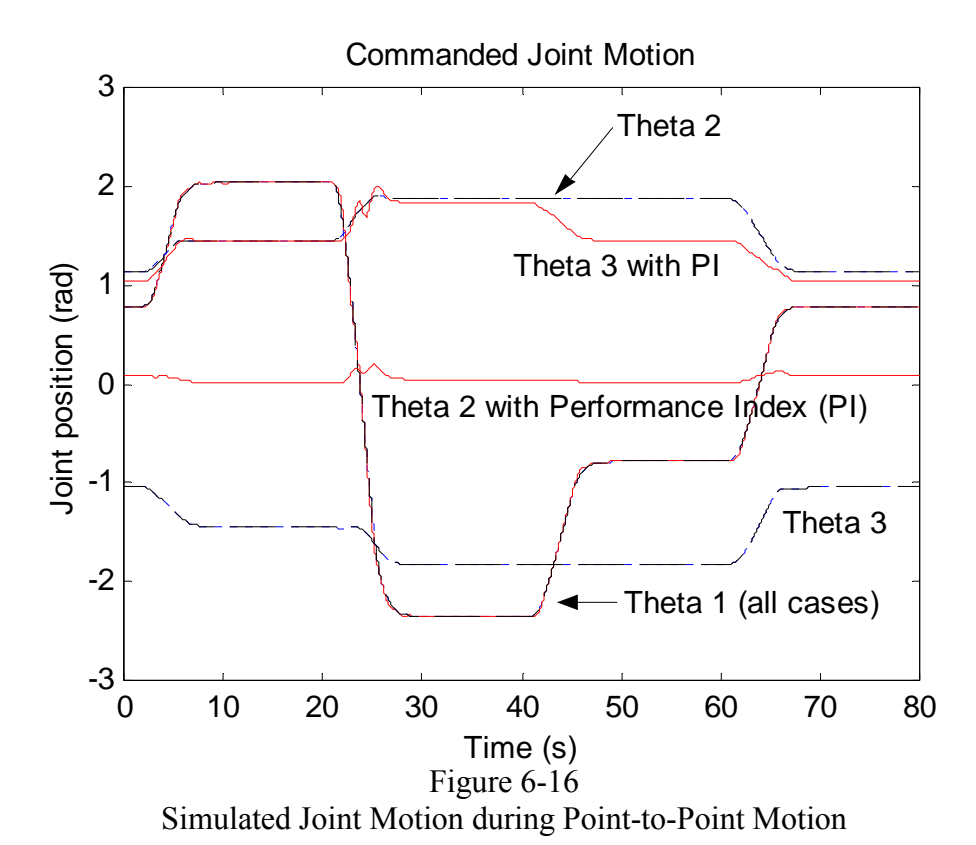


Figure 6-15 Simulated Joint 1 Motion During Point-to-Point Motion



The total end point position in the x and y directions can be seen in Figures 6-17 and 6-18 respectively. The goal is that, provide the rigid robot is controlled so θ_{act} converges to θ_{des} , the vibration controller will damp the base vibration, as shown in Figures 6-12 through 6-14. Thus, the total end point position will also be controlled and will have less vibration than the system without the vibration controller.

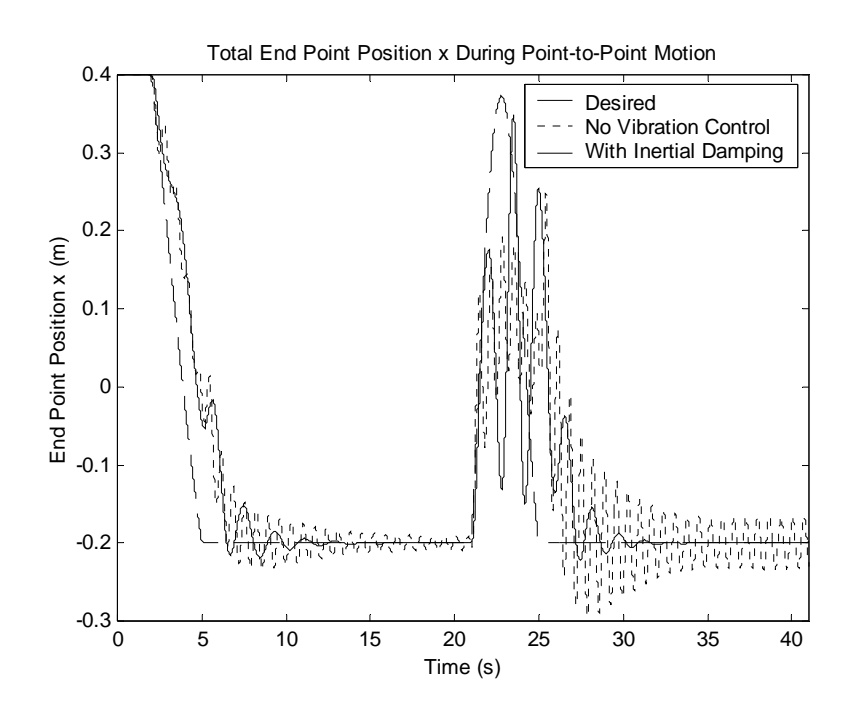


Figure 6-17 Simulated Total End Point Position x During Point-to-Point Motion

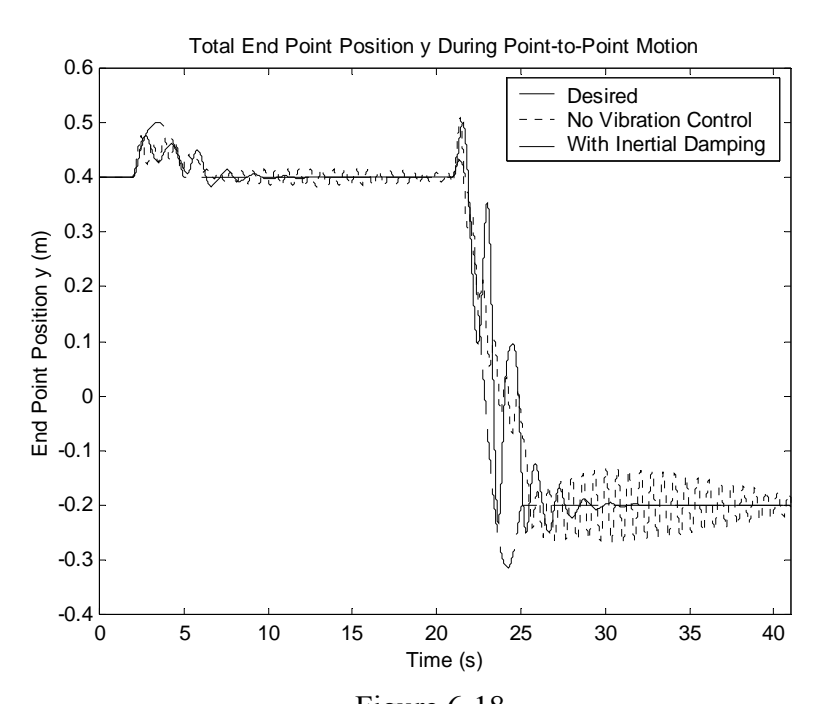


Figure 6-18 Simulated Total End Point Position y During Point-to-Point Motion

Another interesting phenomenon occurs in *multi-degree of freedom* damping simulations that was not predicted by the *ideal single degree of freedom* cases discussed in section 5.4. Observe the base vibration shown in Figure 6-12 with the vibration controller in place (top plot). In this simulation, the vibration control gains were prescribed at the upper limit given by Equation 5-38. Note the decrease in frequency of vibration from approximately 1.5 Hz (undamped) to approximately .57 Hz (with inertial damping). When the same situation was simulated with vibration control gains reduced in half, the damped frequency was slightly higher (.61 Hz) and the damping improvement is slightly better, as shown in Figure 6-19.

Recall these simulations include nonlinearities in both the rigid and coupled dynamics, the flexible base is fully coupled and models multiple modes of vibration, and

the simulations are for a three degree of freedom rigid robot. The root locus of the ideal, linearized case analyzed in Figure 5-10 and shown again below in Figure 6-20, only approximates the true multi-degree of freedom case. These results could indicate several things. First, it could indicate that the maximum damping available occurs at a much lower gain than predicted (case 1). It could also indicate the flexible poles move away from the j ω axis with a steep slope (case 2), which would result in the observed decrease in frequency of vibration with increasing vibration control gains (case 2). Note Figures 5-4 and 5-9 predicted this behavior could occur.

As noted previously, the rigid robot and vibration controllers need to be designed carefully to ensure ideal performance predicted by Figure 5-10. When nonlinearities and other inaccuracies are included, even in simulation, this ideal performance may not occur. It is likely achievable with the proper modification of the rigid joint controller and/or lower vibration control gains. Nevertheless, the multi-degree of freedom simulations do indicate the damping controller can remove overall system energy and improve vibration performance over the system with no vibration damping.

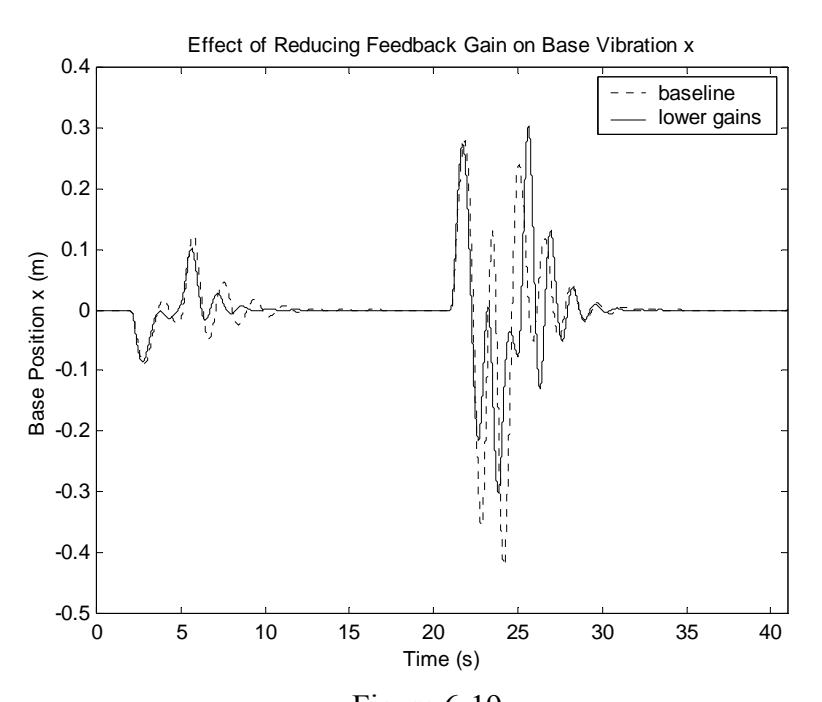


Figure 6-19
Base Vibration x with Reduced Gains for Damping Controller

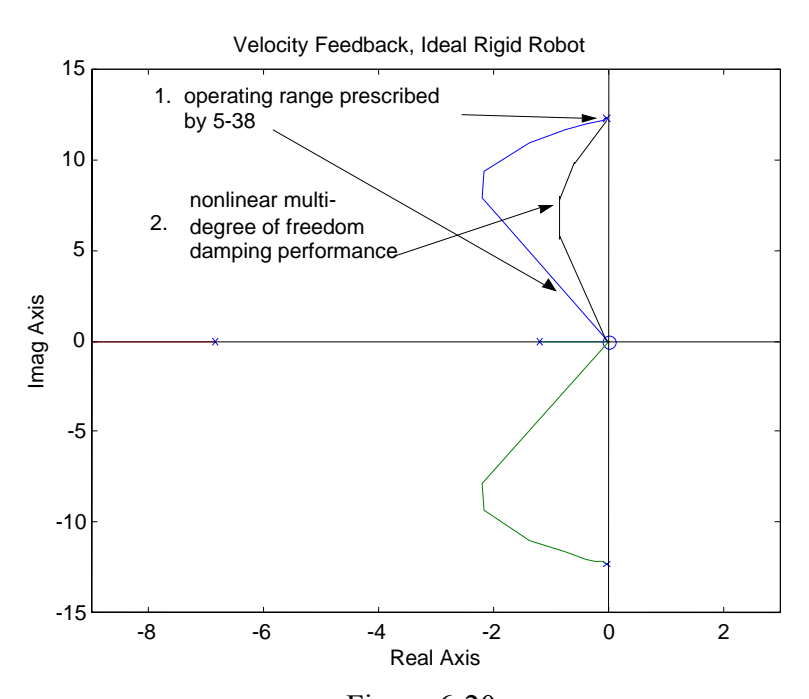


Figure 6-20 Root Locus for Single Degree of Freedom Ideal Linearized Model

6.4 Hydraulic Actuator Effects

The hardware implementation was performed on a hydraulically actuated robot. In order to enhance the clarity of the discussion and focus on the key issue at hand, a single degree of freedom case is discussed here. The simulation is shown in Figure 6-21. The actual robot is hydraulically operated and the joint performance was experimentally determined to be modeled as:

$$\frac{\theta(s)}{\tau(s)} = \frac{K_h}{s(\tau_d s + 1)} \tag{6-9}$$

which is typical of hydraulic actuators [50,48,75]. For more information on the actual robot used in laboratory testing, see Chapter 7.

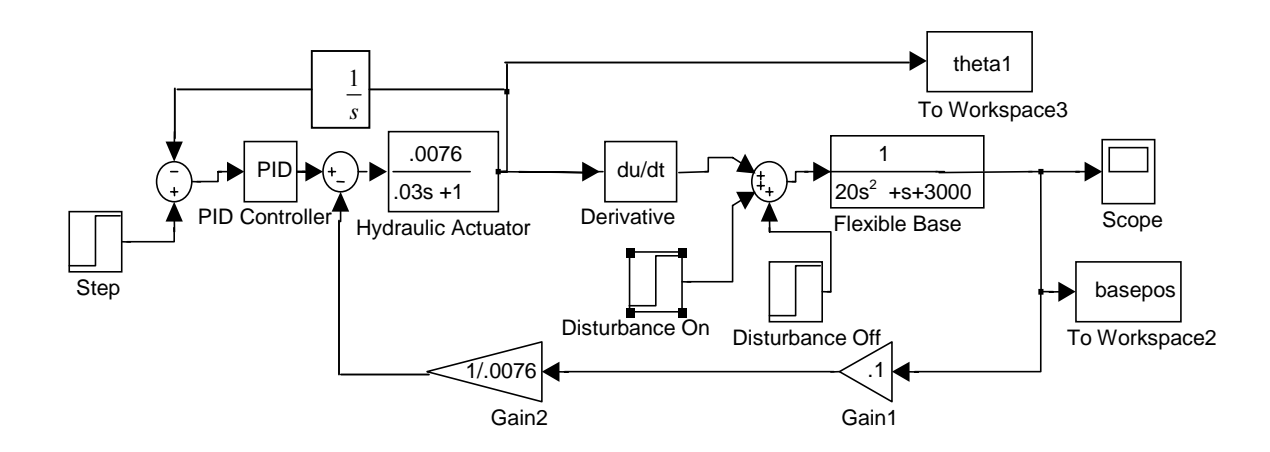


Figure 6-21 Hydraulics Dominated Single Degree of Freedom Model

First, the baseline damping performance for the inertially damped and undamped cases is shown in Figure 6-22 along with the joint motion in Figure 6-23. As these figures indicate, provided the joint acts as a velocity source the control scheme works well. Note the joint motion is nearly out of phase with the vibration displacement as commanded, allowing the vibration energy to be absorbed. Joint 2 was chosen for this particular test case because it demonstrated the largest amount of phase lag. Next, the same situation was simulated except with larger τ_d (as defined in equation 6-9), which increases phase lag. The resulting base vibration and joint motion is shown in Figure 6-24. As shown in 6-24, the phasing of the joint motion relative to the vibration has shifted and no longer effectively removes vibrational energy. As can be seen, the effectiveness of the scheme decreases, but it is still effective. Provided the actuator can truly be modeled as a second order system, the phase lag will be no greater than 90° and the vibration control scheme will still work, although the more phase lag the less effective it will become.

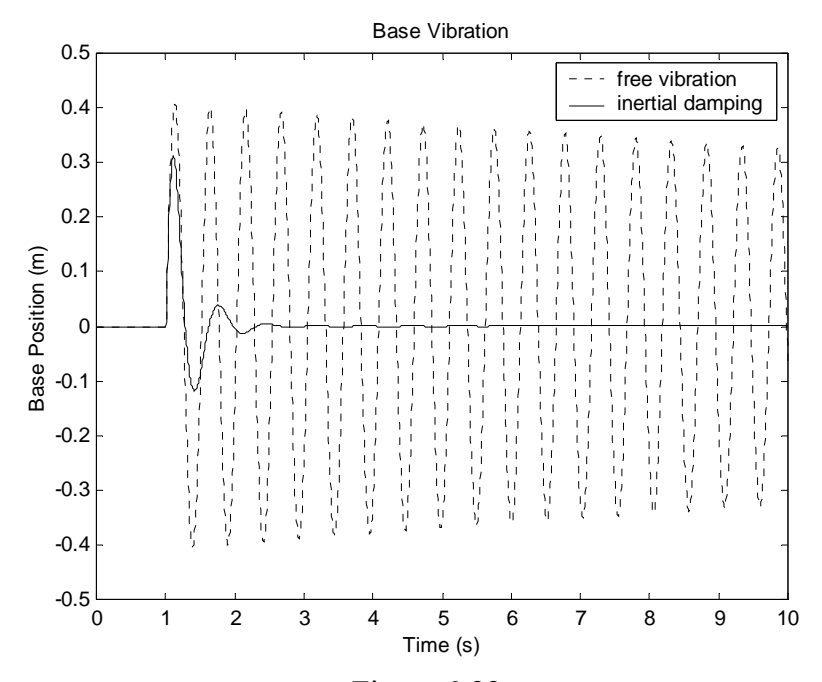


Figure 6-22 Baseline Performance with Joint 2 Hydraulics Model

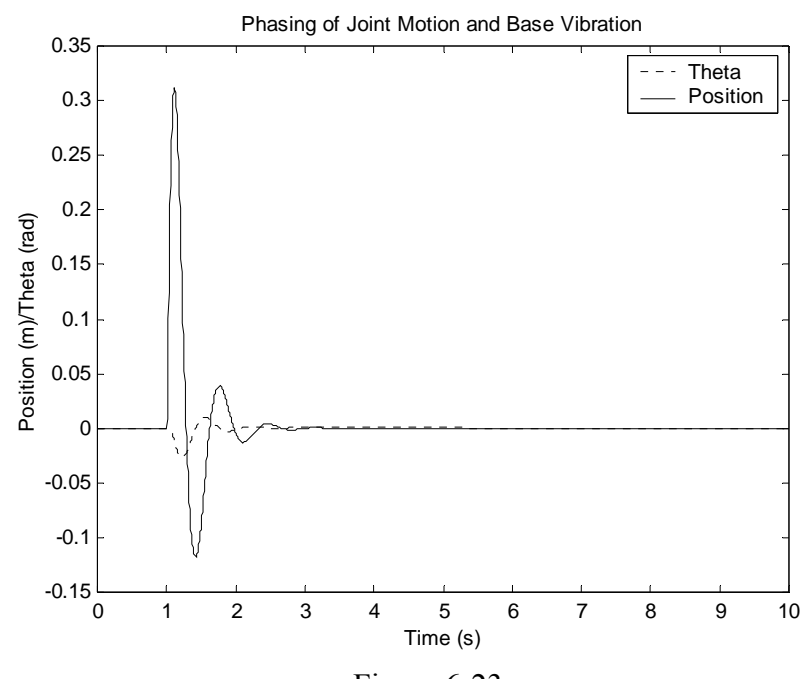


Figure 6-23 Phasing of Joint Actuation and Base Vibration, Hydraulics Model

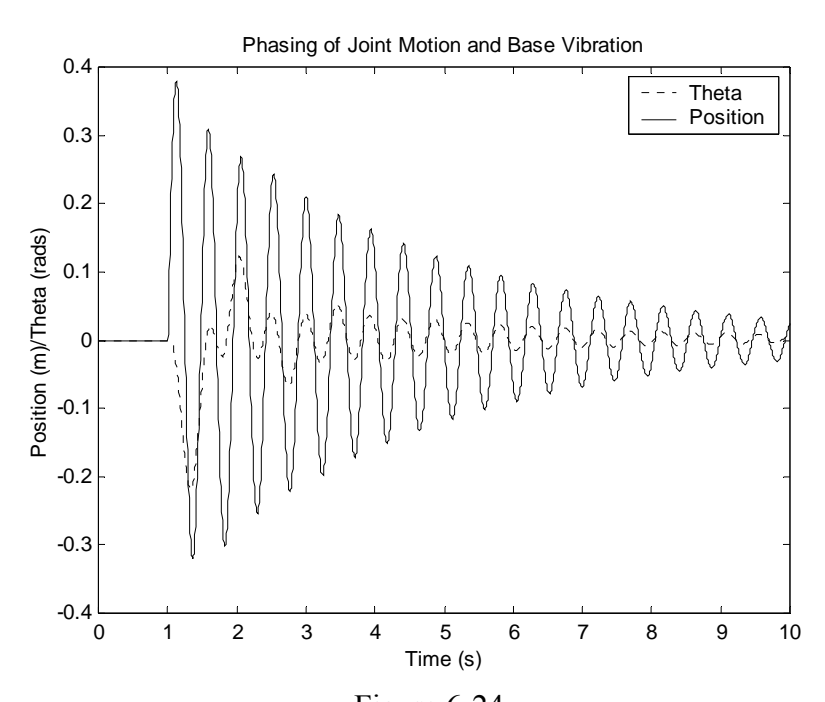


Figure 6-24
Effect of Increasing Phase Lag on Hydraulics Model Vibration Performance

On the other hand, if the hydraulic dynamics are actually higher order, as has been proposed by some authors [50], larger phase shifts may result and create problems using this scheme for vibration control. As as example, consider the hydraulic actuator modeled as a third order system. The phasing between the joint motion and the base vibration is shown in Figure 6-25. In this extreme example very large phase shifts can cause detrimental effects. The conclusion is that, when the robot model is not given by the typical robot model (third equation in 3-27), it is important to perform system identification testing to get an accurate robot model. Provided the robot dynamics are reasonably well known, appropriate motion can be commanded and/or cancelled in the inverse dynamics function.

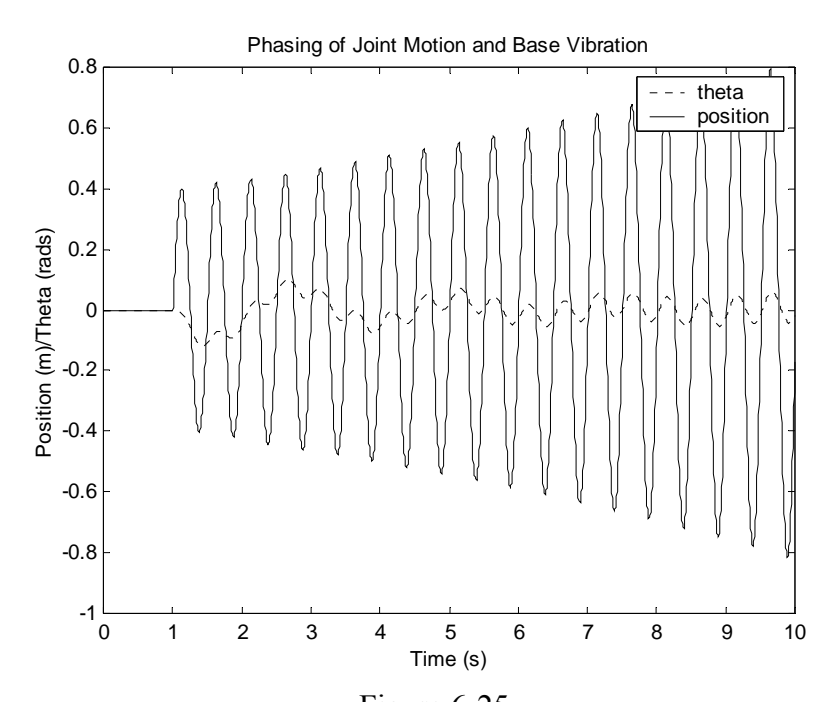


Figure 6-25
Phasing of Joint Actuation and Base Vibration, Hydraulics Modeled with Higher Order Dynamics

CHAPTER VII

EXPERIMENTAL WORK

7.1 Introduction

This chapter describes the experimental testbed and test results. The testbed consisted of a two flexible link macromanipulator with a six degree of freedom anthropomorphic/wrist rigid robot mounted to its last link. The experimental work consisted of two primary areas:

- 1) Experimental verification of the interaction forces and torques and conclusions described in Chapter 4. The main area of interest was on the controllable interactions due to the rigid robot.
- 2) Implementation of the vibration control scheme on a multi-degree of freedom testbed

 This chapter will end with a discussion on issues that arose during hardware implementation and recommendations for improving the existing testbed.

7.2 Experimental Testbed

A schematic overview of the laboratory setup is shown in Figure 7-1. One of the common problems with experimental results performed on macro/micromanipulators is they lack the complexity of real-world applications [10]. For this reason, the testbed was

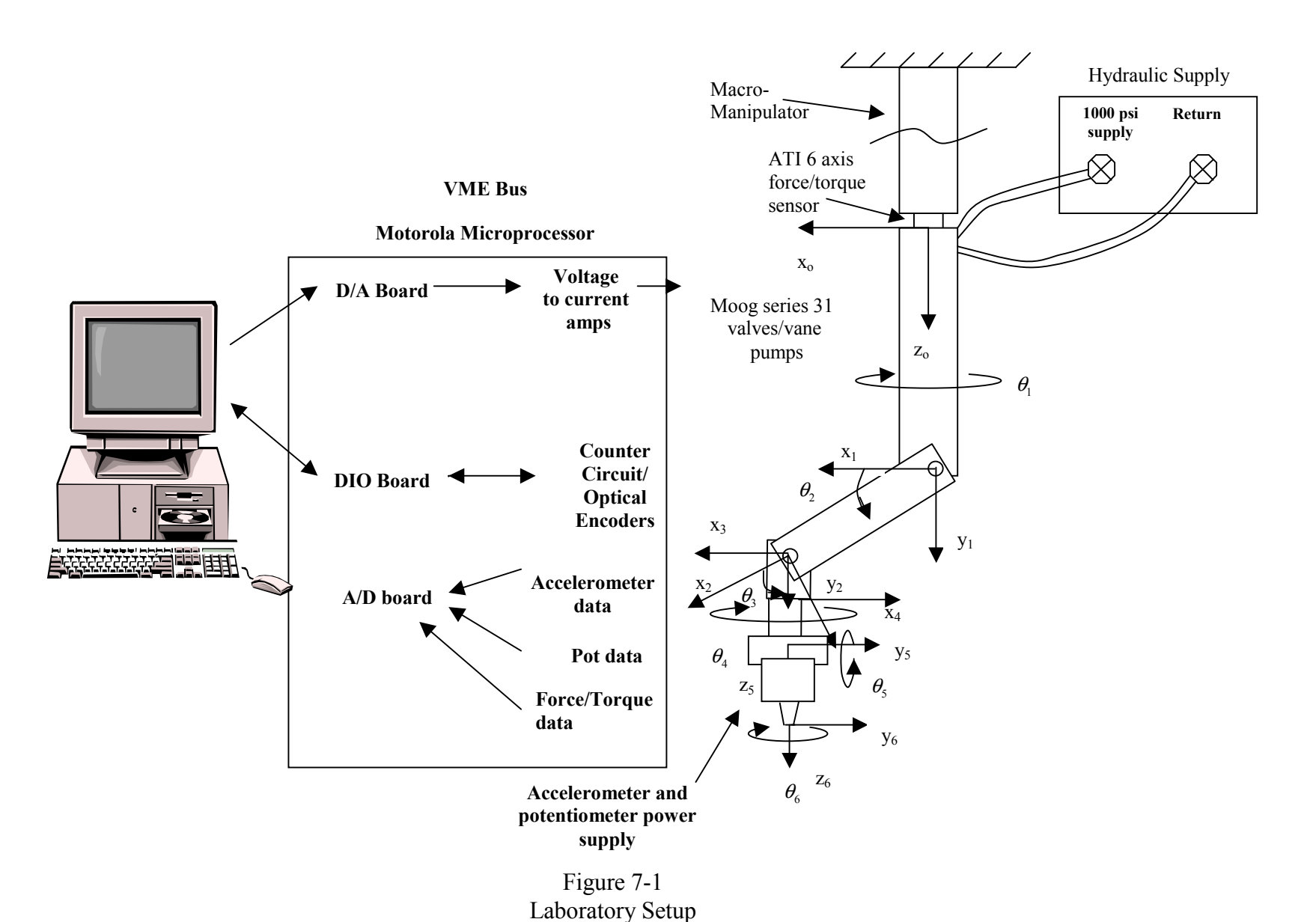
intentionally designed to be as realistic as possible. The testbed was modified from a single link flexible beam/three degree of freedom micromanipulator, used for research in [42], to a two flexible link/six degree of freedom micromanipulator. The real-time control is handled by VxWorks Real Time Control Software, Version 5.2 [85,86]. All of the control functions that interface with VX Works were written in C [29,43]. The control is performed using a Motorola 68040 Microprocessor and Acromag AVME D/A, A/D, and DIO boards for processing of the various signals [44,67].

The rigid robot consists of a hydraulically operated anthropomorphic robot with an IBM 7565 wrist mounted to its last link [27]. The anthropomorphic robot is operated by Micro-Precision Textron SS-.5A double vane, SS-.5A single vane, and SS-1A double vane actuators, while the wrist is operated by similar vane actuators. The servovalves are Moog series 30 and 31, which operate at a constant maximum current of 15 ma [51,76]. The outgoing voltage signal from the D/A board is first sent through voltage to current amplifiers before the signal is sent to the valves. US Digital optical encoders are used to measure the joint position of the first three links of the robot, while potentiometers are used for the last three joints. Vibration is measured by PCB Accelerometers, one mounted along each axis (x, y, and z) [57]. During the initial part of the experimental work, a six axis ATI Delta 9105-T Force/Torque sensor was used to measure interaction forces and torques at the base of the rigid robot [1].

The range of motion of each joint, with coordinates defined in Figure 7-1, is:

$$\begin{aligned} -90^{\circ} & \leq \theta_{1} \leq 180^{\circ} \\ 0^{\circ} & \leq \theta_{2} \leq 95^{\circ} \\ -110^{\circ} & \leq \theta_{3} \leq 110^{\circ} \\ -0^{\circ} & \leq \theta_{4} \leq 270^{\circ} \\ -90^{\circ} & \leq \theta_{5} \leq 90^{\circ} \\ -180^{\circ} & \leq \theta_{6} \leq 180^{\circ} \end{aligned}$$

All angles are defined such that 0° is along the x axis, except for joint 2 which is defined non-conventionally to be at 0° when the arm is up horizontally and 90° when straight down.



oratory be

7.2.1 Rigid Robot Independent Joint Controllers

The dynamics of the experimental robot are dominated by the hydraulic valves. The experimental rigid robot is shown in Figure 7-2. Each joint was independently controlled with a proportional-integral (PI) controller and a dead zone inverse (DZI), as shown in Figure 7-3. The PI gains were chosen based on the hydraulic valve models, which were experimentally determined by open loop system identification testing. DZI is a dead-zone inverse that was designed to compensate for hydraulic actuator dead zone. It is not the common dead zone inverse as described in [74], but only includes an additional constant signal output to counter the effects of the valve dead-zone (zero output is offset).

The rigid robot torque equation, or last equation in 3-27, is given by the actuator specific model. In the case of Moog servovalves, a first order approximation for low frequency performance was used and is given by [75]:

$$\frac{Q(s)}{i(s)} = \frac{K}{\tau_d s + 1} \tag{7-1}$$

Where:

Q=flow rate (cubic inches)

i=current input (ma)

K=servovalve static flow gain at zero load pressure drop (cubic inches/ma)

 τ_d =apparent servovalve time constant (sec)

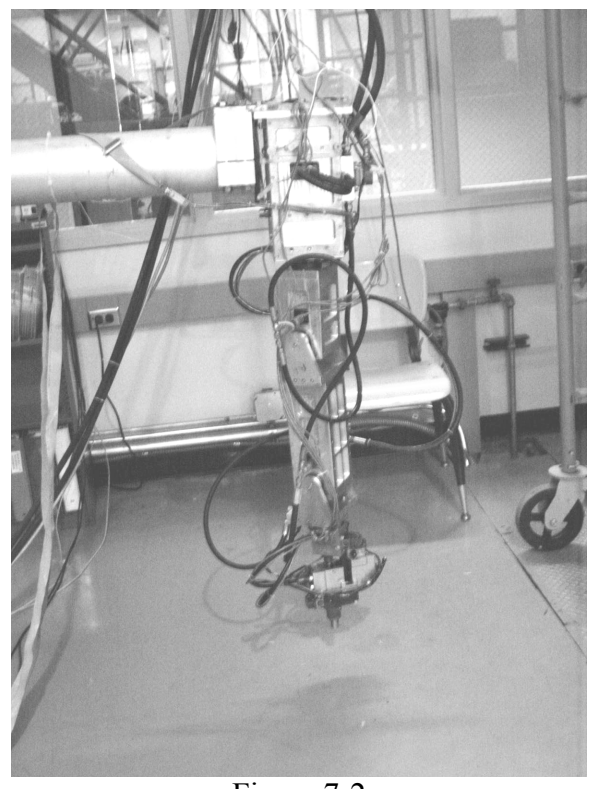


Figure 7-2 Experimental Rigid Robot

Dead Zone Inverse

Dead Zone $\frac{K_p s + K_I}{s}$ $\frac{K_p s + K_I}{s}$

Figure 7-3 Independent Joint Controller

However, the relationship between the commanded computer output, τ , and the resulting joint motion, θ_a , was needed. K generally depends upon the rated flow and input current, while τ_d depends on the flow capacity of the valve. Since the flow rate is proportional to robot velocity and current proportional to the D/A output to the robot, the rigid robot model becomes:

$$\frac{\theta(s)}{\tau(s)} = \frac{K_h}{s(\tau_d s + 1)} \tag{7-2}$$

Open loop tests were performed to determine the appropriate modeling constants for each joint. One representative example may be seen in Figure 7-4, which shows the response of joint 1 to an output signal of –100, which corresponds to an output voltage of approximately -.54 volts. These tests were performed over a range of output values expected for inertial damping control and the results averaged over the range of values. The resulting model parameters may be seen in Table 7-1.

Table 7-1
Model Parameters for Second Order Approximation of Moog Servovalves

| | K_h | $	au_{ m d}$ |
|---------|---------|--------------|
| Joint 1 | 003459 | .00379 |
| Joint 2 | 00076 | .03445 |
| Joint 3 | 001775 | .017704 |
| Joint 4 | .005158 | .031648 |
| Joint 5 | .00394 | .00356 |
| Joint 6 | .006 | .0248 |

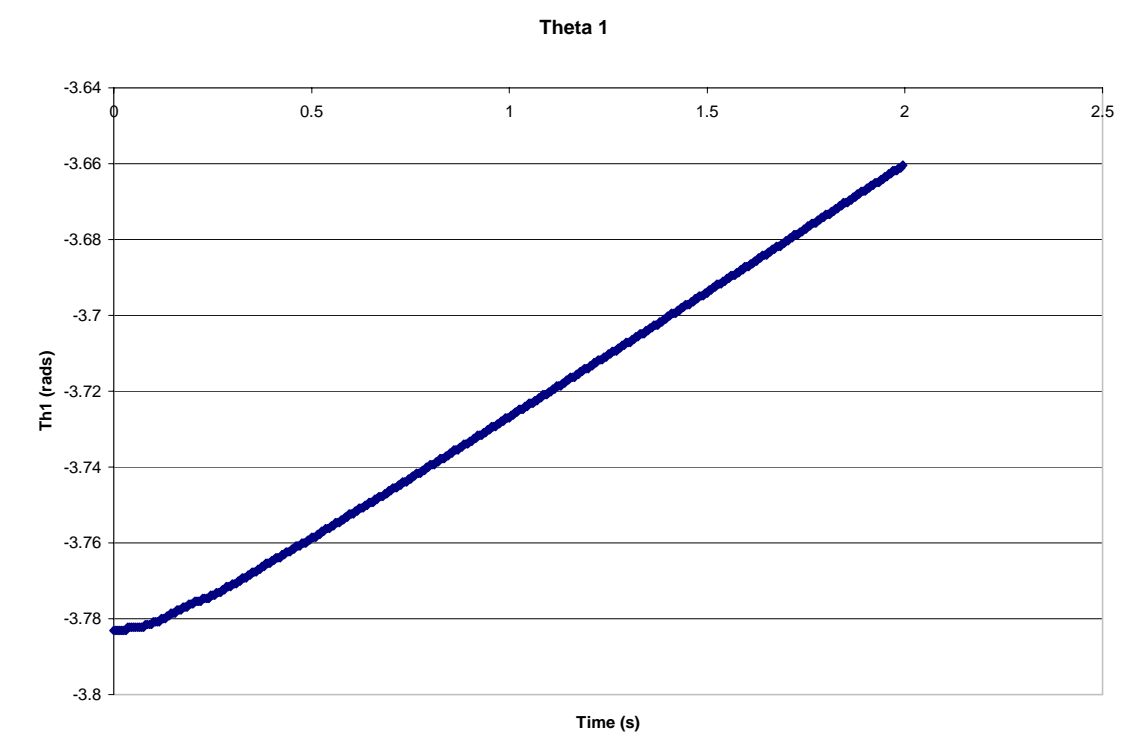


Figure 7-4 Joint 1 Response to D/A Output of -100

An additional concern with the hydraulic actuators is an apparent dead zone behavior at low output values. In this case, the phenomenon manifested itself as a lack of response over a range of outputs. A representative example may be seen in Figure 7-5. This plot clearly shows that when the actuators are operating at a small range of output values, the joint does not move. When it operates outside of this range the joint responds at the approximate velocity predicted by K_h . The first three joints demonstrated a smaller dead zone than the last three joints and were the joints used for active damping in this research. The dead zone has little effect on the performance of the damping controller in this case, but may become more of an issue when additional links are used in future work. In addition, the first three joints of the robot demonstrate a constant null bias and will drift

to the upper or lower joint limit. Unlike many other Moog servovalve models, these do not have a null bias adjustment so a constant feedforward signal was added to the controller to compensate for this. The resulting compensator takes the form of equation 7-3, with the parameters shown in Table 7-2.

If
$$\tau > 0$$
 $\tau = \tau + b_r + d$
If $\tau < 0$ $\tau = \tau - b_t + d$ (7-3)

Table 7-2 Feedforward Dead Zone and Drift Compensator

| | | 1 | |
|---------|-------------|----------|-----|
| | $b_{\rm r}$ | b_l | d |
| Joint 1 | 38 | -38 | -20 |
| Joint 2 | 17 | -17 | 12 |
| Joint 3 | 31 | -31 | 23 |
| Joint 4 | 70* | -70* | 0 |
| Joint 5 | 150* | -150* | 0 |
| Joint 6 | 130* | -130* | 0 |

^{*} Selected slightly lower than measured values to prevent amplification of potentiometer noise

The joint controllers were selected for reasonably good performance using a root locus design method and the performance was experimentally refined by tuning. The resulting gains may be seen in Table 7-3.

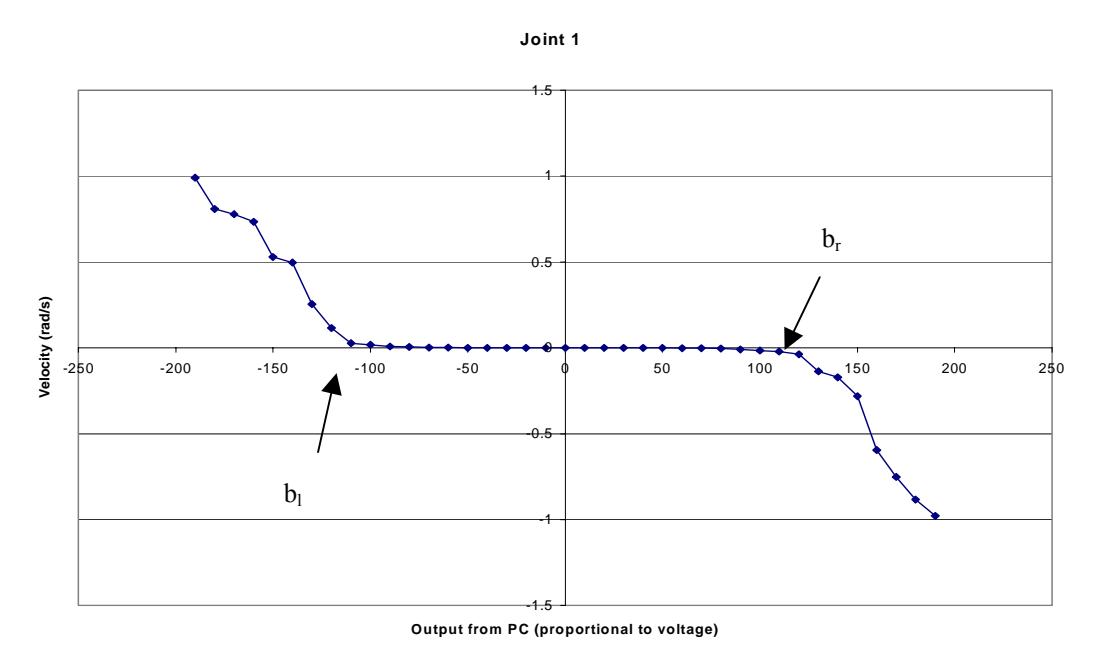


Figure 7-5
Dead Zone Phenomenon in Hydraulic Servovalve

Table 7-3
Selected Gains for Independent Joint Controllers

| | K_p | K_i |
|---------|-------|-------|
| Joint 1 | 2000 | 200 |
| Joint 2 | 2500 | 250 |
| Joint 3 | 1000 | 100 |
| Joint 4 | 1200 | 720 |
| Joint 5 | 1400 | 420 |
| Joint 6 | 1500 | 1350 |

As an example, consider the root locus plot of the selected controller for joint 1, shown in Figure 7-6. The zero at K_i/K_p was chosen near the two poles at the origin in order to provide fast, overdamped performance. Using this ratio of K_i/K_p , the gains were increased so the robot operated smoothly for point-to-point motion. The wrist was designed similarly except with more integral gain. This was selected to provide more

disturbance rejection since its observed lab performance was more nonlinear and it demonstrated a much larger dead zone region than the anthropomorphic robot.

The anthropomorphic robot was originally designed by Cannon [15] so mass properties were available. Mass properties of the wrist were estimated. The inertia properties and dimensions of the robot are given in Table 7-4. The coordinate frames are as defined in Figure 7-1, with dimensions defined per the Denavit and Hartenberg convention [61] as detailed in Table A-1 and A-3 in Appendix A.

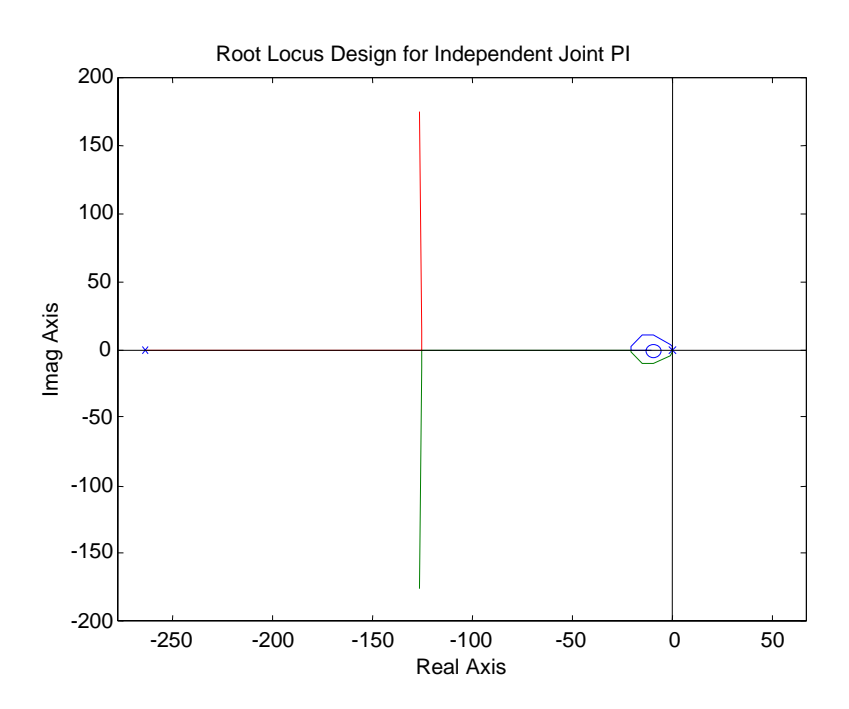


Figure 7-6
Root Locus Design for Independent Joint Controllers

Table 7-4
Dimensions and Properties of Experimental Robot

| | | | | 1 1 | | | |
|-----------|---------|------------|---------------------|-------------|--------------------------------|--------------------------------|-------------------|
| Link i | a_{i} | $d_{i}(m)$ | m _i (kg) | $r_{ci}(m)$ | I_{xxi} (kg-m ²) | I_{yyi} (kg-m ²) | $I_{zzi}(kg-m^2)$ |
| 0 (inert) | 0 | .3302 | 16.0320 | .2413 | .1920 | .1933 | .0936 |
| 1 | 0 | .1969 | 5.0264 | .1354 | .0299 | .0114 | .0270 |
| 2 | .4001 | 0 | 5.5799 | .2924 | .0171 | .0799 | .0728 |
| 3 | .12065 | 0 | 1.488 | .09721 | .019434 | .0186695 | .007131 |
| 4 | 0 | .1 | .26176 | .05 | .000230 | .000174 | .00007332 |
| 5 | 0 | .1 | 2.1095 | .05 | .0059179 | .006032 | .0019024 |
| 6 | 0 | .155 | 1.7103 | .0775 | .0056475 | .004396 | .0017209 |

7.2.2 Macromanipulator

The macromanipulator was assembled from two hollow T6-6061 aluminum beams in an L-shape and mounted vertically from an I-beam mounted to the ceiling of the laboratory. The mounting and attachment to the I-beam is shown in Figure 7-7. The anthropomorphic robot with wrist is mounted to the end of the second link as shown in Figure 7-8.

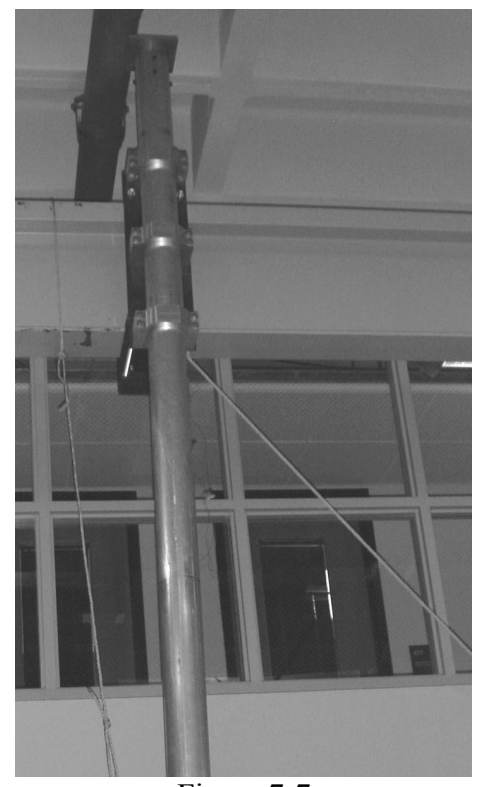


Figure 7-7 Macromanipulator Base Mounting

The macromanipulator parameters are:

d₀=.1412875 m (outside diameter)

d_i=.134188 m (inside diameter)

 ρ =2710 kg/m³ (material density)

 L_1 =4.6482 m (length link 1) L_2 =1.2192 m (length link 2) E=6.8948x10¹⁰ Pa

 $m_1 = 9.76 \text{ kg}$

 $m_2 = 2.56 \text{ kg}$

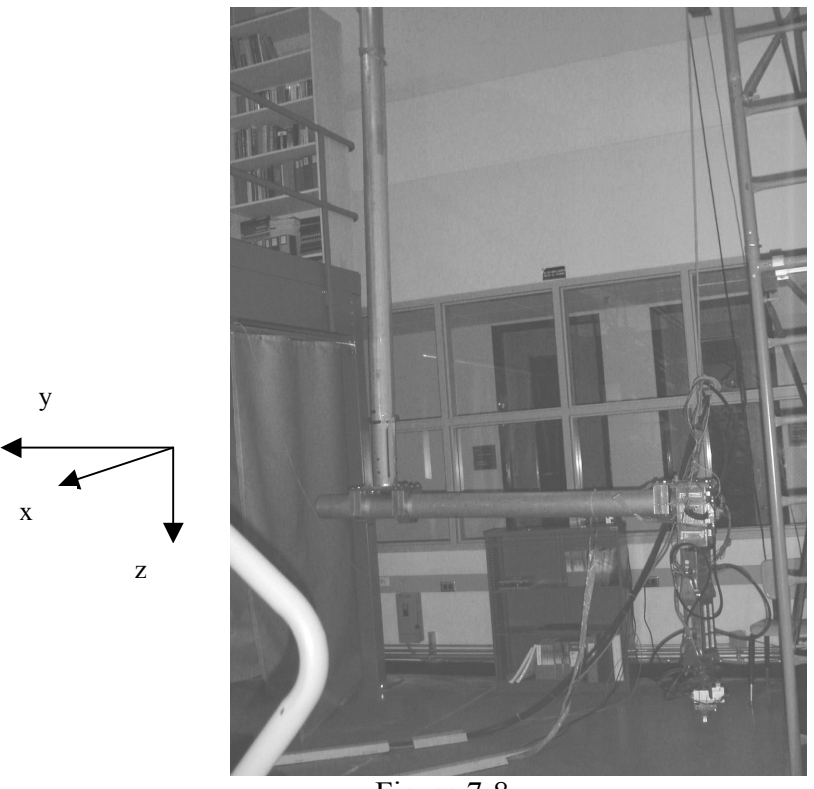


Figure 7-8
Overall Macro/Micromanipulator Testbed

The Lagrangian approach described in section 3.2 was used to model the macromanipulator, with the assumed modes for transverse vibration given by equation 3-5 and torsional modes given by equation 3-9. The system was modeled as described in Chapter 6. The inertia matrix is fully coupled, while the stiffness matrix is diagonally dominant with coupling between modes in each direction.

Lab testing of the macromanipulator allowed some simplification of the model. This allowed scoping the problem to a suitable size to allow simulation in a reasonable timeframe. The configuration results in dominant and *highly coupled* transverse modes and one torsional mode as well as additional higher frequency system modes. As an

example, consider the measured acceleration in the x direction due to an applied disturbance in the x direction, shown in Figure 7-9, along with the frequency response of the data in Figure 7-10 [5,7,21].

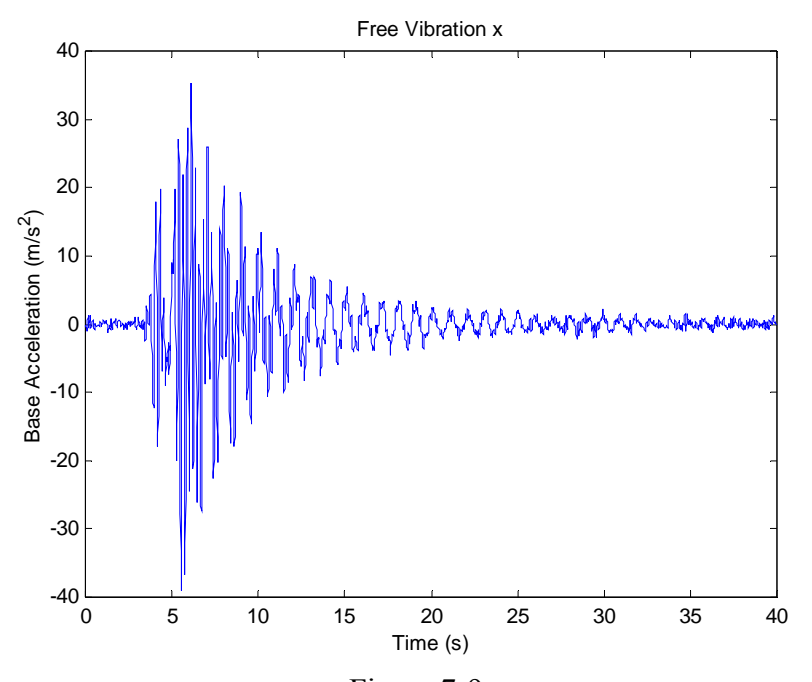


Figure 7-9
Free Vibration x Due to an Applied Disturbance x

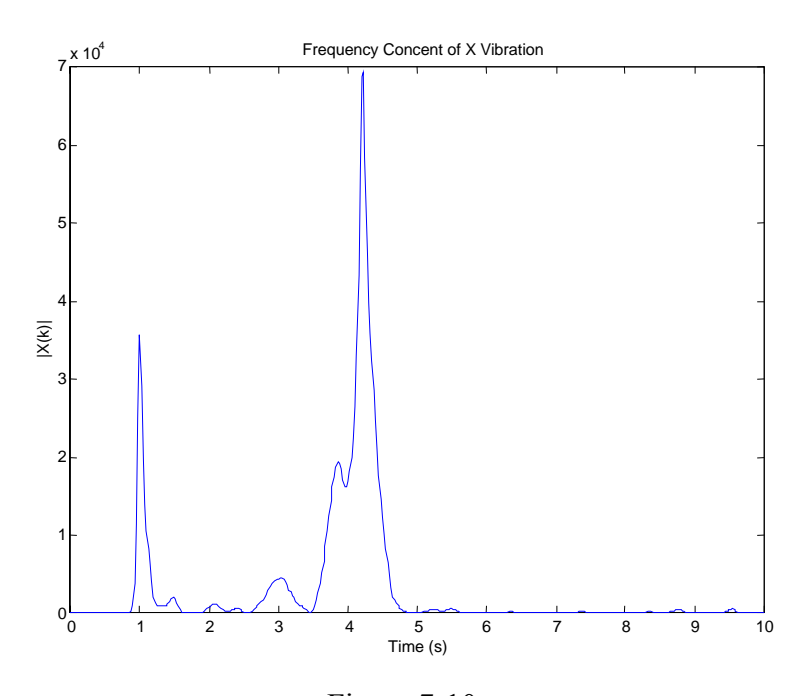


Figure 7-10
Frequency Content of x Vibration Due to an Applied Disturbance x

The acceleration data tends to amplify the higher frequency signals, while the lower frequencies are more of a concern for end point positioning due to their larger amplitude. A more representative measure of the vibration was chosen to be the base position, which requires double integration of the accelerations. It has been noted elsewhere challenges associated with integration of piezoelectric accelerometer data due to low frequency drift [66,84]. A recommended solution is to high pass filter the data prior to integration. For presentation purposes, the raw acceleration data was filtered using a 4th order high pass butterworth filter with a cutoff frequency of .8 Hz [30,54] before double integration. Note this would not be an option for real-time control since phase shift would be introduced in the fundamental modes. Figures 7-11 and 7-12 show the base position and associated frequency content.

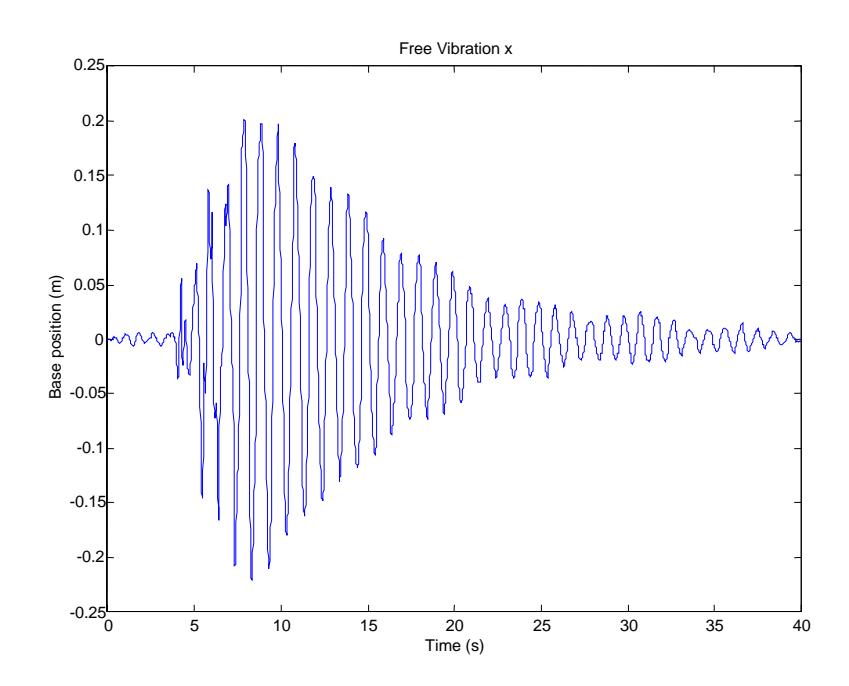


Figure 7-11 Position x Due to an Applied Disturbance x

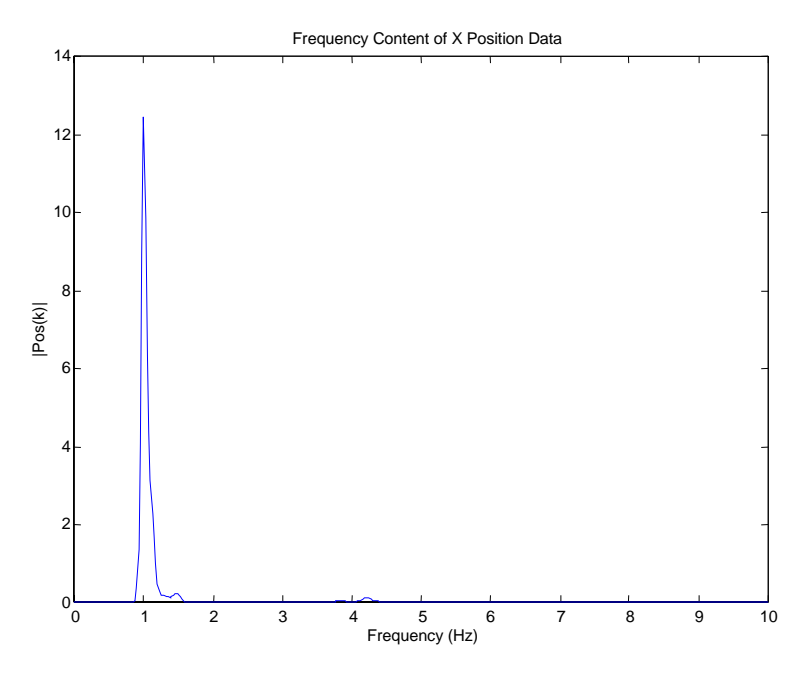


Figure 7-12
Frequency Content of x Position Data Due to an Applied Disturbance x

The testbed has a high degree of coupling between modes. Consider the y vibration due to an applied disturbance in the x direction, shown in Figure 7-13. Since these two fundamental modes of the 15 foot link are very close in frequency (1 and 1.2 Hz), this sometimes created a beating phenomenon, which further complicated the system dynamics. In general, excitation of any of the modes tended to excite one or more additional modes in the system. In order to quantify the performance with and without vibration control, free vibration damping ratios were obtained from the log decrement of the position data when a single mode was dominant. For higher system modes and in cases of multiple mode excitation, the frequency response plots were used to determine the damping ratios. The direction of excitation and observed modes of excitation are summarized in Table 7-5. Table 7-6 summarizes the frequencies and damping ratios of the prominent modes.

Table 7-5
Modes of Vibration on Experimental Testbed

| 1710des of Violation on Experimental Testeed | | | | | | |
|--|---------------|---------------|---------------|--|--|--|
| Direction of | Excited Modes | Excited Modes | Excited Modes | | | |
| Applied | Position x | Position y | Position z | | | |
| Disturbance | (Hz) | (Hz) | (Hz) | | | |
| X | 1, 4.2 | 1,1.2 | 1,1.2 | | | |
| y | 1,1.2,4.2 | 1.2,7,9.5 | 1.2,7,9.5 | | | |
| Z | 1,1.2,4.2 | 1.2,7,9.5 | 1,1.2,7,9.5 | | | |
| general | 1,1.2,4.2 | 1.2,7,9.5 | 1,1.2,7,9.5 | | | |

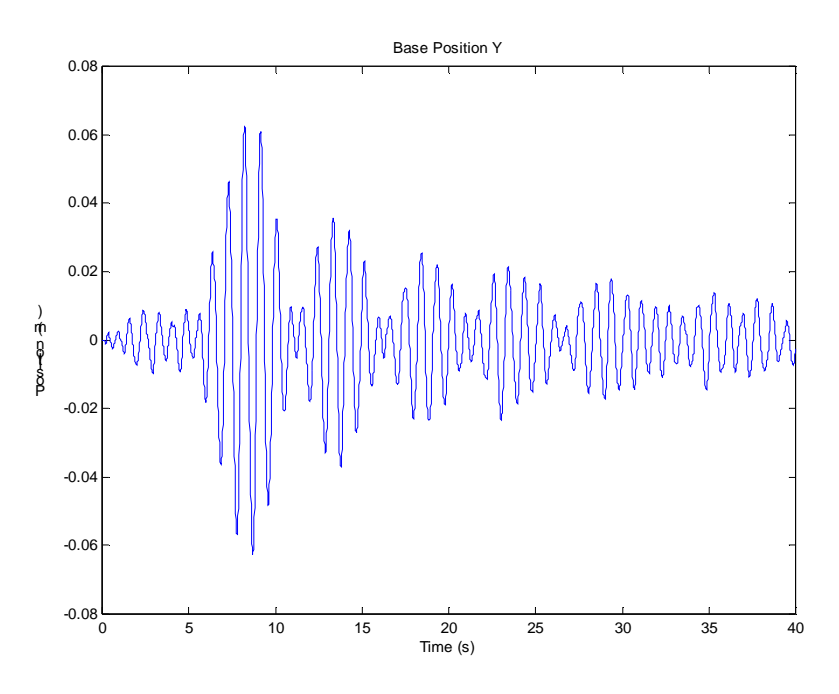


Figure 7-13
Position y Due to an Applied Disturbance x

Table 7-6
Damping Ratios for Macromanipulator Free Vibration Modes

| Mode | Frequency (Hz) | Damping Ratio |
|------------------------|----------------|------------------|
| Link 1 transverse x | 1 | .0186 |
| Link 1 transverse y | 1.2 | .0067 |
| Link 1 torsion | 4.2 | .0087 |
| Higher Mode | 7 | .00513 |
| Higher Mode | 9.5 | .00281 |

181

7.3 Interaction Forces and Torques

The first part of the experimental work was intended to verify the method used to predict the interaction forces and torques and verify work discussed in Chapter 4. Recall the controllable interactions are given by:

$$\mathbf{F}_{IF} = B_{f}(\boldsymbol{\theta})\ddot{\boldsymbol{\theta}} + N_{f}(\boldsymbol{\theta}, \dot{\boldsymbol{\theta}}_{i}\dot{\boldsymbol{\theta}}_{j}) + C_{f}(\boldsymbol{\theta})\ddot{\mathbf{q}} + N_{fc}(\mathbf{q}, \dot{\mathbf{q}}, \boldsymbol{\theta}, \dot{\boldsymbol{\theta}})$$

$$\boldsymbol{\tau}_{IF} = B_{\tau 0}(\boldsymbol{\theta})\ddot{\boldsymbol{\theta}} + N_{\tau 0}(\boldsymbol{\theta}, \dot{\boldsymbol{\theta}}_{i}\dot{\boldsymbol{\theta}}_{j}) + C_{\tau 0}(\boldsymbol{\theta})\ddot{\mathbf{q}} + N_{\tau 0c}(\mathbf{q}, \dot{\mathbf{q}}, \boldsymbol{\theta}, \dot{\boldsymbol{\theta}})$$
(7-4)

The directly controllable interactions that were the subject of Chapter 4 are given by the first two terms in each equation. However, the actual interaction forces and torques are governed by all of the effects, including those due to the motion of the macromanipulator. In order to isolate the effects due to the micromanipulator, the base of the macromanipulator was braced as shown in Figure 7-14. An ATI six-axis force/torque sensor [1] was mounted between the micromanipulator and the base of the macromanipulator. Input signals were sent to the rigid robot similar to the motion expected during active inertial damping, where the motion is harmonic and given by the last equation 5-12.

7.3.1 Single Degree of Freedom Interaction Forces and Torques

The first goal of this work was to determine if the relationship given by equations 4-4 and 4-8, governing the inertia interaction forces and torques, provide a reasonable approximation of the dominant interactions. Masses and dimensions of the rigid robot were estimated as given in Table 7-4. In addition to proving the validity of the

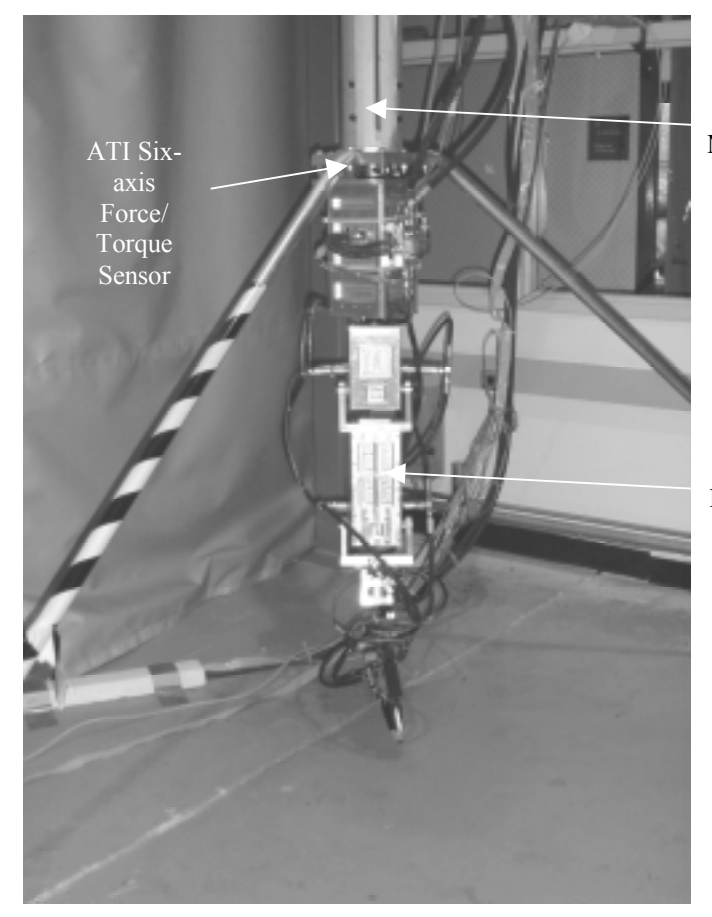
relationship for the interactions, it also provided an opportunity to obtain mass property updates. The first part of this work involved actuating each joint independently, with constant amplitude sine inputs at 1 and 2 Hz, approximately the lowest natural frequencies of interest on the tested. It was expected that this would create dominant inertia forces and torques since:

$$\theta = 20^{\circ} * \frac{\pi}{180} \cos(2 * \pi * 1t)$$

$$|\ddot{\theta}|_{\text{max}} \approx 14 \ rad / s^{2}$$

$$|\dot{\theta}|_{\text{max}}^{2} \approx 5 \ rad / s^{2}$$
(7-5)

An example of the predicted and measured interaction forces and torques due to joint one can be seen in Figures 7-15 and 7-16, respectively, in a configuration of [-90°, 45°, 45°]. This configuration was chosen because it is near the singularity region, as predicted in Figure 4-5, but not near enough that it should affect the ability of the robot to create effective interactions. Thus this configuration would be representative of performance throughout most of the usable workspace (performance would be better than this in most locations). The nonlinear force effects are included in Figure 7-15 for magnitude comparison purposes.



Base of Macromanipulator

Micromanipulator

Figure 7-14 Braced Micromanipulator

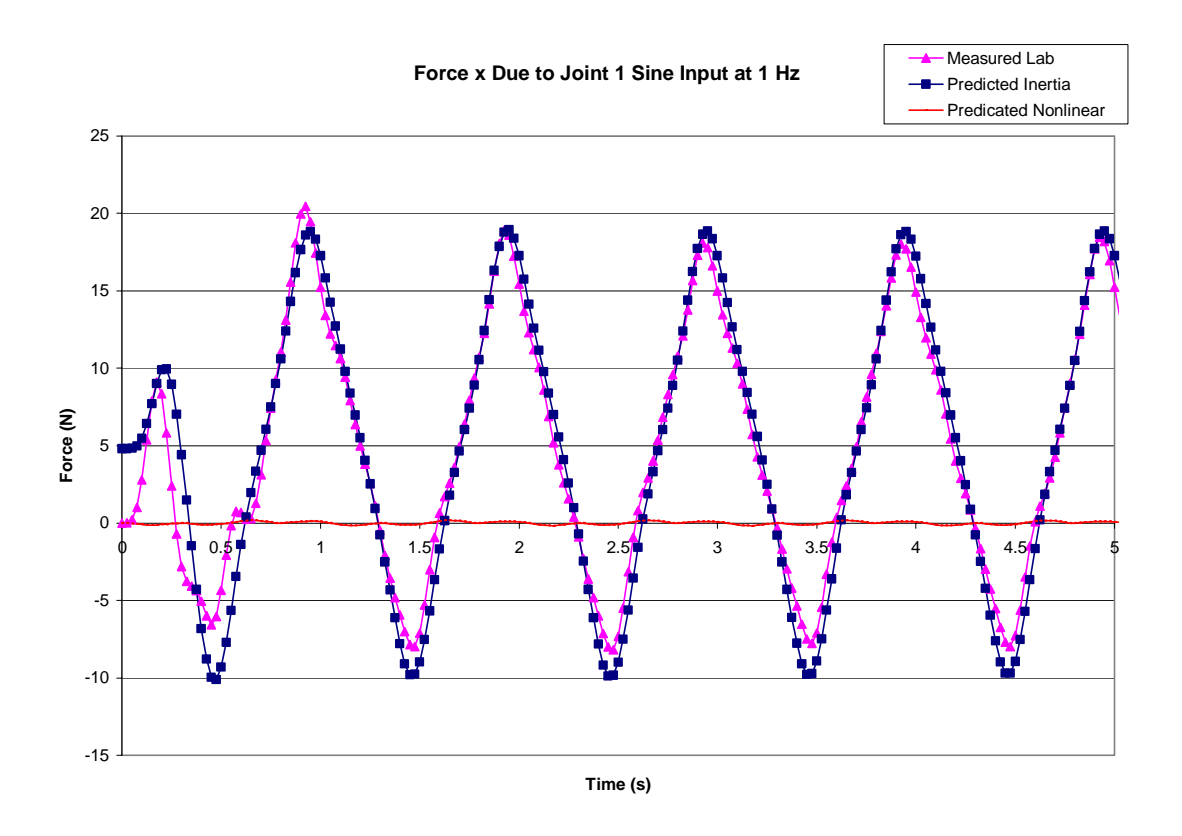


Figure 7-15
Predicted and Measured Interaction Forces at the Base of the Micromanipulator Due to
Joint 1 Harmonic Motion

In order to quantify the results, a goodness of fit parameter was chosen [6] where:

$$\rho = \frac{E\{xy\} - E\{x\}E\{y\}}{\sigma_x \sigma_y}, -1 \le \rho \le 1$$
 (7-6)

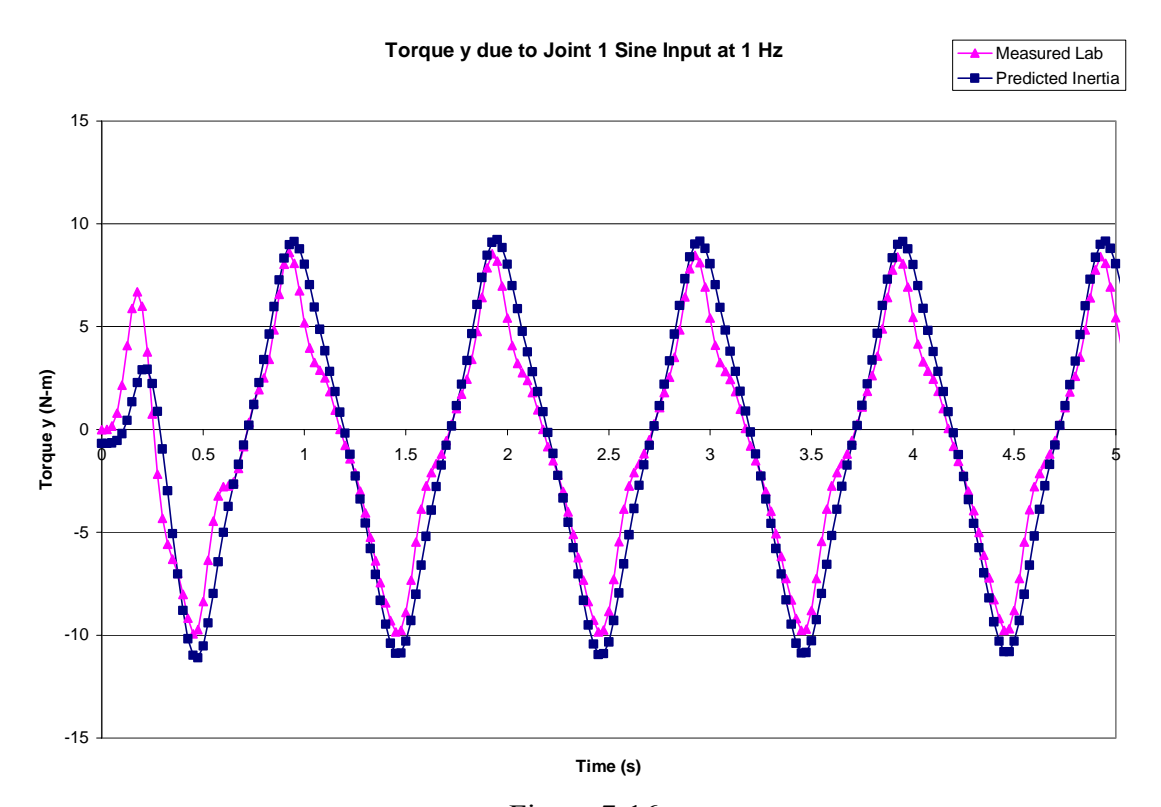


Figure 7-16
Predicted and Measured Interaction Torques at the Base of the Micromanipulator Due to
Joint 1 Harmonic Motion

Here x represents the measured interaction forces or torques and y represents the predicted interaction forces or torques calculated *from the inertia effects only* and σ_x and σ_y are the standard deviations of each. Table 7-7 summarizes these test cases, the matrix terms isolated by each test case, and the resulting goodness of fit. In general, the fits are very good with a few exceptions involving actuation of the third link only. The reason for this is because when these tests were performed, link 3 had little inertia (approximately 32.9 kg or 7.4 lbs). In order to create enough inertia to create interactions detectable by the force/torque sensor, a relatively large joint amplitude had to be used. Nevertheless, the resulting interaction torques were still only around +/-60.8 N-m (+/- 5

in-lbs). Either larger amplitudes would be needed for joint 3, or additional inertia would need to be added. The latter approach was taken for this research.

Table 7-7
Single Degree of Freedom Interaction Force and Torque Test Cases

| Test | Joint | Configuration | Amplitude | Frequency | Matrix | ρ |
|------|-----------|---------------|-----------|-----------|-------------------|------|
| Case | Actuated | (Degrees) | (Degrees) | (Hz) | Parameters | Р |
| Cusc | Tictuated | (Degrees) | (Degrees) | (IIL) | Isolated | |
| 1 | 1 | -90,45,45 | 10 | 1 | $B_{\rm f}(1,1)$ | .989 |
| 1 | • | , , , , , | 10 | 1 | $B_{\tau 0}(2,1)$ | .984 |
| 2 | 1 | -90,45,45 | 10 | 2 | $B_{\rm f}(1,1)$ | .979 |
| | - | , , , , , , | 10 | _ | $B_{\tau 0}(2,1)$ | .977 |
| 3 | 2 | 0,90,45 | 10 | 1 | $B_{\rm f}(1,2)$ | .985 |
| | | | | | $B_{\tau 0}(2,2)$ | .990 |
| 4 | 2 | 0,90,45 | 10 | 2 | $B_{\rm f}(1,2)$ | .971 |
| - | | ,,,,,,, | | _ | $B_{\tau 0}(2,2)$ | .969 |
| 5 | 3 | 0,90,0 | 20 | 1 | $B_{\rm f}(1,3)$ | .967 |
| | | - 9 9- | | | $B_{\tau 0}(2,3)$ | .987 |
| 6 | 3 | 0,90,0 | 20 | 2 | $B_{\rm f}(1,3)$ | .973 |
| | | , , | | | $B_{\tau 0}(2,3)$ | .608 |
| 7 | 1 | 0,45,45 | 10 | 1 | $B_{\rm f}(2,1)$ | .977 |
| | | , , | | | $B_{\tau 0}(1,1)$ | .978 |
| 8 | 1 | 0,45,45 | 10 | 2 | $B_{\rm f}(2,1)$ | .985 |
| | | , , | | | $B_{\tau 0}(1,1)$ | .979 |
| 9 | 2 | -90,90,45 | 10 | 1 | $B_{\rm f}(2,2)$ | .977 |
| | | | | | $B_{\tau 0}(1,2)$ | .978 |
| 10 | 2 | -90,90,45 | 10 | 2 | $B_{\rm f}(2,2)$ | .966 |
| | | | | | $B_{\tau 0}(1,2)$ | .976 |
| 11 | 3 | -90,90,0 | 20 | 1 | $B_{\rm f}(2,3)$ | .973 |
| | | | | | $B_{\tau 0}(1,3)$ | .962 |
| 12 | 3 | -90,90,0 | 20 | 2 | $B_{f}(2,3)$ | .973 |
| | | | | | $B_{\tau 0}(1,3)$ | .973 |
| 13 | 2 | 0,45,45 | 10 | 1 | $B_{f}(3,2)$ | .975 |
| | | | | | $B_{\tau 0}(2,2)$ | .969 |
| 14 | 2 | 0,45,45 | 10 | 2 | $B_{f}(3,2)$ | .940 |
| | | | | | $B_{\tau 0}(2,2)$ | .991 |
| 15 | 3 | 0,90,75 | 20 | 1 | $B_f(3,3)$ | .969 |
| | | | | | $B_{\tau 0}(2,3)$ | .974 |
| 16 | 3 | 0,90,75 | 20 | 2 | $B_f(3,3)$ | .978 |
| | | | | | $B_{\tau 0}(2,3)$ | .727 |

7.3.2 Multi-Degree of Freedom Interaction Forces and Torques

The next part of this effort involved extending this to interactions due to multiple joints actuating simultaneously, which was required to implement inertial damping in multi-DOF. Figure 7-17 shows an example of the interaction forces created by joint 1 actuating at 1 Hz, joint 2 at 1.5 Hz, and joint 3 at 2 Hz in a configuration of [45°, 45°, 60°]. It was predicted that the inertia effects would be dominant in this configuration and the effect of higher harmonics would be negligible. The associated frequency response is shown in Figure 7-18. Some higher harmonics are noticeable in the interactions but with increasing frequency quickly become less important compared with the inertia effects.

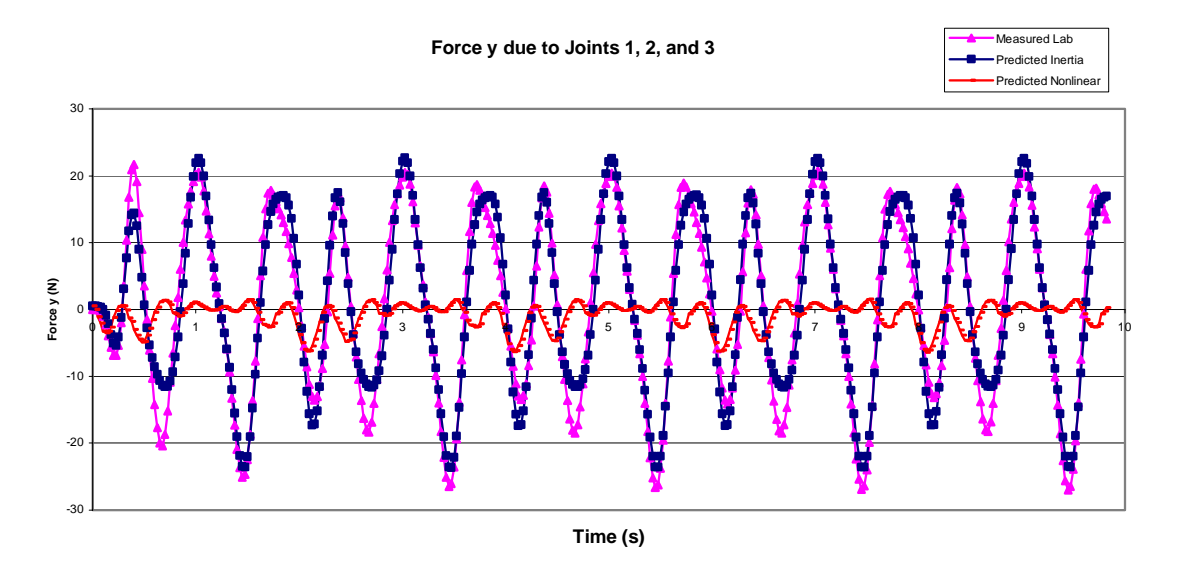
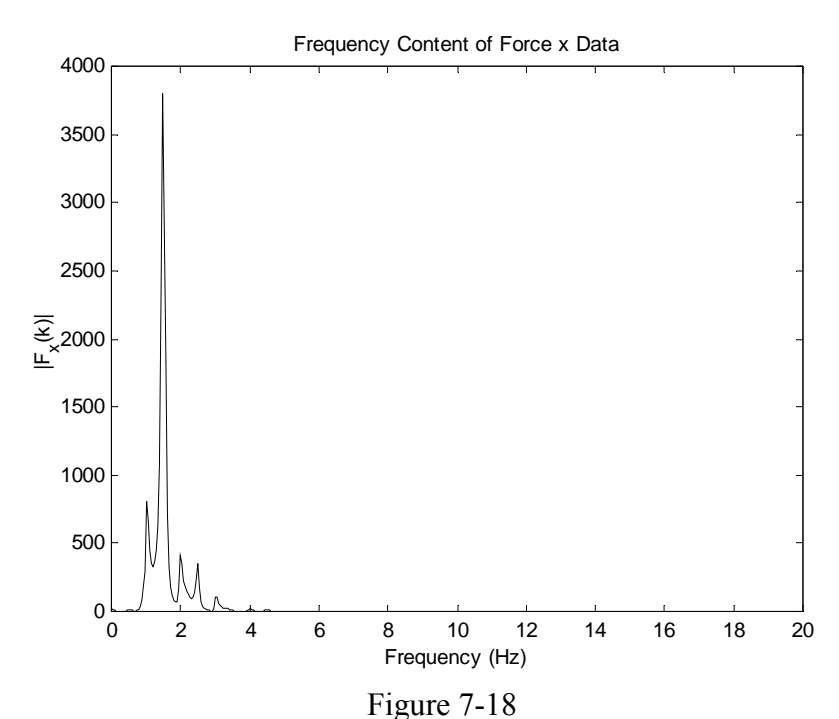


Figure 7-17
Predicated and Measured Interaction Forces Due to Joints 1,2, and 3 Actuating Simultaneously



Frequency Content of Force y Data Due to Joints 1,2,and 3 Actuating Simultaneously

Figure 4-5 predicted poor inertia performance near the inertial singularity region and Figures 4-13 and 4-14 predicted the nonlinear coriolis effects would be more of a concern in these regions. Consider the robot in a configuration of [0°, 87°, 56°] (shown in Figure 7-19) with joint 1 actuating at 1 Hz and joint 2 at 1.5 Hz. The resulting interaction forces along with predicted total forces (inertia plus nonlinear) in the y directions are shown in Figure 7-20. The total interaction forces due to the actuation of joint 1 is small in this configuration, so the force in the y direction, as expected, is relatively small. The coriolis effects are expected to be large in this region, which would result in combinations of the harmonics at approximately .5 and 2.5 Hz, in this case. The frequency content of the

measured force data is shown in Figure 7-21 and it can be seen that and the higher harmonics have more of an effect here.

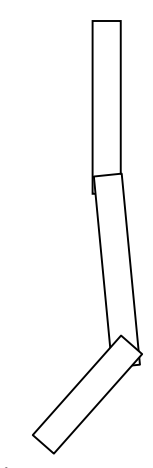


Figure 7-19
Anthropomorphic Robot Configuration [0°, 87°, 56°]

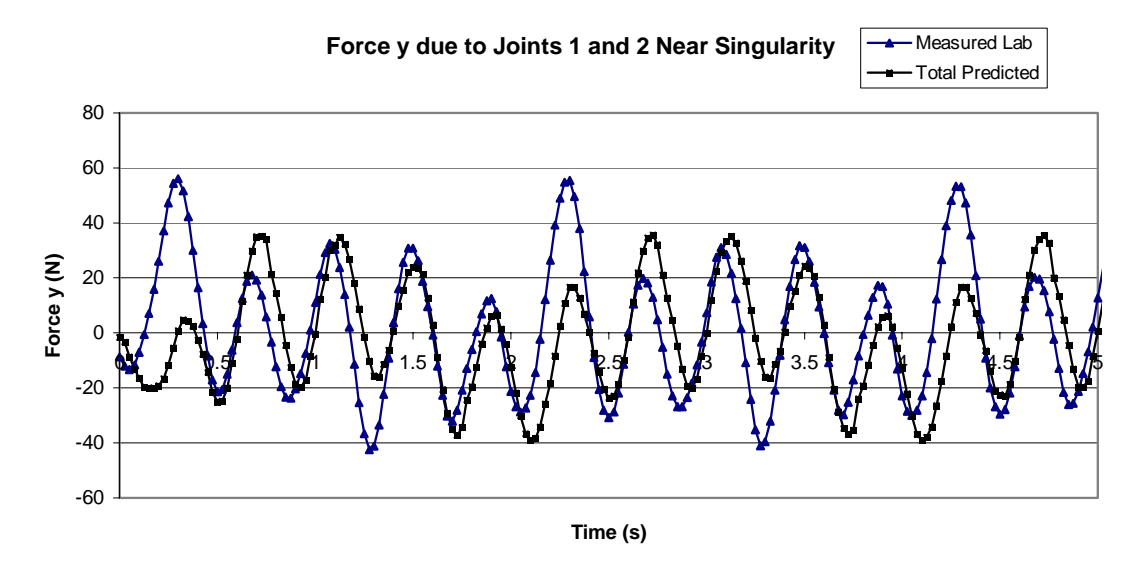
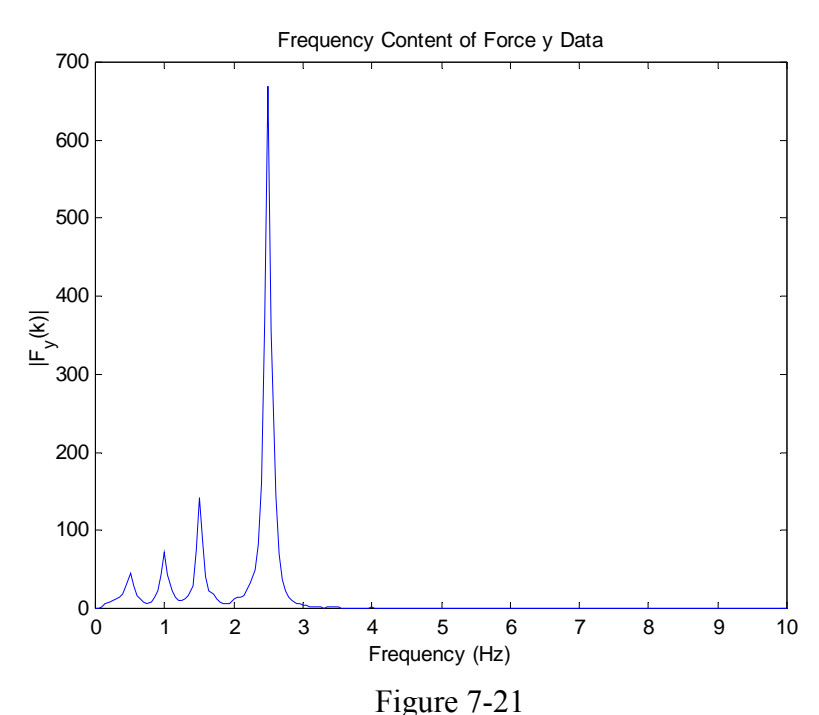


Figure 7-20 Interaction Forces Due to Joints 1 and 2 Actuating Near an Inertial Singularity



Frequency Content of Force Data due to Joints 1 and 2 Actuating Near an Inertial Singularity

As an example of a region where nonlinear centrifugal forces are expected to be larger, consider the configuration [0°,38°,0°], shown in Figure 7-22. In this configuration, it was predicted by Figure 4-14 that the centrifugal force effects would be greater. The resulting force data in the x direction and frequency content are shown in Figures 7-23 and 7-24. Joints 1, 2, and 3 are actuating harmonically at 1, 1.5, and 2 Hz, respectively. In this case, the interaction force effects in the x direction will be primarily due to joints 2 and 3. As discussed previously, joint 3 has relatively little inertia so it was expected the higher harmonics consist mainly of 3 Hz content, or twice the frequency of joint 2. Now consider the interaction torques and associated frequency content, as shown in Figures 7-25 and 7-26, respectively. Here instead of the twice the frequency of

actuation, the higher harmonics consist of the combination of frequencies, indicative of increased coriolis effects, as expected.

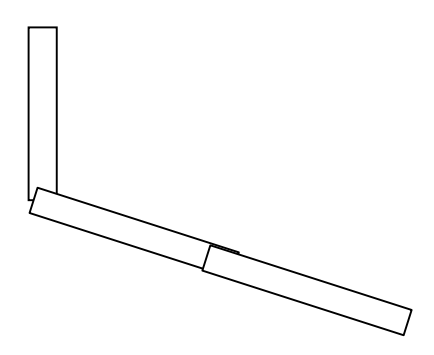


Figure 7-22 Anthropomorphic Robot Configuration [0°,38°,0°]

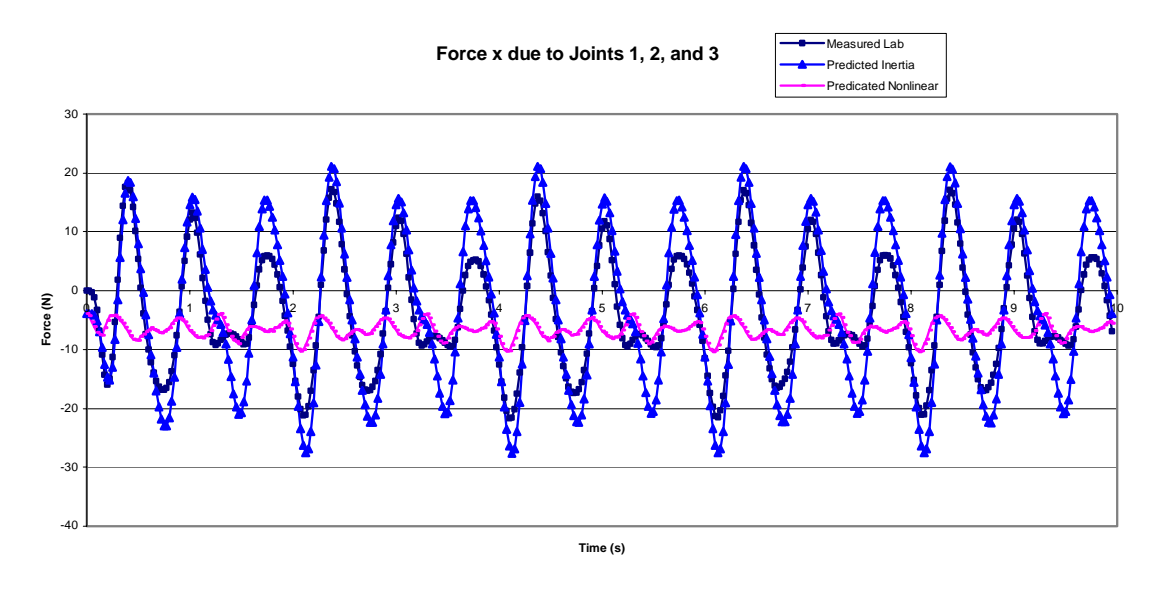


Figure 7-23
Interaction Forces with Large Centrifugal Effects Due to Joints 1, 2, and 3 Actuating Simultaneously

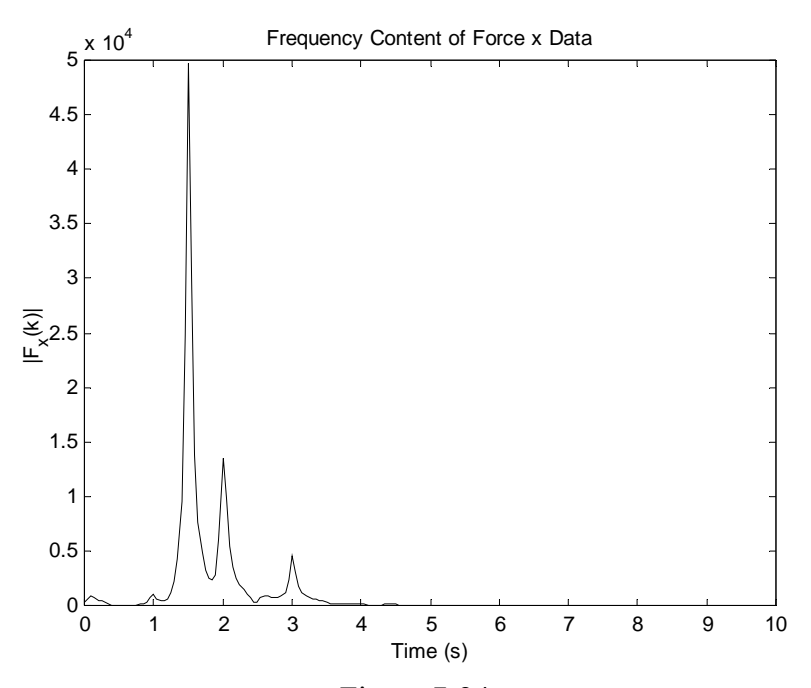


Figure 7-24
Frequency Content of Force x data with Large Centrifugal Effects

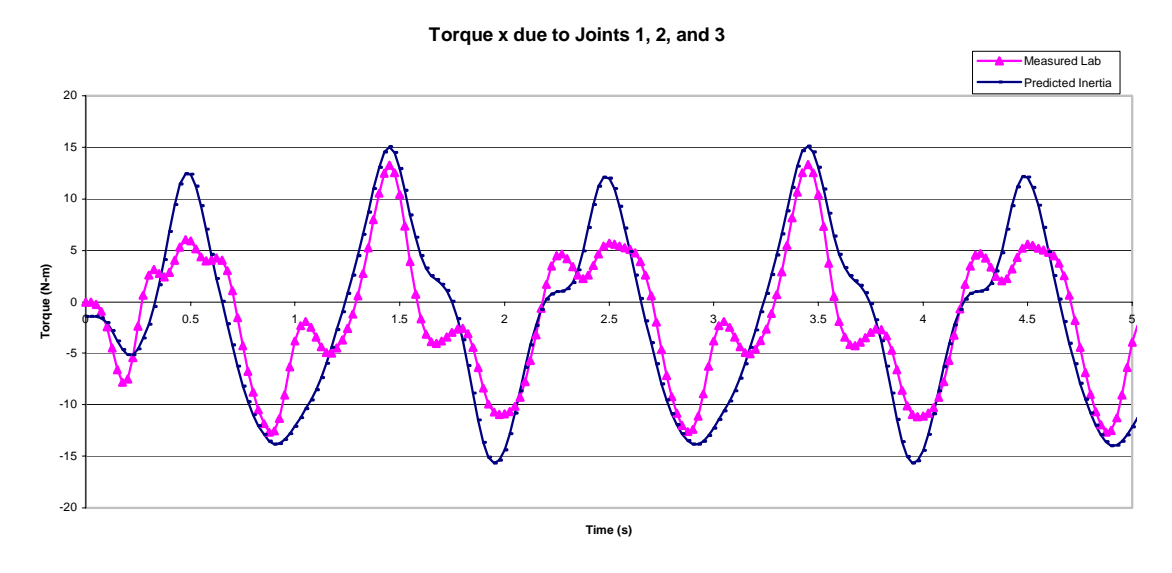
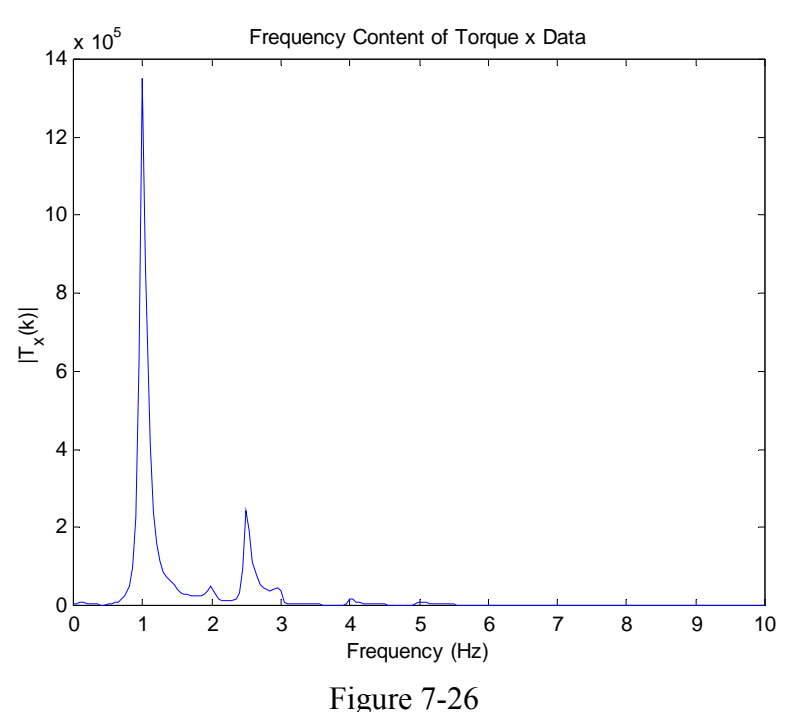


Figure 7-25 Interaction Torques due to Joints 1, 2, and 3 in Configuration $(0^{\circ},38^{\circ},0^{\circ})$



Frequency Content of Interaction Torque Data Due to Joints 1, 2, and 3

There are two main conclusions to be drawn from this portion of the experimental work. First, the form of the interaction forces and torques given by equation 4-1 is valid, regardless of the rigid robot dynamics. In the case of this experimental work, the joint torque dynamics are dominated by the hydraulic servovalves and are hence very different from the ideal robot model cited in most robotics texts. However, the model for the interaction forces and torques is still valid. The second important point is that, regardless of the orientation of the robot, higher (and sometimes lower) harmonics will be generated by the robot. If higher system modes exist, which will be the case with a continuous system, higher frequency modes can become excited. However, the relative importance of the harmonics varies throughout the workspace. With a good

understanding of these issues, either these regions can be avoided or the control gains selected to ensure overall energy removal from the system. Note this part of the work has assumed constant joint amplitudes, and the ratio of the inertia to nonlinear effects will improve as the vibration is reduced. The next step was to proceed forward with implementation of the vibration controller described in Chapter 5.

7.4 Multi-Degree of Freedom Vibration Damping

The final goal of this research was to extend the inertial damping control scheme to multiple degrees of freedom. This is a challenging extension from previous work at Georgia Tech for two main reasons. First, the testbed now has highly coupled modes and general system motion in many directions is possible, as discussed in Section 7.2.2. Previous testbeds at Georgia Tech demonstrated clear decoupled vibration i.e. the two transverse fundamental modes of vibration of the beam were at different frequencies and there was little coupling between the two. Second, the use of three links of the micromanipulator requires cooperation between joints because links 2 and 3 of the testbed robot both create interaction forces and torques in the same plane. Hence, their movements have to be cooperatively prescribed in order to damp the motion because damping motion by either one requires motion in the other. This forces accurate modeling and a better understanding of issues that may result when the robot model contains inaccuracies.

The block diagram for the multi-degree of freedom case can be seen in Figure 7-27. The parameters for the assumed rigid robot model were given in Table 7-1 and the feedforward and drift compensators were given in Table 7-2 (only the first three joints are

shown in the block diagram below since they are the only joints used for inertial damping). The rigid robot PI gains chosen were given in Table 7-3. The ID (inverse dynamics) function is defined as:

$$ID = B_{\tau}B_f^{-1}(\theta) \tag{7-7}$$

 ID_{ij} in figure 7-27 is the i^{th} row and j^{th} column of the resulting matrix. The rigid robot actuators respond as a near velocity source so B_{τ} is given by:

$$B_{\tau} = \begin{bmatrix} \frac{1}{K_{h1}} & 0 & 0 \\ 0 & \frac{1}{K_{h2}} & 0 \\ 0 & 0 & \frac{1}{K_{h3}} \end{bmatrix}$$
 (7-8)

 $B_f(\boldsymbol{\theta})$ is given by equation 4-4 and $\boldsymbol{\theta}$ are the actual robot joint angles measured from optical encoders.

The scheme relies on the inverse dynamics function to cancel the rigid robot and coupling effects and assumes the inertia effects are the most significant coupling effects. As discussed in sections 4.3 and 7.3.1, the inertia effects are dominant in the single degree of freedom case. However, nonlinear effects can become more significant with multiple links actuating harmonically. Thus, the controller also relies on the gain limits established in section 5.3.1 to limit the joint amplitudes such that the inertia effects adequately capture the significant interaction effects.

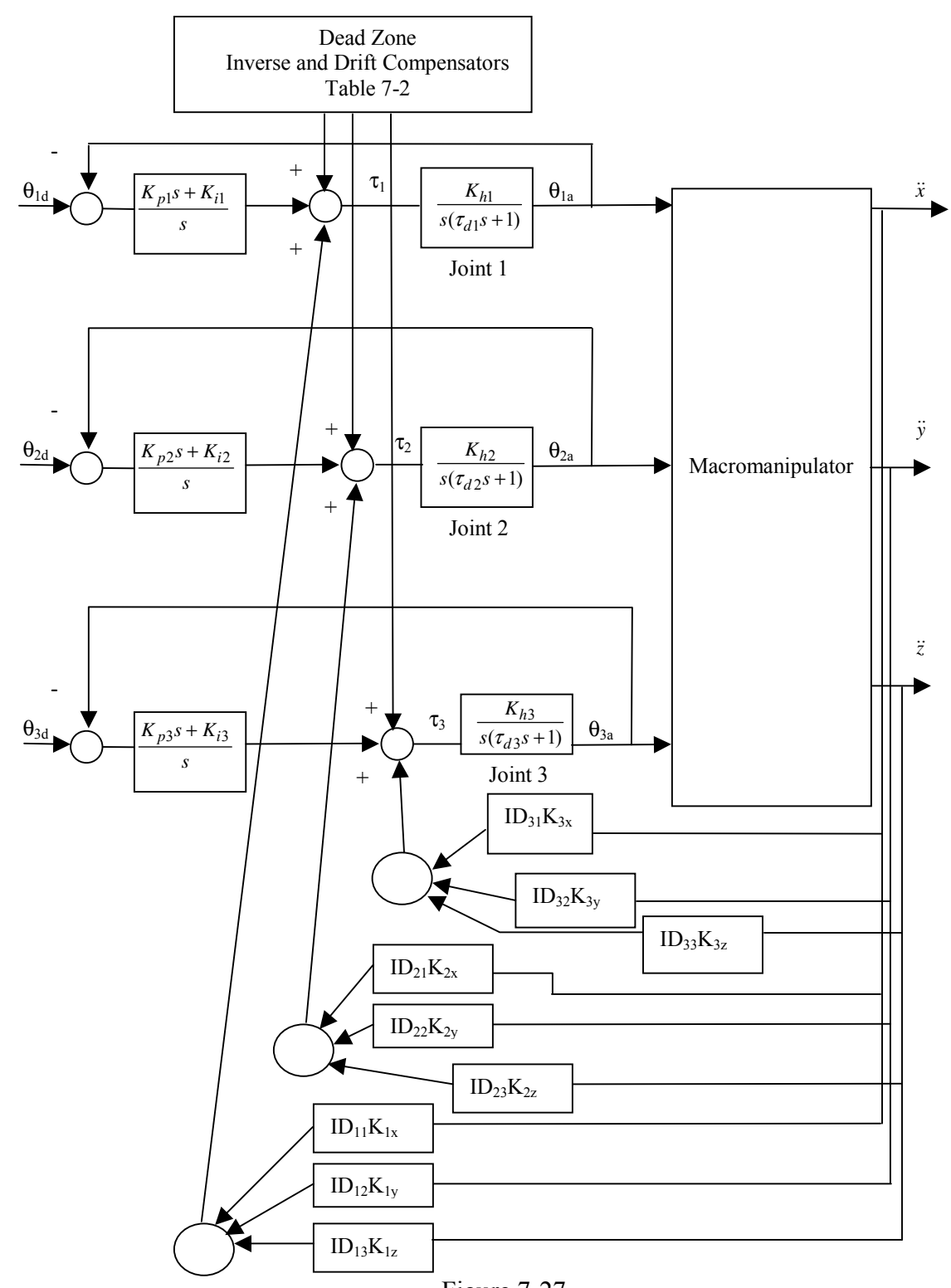


Figure 7-27
Block Diagram of Multi-Degree of Freedom Vibration Damping

7.4.1 Disturbance Rejection

First, the vibration controller was tested in a configuration of (0°, 45°,-45°) and an excitation was applied to the macromanipulator. The first case considered was with the vibration controller turned on during the free vibration, and the resulting base vibration and joint motion recorded. The second case was with the vibration controller on and a disturbance is applied to the macromanipulator. A summary of the test cases and calculated damping ratios is shown in Table 7-8. In most cases, two tests were performed for each case and the damping ratios were averaged. In nearly all cases, as expected, multiple modes were excited, but the lower frequency modes were those responsible for the largest amplitude of vibration. In all of the test cases vibration energy is removed from the overall system. The damping controller performance works best for damping the fundamental mode at 1.2 Hz, which is the transverse mode of the first link in the y direction. The controller gains for x direction vibration were selected to be low compared to the y gains in order to help avoid excitation of the higher frequency modes, notably modes at 4.2 and 9 Hz. A representative example of the recorded base position and joint motion can be seen in Figures 7-28 and 7-29.

Table 7-8
Summary of Active Damping Controller Disturbance Rejection

| Disturbance | Mode | Detected | γ % | | |
|-------------|------|--------------|-------|-------------|--|
| | | | ζ | | |
| Applied | (Hz) | Primarily in | | Improvement | |
| | | Directions | | | |
| X | 1 | X | .0239 | 28.5 | |
| X | 1.2 | y,z | .0392 | 485.1 | |
| X | 2 | x,y,z | .0231 | | |
| X | 4.2 | x,z | .0164 | 88.5 | |
| y | 1 | X,Z | .0499 | 168.3 | |
| y | 1.2 | y,z | .0332 | 395.5 | |
| y | 4.2 | X,Z | .0111 | 27.6 | |
| y | 7 | y,z | .0132 | 157.3 | |
| y | 9 | y,z | .0081 | 188.3 | |
| Z | 1 | X | .0311 | 67.2 | |
| Z | 1.2 | y,z | .0419 | 525.3 | |
| Z | 4 | X,Z | .0163 | 87.4 | |
| Z | 7 | y,z | .0166 | 224.6 | |
| Z | 9 | y,z | .0082 | 191.8 | |
| General | 1 | X | .0256 | 37.6 | |
| General | 1.2 | y,z | .0359 | 435.8 | |
| General | 4.2 | X,Z | .0120 | 37.9 | |
| General | 7 | y,z | .0197 | 284.0 | |
| General | 9 | y,z | .0086 | 206.0 | |

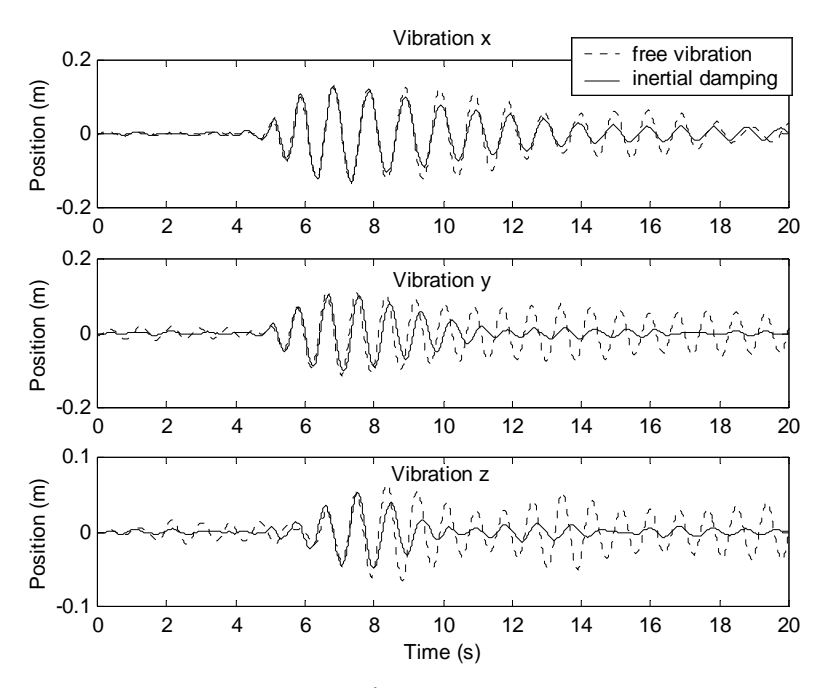


Figure 7-28 Vibration Control Due to an Applied Disturbance

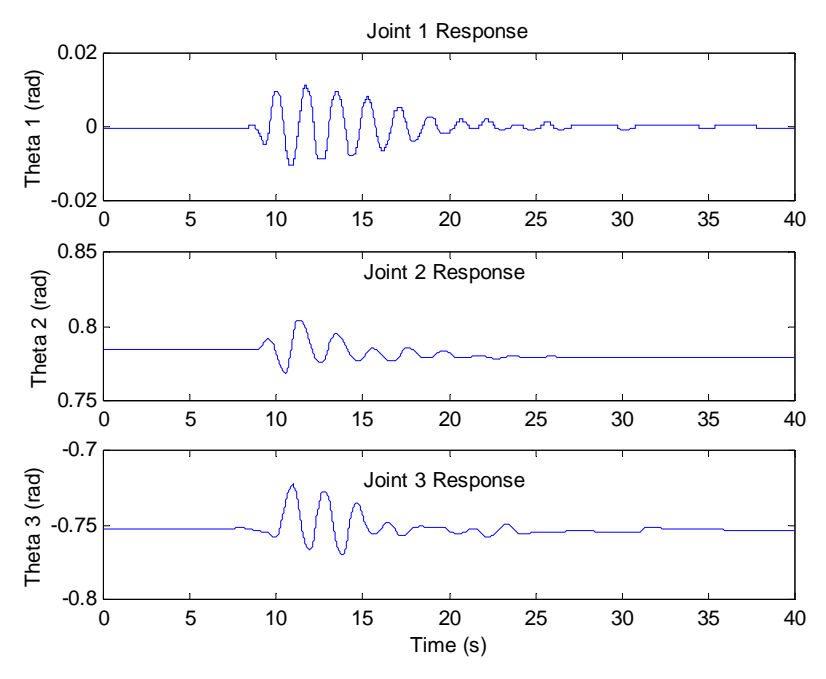


Figure 7-29
Joint Response Due to an Applied Disturbance

7.4.2 Combined Movement and Vibration Control

The second set of experiments was intended to verify the use of the performance index to predict regions of good inertial damping performance. The robot was commanded to move from a configuration of (-27°,0°,83°,0°,30°,90°) to (45°,5°,60°,0°,90°,90°), which is one of the legs presented in section 6.3.4 for simulated point-to-point motion in a configuration predicted better for inertial damping performance. The resulting base vibration and commanded joint movement may be seen in Figures 7-30 and 7-31. Note the very low amplitude of vibration in the x and z directions compared with vibration in the y direction. The base vibration with and without the vibration controller for the robot moving from (-27°,83°,- $100^{\circ}, 0^{\circ}, 90^{\circ}, 90^{\circ}$) to $(45^{\circ}, 65^{\circ}, -60^{\circ}, 0^{\circ}, 90^{\circ}, 90^{\circ})$, which is the alternate inverse kinematics path, may be seen in Figure 7-32. As expected, lower amplitude of vibration results in the regions of low coupling, but the vibration controller is much less effective. The tradeoff in the better configuration is the impact on joint positioning, since the controller requires small joint movements about the desired end point position. These occurs primarily at the end of the path, although there are a few correctional movements made just before the end of the trajectory which helps reduce the level of vibration.

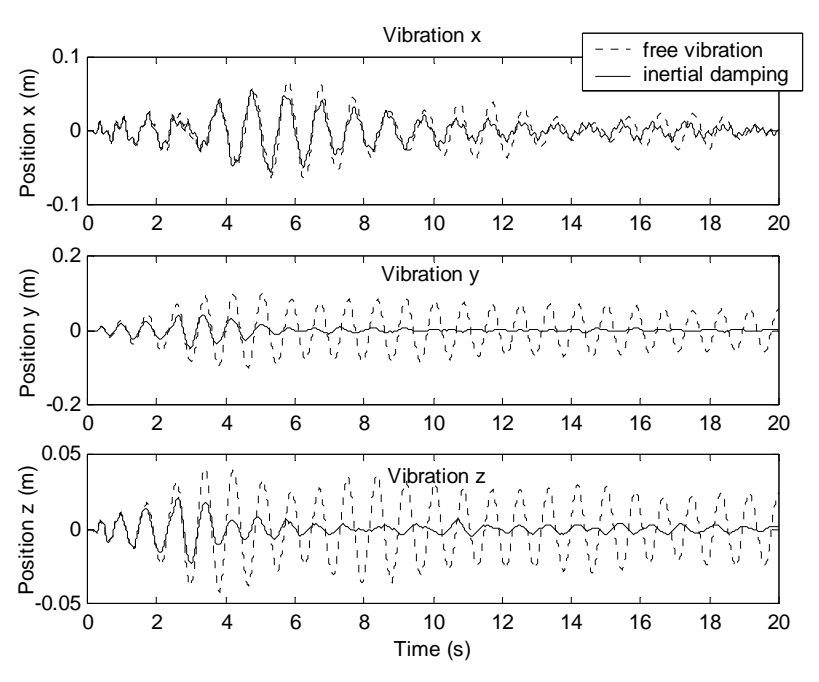


Figure 7-30
Base Vibration Due to Commanded Movement

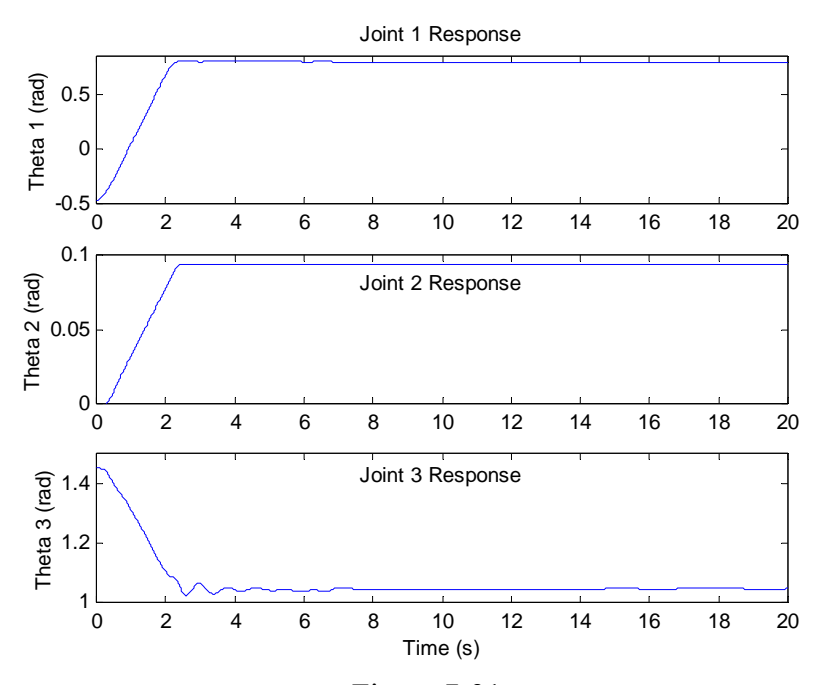


Figure 7-31
Joint Motion During Commanded Point-to-Point Movement with Vibration Control

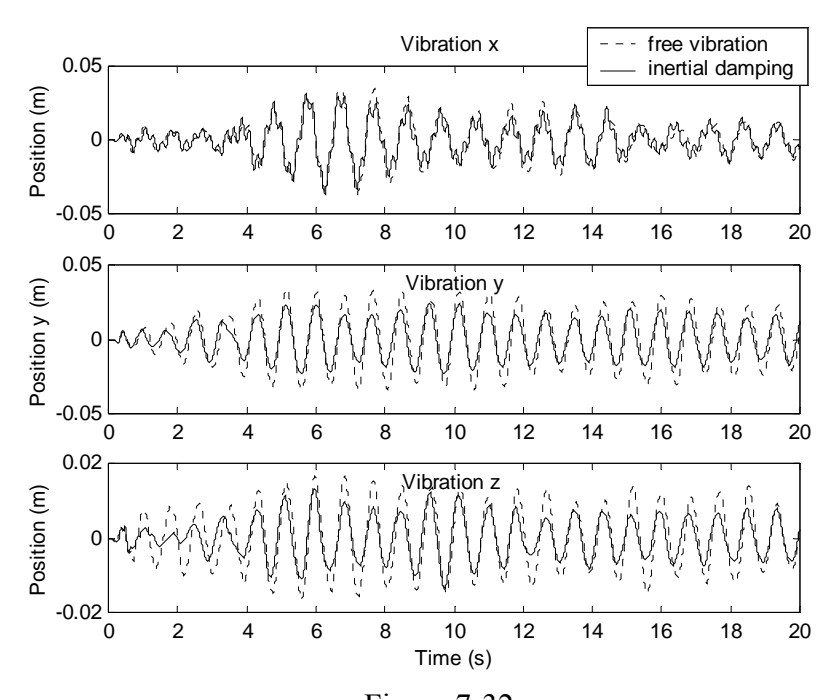


Figure 7-32
Base Vibration Due to Commanded Movement in Region with Predicted Poor Inertial
Damping Performance

7.5 Implementation Issues

Many implementation issues arose with the experimental testing of the control scheme in multiple degrees of freedom. These will be discussed along with recommendations for improving the testbed for future work.

7.5.1 Acceleration Data

The available vibration measurements were PCB piezoelectric accelerometers. The fundamental frequencies of the testbed were very low, approximately .98 and 1.2 Hz. For the model 303A accelerometers, used for x and y vibration measurements, the \pm - 5% frequency range of these accelerometers is from 1 – 10000 Hz and for the model 308B

accelerometers is from 1 – 3000 Hz [57]. The modes of vibration on the new testbed were very low and the accelerometers were operating toward the lower limit of their useful range. This was further complicated by the beating phenomenon between the first two fundamental modes discussed in Section 7.2.2. In addition, ideally, the measured accelerations would need to be integrated as noted in section 5.4.5. As noted in several sources [66,84], integration of piezoelectric acceleration time histories generally results in calculated displacements that are dominated by large, low frequency drifts unless low frequency spectral content is filtered out. In the case of the experimental hardware, it is extremely important to get the fundamental (low) frequency modes of vibration and any filtering would need to be performed real-time for use in the control scheme. The use of a finite impulse response filter could be designed to avoid introduction of phasing, but not implementable real-time. The use of an infinite impulse response or analog filter could be used but higher order filters would be needed to provide a sharp enough cutoff to avoid attenuation of the low frequency modes.

For lab implementation, a second order high pass digital Butterworth filter with a cutoff frequency of .15 was used. This was necessary due to offsets in the accelerometer data and it added little phase shift into the fundamental modes. For this work, it was considered a reasonable approximation to use the measured acceleration data and it provided reasonable performance. For future work, it is recommended that direct position measurements be used that allow for very low frequency vibration measurement.

7.5.2 Hydraulics Effects

As discussed in Sections 6.4 and 7.2.1, it was assumed, and experimentally verified by open loop testing, the hydraulic actuators followed a model of the form of Equation 7-2. Figure 7-33 shows the commanded output from the PC (unitless) and the resulting joint response at a low frequency command. The response is very nearly like an integrator, as expected. The same comparison for a higher frequency commanded output is shown in Figure 7-34, which shows much poorer tracking at higher frequencies. The second order servovalve models and parameters in Table 7-1 do not predict this behavior. Second order servovalve models were noted by the vendor as being a good approximation at frequencies lower than 50 Hz [75,76]. However, the observed behavior indicates that a higher order system model is required for accuracy. Merritt [50] recommends a third or fourth order system model, depending on the accuracy of the model required. For future work it is recommended that higher order servovalve models be developed from system testing. Better high frequency response could then be obtained by developing phase compensators from the known models.

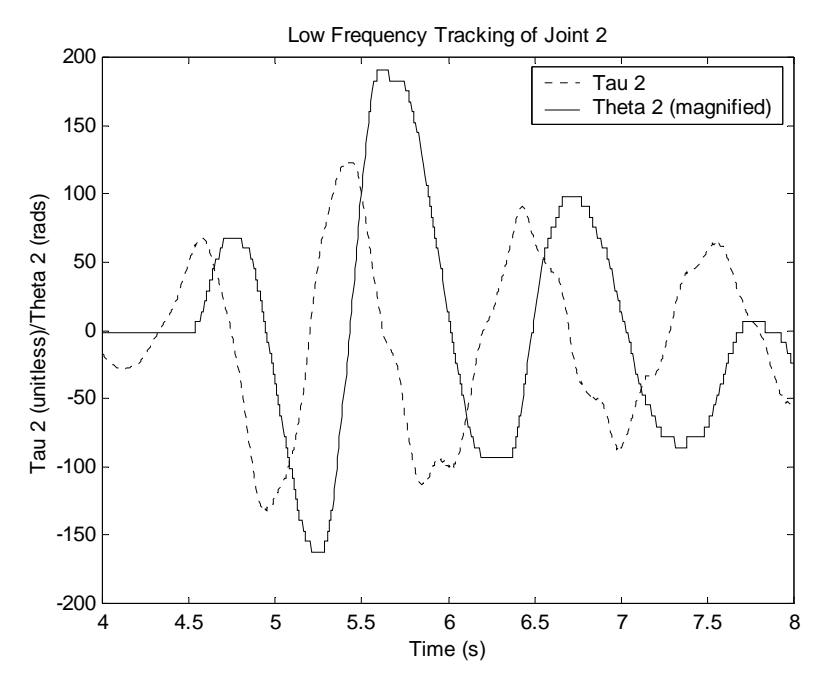


Figure 7-33 Low Frequency Tracking of Joint 2

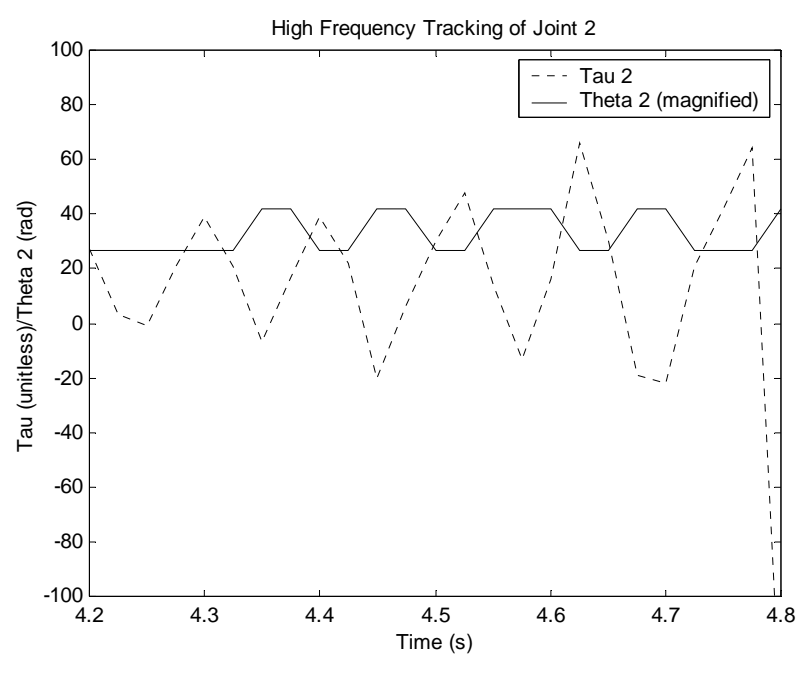


Figure 7-34 High Frequency Tracking of Joint 2

7.5.3 Joint Torque Effects

The vibration controller gives reasonably good performance in approximately half of the workspace. Whenever the robot is facing away from the macromanipulator, the controller does not function properly to remove energy from the system (Figure 7-35). This is due to a combination of two reasons. First, joint 1 provides a direct, amplified input into the torsional mode of the first link in these configurations. As discussed in Section 6.3.2, when the interaction torques are not considered it makes little difference in the controller performance in some workspace configurations. However, in the configuration shown in Figure 7-35, the interaction torques have a much greater effect on the performance of the vibration controller and should be included in the controller. This effect is magnified even more on the testbed due to the additional leverage provided by the second flexible link. Given the mode shape equation in 3-9, the torsional mode shape is largest at the tip of the beam, hence application of the torque here has the greatest effect in exciting it. This direct excitation combined with poor high frequency tracking, as discussed in Sections 6.4 and 7.5.2, rendered these configurations unusable for active damping on the current testbed.

As an example, consider the top view of the macro/micromanipulator shown at the bottom of Figure 7-35. The figure on the left shows a configuration of poor inertial damping performance, while the figure on the right shows a configuration in which the controller performed better. Recall the generalized forces due to the micromanipulator are given by equation 3-17. In the case on the left, the interaction forces remove vibrational energy from the system, but the torques may add energy. In the case on the

right, both the interaction forces and torques remove vibrational energy from the system.

This further reiterates the need for including interaction torques in the control scheme.

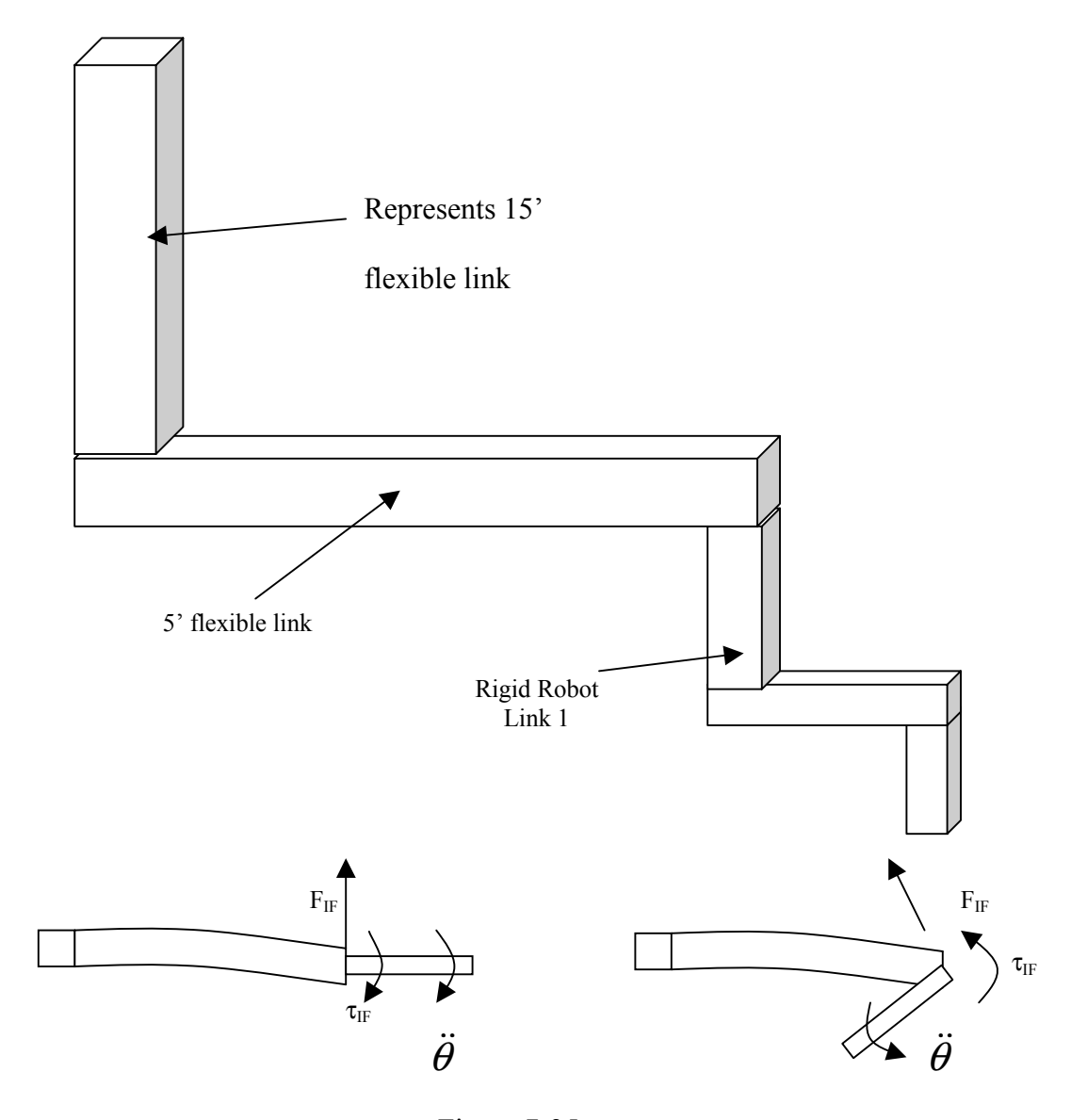


Figure 7-35
Testbed Configuration with Poor Inertial Damping Performance

CHAPTER VIII

CONCLUSIONS

7.1 Conclusions

This dissertation has developed, simulated, and demonstrated a position and enhanced vibration control scheme for a macro/micromanipulator. The analogous case of a rigid manipulator attached to a flexible but unactuated base was used to study the directly controllable inertial interaction forces and torques acting between the robot and its base. The "inertial singularities" in the joint workspace were investigated in detail, namely the regions where the robot loses its ability to create interactions in one or more degrees of freedom. A performance index was developed to predict the ability of the robot to generate interactions and can be used to ensure the robot operates in joint space configurations favorable for inertial damping. It was shown that when this is used along with the appropriate choice of vibration control feedback gains, the inertia effects, or those directly due to accelerating the links of the robot, have the greatest influence on the interactions. By commanding the link accelerations proportional to the base vibration, energy will be removed from the system. The vibration control signal is added to the position control signal. Simulated and measured interaction forces and torques generated at the base of a rigid robot were compared to verify conclusions drawn about the

controllable interactions. In addition, simulation and experimental results demonstrated the combined position control and vibration damping ability of the scheme.

The true contributions began in Chapter 4 with a detailed discussion of the controllable interaction force and torques. A performance measure was introduced which predicts the effectiveness of the rigid robot in creating these interactions. The rigid inertia effects $(B_f, B_{\tau 0})$ were studied in more detail and the "inertial singularities" investigated. It was pointed out that these singularities are, in general, different from the kinematic singularities. However, since the variation in performance is governed by the joint space configuration of the rigid robot, the performance measure could be used to quickly assess predicted inertial damping performance at the multiple inverse kinematic joint space solutions and used to operate the rigid robot in configurations better suited for inertial damping.

The inertia effects dominate the interactions in most non-singular configurations, but in certain cases, the nonlinear rigid effects may also become significant and these cases are discussed. The control scheme was discussed in Chapter 5. The vibration controller requires an inverse dynamics function to cancel the most important coupled interaction effects. Guidelines on choosing controller gains to ensure the inertia effects are the dominant terms were presented.

Simulation results were presented in Chapter 6 demonstrating vibration damping of a three degree of freedom anthropomorphic robot mounted on a flexible base. Simulations demonstrating disturbance rejection as well as the use of the performance index in predicting better joint space configurations for vibration damping during commanded

motion were included. Chapter 7 discussed the experimental testbed and presented results from two areas of testing. The first was verification of the interaction force and torque effects and work discussed in Chapter 4. The second was implementation of the vibration control scheme on a multi-degree of freedom experimental testbed. Although there were problems that arose with damping in certain workspace configurations, in most of the workspace the vibration controller performed well to remove energy from the system. This included both disturbance rejection as well as vibration control during commanded movements. Finally, implementation issues were discussed.

7.2 Contributions

Contributions of this work are:

- Extension of the macro/micromanipulator control problem to multiple degrees of freedom by considering the analogous problem of a rigid manipulator mounted on a flexible base.
- 2. Detailed investigation of inertial singularities and variation in performance throughout the workspace and development of a performance measure that predicts the ability of the micromanipulator to effectively damp base vibration using an inertial damping scheme.
- 3. Development of a control scheme that provides active base vibration damping in parallel with rigid robot position control. This includes the use of the performance index to improve the vibration damping capability of the micromanipulator given a desired end point position and establishing appropriate limits on control gains.

- 4. Verification of the above control scheme via simulation
- 5. Verification of the above control scheme via experimental work. This included verification of the accuracy of the interaction force and torque predictions and demonstration of the effectiveness of the control scheme on a realistic multi-degree of freedom testbed.

This work primarily builds on that performed previously by Lee [11,33], Cannon [15,16], Loper [12,42], and Lew [34-40]. This extends their work to include some concepts introduced in space robotics research by Papadopoulos, Evangelos, and Dubowsky [56] and Torres and Dubowsky [77-79]. In particular, this is the first work to develop the complete interaction forces and torque effects for a macro/micromanipulator and investigate the variation in performance throughout the workspace. In addition, this is the first work to introduce "inertial singularities," determine when and why they occur, and propose a solution to work around them. This is also the first work to consider multiple modes of vibration and propose control gain limits to ensure overall energy removal from the system. Finally, this is the first work demonstrating multiple-degrees of freedom of vibration damping on an experimental testbed, involving multiple joints actuating cooperatively for vibration damping. Although the scheme could not be shown to be effective in all configurations, mainly due to implementation issues and simplifying assumptions made to scale the inverse dynamics function to an implementable level, this work demonstrates a clear contribution to the field.

7.3 Recommendations for Future Research

There are many areas of research that could be further investigated including implementation issues that were discussed in section 7.5. As noted in Chapters 6 and 7 a more reasonable method of modeling the interaction torque effects is needed. The algorithm described in Section 4.4 allowed for a much easier derivation of the interaction forces than the symbolic method described in Section 3.3, but a similar method was not found for the interaction torques. Mainly, the length of the interaction torque equations, detailed in Section A.1.2 for the three degree of freedom case, made simulating and studying them in detail cumbersome and unimplementable in practice. More work needs to be done in this area, either to discover a much more efficient method of deriving expressions for the interaction torques or eliminating effects that are less important.

The use of input shaping in combination with an inertial damping control scheme is an area worthy of future research. Input shaping techniques are effective at reducing the amplitude of vibration induced by commanded movements but typically do not add damping to the system. This becomes particularly noticeable in an example such as that shown in section 6.3.4 and 7.4.2, where damping was compared for commanded rigid robot movement with and without inertial damping. If implemented with input shaping, vibration created by motion of the robot itself would be reduced and, assuming the robot is operating in a region of predicted good performance, the controller could still provide disturbance rejection. Hence, the combination of the two schemes should provide the best performance for both commanded movement vibration control as well as disturbance rejection.

Another area worthy of future research is the effect of implementation of the control scheme on a digital controller. Simulations as well as experimental work were performed using continuous system theory. Implementation involved real-time calculation of the control signals during each control loop, based on sampling the appropriate control signals (positions and accelerations). However, with increased computation time, which will occur especially if interaction torques are included, sample and hold effects as well as finite precision effects may become more of an issue.

Another area that should be considered is implementation of the proposed controller with a macromanipulator at varying joint angles. This would change the natural frequencies and damping ratios of the modes of vibration, as well as the orientation of the applied interaction forces. The proposed controller should theoretically apply as long as the frequency of vibration is measurable, but other unforeseen problems could occur.

As discussed in section 6.3.1, vibration control performance is not as efficient in regions of high nonlinear effects when higher modes exist in the system, which requires lower control gains. Performance could possibly be improved by canceling those effects in the vibration control scheme or using some alternate controller form. Another area of future research should consider the effect of contact on the tip of the micromanipulator. The work performed thus far assumes no contact on the system, whereas the more general case would likely involve contact by the micromanipulator. Appropriate modifications to the controller and/or inverse dynamics function may be necessary in these cases.

APPENDIX A

EQUATIONS OF MOTION

For completeness, this appendix includes the symbolic form of the fully coupled equations of motion for the anthropomorphic robot as well as some of the more important equations for the other configurations studied in this work. As discussed in chapter four, some of these effects are more significant than others. The general form of the interaction forces and torques and notation used is:

$$\begin{split} \mathbf{F}_{IF} &= B_{f}(\boldsymbol{\theta}) \begin{bmatrix} \dot{\theta}_{1} \\ \dot{\theta}_{2} \\ \dot{\theta}_{3} \end{bmatrix} + N_{Rf}(\boldsymbol{\theta}) \begin{bmatrix} \dot{\theta}_{1} \dot{\theta}_{2} \\ \dot{\theta}_{1} \dot{\theta}_{3} \\ \dot{\theta}_{2} \dot{\theta}_{3} \end{bmatrix} + N_{Cf}(\boldsymbol{\theta}) \begin{bmatrix} \dot{\theta}_{1}^{2} \\ \dot{\theta}_{2}^{2} \\ \dot{\theta}_{3}^{2} \end{bmatrix} + G_{f}(\boldsymbol{\theta}) + A_{f} \begin{bmatrix} \ddot{x} \\ \ddot{y} \\ \ddot{z} \end{bmatrix} + N_{RCf}(\boldsymbol{\theta}) \begin{bmatrix} \dot{\theta}_{x} \dot{\theta}_{y} \\ \dot{\theta}_{x} \dot{\theta}_{z} \\ \dot{\theta}_{y} \dot{\theta}_{z} \end{bmatrix} + N_{CCf}(\boldsymbol{\theta}) \begin{bmatrix} \dot{\theta}_{x}^{2} \\ \dot{\theta}_{y}^{2} \\ \dot{\theta}_{z}^{2} \end{bmatrix} \\ &+ B_{wf}(\boldsymbol{\theta}) \begin{bmatrix} \ddot{\theta}_{x} \\ \ddot{\theta}_{y} \\ \ddot{\theta}_{y} \end{bmatrix} + N_{CMf}(\boldsymbol{\theta}) \begin{bmatrix} \dot{\theta}_{1} \dot{\theta}_{x} & \dot{\theta}_{1} \dot{\theta}_{y} & \dot{\theta}_{1} \dot{\theta}_{z} & \dot{\theta}_{2} \dot{\theta}_{x} & \dot{\theta}_{2} \dot{\theta}_{y} & \dot{\theta}_{2} \dot{\theta}_{z} & \dot{\theta}_{3} \dot{\theta}_{x} & \dot{\theta}_{3} \dot{\theta}_{y} & \dot{\theta}_{3} \dot{\theta}_{z} \end{bmatrix}^{T} \\ &\mathbf{\tau}_{IF} = B_{\tau 0}(\boldsymbol{\theta}, \ddot{\boldsymbol{\theta}}) + N_{R\tau 0}(\boldsymbol{\theta}, \dot{\theta}_{i} \dot{\theta}_{j}) + N_{C\tau 0}(\boldsymbol{\theta}, \dot{\theta}_{i}^{2}) + G_{\tau 0}(\boldsymbol{\theta}) + A_{\tau 0}(\boldsymbol{\theta}, \ddot{\mathbf{q}}) + N_{RC\tau 0}(\boldsymbol{\theta}, \dot{\theta}_{k} \dot{\theta}_{l}) + N_{CC\tau 0}(\boldsymbol{\theta}, \dot{\theta}_{k}^{2}) \\ &+ B_{w\tau 0}(\boldsymbol{\theta}, \ddot{\boldsymbol{\theta}}_{k}) + N_{CM\tau 0}(\boldsymbol{\theta}, \dot{\theta}_{i} \dot{\boldsymbol{\theta}}_{k}) \\ &\mathbf{\tau} = B_{\tau}(\boldsymbol{\theta}, \ddot{\boldsymbol{\theta}}_{k}) + N_{R\tau}(\boldsymbol{\theta}, \dot{\theta}_{i} \dot{\boldsymbol{\theta}}_{j}) + N_{C\tau}(\boldsymbol{\theta}, \dot{\theta}_{i}^{2}) + G_{\tau}(\boldsymbol{\theta}) + A_{\tau}(\boldsymbol{\theta}, \ddot{\mathbf{q}}) + N_{RC\tau}(\boldsymbol{\theta}, \dot{\theta}_{k} \dot{\boldsymbol{\theta}}_{l}) + N_{CC\tau}(\boldsymbol{\theta}, \dot{\theta}_{k}^{2}) \\ &+ B_{w\tau}(\boldsymbol{\theta}, \ddot{\boldsymbol{\theta}}_{k}) + N_{CM\tau}(\boldsymbol{\theta}, \dot{\boldsymbol{\theta}}_{i} \dot{\boldsymbol{\theta}}_{k}) \end{split}$$

where:

B matrices are rigid body inertia-like matrices (B_{τ} is the inertia matrix)

N_R matrices are rigid body coriolis effects

N_C matrices are rigid body centrifugal effects

G matrices are rigid body gravity effects

A are flexible body inertia matrices (due to base acceleration)

N_{RC} are flexible body coriolis effects (due to base rotational velocities)

N_{CC} are flexible body centrifugal effects (due to base rotational velocities)

B_W are flexible body rotational inertia matrices (due to base rotational accelerations)

N_{CM} are cross coupling effects due to both joint velocities and base rotational velocities

This notation will be used for all robot configurations studied in this work. As discussed in Chapter 3, equations were derived from a Matlab m-file using a Newton Euler method. Due to their length and complexity, great pain was taken to find forms that are more useful for the critical rigid and flexible inertia and nonlinear rigid effects. However, due to the complexity of the equations this was only done for the some of the equations. The remainder are included in the general ("simple" format) form provided by Matlab.

A.1 Three Degree of Freedom Anthropomorphic Robot

The anthropomorphic robot configuration used here is similar to that used in experimental work. The same link parameters and Denavit-Hartenberg parameters were used as for the actual robot and the parameters are defined Figure 4-1. Notice the alternate definition of joint angle two. This was chosen because software code was already written to control the robot using these parameters and it avoided numerous changes to the software code. The Denavit and Hartenberg parameters are shown in Table A-1.

Table A-1
Denavit-Hartenberg Parameters for Anthropomorphic Robot

| Link | a_{i} | $\alpha_{\rm i}$ | di | $\mathbf{\theta}_{\mathrm{i}}$ |
|------|---------|------------------|-------|--------------------------------|
| 0 | 0 | 0 | d_0 | inert |
| 1 | 0 | $\pi/2$ | d_1 | θ_1 |
| 2 | a_2 | 0 | 0 | θ_2 |
| 3 | a_3 | 0 | 0 | θ_3 |

Rotation Matrices

$$R_{1}^{0} = \begin{bmatrix} \cos(\theta_{1}) & 0 & \sin(\theta_{1}) \\ \sin(\theta_{1}) & 0 & -\cos(\theta_{1}) \\ 0 & 1 & 0 \end{bmatrix}$$

$$R_{2}^{1} = \begin{bmatrix} \cos(\theta_{2}) & -\sin(\theta_{2}) & 0 \\ \sin(\theta_{2}) & \cos(\theta_{2}) & 0 \\ 0 & 0 & 1 \end{bmatrix}$$

$$R_{3}^{2} = \begin{bmatrix} \cos(\theta_{3}) & -\sin(\theta_{3}) & 0 \\ \sin(\theta_{3}) & \cos(\theta_{3}) & 0 \\ 0 & 0 & 1 \end{bmatrix}$$
(A-2)

It will be useful to define some constants to help simplify the equations of motion:

$$A = m_{2}r_{2} + m_{3}a_{2}$$

$$B = m_{3}r_{3}$$

$$D = d_{0} + d_{1}$$

$$E = m_{3}r_{3}^{2}$$

$$F = m_{3}a_{2}$$

$$G = I_{2xx} - I_{2yy}$$

$$H = I_{2zz} + I_{3zz}$$

$$J = -(I_{3xx} - I_{3yy})$$

$$K = m_{2}r_{2}^{2} + m_{3}a_{2}^{2}$$

$$L = I_{1yy} + I_{2xx} + I_{3yy}$$

$$M = m_0 + m_1 + m_2 + m_3$$

$$N = m_3 a_2 r_3$$

$$O = m_0 r_0 + m_1 (d_0 + r_1) + (m_2 + m_3) D$$

$$P = -I_{1xx} + I_{1zz} + I_{2zz} + I_{3zz}$$

$$Q = I_{2xx} + I_{2yy} + I_{3xx} + I_{3yy}$$
(A-3)

Postion Vector to CG

$$\mathbf{r}_{CG} = \frac{1}{M} \begin{bmatrix} c_1 (Ac_2 + Bc_{23}) \\ s_1 (Ac_2 + Bc_{23}) \\ O + As_2 + Bs_{23} \end{bmatrix}$$
 (A-4)

A.1.1 Interaction Force Effects

Rigid Inertia Forces

$$B_{f} = \begin{bmatrix} -s_{1}(Ac_{2} + Bc_{23}) & -c_{1}(As_{2} + Bs_{23}) & -Bc_{1}s_{23} \\ c_{1}(Ac_{2} + Bc_{23}) & -s_{1}(As_{2} + Bs_{23}) & -Bs_{1}s_{23} \\ 0 & Ac_{2} + Bc_{23} & Bc_{23} \end{bmatrix}$$

$$|B_{f}| = -ABs_{3}(Ac_{2} + Bc_{23})$$
(A-5)

Rigid Coriolis Forces

$$N_{Rf} = \begin{bmatrix} 2s_1(As_2 + Bs_{23}) & 2Bs_1s_{23} & -2Bc_1c_{23} \\ -2c_1(As_2 + 2Bs_{23}) & -2Bc_1s_{23} & -2Bs_1c_{23} \\ 0 & 0 & -2Bs_{23} \end{bmatrix}$$
(A-6)

Rigid Centrifugal Forces

$$N_{Cf} = \begin{bmatrix} -c_1(Ac_2 + Bc_{23}) & -c_1(Ac_2 + Bc_{23}) & -Bc_1c_{23} \\ -s_1(Ac_2 + Bc_{23}) & -s_1(Ac_2 + Bc_{23}) & -Bs_1c_{23} \\ 0 & -(As_2 + Bs_{23}) & -Bs_{23} \end{bmatrix}$$
(A-7)

Rigid Gravitational Forces

$$G_f = \begin{bmatrix} 0 \\ 0 \\ Mg \end{bmatrix} \tag{A-8}$$

Flexible Body Inertia Forces

$$A_f = \begin{bmatrix} M & 0 & 0 \\ 0 & M & 0 \\ 0 & 0 & M \end{bmatrix}$$
 (A-9)

Flexible Body Coriolis Forces

$$N_{RCf}(1,1) = s_1(Ac_2 + Bc_{23})$$

$$N_{RCf}(1,2) = O + As_2 + Bs_{23}$$

$$N_{RCf}(1,3) = N_{RCf}(2,2) = N_{RCf}(3,1) = 0$$

$$N_{RCf}(2,1) = c_1(Ac_2 + Bc_{23})$$

$$N_{RCf}(2,3) = O + As_2 + Bs_{23}$$

$$N_{RCf}(3,2) = c_1(Ac_2 + Bc_{23})$$

$$N_{RCf}(3,3) = s_1(Ac_2 + Bc_{23})$$

$$N_{RCf}(3,3) = s_1(Ac_2 + Bc_{23})$$
(A-10)

Flexible Body Centipetal Forces

$$\begin{split} N_{CCf}(1,1) &= N_{CCf}(2,2) = N_{CCf}(3,3) = 0 \\ N_{CCf}(1,2) &= -c_1(Ac_2 + Bc_{23}) \\ N_{CCf}(1,3) &= -c_1(Ac_2 + Bc_{23}) \\ N_{CCf}(2,1) &= -s_1(Ac_2 + Bc_{23}) \\ N_{CCf}(2,3) &= -s_1(Ac_2 + Bc_{23}) \\ N_{CCf}(3,1) &= -(O + As_2 + Bs_{23}) \\ N_{CCf}(3,2) &= -(O + As_2 + Bs_{23}) \end{split}$$
(A-11)

Flexible Body Rotational Inertia Forces

$$B_{v,f}(1,1) = B_{v,f}(2,2) = B_{v,f}(3,3) = 0$$

$$B_{v,f}(1,2) = O + As_2 + Bs_{23}$$

$$B_{v,f}(1,3) = -s_1(Ac_2 + Bc_{23})$$

$$B_{v,f}(2,1) = -(O + As_2 + Bs_{23})$$

$$B_{v,f}(2,3) = c_1(Ac_2 + Bc_{23})$$

$$B_{v,f}(3,1) = s_1(Ac_2 + Bc_{23})$$

$$B_{v,f}(3,2) = -c_1(Ac_2 + Bc_{23})$$
(A-12)

Cross Coupling Force Effects

$$N_{CMf} = \begin{bmatrix} 0 & 0 & 2c_1(Ac_2 + Bc_{23}) \\ 0 & 0 & 2s_1(Ac_2 + Bc_{23}) \\ -2c_1(Ac_2 + Bc_{23}) & -2s_1(Ac_2 + Bc_{23}) & 0 \\ 0 & -2(Ac_2 + Bc_{23}) & -2s_1(As_2 + Bs_{23}) \\ 2(Ac_2 + Bc_{23}) & 0 & 2c_1(As_2 + Bs_{23}) \\ 2s_1(As_2 + Bs_{23}) & -2c_1(As_2 + Bs_{23}) & 0 \\ 0 & -2Bc_{23} & -2Bs_1s_{23} \\ 2Bc_{23} & 0 & 2Bc_1s_{23} \\ 2Bs_1s_{23} & -2Bc_1s_{23} & 0 \end{bmatrix}$$

$$(A-13)$$

A.1.2. Interaction Torque Effects

Rigid Inertia Interaction Torques

$$B_{\tau 0}(1,1) = c_{1}\{-2c_{2}s_{23}[c_{3}(E+J)+Ba_{2}]+(E+J)(s_{2}c_{2}+s_{3}c_{3})+B(a_{2}s_{3}-Dc_{23})+(G-K)s_{2}c_{2}-ADc_{2}\}$$

$$B_{\tau 0}(1,2) = s_{1}\{B(2a_{2}c_{3}+Ds_{23})+ADs_{2}+(E+H+K)\}$$

$$B_{\tau 0}(1,3) = s_{1}\{B(a_{2}c_{3}+Ds_{23})+E+I_{3zz}\}$$

$$B_{\tau 0}(2,1) = s_{1}\{-2c_{2}s_{23}[c_{3}(E+J)+Ba_{2}]+(E+J)(s_{2}c_{2}+s_{3}c_{3})+B(a_{2}s_{3}-Dc_{23})+(G-K)s_{2}c_{2}-ADc_{2}\}$$

$$B_{\tau 0}(2,2) = -c_{1}\{B(2a_{2}c_{3}+Ds_{23})+ADs_{2}+(E+H+K)\}$$

$$B_{\tau 0}(2,3) = -c_{1}\{B(a_{2}c_{3}+Ds_{23})+(E+I_{3zz})\}$$

$$B_{\tau 0}(3,1) = 2c_{2}c_{23}[c_{3}(E+J)+Ba_{2}]-(E+J)(c_{2}^{2}+c_{3}^{2})+(K-G)c_{2}^{2}+E+L$$

$$B_{\tau 0}(3,2) = B_{\tau 0}(3,3) = 0$$
(A-14)

Rigid Coriolis Interaction Torques

$$NR_{\tau 0}(1,1) = c_{1}\{-4c_{2}c_{23}[c_{3}(E+J)+Ba_{2}]+2(E+J)(c_{2}^{2}+c_{3}^{2})+2B(2a_{2}c_{3}+Ds_{23}) +2(G-K)c_{2}^{2}+2ADs_{2}+2K+H-G-J\}$$

$$NR_{\tau 0}(1,2) = c_{1}\{-2c_{2}c_{23}[2c_{3}(E+J)+Ba_{2}]+2(E+J)(c_{2}^{2}+c_{3}^{2})+2B(a_{2}c_{3}+Ds_{23}) -J+I_{3zz}\}$$

$$NR_{\tau 0}(1,3) = -2Bs_{1}\{a_{2}s_{3}-Dc_{23}\}$$

$$NR_{\tau 0}(2,1) = s_{1}\{-4c_{2}c_{23}[c_{3}(E+J)+Ba_{2}]+2(E+J)(c_{2}^{2}+c_{3}^{2})+2B(2a_{2}c_{3}+Ds_{23}) +2(G-K)c_{2}^{2}+2ADs_{2}+2K+H-G-J\}$$

$$NR_{\tau 0}(2,2) = s_{1}\{-2c_{2}c_{23}[2c_{3}(E+J)+Ba_{2}]+2(E+J)(c_{2}^{2}+c_{3}^{2})+2B(a_{2}c_{3}+Ds_{23}) -J+I_{3zz}\}$$

$$NR_{\tau 0}(2,3) = 2Bc_{1}\{a_{2}s_{3}-Dc_{23}\}$$

$$NR_{\tau 0}(3,1) = 2\{-2c_{2}s_{23}[c_{3}(E+J)+Ba_{2}]+(E+J)(s_{2}c_{2}+s_{3}c_{3})+Ba_{2}s_{3}+(G-K)s_{2}c_{2}\}$$

$$NR_{\tau 0}(3,2) = 2\{-c_{2}s_{23}[2c_{3}(E+J)+Ba_{2}]+(E+J)(s_{2}c_{2}+s_{3}c_{3})\}$$

$$NR_{\tau 0}(3,3) = 0$$

$$(A-15)$$

Rigid Centrifugal Interaction Torques

$$\begin{split} N_{C\tau 0}(1,1) &= s_1 \{ 2c_2 s_{23} [c_3(E+J) + Ba_2] - (E+J)(s_2 c_2 + s_3 c_3) - B(a_2 s_3 - Dc_{23}) \\ &- (G-K) s_2 c_2 + ADc_2 \} \\ N_{C\tau 0}(1,2) &= Ds_1 \{ Ac_2 + Bc_{23} \} \\ N_{C\tau 0}(1,3) &= -Bs_1 \{ a_2 s_3 - Dc_{23} \} \\ N_{C\tau 0}(2,1) &= c_1 \{ -2c_2 s_{23} [c_3(E+J) + 2Ba_2] + (E+J)(s_2 c_2 + s_3 c_3) + B(a_2 s_3 - Dc_{23}) \\ &+ (G-K) s_2 c_2 - ADc_2 \} \\ N_{C\tau 0}(2,2) &= -Dc_1 \{ Bc_{23} + Ac_2 \} \\ N_{C\tau 0}(2,3) &= Bc_1 \{ a_2 s_3 - Dc_{23} \} \\ N_{C\tau 0}(3,1) &= N_{C\tau 0}(3,2) = N_{C\tau 0}(3,3) = 0 \end{split} \tag{A-16}$$

Rigid Gravitational Interaction Torques

$$G_{\tau 0} = \begin{bmatrix} g \, \mathbf{s}_1 (A c_2 + B c_{23}) \\ -g c_1 (A c_2 + B c_{23}) \\ 0 \end{bmatrix}$$
 (A-17)

Flexible Body Inertia Interaction Torques

$$A_{\tau 0} = \begin{bmatrix} 0 & -(O + As_2 + Bs_{23}) & s_1(Ac_2 + Bc_{23}) \\ O + As_2 + Bs_{23} & 0 & -c_1(Ac_2 + Bc_{23}) \\ -s_1(Ac_2 + Bc_{23}) & c_1(Ac_2 + Bc_{23}) & 0 \end{bmatrix}$$
(A-18)

Flexible Body Coriolis Interaction Torques

```
NRC_{\tau 0}(1,1) = -\cos(th1)*(\cos(th2)*I2yy*\sin(th2)-\sin(th2)*I2xx*\cos(th2)+\cos(th2)*I3xx*\sin(th2)
 -m3*sin(th3)*sin(th2)*rc3*d1+sin(th2)*m2*cos(th2)*rc2^2+m3*cos(th3)*cos(th2)*rc3*d1+sin(th2)*rc3*d1+sin(th2)*rc3*d1+sin(th2)*rc3*d1+sin(th2)*rc3*d1+sin(th2)*rc3*d1+sin(th2)*rc3*d1+sin(th2)*rc3*d1+sin(th2)*rc3*d1+sin(th2)*rc3*d1+sin(th2)*rc3*d1+sin(th2)*rc3*d1+sin(th2)*rc3*d1+sin(th2)*rc3*d1+sin(th2)*rc3*d1+sin(th2)*rc3*d1+sin(th2)*rc3*d1+sin(th2)*rc3*d1+sin(th2)*rc3*d1+sin(th2)*rc3*d1+sin(th2)*rc3*d1+sin(th2)*rc3*d1+sin(th2)*rc3*d1+sin(th2)*rc3*d1+sin(th2)*rc3*d1+sin(th2)*rc3*d1+sin(th2)*rc3*d1+sin(th2)*rc3*d1+sin(th2)*rc3*d1+sin(th2)*rc3*d1+sin(th2)*rc3*d1+sin(th2)*rc3*d1+sin(th2)*rc3*d1+sin(th2)*rc3*d1+sin(th2)*rc3*d1+sin(th2)*rc3*d1+sin(th2)*rc3*d1+sin(th2)*rc3*d1+sin(th2)*rc3*d1+sin(th2)*rc3*d1+sin(th2)*rc3*d1+sin(th2)*rc3*d1+sin(th2)*rc3*d1+sin(th2)*rc3*d1+sin(th2)*rc3*d1+sin(th2)*rc3*d1+sin(th2)*rc3*d1+sin(th2)*rc3*d1+sin(th2)*rc3*d1+sin(th2)*rc3*d1+sin(th2)*rc3*d1+sin(th2)*rc3*d1+sin(th2)*rc3*d1+sin(th2)*rc3*d1+sin(th2)*rc3*d1+sin(th2)*rc3*d1+sin(th2)*rc3*d1+sin(th2)*rc3*d1+sin(th2)*rc3*d1+sin(th2)*rc3*d1+sin(th2)*rc3*d1+sin(th2)*rc3*d1+sin(th2)*rc3*d1+sin(th2)*rc3*d1+sin(th2)*rc3*d1+sin(th2)*rc3*d1+sin(th2)*rc3*d1+sin(th2)*rc3*d1+sin(th2)*rc3*d1+sin(th2)*rc3*d1+sin(th2)*rc3*d1+sin(th2)*rc3*d1+sin(th2)*rc3*d1+sin(th2)*rc3*d1+sin(th2)*rc3*d1+sin(th2)*rc3*d1+sin(th2)*rc3*d1+sin(th2)*rc3*d1+sin(th2)*rc3*d1+sin(th2)*rc3*d1+sin(th2)*rc3*d1+sin(th2)*rc3*d1+sin(th2)*rc3*d1+sin(th2)*rc3*d1+sin(th2)*rc3*d1+sin(th2)*rc3*d1+sin(th2)*rc3*d1+sin(th2)*rc3*d1+sin(th2)*rc3*d1+sin(th2)*rc3*d1+sin(th2)*rc3*d1+sin(th2)*rc3*d1+sin(th2)*rc3*d1+sin(th2)*rc3*d1+sin(th2)*rc3*d1+sin(th2)*rc3*d1+sin(th2)*rc3*d1+sin(th2)*rc3*d1+sin(th2)*rc3*d1+sin(th2)*rc3*d1+sin(th2)*rc3*d1+sin(th2)*rc3*d1+sin(th2)*rc3*d1+sin(th2)*rc3*d1+sin(th2)*rc3*d1+sin(th2)*rc3*d1+sin(th2)*rc3*d1+sin(th2)*rc3*d1+sin(th2)*rc3*d1+sin(th2)*rc3*d1+sin(th2)*rc3*d1+sin(th2)*rc3*d1+sin(th2)*rc3*d1+sin(th2)*rc3*d1+sin(th2)*rc3*d1+sin(th2)*rc3*d1+sin(th2)*rc3*d1+sin(th2)*rc3*d1+sin(th2)*rc3*d1+sin(th2)*rc3*d1+sin(th2)*rc3*d1+sin(th2)*rc3*d1+sin(th2)*rc3*d1+sin(th2)
+2*sin(th2)*m3*rc3^2*cos(th3)^2*cos(th2)-sin(th2)*sin(th3)*m3*rc3*d0
+2*m3*cos(th2)*rc3*cos(th3)*sin(th2)*a2+cos(th2)*cos(th3)*m3*rc3*d0
+2*cos(th3)*m3*rc3^2*sin(th3)*cos(th2)^2-sin(th2)*I3yy*cos(th2)-a2*rc3*sin(th3)*m3
-2*\cos(th3)*I3xx*\sin(th3)*\cos(th2)^2-2*\sin(th2)*I3xx*\cos(th3)^2*\cos(th2)
+2*sin(th2)*I3vy*cos(th2)*cos(th3)^2+m3*cos(th2)*a2*d0+m2*cos(th2)*rc2*d1
-\cos(th2)*m3*rc3^2*\sin(th2)+\cos(th2)*m2*rc2*d0+\sin(th2)*m3*\cos(th2)*a2^2
+m3*cos(th2)*a2*d1+2*sin(th3)*I3yy*cos(th3)*cos(th2)^2-sin(th3)*rc3^2*m3*cos(th3)
 -\cos(th3)*I3yy*\sin(th3)+2*m3*\sin(th3)*rc3*a2*\cos(th2)^2+\sin(th3)*I3xx*\cos(th3)
NRC_{\tau 0}(1,2) = -\cos(th1) * \sin(th1) * (-m3 * rc3^2 + I3xx + I2yy - I3xx * \cos(th3)^2 - I3xx * \cos(th2)^2
+13yy*\cos(th2)^2+13yy*\cos(th3)^2+m3*rc3^2*\cos(th2)^2+m3*rc3^2*\cos(th3)^2-m2*\cos(th2)^2+rc2^2
-2*I3vv*cos(th3)^2*cos(th2)^2-m3*a2^2*cos(th2)^2-I2vv*cos(th2)^2-2*m3*rc3^2*cos(th3)^2*cos(th2)^2
+cos(th2)^2*I2xx+2*cos(th2)*sin(th3)*m3*rc3*sin(th2)*a2+2*cos(th2)*cos(th3)*I3vv*sin(th3)*sin(th2)
-2*\cos(th2)*\sin(th3)*I3xx*\cos(th3)*\sin(th2)+2*I3xx*\cos(th3)^2*\cos(th2)^2
+2*cos(th2)*sin(th3)*m3*rc3^2*cos(th3)*sin(th2)-2*m3*rc3*cos(th3)*cos(th2)^2*a2+I1xx-I3zz-I2zz-
I1zz)
NRC_{\tau 0}(1,3) = -2*rc1*m1*d0+3/4*I3yy*cos(2*th3+2*th2)+3/4*m3*a2^2*cos(2*th2)-I0yy-2*m3*d0*d1*a12*th2+3/4*m3*a2^2*cos(2*th2)-I0yy-2*m3*d0*d1*a12*th2+3/4*m3*a2^2*cos(2*th2)-I0yy-2*m3*d0*d1*a12*th2+3/4*m3*a2^2*cos(2*th2)-I0yy-2*m3*d0*d1*a12*th2+3/4*m3*a2^2*cos(2*th2)-I0yy-2*m3*d0*d1*a12*th2+3/4*m3*a2^2*cos(2*th2)-I0yy-2*m3*d0*d1*a12*th2+3/4*m3*a2^2*cos(2*th2)-I0yy-2*m3*d0*d1*a12*th2+3/4*m3*a2^2*cos(2*th2)-I0yy-2*m3*d0*d1*a12*th2+3/4*m3*a2^2*cos(2*th2)-I0yy-2*m3*d0*d1*a12*th2+3/4*m3*a2^2*cos(2*th2)-I0yy-2*m3*d0*d1*a12*th2+3/4*m3*a2^2*cos(2*th2)-I0yy-2*m3*d0*d1*a12*th2+3/4*m3*a2^2*cos(2*th2)-I0yy-2*m3*d0*d1*a12*th2+3/4*m3*a2^2*cos(2*th2)-I0yy-2*m3*d0*d1*a12*th2+3/4*m3*a2^2*cos(2*th2)-I0yy-2*m3*d0*d1*a12*th2+3/4*m3*a2^2*cos(2*th2)-I0yy-2*m3*d0*d1*a12*th2+3/4*m3*a2^2*cos(2*th2)-I0yy-2*m3*d0*d1*a12*th2+3/4*m3*a2^2*cos(2*th2)-I0yy-2*m3*d0*d1*a12*th2+3/4*m3*a2^2*cos(2*th2)-I0yy-2*m3*d0*d1*a12*th2+3/4*m3*a2^2*cos(2*th2)-I0yy-2*m3*d0*d1*a12*th2+3/4*m3*a2^2*cos(2*th2)-I0yy-2*m3*d0*d1*a12*th2+3/4*m3*a2^2*cos(2*th2)-I0yy-2*m3*d0*d1*a12*th2+3/4*m3*a2^2*cos(2*th2)-I0yy-2*m3*d0*d1*a12*th2+3/4*m3*a2^2*cos(2*th2)-I0yy-2*m3*d0*d1*a12*th2+3/4*m3*a2^2*cos(2*th2)-I0yy-2*m3*d0*d1*a12*th2+3/4*m3*d0*d1*a12*th2+3/4*m3*d0*d1*a12*th2+3/4*m3*d0*d1*a12*th2+3/4*m3*d0*d1*a12*th2+3/4*m3*d0*d1*a12*th2+3/4*th2+3/4*th2+3/4*th2+3/4*th2+3/4*th2+3/4*th2+3/4*th2+3/4*th2+3/4*th2+3/4*th2+3/4*th2+3/4*th2+3/4*th2+3/4*th2+3/4*th2+3/4*th2+3/4*th2+3/4*th2+3/4*th2+3/4*th2+3/4*th2+3/4*th2+3/4*th2+3/4*th2+3/4*th2+3/4*th2+3/4*th2+3/4*th2+3/4*th2+3/4*th2+3/4*th2+3/4*th2+3/4*th2+3/4*th2+3/4*th2+3/4*th2+3/4*th2+3/4*th2+3/4*th2+3/4*th2+3/4*th2+3/4*th2+3/4*th2+3/4*th2+3/4*th2+3/4*th2+3/4*th2+3/4*th2+3/4*th2+3/4*th2+3/4*th2+3/4*th2+3/4*th2+3/4*th2+3/4*th2+3/4*th2+3/4*th2+3/4*th2+3/4*th2+3/4*th2+3/4*th2+3/4*th2+3/4*th2+3/4*th2+3/4*th2+3/4*th2+3/4*th2+3/4*th2+3/4*th2+3/4*th2+3/4*th2+3/4*th2+3/4*th2+3/4*th2+3/4*th2+3/4*th2+3/4*th2+3/4*th2+3/4*th2+3/4*th2+3/4*th2+3/4*th2+3/4*th2+3/4*th2+3/4*th2+3/4*th2+3/4*th2+3/4*th2+3/4*th2+3/4*th2+3/4*th2+3/4*th2+3/4*th2+3/4*th2+3/4
+3/4*m2*rc2^2*cos(2*th2)+3/4*m3*rc3^2*cos(2*th3+2*th2)-1/8*I2yy*cos(2*th1+2*th2)-2*m2*d0*d1
+1/4*I3xx*cos(2*th1)-1/8*I3xx*cos(2*th2-2*th1+2*th3)+1/8*I3xx*cos(2*th2+2*th1+2*th3)
-1/4*m3*a2^2*\cos(2*th1)-1/8*m3*a2^2*\cos(-2*th1+2*th2)-1/8*m3*a2^2*\cos(2*th1+2*th2)
+1/8*I2xx*cos(2*th1+2*th2)-1/8*I2yy*cos(-2*th1+2*th2)+1/8*I2xx*cos(-2*th1+2*th2)
+1/4*I2xx*cos(2*th1)-2*m2*rc2*d0*sin(th2)-2*m2*rc2*d1*sin(th2)-2*m3*a2*d0*sin(th2)
-2*m3*a2*d1*sin(th2)-1/2*m3*rc3*cos(th3)*a2-3/4*I2xx*cos(2*th2)+1/4*I3xx+1/4*I2vv+1/4*I3vv
-m0*rc0^2 + I1vy - 1/2*I2zz + 1/4*I2xx - 1/2*I3zz - 1/2*I1xx + I0zz - m1*rc1^2 - 1/4*m3*rc3^2 - 1/2*I1zz
-m3*d0^2-m1*d0^2-m3*d1^2-1/4*m3*a2^2-1/4*m2*rc2^2-m2*d0^2-m2*d1^2-1/4*m2*rc2^2-m2*d0^2-m2*d1^2-1/4*m2*rc2^2-m2*d0^2-m2*d1^2-1/4*m2*rc2^2-m2*d0^2-m2*d1^2-1/4*m2*rc2^2-m2*d0^2-m2*d1^2-1/4*m2*rc2^2-m2*d0^2-m2*d1^2-1/4*m2*rc2^2-m2*d0^2-m2*d1^2-1/4*m2*rc2^2-m2*d0^2-m2*d1^2-1/4*m2*rc2^2-m2*d0^2-m2*d1^2-1/4*m2*rc2^2-m2*d0^2-m2*d1^2-1/4*m2*rc2^2-m2*d0^2-m2*d1^2-1/4*m2*rc2^2-m2*d0^2-m2*d1^2-1/4*m2*rc2^2-m2*d0^2-m2*d1^2-1/4*m2*rc2^2-m2*d0^2-m2*d1^2-1/4*m2*rc2^2-m2*d0^2-m2*d1^2-1/4*m2*rc2^2-m2*d0^2-m2*d1^2-1/4*m2*rc2^2-m2*d0^2-m2*d1^2-1/4*m2*rc2^2-m2*d0^2-m2*d1^2-1/4*m2*rc2^2-m2*d0^2-m2*d1^2-1/4*m2*rc2^2-m2*d1^2-1/4*m2*rc2^2-m2*d1^2-1/4*m2*rc2^2-m2*d1^2-1/4*m2*rc2^2-m2*d1^2-1/4*m2*rc2^2-m2*d1^2-1/4*m2*rc2^2-m2*d1^2-1/4*m2*rc2^2-m2*d1^2-1/4*m2*rc2^2-m2*d1^2-1/4*m2*rc2^2-m2*d1^2-1/4*m2*rc2^2-m2*d1^2-1/4*m2*rc2^2-m2*d1^2-1/4*m2*rc2^2-m2*d1^2-1/4*m2*rc2^2-m2*d1^2-1/4*m2*rc2^2-m2*d1^2-1/4*m2*rc2^2-m2*d1^2-1/4*m2*rc2^2-m2*d1^2-1/4*m2*rc2^2-m2*d1^2-1/4*m2*rc2^2-m2*d1^2-1/4*m2*rc2^2-m2*d1^2-1/4*m2*rc2^2-m2*d1^2-1/4*m2*rc2^2-m2*d1^2-1/4*m2*rc2^2-m2*d1^2-1/4*m2*rc2^2-m2*d1^2-1/4*m2*rc2^2-m2*d1^2-1/4*m2*rc2^2-m2*d1^2-1/4*m2*rc2^2-m2*d1^2-1/4*m2*rc2^2-m2*d1^2-1/4*m2*rc2^2-m2*d1^2-1/4*m2*rc2^2-m2*d1^2-1/4*m2*rc2^2-m2*d1^2-1/4*m2*rc2^2-m2*d1^2-1/4*m2*rc2^2-m2*d1^2-1/4*m2*rc2^2-m2*d1^2-1/4*m2*rc2^2-m2*d1^2-1/4*m2*rc2^2-m2*d1^2-1/4*m2*rc2^2-m2*d1^2-1/4*m2*rc2^2-m2*d1^2-1/4*m2*rc2^2-m2*d1^2-1/4*m2*rc2^2-m2*d1^2-1/4*m2*rc2^2-m2*d1^2-1/4*m2*rc2^2-m2*d1^2-1/4*m2*rc2^2-m2*d1^2-1/4*m2*rc2^2-m2*d1^2-1/4*m2*rc2^2-m2*d1^2-1/4*m2*rc2^2-m2*d1^2-1/4*m2*rc2^2-m2*d1^2-1/4*m2*rc2^2-m2*d1^2-1/4*m2*rc2^2-m2*d1^2-1/4*m2*rc2^2-m2*d1^2-1/4*m2*rc2^2-m2*d1^2-1/4*m2*rc2^2-m2*d1^2-1/4*m2*rc2^2-m2*d1^2-1/4*m2*rc2^2-m2*d1^2-1/4*m2*rc2^2-m2*d1^2-1/4*m2*rc2^2-m2*d1^2-1/4*m2*rc2^2-m2*d1^2-1/4*m2*rc2^2-m2*d1^2-1/4*m2*d1^2-1/4*m2*d1^2-1/4*m2*d1^2-1/4*m2*d1^2-1/4*m2*d1^2-1/4*m2*d1^2-1/4*m2*d1^2-1/4*m2*d1^2-1/4*m2*d1^2-1/4*m2*d1^2-1/4*m2*d1^2-1/4*m2*d1^2-1/4*m2*d1^2-1/4*m2*d1^2-1/4*m2*d1^2-1/4*m2*d1^2-1/4*m2*d1^2-1/4*m2*d1^2-1/4*m2*d1^2-1/4*m2*d1^2-1/4*m2*d1^2-1/4*m2*
-1/4*m3*rc3^2*cos(2*th1)-1/8*I3yy*cos(2*th2-2*th1+2*th3)-1/8*I3yy*cos(2*th2+2*th1+2*th3)
+1/4*I3yy*cos(2*th1)-1/4*m2*rc2^2*cos(2*th1)-1/8*m2*rc2^2*cos(-2*th1+2*th2)
-1/8*m2*rc2^2*cos(2*th1+2*th2)-1/4*m3*rc3*a2*cos(th3+2*th2+2*th1)
-1/4*m3*rc3*a2*cos(th3+2*th2-2*th1)+3/2*m3*rc3*a2*cos(2*th2+th3)-2*m3*rc3*d0*sin(th3+th2)
-1/4*m3*rc3*a2*cos(th3-2*th1)-1/4*m3*rc3*a2*cos(th3+2*th1)-2*m3*rc3*d1*sin(th3+th2)
-1/8*m3*rc3^2*cos(2*th2-2*th1+2*th3)-1/8*m3*rc3^2*cos(2*th2+2*th1+2*th3)
-1/2*I3zz*cos(2*th1)+1/2*I1xx*cos(2*th1)-1/2*I2zz*cos(2*th1)-1/2*I1zz*cos(2*th1)
NRC_{\tau 0}(2,1) = \sin(th1)*(m3*\cos(th2)*a2*d1-\cos(th2)*m3*rc3^2*\sin(th2)
+2*cos(th2)*I3yy*cos(th3)^2*sin(th2)+m3*cos(th2)*a2*d0+sin(th2)*m3*cos(th2)*a2^2
-2*\cos(th2)*I3xx*\sin(th2)*\cos(th3)^2+\sin(th2)*m2*\cos(th2)*rc2^2+m2*\cos(th2)*rc2*d1
-\cos(th3)*m3*rc3^2*\sin(th3)+m2*\cos(th2)*rc2*d0+2*\sin(th3)*I3yy*\cos(th3)*\cos(th2)^2
-2*\cos(th3)*I3xx*\sin(th3)*\cos(th2)^2-\sin(th3)*m3*rc3*a2+\cos(th2)*I3xx*\sin(th2)
```

```
+\cos(th3)*I3xx*\sin(th3)-\sin(th3)*I3yy*\cos(th3)+\cos(th2)*I2yy*\sin(th2)-\sin(th2)*I2xx*\cos(th2)
+2*sin(th3)*m3*rc3*cos(th2)^2*a2+2*cos(th3)*m3*rc3^2*sin(th3)*cos(th2)^2
-m3*\sin(th3)*\sin(th2)*rc3*d0-m3*\sin(th3)*\sin(th2)*rc3*d1+2*\sin(th2)*m3*rc3^2*\cos(th3)^22*\cos(th3)
 +2*sin(th2)*cos(th3)*m3*rc3*cos(th2)*a2+m3*cos(th3)*cos(th2)*rc3*d1+m3*cos(th3)*cos(th3)*rc3*d0
-\cos(th2)*I3yy*\sin(th2)
NRC_{\tau 0}(2,2) = -3/4*I2vy*cos(2*th2)+1/4*I2vy*cos(2*th1)+1/4*I3xx*cos(2*th1)
-1/8*I2yy*cos(2*th1+2*th2)-1/8*I2yy*cos(-2*th1+2*th2)-1/8*m2*rc2^2*cos(2*th1+2*th2)
-1/8*m2*rc2^2*cos(-2*th1+2*th2)-1/8*m3*a2^2*cos(2*th1+2*th2)-1/4*m3*a2^2*cos(2*th1)
-1/4*m2*rc2^2*cos(2*th1) - 1/8*m3*a2^2*cos(-2*th1 + 2*th2) - 1/4*m3*rc3*a2*cos(th3 + 2*th1)
-1/4*m3*rc3*a2*cos(th3-2*th1)+1/4*I3yy*cos(2*th1)+1/4*I2xx*cos(2*th1)+3/4*I3xx*cos(2*th3+2*th2)
-1/4*I3xx-1/4*I2vy-1/4*I3vy-1/4*I2xx+3/4*I2xx*cos(2*th2)+1/2*cos(th3)*m3*rc3*a2
+1/8*12xx*cos(-2*th1+2*th2)+2*m2*d0*d1+2*rc1*m1*d0-11yy+1/2*11zz-10zz+1/2*11xx+m0*rc0^2
+I0xx+2*sin(th2)*rc2*m2*d0+2*sin(th2)*m3*d1*a2+2*sin(th2)*rc2*m2*d1+2*sin(th2)*m3*d0*a2
+1/2*I3zz-3/4*I3yy*cos(2*th3+2*th2)+1/8*I2xx*cos(2*th1+2*th2)+1/4*m3*a2^2+m2*d1^2+m1*rc1^2
+m3*d1^2+m1*d0^2+m3*d0^2+m2*d0^2+1/2*12zz+1/4*m2*rc2^2+2*m3*d0*d1-1/2*12zz*cos(2*th1)
+1/2*I1xx*cos(2*th1)+1/4*m3*rc3^2-1/4*m3*rc3^2*cos(2*th1)-1/2*I1zz*cos(2*th1)
-3/4*m3*rc3^2*cos(2*th3+2*th2)-3/4*m3*a2^2*cos(2*th2)+1/8*I3xx*cos(2*th2-2*th1+2*th3)
+1/8*I3xx*cos(2*th2+2*th1+2*th3)-1/8*I3yy*cos(2*th2-2*th1+2*th3)
-1/8*I3vv*cos(2*th2+2*th1+2*th3)-1/2*I3zz*cos(2*th1)-3/4*m2*rc2^2*cos(2*th2)
-1/8*m3*rc3^2*cos(2*th2-2*th1+2*th3)-1/8*m3*rc3^2*cos(2*th2+2*th1+2*th3)
-1/4*m3*rc3*a2*cos(th3+2*th2+2*th1)-1/4*m3*rc3*a2*cos(th3+2*th2-2*th1)
-3/2*m3*rc3*a2*cos(2*th2+th3)+2*m3*rc3*d1*sin(th3+th2)+2*m3*rc3*d0*sin(th3+th2)
NRC_{\tau 0}(2,3) = -\sin(th1)*\cos(th1)*(-13xx-12yy+m3*rc3^2+11zz-m3*rc3^2*\cos(th3)^2-11xx+13zz+12zz
-\cos(th3)^2 *13yy + \cos(th3)^2 *13xx + 12yy *\cos(th2)^2 + 13xx *\cos(th2)^2 + 2*m3*rc3*\cos(th3)*\cos(th2)^2 *a2x + 12yy *\cos(th2)^2 + 13xx 
-I3yy*cos(th2)^2-cos(th2)^2*I2xx-2*cos(th2)*sin(th3)*m3*rc3*sin(th2)*a2
-2*\cos(th2)*\cos(th3)*i3yy*\sin(th3)*\sin(th2)+2*\cos(th2)*\sin(th3)*i3xx*\cos(th3)*\sin(th2)
-2*\cos(th2)*\sin(th3)*m3*rc3^2*\cos(th3)*\sin(th2)+2*I3vv*\cos(th3)^2*\cos(th2)^2+m3*\cos(th2)^2*a2^2
-m3*rc3^2*cos(th2)^2-2*I3xx*cos(th3)^2*cos(th2)^2+m2*cos(th2)^2*rc2^2
+2*m3*rc3^2*cos(th3)^2*cos(th2)^2
NRC_{\tau 0}(3,1) = 12zz*cos(2*th1)+1/2*m3*rc3*a2*cos(th3-2*th1)+1/2*m3*rc3*a2*cos(th3+2*th1)
+1/4*m3*rc3^2*cos(2*th2-2*th1+2*th3)+1/4*m3*rc3^2*cos(2*th2+2*th1+2*th3)
-1/4*I3xx*cos(2*th2-2*th1+2*th3)-1/4*I3xx*cos(2*th2+2*th1+2*th3)
+1/2*m3*rc3*a2*cos(th3+2*th2-2*th1)+1/2*m3*rc3*a2*cos(th3+2*th2+2*th1)
+1/4*I2yy*cos(-2*th1+2*th2)+1/4*I2yy*cos(2*th1+2*th2)+I1zz*cos(2*th1)
+1/4*m2*rc2^2*cos(-2*th1+2*th2)+1/4*m2*rc2^2*cos(2*th1+2*th2)+1/2*m2*rc2^2*cos(2*th1)
-1/2*I2vv*cos(2*th1)+1/2*m3*rc3^2*cos(2*th1)-1/4*I2xx*cos(-2*th1+2*th2)
-1/4*I2xx*cos(2*th1+2*th2)-1/2*I2xx*cos(2*th1)-I1xx*cos(2*th1)
+1/4*m3*a2^2*cos(-2*th1+2*th2)+1/4*m3*a2^2*cos(2*th1+2*th2)+1/2*m3*a2^2*cos(2*th1)
-1/2*I3xx*cos(2*th1)+I3zz*cos(2*th1)+I0yy-I0xx-1/2*I3yy*cos(2*th1)
+1/4*I3yy*cos(2*th2+2*th1+2*th3)+1/4*I3yy*cos(2*th2-2*th1+2*th3)
NRC_{\tau 0}(3,2) = -\sin(th1)*(2*\cos(th3)*m3*rc3^2*\sin(th3)*\cos(th2)^2 + \cos(th2)*rc2*m2*d0
+2*\sin(th2)*I3yy*\cos(th3)^2*\cos(th2)+\cos(th2)*m2*\sin(th2)*rc2^2-2*\cos(th2)*I3xx*\cos(th3)^2*\sin(th2)
+cos(th2)*m3*d1*a2-sin(th3)*m3*rc3*a2+2*sin(th3)*I3yy*cos(th3)*cos(th2)^2
-\sin(th2)*\sin(th3)*m3*rc3*d1-\sin(th2)*\sin(th3)*m3*rc3*d0-\cos(th2)*I2xx*\sin(th2)
-\sin(th3)*I3yy*\cos(th3)+\sin(th3)*I3xx*\cos(th3)+2*\cos(th2)*m3*rc3^2*\cos(th3)^2*\sin(th2)
+2*cos(th2)*cos(th3)*m3*rc3*sin(th2)*a2+2*m3*sin(th3)*cos(th2)^2*rc3*a2+cos(th2)*cos(th3)*m3*rc3
*d0+cos(th2)*cos(th3)*m3*rc3*d1-cos(th2)*m3*rc3^2*sin(th2)+cos(th2)*m3*d0*a2
-2*cos(th3)*I3xx*sin(th3)*cos(th2)^2-sin(th3)*m3*rc3^2*cos(th3)+cos(th2)*m3*sin(th2)*a2^2
```

```
-\sin(th2)*I3yy*\cos(th2)+\cos(th2)*I3xx*\sin(th2)+\sin(th2)*I2yy*\cos(th2)+\cos(th2)*rc2*m2*d1
NRC_{\tau 0}(3,3) = -\cos(th1)*(\sin(th2)*m3*rc3^2*\cos(th2)-\cos(th2)*rc2*m2*d0
-2*sin(th3)*I3yy*cos(th3)*cos(th2)^2+sin(th2)*sin(th3)*m3*rc3*d1-cos(th2)*m3*d0*a2
-2*\sin(th2)*I3yy*\cos(th3)^2*\cos(th2)-\cos(th2)*m3*\sin(th2)*a2^2-\cos(th2)*m3*d1*a2
+2*cos(th2)*I3xx*cos(th3)^2*sin(th2)+cos(th2)*I3vy*sin(th2)+sin(th3)*I3vy*cos(th3)
-\sin(th2)*I2yy*\cos(th2)+\cos(th2)*I2xx*\sin(th2)-\cos(th2)*I3xx*\sin(th2)
-2*cos(th2)*cos(th3)*m3*rc3*sin(th2)*a2-cos(th2)*cos(th3)*m3*rc3*d0
-2*cos(th2)*m3*rc3^2*cos(th3)^2*sin(th2)-cos(th2)*cos(th3)*m3*rc3*d1
-\cos(th3)*I3xx*\sin(th3)+m3*\sin(th3)*rc3*a2-\cos(th2)*m2*\sin(th2)*rc2^2-\cos(th2)*rc2*m2*d1
-2*\cos(th3)*m3*rc3^2*\sin(th3)*\cos(th2)^2+\sin(th2)*\sin(th3)*m3*rc3*d0
-2*m3*sin(th3)*cos(th2)^2*rc3*a2+2*cos(th3)*I3xx*sin(th3)*cos(th2)^2+sin(th3)*m3*rc3^2*cos(th3))
                                                                                               (A-19)
                         Flexible Body Centrifugal Interaction Torques
NCC_{\tau 0}(1,1)=0
NCC_{\tau 0}(1,2) = \sin(th1)*(-13xx*\sin(th2)*\cos(th2)-\cos(th2)*I2yy*\sin(th2)-I3xx*\sin(th3)*\cos(th3)
+I3yy*sin(th3)*cos(th3)+sin(th2)*I2xx*cos(th2)+I3yy*sin(th2)*cos(th2)
-2*m3*rc3^2*cos(th3)^2*cos(th2)*sin(th2)-m3*rc3*cos(th3)*cos(th2)*d0-m3*rc3*cos(th3)*cos(th3)*d1
-2*m3*rc3*cos(th3)*cos(th2)*sin(th2)*a2+m3*rc3*sin(th3)*sin(th2)*d0
-2*m3*rc3*sin(th3)*a2*cos(th2)^2-2*m3*rc3^2*sin(th3)*cos(th3)*cos(th2)^2
+m3*rc3*sin(th3)*sin(th2)*d1-m3*cos(th2)*sin(th2)*a2^2-m3*cos(th2)*d1*a2
+2*I3xx*cos(th3)^2*cos(th2)*sin(th2)-rc2*m2*cos(th2)*d1-2*I3yy*cos(th3)^2*cos(th2)*sin(th2)
-m3*cos(th2)*d0*a2+m3*rc3^2*sin(th2)*cos(th2)-m2*cos(th2)*sin(th2)*rc2^2
+2*I3xx*cos(th3)*cos(th2)^2*sin(th3)-2*I3yy*sin(th3)*cos(th3)*cos(th2)^2
-rc2*m2*cos(th2)*d0+m3*rc3^2*sin(th3)*cos(th3)+m3*rc3*sin(th3)*a2)
NCC_{\tau 0}(1,3) = \sin(th1)*(\cos(th2)*I2yy*\sin(th2)-I3yy*\sin(th3)*\cos(th3)-I3yy*\sin(th2)*\cos(th2)
+I3xx*sin(th2)*cos(th2)+2*m3*rc3*cos(th3)*cos(th2)*sin(th2)*a2+2*m3*rc3*sin(th3)*a2*cos(th2)^2
+m3*rc3*cos(th3)*cos(th2)*d0+2*m3*rc3^2*cos(th3)^2*cos(th2)*sin(th2)+m3*rc3*cos(th3)*cos(th2)*d1
+2*m3*rc3^2*sin(th3)*cos(th3)*cos(th2)^2-2*I3xx*cos(th3)*cos(th2)^2*sin(th3)
- m3*rc3*sin(th3)*sin(th2)*d0-m3*rc3*sin(th3)*sin(th2)*d1-sin(th2)*I2xx*cos(th2)
+I3xx*sin(th3)*cos(th3)-m3*rc3*sin(th3)*a2-m3*rc3^2*sin(th3)*cos(th3)- m3*rc3^2*sin(th2)*cos(th2)
+m3*\cos(th2)*\sin(th2)*a2^2+m3*\cos(th2)*d0*a2+m2*\cos(th2)*\sin(th2)*rc2^2
-2*I3xx*cos(th3)^2*cos(th2)*sin(th2) + 2*I3vv*sin(th3)*cos(th3)*cos(th2)^2
+m3*\cos(th2)*d1*a2+rc2*m2*\cos(th2)*d0+rc2*m2*\cos(th2)*d1+2*I3yy*\cos(th3)^22*\cos(th2)*\sin(th2)
NCC_{\tau 0}(2.1) = \cos(th1)*(-\sin(th3)*I3vv*\cos(th3)+\cos(th3)*I3xx*\sin(th3)-\sin(th2)*I3vv*\cos(th2)
-\sin(th2)*I2xx*\cos(th2)+\cos(th2)*I2yy*\sin(th2)+\cos(th2)*I3xx*\sin(th2)
+2*sin(th3)*m3*rc3^2*cos(th3)*cos(th2)^2- m3*rc3*sin(th3)*sin(th2)*d0
+2*m3*sin(th3)*rc3*a2*cos(th2)^2+2*sin(th2)*m3*rc3^2*cos(th3)^2*cos(th2)
-m3*sin(th3)*sin(th2)*rc3*d1+2*cos(th3)*I3yy*sin(th3)*cos(th2)^2-2*sin(th2)*I3xx*cos(th3)^2*cos(th2)
+\sin(th_2)*m_2*\cos(th_2)*re_2^2+m_3*re_3*\cos(th_3)*\cos(th_2)*d_0+m_3*\cos(th_3)*\cos(th_2)*re_3*d_1
+m2*cos(th2)*rc2*d1+2*sin(th2)*cos(th3)*m3*rc3*cos(th2)*a2+m3*cos(th2)*d0*a2
+2*cos(th2)*I3yy*cos(th3)^2*sin(th2)-cos(th2)*m3*rc3^2*sin(th2)-2*cos(th3)*I3xx*sin(th3)*cos(th2)^2
-cos(th3)*m3*rc3^2*sin(th3)- m3*sin(th3)*rc3*a2+sin(th2)*m3*cos(th2)*a2^2
+m3*\cos(th2)*a2*d1+rc2*m2*\cos(th2)*d0
```

 $NCC_{\tau 0}(2,2)=0$

```
NCC_{\tau 0}(2,3) = -\cos(th1)*(-\sin(th2)*I3yy*\cos(th2)+\cos(th3)*I3xx*\sin(th3)-\sin(th2)*I2xx*\cos(th2)
+\cos(th2)*I3xx*\sin(th2)-\sin(th3)*I3yy*\cos(th3)+2*\sin(th2)*m3*rc3^2*\cos(th3)^2*\cos(th2)
+2*m3*sin(th3)*rc3*a2*cos(th2)^2- m3*sin(th3)*sin(th2)*rc3*d1+m3*rc3*cos(th3)*cos(th2)*d0
+2*sin(th3)*m3*rc3^2*cos(th3)*cos(th2)^2+m3*cos(th3)*cos(th2)*rc3*d1- m3*rc3*sin(th3)*sin(th2)*d0
+2*sin(th2)*cos(th3)*m3*rc3*cos(th2)*a2-cos(th3)*m3*rc3^2*sin(th3)-cos(th2)*m3*rc3^2*sin(th2)
+rc2*m2*cos(th2)*d0+sin(th2)*m3*cos(th2)*a2^2+m3*cos(th2)*a2*d1+sin(th2)*m2*cos(th2)*rc2^2
-2*\sin(th2)*I3xx*\cos(th3)^2*\cos(th2)+m2*\cos(th2)*rc2*d1+m3*\cos(th2)*d0*a2
+2*cos(th3)*I3yy*sin(th3)*cos(th2)^2-m3*sin(th3)*rc3*a2+2*cos(th2)*I3yy*cos(th3)^2*sin(th2)
-2*\cos(th3)*I3xx*\sin(th3)*\cos(th2)^2+\cos(th2)*I2yy*\sin(th2)
NCC_{\tau 0}(3,1) = -\sin(th1) *\cos(th1) *(I3zz+I2zz+rc2^2*\cos(th2)^2*m2+a2^2*\cos(th2)^2*m3
-2*\cos(th2)^2*\cos(th3)^2*I3xx-\cos(th3)^2*rc3^2*m3-\cos(th2)^2*rc3^2*m3
+2*cos(th3)^2*cos(th2)^2*I3vv-I3xx-I2vv+rc3^2*m3-cos(th3)^2*I3vv-cos(th2)^2*I3vv
+2*cos(th2)^2*cos(th3)^2*rc3^2*m3+cos(th2)^2*I3xx+2*cos(th2)*cos(th3)*I3xx*sin(th3)*sin(th2)
-2*\cos(th2)*\cos(th3)*rc3^2*m3*\sin(th3)*\sin(th2)+2*a2*\cos(th2)^2*rc3*m3*\cos(th3)
-2*a2*cos(th2)*rc3*m3*sin(th3)*sin(th2)-2*cos(th2)*sin(th3)*I3yy*cos(th3)*sin(th2)
-\cos(th2)^2*I2xx+\cos(th2)^2*I2yy+\cos(th3)^2*I3xx-I1xx+I1zz
NCC_{\tau 0}(3.2) = \sin(th1) * \cos(th1) * (I3zz+I2zz-I3xx-I2vv+rc3^2*m3-I1xx+I1zz-\cos(th2)^2*I2xx
+\cos(th2)^2*I2vv+\cos(th2)^2*I3xx-\cos(th2)^2*I3vv+\cos(th3)^2*I3xx
+2*a2*cos(th2)^2*rc3*m3*cos(th3)-2*cos(th2)^2*cos(th3)^2*I3xx+2*cos(th2)^2*cos(th3)^2*rc3^2*m3
-\cos(th3)^2*rc3^2*m3+a2^2*\cos(th2)^2*m3+2*\cos(th3)^2*\cos(th2)^2*I3yy+rc2^2*\cos(th2)^2*m2
+2*cos(th2)*cos(th3)*I3xx*sin(th3)*sin(th2)-2*cos(th2)*sin(th3)*I3vy*cos(th3)*sin(th2)
-2*\cos(th2)*\cos(th3)*rc3^2*m3*\sin(th3)*\sin(th2)-\cos(th3)^2*I3yy
-2*a2*cos(th2)*rc3*m3*sin(th3)*sin(th2)-cos(th2)^2*rc3^2*m3
```

 $NCC_{\tau 0}(3,3)=0$ (A-20)

Flexible Body Rotational Inertia Interaction Torques

```
B_{w0}(1,1) = 2*rc2*m2*sin(th2)*d1+2*m3*rc3*cos(th3)*a2-m3*rc3^2*cos(th1)^2
+13yy*\cos(th3)^2*\cos(th1)^2-13xx*\cos(th1)^2*\cos(th2)^2-2*13yy*\cos(th2)^2*\cos(th1)^2*\cos(th3)^2
-I2zz*\cos(th1)^2+m3*d0^2+I3xx*\cos(th1)^2+2*I3xx*\cos(th3)^2*\cos(th2)^2*\cos(th1)^2
-I1zz*\cos(th1)^2 + I1zz + 2*rc2*m2*\sin(th2)*d0 + m3*rc3^2 + I1xx*\cos(th1)^2 + 2*m3*\sin(th2)*d0*a2
-12yy*cos(th1)^2*cos(th2)^2+13yy*cos(th2)^2*cos(th1)^2+2*m3*sin(th2)*d1*a2
+2*cos(th2)*sin(th3)*m3*rc3*sin(th2)*cos(th1)^2*a2-
2*cos(th2)*I3xx*cos(th3)*sin(th3)*sin(th2)*cos(th1)^2-2*m3*rc3*cos(th3)*a2*cos(th1)^2*cos(th2)^2
+2*cos(th2)*sin(th3)*m3*rc3^2*cos(th3)*sin(th2)*cos(th1)^2
+2*\cos(th2)*\sin(th3)*i3yy*\cos(th3)*\sin(th2)*\cos(th1)^2+2*m3*rc3*\cos(th3)*\sin(th2)*d0
+2*m3*rc3*sin(th3)*cos(th2)*d0-I3xx*cos(th1)^2*cos(th3)^2+I2xx*cos(th2)^2*cos(th1)^2
-2*m3*rc3^2*cos(th2)^2*cos(th1)^2*cos(th3)^2+2*m3*rc3*cos(th3)*sin(th2)*d1
+2*m3*rc3*sin(th3)*cos(th2)*d1+I2zz+I3zz+I2yy*cos(th1)^2+m3*d1^2+m1*d0^2
-13zz*\cos(th1)^2 + m3*rc3^2*\cos(th2)^2*\cos(th1)^2 + 10xx + m0*rc0^2 + m2*rc2^2 + m2*d0^2 + m1*rc1^2
+m2*d1^2-m2*rc2^2*cos(th1)^2*cos(th2)^2+m3*rc3^2*cos(th3)^2*cos(th1)^2
B_{w0}(1,2) = -\cos(th1) \sin(th1) (m3 \cos^2-13xx-12yy-m3 \cos^2+\cos(th2)^2 + m3 \cos^2+\cos(th2)^2
-2*I3xx*cos(th3)^2*cos(th2)^2+2*I3yy*cos(th3)^2*cos(th2)^2
-2*\cos(th2)*\sin(th3)*m3*rc3^2*\cos(th3)*\sin(th2)+2*\cos(th2)*I3xx*\cos(th3)*\sin(th3)*\sin(th2)
```

```
+2*m3*rc3*cos(th3)*a2*cos(th2)^2-2*cos(th2)*sin(th3)*I3vv*cos(th3)*sin(th2)
-cos(th3)^2*rc3^2*m3+m2*rc2^2*cos(th2)^2-2*cos(th2)*sin(th3)*m3*rc3*sin(th2)*a2+cos(th3)^2*I3xx
-\cos(th_3)^2*I_3yy-I_3yy*\cos(th_2)^2+I_3xx*\cos(th_2)^2+I_2yy*\cos(th_2)^2
-I2xx*cos(th2)^2+2*m3*rc3^2*cos(th2)^2*cos(th3)^2+I1zz-I1xx+I2zz+I3zz
B_{w0}(1,3) = -\cos(th1)*(m3*\cos(th3)*\cos(th2)*rc3*d0+\sin(th2)*m3*\cos(th2)*a2^2
+\sin(th2)*m2*\cos(th2)*rc2^2+m2*\cos(th2)*rc2*d1-\cos(th2)*I2xx*\sin(th2)
+2*sin(th2)*cos(th3)*m3*rc3*cos(th2)*a2-m3*sin(th3)*sin(th2)*rc3*d1-cos(th2)*m3*rc3^2*sin(th2)
-cos(th3)*I3vv*sin(th3)-a2*rc3*sin(th3)*m3-sin(th3)*rc3^2*m3*cos(th3)+m2*cos(th2)*rc2*d0
+m3*\cos(th2)*a2*d1+\sin(th2)*I2yy*\cos(th2)+m3*\cos(th2)*a2*d0-2*\cos(th2)*I3xx*\cos(th3)^2*\sin(th2)
+sin(th3)*cos(th3)*I3xx+sin(th2)*I3xx*cos(th2)+2*sin(th3)*m3*rc3^2*cos(th3)*cos(th2)^2
-2*I3xx*cos(th3)*sin(th3)*cos(th2)^2+2*sin(th2)*I3vv*cos(th3)^2*cos(th2)
+2*sin(th3)*I3yy*cos(th3)*cos(th2)^2+m3*cos(th3)*cos(th2)*rc3*d1- m3*sin(th3)*sin(th2)*rc3*d0
+2*sin(th3)*m3*rc3*cos(th2)^2*a2+2*sin(th2)*m3*rc3^2*cos(th3)^2*cos(th2)-cos(th2)*I3vy*sin(th2))
B_{w0}(2,1) = -\sin(th1) *\cos(th1) *(m3*rc3^2-I3xx-I2yy-2*\cos(th2)*\sin(th3)*m3*rc3*\sin(th2)*a2
-2*cos(th2)*sin(th3)*m3*rc3^2*cos(th3)*sin(th2)+2*m3*rc3*cos(th3)*a2*cos(th2)^2
-2*\cos(th2)*\sin(th3)*I3yy*\cos(th3)*\sin(th2)+2*\cos(th2)*I3xx*\cos(th3)*\sin(th3)*\sin(th2)
+2*m3*rc3^2*cos(th2)^2*cos(th3)^2+I2yy*cos(th2)^2-I2xx*cos(th2)^2+I3xx*cos(th2)^2
-13vv*cos(th2)^2+cos(th3)^2*13xx-cos(th3)^2*13vv+2*13vv*cos(th3)^2*cos(th2)^2+m3*a2^2*cos(th2)^2
-m3*rc3^2*cos(th2)^2-cos(th3)^2*rc3^2*m3+m2*rc2^2*cos(th2)^2-2*I3xx*cos(th3)^2*cos(th2)^2
-I1xx+I1zz+I2zz+I3zz)
B_{w0}(2,2) = \frac{1}{4}12xx \cos(2 + 1) - \frac{1}{4}12yy \cos(2 + 1) + \frac{1}{4}13xx + \frac{1}{4}12yy + \frac{1}{4}13yy + \frac{1}{4}12xx
+1/4*I3xx*cos(2*th3+2*th2)-1/4*I3yy*cos(2*th3+2*th2)+2*m3*rc3*d1*sin(th3+th2)
-1/4*m3*rc3^2*cos(2*th3+2*th2)+3/4*m3*rc3^2+2*rc1*m1*d0+m3*d1^2+m2*d1^2
+2*m3*d0*d1+2*m2*d0*d1+2*sin(th2)*m3*d0*a2+2*sin(th2)*m3*d1*a2+2*sin(th2)*rc2*m2*d1*a2+2*sin(th2)*rc2*m2*d1*a2+2*sin(th2)*rc2*m2*d1*a2+2*sin(th2)*rc2*m2*d1*a2+2*sin(th2)*rc2*m2*d1*a2+2*sin(th2)*rc2*m2*d1*a2+2*sin(th2)*rc2*m2*d1*a2+2*sin(th2)*rc2*m2*d1*a2+2*sin(th2)*rc2*m2*d1*a2+2*sin(th2)*rc2*m2*d1*a2+2*sin(th2)*rc2*m2*d1*a2+2*sin(th2)*rc2*m2*d1*a2+2*sin(th2)*rc2*m2*d1*a2+2*sin(th2)*rc2*m2*d1*a2+2*sin(th2)*rc2*m2*d1*a2+2*sin(th2)*rc2*m2*d1*a2+2*sin(th2)*rc2*m2*d1*a2+2*sin(th2)*rc2*m2*d1*a2+2*sin(th2)*rc2*m2*d1*a2+2*sin(th2)*rc2*m2*d1*a2+2*sin(th2)*rc2*m2*d1*a2+2*sin(th2)*rc2*m2*d1*a2+2*sin(th2)*rc2*m2*d1*a2+2*sin(th2)*rc2*m2*d1*a2+2*sin(th2)*rc2*m2*d1*a2+2*sin(th2)*rc2*m2*d1*a2+2*sin(th2)*rc2*m2*d1*a2+2*sin(th2)*rc2*m2*d1*a2+2*sin(th2)*rc2*m2*d1*a2+2*sin(th2)*rc2*m2*d1*a2+2*sin(th2)*rc2*m2*d1*a2+2*sin(th2)*rc2*m2*d1*a2+2*sin(th2)*rc2*m2*d1*a2+2*sin(th2)*rc2*m2*d1*a2+2*sin(th2)*rc2*m2*d1*a2+2*sin(th2)*rc2*m2*d1*a2+2*sin(th2)*rc2*m2*d1*a2+2*sin(th2)*rc2*m2*d1*a2+2*sin(th2)*rc2*m2*d1*a2+2*sin(th2)*rc2*m2*d1*a2+2*sin(th2)*rc2*m2*d1*a2+2*sin(th2)*rc2*m2*d1*a2+2*sin(th2)*rc2*m2*d1*a2+2*sin(th2)*rc2*m2*d1*a2+2*sin(th2)*rc2*m2*d1*a2+2*sin(th2)*rc2*m2*d1*a2+2*sin(th2)*rc2*m2*d1*a2+2*sin(th2)*rc2*m2*d1*a2+2*sin(th2)*rc2*m2*d1*a2+2*sin(th2)*rc2*m2*d1*a2+2*sin(th2)*rc2*m2*d1*a2+2*sin(th2)*rc2*m2*d1*a2+2*sin(th2)*rc2*m2*d1*a2+2*sin(th2)*rc2*m2*d1*a2+2*sin(th2)*rc2*m2*d1*a2+2*sin(th2)*rc2*m2*d1*a2+2*sin(th2)*rc2*m2*d1*a2+2*sin(th2)*rc2*m2*d1*a2+2*sin(th2)*rc2*m2*d1*a2+2*sin(th2)*rc2*m2*d1*a2+2*sin(th2)*rc2*m2*d1*a2+2*sin(th2)*rc2*m2*d1*a2+2*sin(th2)*rc2*m2*d1*a2+2*sin(th2)*rc2*m2*d1*a2*d1*a2*d1*a2*d1*a2*d1*a2*d1*a2*d1*a2*d1*a2*d1*a2*d1*a2*d1*a2*d1*a2*d1*a2*d1*a2*d1*a2*d1*a2*d1*a2*d1*a2*d1*a2*d1*a2*d1*a2*d1*a2*d1*a2*d1*a2*d1*a2*d1*a2*d1*a2*d1*a2*d1*a2*d1*a2*d1*a2*d1*a2*d1*a2*d1*a2*d1*a2*d1*a2*d1*a2*d1*a2*d1*a2*d1*a2*d1*a2*d1*a2*d1*a2*d1*a2*d1*a2*d1*a2*d1*a2*d1*a2*d1*a2*d1*a2*d1*a2*d1*a2*d1*a2*d1*a2*d1*a2*d1*a2*d1*a2*d1*a2*d1*a2*d1*a2*d1*a2*d1*a2*d1*a2*d1*a2*d1*a2*d1*a2*d1*a2*d1*a2*d1*a2*d1*a2*d1*a2*d1*a2*d1*a2*d1*a2*d1*a2*d
+m1*d0^2+m1*rc1^2+1/4*m3*rc3*a2*cos(th3+2*th1)+2*m3*rc3*d0*sin(th3+th2)+10vv
+1/4*m3*rc3*a2*cos(th3+2*th2-2*th1)+1/4*m3*rc3*a2*cos(th3+2*th2+2*th1)
+1/4*m3*rc3*a2*cos(th3-2*th1)+m0*rc0^2+3/4*m3*a2^2-1/4*m3*a2^2*cos(2*th2)
-1/2*m3*rc3*a2*cos(2*th2+th3)-1/4*m2*rc2^2*cos(2*th2)-\frac{1}{4}*I3xx*cos(2*th1)
+1/4*m3*rc3^2*cos(2*th1)-1/4*I3yy*cos(2*th1)-1/4*I2yy*cos(2*th1)
+1/8*I2yy*cos(-2*th1+2*th2)+1/8*I2yy*cos(2*th1+2*th2)-1/4*I2xx*cos(2*th1)+2*sin(th2)*rc2*m2*d0
-1/8*I2xx*cos(-2*th1+2*th2)-1/8*I2xx*cos(2*th1+2*th2)+1/4*m2*rc2^2*cos(2*th1)
+1/8*m2*rc2^2*cos(-2*th1+2*th2)+1/8*m2*rc2^2*cos(2*th1+2*th2)+1/4*m3*a2^22*cos(2*th1)
+1/8*m3*a2^2*cos(-2*th1+2*th2)+1/8*m3*a2^2*cos(2*th1+2*th2)
+1/8*m3*rc3^2*cos(2*th2-2*th1+2*th3)+1/8*m3*rc3^2*cos(2*th2+2*th1+2*th3)
+1/8*I3yy*cos(2*th2-2*th1+2*th3)+1/8*I3yy*cos(2*th2+2*th1+2*th3)
-1/8*I3xx*cos(2*th2-2*th1+2*th3)-1/8*I3xx*cos(2*th2+2*th1+2*th3)-\frac{1}{2}*I1xx*cos(2*th1)
+1/2*I3zz*cos(2*th1)+1/2*I1zz*cos(2*th1)+1/2*I2zz*cos(2*th1)
B_{w0}(2.3) = \sin(th1)*(\cos(th2)*I3yy*\sin(th2)-I3xx*\sin(th3)*\cos(th3)-\sin(th2)*I3xx*\cos(th2)
-\sin(th2)*I2yy*\cos(th2)+2*\cos(th2)*I3xx*\cos(th3)^2*\sin(th2)-m3*\cos(th2)*a2*d1
-m3*cos(th3)*cos(th2)*rc3*d0+m3*sin(th3)*rc3*a2-sin(th2)*m3*cos(th2)*a2^2
-2*sin(th3)*m3*rc3^2*cos(th3)*cos(th2)^2+cos(th3)*I3yy*sin(th3)-m3*cos(th2)*a2*d0
-2*sin(th2)*m3*rc3^2*cos(th3)^2*cos(th2)-2*sin(th2)*cos(th3)*m3*rc3*cos(th2)*a2
-2*\sin(th2)*I3yy*\cos(th3)^2*\cos(th2)-m3*\cos(th3)*\cos(th2)*rc3*d1-m2*\cos(th2)*rc2*d1
-m2*cos(th2)*rc2*d0+2*I3xx*cos(th3)*sin(th3)*cos(th2)^2-2*sin(th3)*I3yy*cos(th3)*cos(th2)^2
+m3*sin(th3)*sin(th2)*rc3*d0+cos(th3)*m3*rc3^2*sin(th3)+m3*sin(th3)*sin(th2)*rc3*d1
+\cos(th2)*I2xx*\sin(th2)-2*\sin(th3)*m3*rc3*\cos(th2)^2*a2+\cos(th2)*m3*rc3^2*\sin(th2)
-\sin(th2)*m2*\cos(th2)*rc2^2
```

```
B_{w0}(3,1) = -\cos(th1)*(\cos(th2)*rc2*m2*d0+\cos(th2)*m3*d0*a2-\sin(th3)*m3*rc3^2*\cos(th3)
-\sin(th3)*m3*rc3*a2+\cos(th2)*\cos(th3)*m3*rc3*d1-\sin(th2)*\sin(th3)*m3*rc3*d0
 - sin(th2)*sin(th3)*m3*rc3*d1+2*cos(th2)*cos(th3)*m3*rc3*sin(th2)*a2
+cos(th2)*cos(th3)*m3*rc3*d0+2*cos(th2)*I3yy*cos(th3)^2*sin(th2)+cos(th2)*rc2*m2*d1
+2*m3*sin(th3)*cos(th2)^2*rc3*a2+2*cos(th2)*m3*rc3^2*cos(th3)^2*sin(th2)
+2*cos(th3)*m3*rc3^2*sin(th3)*cos(th2)^2+2*cos(th3)*I3vy*sin(th3)*cos(th2)^2
-2*sin(th2)*I3xx*cos(th3)^2*cos(th2)+cos(th2)*m3*d1*a2-2*I3xx*sin(th3)*cos(th3)*cos(th2)^2
-\sin(th2)*m3*rc3^2*\cos(th2)+\cos(th2)*m2*\sin(th2)*rc2^2+\cos(th2)*m3*\sin(th2)*a2^2
 -\sin(th2)*I3yy*\cos(th2)+I3xx*\cos(th3)*\sin(th3)-\sin(th3)*I3yy*\cos(th3)+\cos(th2)*I3xx*\sin(th2)
 +\cos(th2)*I2vv*\sin(th2)-\sin(th2)*I2xx*\cos(th2)
 B_{w0}(3.2) = -\sin(th1)*(I3xx*\sin(th3)*\cos(th3) - \cos(th2)*I2xx*\sin(th2) + \sin(th2)*I3xx*\cos(th2)
+sin(th2)*I2yy*cos(th2)-cos(th2)*I3yy*sin(th2)-cos(th3)*I3yy*sin(th3)-m3*sin(th3)*rc3*d1
-m3*sin(th3)*sin(th2)*rc3*d0+2*sin(th3)*m3*rc3*cos(th2)^2*a2-cos(th3)*m3*rc3^2*sin(th3)
+2*sin(th3)*I3yy*cos(th3)*cos(th2)^2+2*sin(th3)*m3*rc3^2*cos(th3)*cos(th2)^2+m2*cos(th2)*rc2*d1
+m2*\cos(th2)*rc2*d0+m3*\cos(th3)*\cos(th2)*rc3*d0+m3*\cos(th2)*a2*d0+m3*\cos(th2)*a2*d1+m2*\cos(th2)*a2*d1+m2*\cos(th2)*a2*d1+m2*\cos(th2)*a2*d1+m2*\cos(th2)*a2*d1+m2*\cos(th2)*a2*d1+m2*\cos(th2)*a2*d1+m2*\cos(th2)*a2*d1+m2*\cos(th2)*a2*d1+m2*\cos(th2)*a2*d1+m2*\cos(th2)*a2*d1+m2*\cos(th2)*a2*d1+m2*\cos(th2)*a2*d1+m2*\cos(th2)*a2*d1+m2*\cos(th2)*a2*d1+m2*\cos(th2)*a2*d1+m2*\cos(th2)*a2*d1+m2*\cos(th2)*a2*d1+m2*\cos(th2)*a2*d1+m2*\cos(th2)*a2*d1+m2*\cos(th2)*a2*d1+m2*\cos(th2)*a2*d1+m2*\cos(th2)*a2*d1+m2*\cos(th2)*a2*d1+m2*\cos(th2)*a2*d1+m2*\cos(th2)*a2*d1+m2*\cos(th2)*a2*d1+m2*\cos(th2)*a2*d1+m2*\cos(th2)*a2*d1+m2*\cos(th2)*a2*d1+m2*\cos(th2)*a2*d1+m2*\cos(th2)*a2*d1+m2*\cos(th2)*a2*d1+m2*\cos(th2)*a2*d1+m2*\cos(th2)*a2*d1+m2*\cos(th2)*a2*d1+m2*\cos(th2)*a2*d1+m2*o2*d1+m2*o2*d1+m2*o2*d1+m2*o2*d1+m2*o2*d1+m2*o2*d1+m2*o2*d1+m2*o2*d1+m2*o2*d1+m2*o2*d1+m2*o2*d1+m2*o2*d1+m2*o2*d1+m2*o2*d1+m2*o2*d1+m2*o2*d1+m2*o2*d1+m2*o2*d1+m2*o2*d1+m2*o2*d1+m2*o2*d1+m2*o2*d1+m2*o2*d1+m2*o2*d1+m2*o2*d1+m2*o2*d1+m2*o2*d1+m2*o2*d1+m2*o2*d1+m2*o2*d1+m2*o2*d1+m2*o2*d1+m2*o2*d1+m2*o2*d1+m2*o2*d1+m2*o2*d1+m2*o2*d1+m2*o2*d1+m2*o2*d1+m2*o2*d1+m2*o2*d1+m2*o2*d1+m2*o2*d1+m2*o2*d1+m2*o2*d1+m2*o2*d1+m2*o2*d1+m2*o2*d1+m2*o2*d1+m2*o2*d1+m2*o2*d1+m2*o2*d1+m2*o2*d1+m2*o2*d1+m2*o2*d1+m2*o2*d1+m2*o2*d1+m2*o2*d1+m2*o2*d1+m2*o2*d1+m2*o2*d1+m2*o2*d1+m2*o2*d1+m2*o2*d1+m2*o2*d1+m2*o2*d1+m2*o2*d1+m2*o2*d1+m2*o2*d1+m2*o2*d1+m2*o2*d1+m2*o2*d1+m2*o2*d1+m2*o2*d1+m2*o2*d1+m2*o2*d1+m2*o2*d1+m2*o2*d1+m2*o2*d1+m2*o2*d1+m2*o2*d1+m2*o2*d1+m2*o2*d1+m2*o2*d1+m2*o2*d1+m2*o2*d1+m2*o2*d1+m2*o2*d1+m2*o2*d1+m2*o2*d1+m2*o2*d1+m2*o2*d1+m2*o2*d1+m2*o2*d1+m2*o2*d1+m2*o2*d1+m2*o2*d1+m2*o2*d1+m2*o2*d1+m2*o2*d1+m2*o2*d1+m2*o2*d1+m2*o2*d1+m2*o2*d1+m2*o2*d1+m2*o2*d1+m2*o2*d1+m2*o2*d1+m2*o2*d1+m2*o2*d1+m2*o2*d1+m2*o2*d1+m2*o2*d1+m2*o2*d1+m2*o2*d1+m2*o2*d1+m2*o2*d1+m2*o2*d1+m2*o2*d1+m2*d1+m2*o2*d1+m2*o2*d1+m2*o2*d1+m2*o2*d1+m2*o2*d1+m2*o2*d1+m2*o2*d1+m2*o2*d1+m2*o2*d1+m2*o2*d1+m2*o2*d1+m2*o2*d1+m2*o2*d1+m2*o2*d1+m2*o2*d1+m2*o2*d1+m2*o2*d1+m2*o2*d1+m2*o2*d1+m2*o2*d1+m2*o2*d1+m2*o2*d1+m2*o2*d1+m2*o2*d1+m2*o2*d1+m2*o2*d1+m2*o2*d1+m2*o2*d1+m2*o2*d1+m2*o2*d1+m2*o2*d1+m2*o2*d1+m2*o2*d1+m2*o2*d1+m2*o2*d1+m2
 -m3*sin(th3)*rc3*a2-2*cos(th2)*I3xx*cos(th3)^2*sin(th2)+sin(th2)*m3*cos(th2)*a2^2
 +sin(th2)*m2*cos(th2)*rc2^2+2*sin(th2)*cos(th3)*m3*rc3*cos(th2)*a2-cos(th2)*m3*rc3^2*sin(th2)
 +m3*cos(th3)*cos(th2)*rc3*d1+2*sin(th2)*m3*rc3^2*cos(th3)^2*cos(th2)+2*sin(th2)*I3vv*cos(th3)^2*c
 os(th2)-2*I3xx*cos(th3)*sin(th3)*cos(th2)^2
 B_{w0}(3,3) = I1vv + I0zz + 1/2*m3*rc3^2 - 1/2*I3xx*cos(2*th3 + 2*th2) + 1/2*I3xx + 1/2*I2vv
+1/2*I3yy+1/2*I2xx+\cos(th3)*m3*rc3*a2+1/2*I2yy*\cos(2*th2)+1/2*m3*a2^2+1/2*m3*a2^2*\cos(2*th2)
+1/2*I3yy*cos(2*th3+2*th2)+1/2*m2*rc2^2-
 1/2*12xx*\cos(2*th2)+m3*rc3*a2*\cos(2*th2+th3)+1/2*m2*rc2^2*\cos(2*th2)+1/2*m3*rc3^22*\cos(2*th3+2)
 *th2)
                                                                                                                                                                                                                                                                                         (A-21)
                                                                                Cross Coupling Interaction Torque Effects
 NCM_{\tau 0}(1,1) = 2*\sin(th1)*\cos(th1)*(I3zz+I2zz+\cos(th2)^2*I2vv+\cos(th3)^2*I3xx-\cos(th2)^2*I2xx-I3xx
-I2vy + \cos(th2)^2 * I3xx - \cos(th2)^2 * I3yy + rc3^2 * m3 + 2*\cos(th2)^2 * \cos(th3)^2 * rc3^2 * m3 + 2*\cos(th2)^2 * (th2)^2 * (th2)^2
-2*cos(th2)*sin(th3)*I3yy*cos(th3)*sin(th2)+2*cos(th3)^2*cos(th2)^2*I3yy
-2*\cos(th2)^2+\cos(th3)^2+13xx+a2^2+\cos(th2)^2+m3+rc2^2+\cos(th2)^2+m2-\cos(th2)^2+rc3^2+m3+rc2^2+\cos(th2)^2+rc3^2+m3+rc2^2+\cos(th2)^2+rc3^2+rc3^2+m3+rc2^2+rc3^2+m3+rc2^2+rc3^2+m3+rc2^2+rc3^2+rc3^2+rc3^2+rc3^2+rc3^2+rc3^2+rc3^2+rc3^2+rc3^2+rc3^2+rc3^2+rc3^2+rc3^2+rc3^2+rc3^2+rc3^2+rc3^2+rc3^2+rc3^2+rc3^2+rc3^2+rc3^2+rc3^2+rc3^2+rc3^2+rc3^2+rc3^2+rc3^2+rc3^2+rc3^2+rc3^2+rc3^2+rc3^2+rc3^2+rc3^2+rc3^2+rc3^2+rc3^2+rc3^2+rc3^2+rc3^2+rc3^2+rc3^2+rc3^2+rc3^2+rc3^2+rc3^2+rc3^2+rc3^2+rc3^2+rc3^2+rc3^2+rc3^2+rc3^2+rc3^2+rc3^2+rc3^2+rc3^2+rc3^2+rc3^2+rc3^2+rc3^2+rc3^2+rc3^2+rc3^2+rc3^2+rc3^2+rc3^2+rc3^2+rc3^2+rc3^2+rc3^2+rc3^2+rc3^2+rc3^2+rc3^2+rc3^2+rc3^2+rc3^2+rc3^2+rc3^2+rc3^2+rc3^2+rc3^2+rc3^2+rc3^2+rc3^2+rc3^2+rc3^2+rc3^2+rc3^2+rc3^2+rc3^2+rc3^2+rc3^2+rc3^2+rc3^2+rc3^2+rc3^2+rc3^2+rc3^2+rc3^2+rc3^2+rc3^2+rc3^2+rc3^2+rc3^2+rc3^2+rc3^2+rc3^2+rc3^2+rc3^2+rc3^2+rc3^2+rc3^2+rc3^2+rc3^2+rc3^2+rc3^2+rc3^2+rc3^2+rc3^2+rc3^2+rc3^2+rc3^2+rc3^2+rc3^2+rc3^2+rc3^2+rc3^2+rc3^2+rc3^2+rc3^2+rc3^2+rc3^2+rc3^2+rc3^2+rc3^2+rc3^2+rc3^2+rc3^2+rc3^2+rc3^2+rc3^2+rc3^2+rc3^2+rc3^2+rc3^2+rc3^2+rc3^2+rc3^2+rc3^2+rc3^2+rc3^2+rc3^2+rc3^2+rc3^2+rc3^2+rc3^2+rc3^2+rc3^2+rc3^2+rc3^2+rc3^2+rc3^2+rc3^2+rc3^2+rc3^2+rc3^2+rc3^2+rc3^2+rc3^2+rc3^2+rc3^2+rc3^2+rc3^2+rc3^2+rc3^2+rc3^2+rc3^2+rc3^2+rc3^2+rc3^2+rc3^2+rc3^2+rc3^2+rc3^2+rc3^2+rc3^2+rc3^2+rc3^2+rc3^2+rc3^2+rc3^2+rc3^2+rc3^2+rc3^2+rc3^2+rc3^2+rc3^2+rc3^2+rc3^2+rc3^2+rc3^2+rc3^2+rc3^2+rc3^2+rc3^2+rc3^2+rc3^2+rc3^2+rc3^2+rc3^2+rc3^2+rc3^2+rc3^2+rc3^2+rc3^2+rc3^2+rc3^2+rc3^2+rc3^2+rc3^2+rc3^2+rc3^2+rc3^2+rc3^2+rc3^2+rc3^2+rc3^2+rc3^2+rc3^2+rc3^2+rc3^2+rc3^2+rc3^2+rc3^2+rc3^2+rc3^2+rc3^2+rc3^2+rc3^2+rc3^2+rc3^2+rc3^2+rc3^2+rc3^2+rc3^2+rc3^2+rc3^2+rc3^2+rc3^2+rc3^2+rc3^2+rc3^2+rc3^2+rc3^2+rc3^2+rc3^2+rc3^2+rc3^2+rc3^2+rc3^2+rc3^2+rc3^2+rc3^2+rc3^2+rc3^2+rc3^2+rc3^2+rc3^2+rc3^2+rc3^2+rc3^2+rc3^2+rc3^2+rc3^2+rc3^2+rc3^2+rc3^2+rc3^2+rc3^2+rc3^2+rc3^2+rc3^2+rc3^2+rc3^2+rc3^2+rc3^2+rc3^2+rc3^2+rc3^2+rc3^2+rc3^2+rc3^2+rc3^2+rc3^2+rc3^2+rc3^2+rc3^2+rc3^2+rc3^2+rc3^2+rc3^2+rc3^2+rc3^2+rc3^2+rc3^2+rc3^2+rc3^2+rc3^2+rc3^2+rc3
-\cos(th3)^2*I3yy+2*\cos(th2)*\cos(th3)*I3xx*\sin(th3)*\sin(th2)-2*a2*\cos(th2)*rc3*m3*\sin(th3)*\sin(th2)
+2*a2*cos(th2)^2*rc3*m3*cos(th3)-2*cos(th2)*cos(th3)*rc3^2*m3*sin(th3)*sin(th2)
-\cos(th3)^2*rc3^2*m3-I1xx+I1zz
NCM_{\tau 0}(1,2) = -1/2*I3xx*cos(2*th3+2*th2)-I2zz*cos(2*th1)+I1xx*cos(2*th1)
+1/4*I3xx*cos(2*th2-2*th1+2*th3)+1/4*I3xx*cos(2*th2+2*th1+2*th3)-1/2*a2*rc3*m3*cos(th3-2*th1)
-1/2*a2*rc3*m3*cos(th3+2*th1)-1/4*rc2^2*m2*cos(-2*th1+2*th2)-1/4*rc2^2*m2*cos(2*th1+2*th2)
-1/2*rc2^2*m2*cos(2*th1)+1/2*I3yy*cos(2*th3+2*th2)-1/4*a2^2*m3*cos(-2*th1+2*th2)
-1/2*a2^2*m3*\cos(2*th1) + 1/2*I2yy*\cos(2*th1) + 1/2*I3xx + 1/2*I2yy + 1/2*I3yy + 1/2*I2xx + 1/2*a2^2*m3
```

 $+1/2*a2^2*m3*cos(2*th2)+a2*rc3*m3*cos(th3)+1/2*rc3^2*m3+1/2*rc2^2*m2$

-1/4*rc3^2*m3*cos(2*th2-2*th1+2*th3)-1/4*rc3^2*m3*cos(2*th2+2*th1+2*th3)
-1/2*rc3^2*m3*cos(2*th1)+I1yy+1/2*I3yy*cos(2*th1)+1/2*I2yy*cos(2*th2)
-1/2*a2*rc3*m3*cos(th3+2*th2-2*th1)-1/2*a2*rc3*m3*cos(th3+2*th2+2*th1)

+1/2*rc2^2*m2*cos(2*th2)-1/4*a2^2*m3*cos(2*th1+2*th2)+a2*rc3*m3*cos(2*th2+th3) -1/4*I2yy*cos(2*th1+2*th2)-1/4*I2yy*cos(-2*th1+2*th2)+1/4*I2xx*cos(2*th1+2*th2) +1/4*I2xx*cos(-2*th1+2*th2)+1/2*I3xx*cos(2*th1)+1/2*I2xx*cos(2*th1)-I1zz*cos(2*th1)

-1/4*I3yy*cos(2*th2+2*th1+2*th3)-1/4*I3yy*cos(2*th2-2*th1+2*th3)-1/2*I2xx*cos(2*th2)

```
NCM_{\tau 0}(1,3) = -1/2*I3yy*cos(2*th3+2*th2+th1)+1/2*I3yy*cos(2*th3+2*th2-th1)
-1/2*I3xx*cos(2*th3+2*th2-th1)+1/2*I3xx*cos(2*th3+2*th2+th1)-m3*rc3*d1*sin(-th1+th3+th2)
+m3*rc3*d1*sin(th1+th3+th2)+1/2*rc3^2*m3*cos(2*th3+2*th2-th1)
-1/2*rc3^2*m3*cos(2*th3+2*th2+th1) -1/2*m2*rc2^2*cos(2*th2+th1)+1/2*m2*rc2^2*cos(2*th2-th1)
+m3*rc3*a2*cos(2*th2+th3-th1)-m3*rc3*a2*cos(2*th2+th3+th1)-1/2*m3*a2^22*cos(2*th2+th1)
+1/2*m3*a2^2*cos(2*th2-th1)+1/2*I2xx*cos(2*th2+th1)-1/2*I2xx*cos(2*th2-th1)
-1/2*I2yy*cos(2*th2+th1)+1/2*I2yy*cos(2*th2-th1)-m3*rc3*d0*sin(-th1+th3+th2)
+m3*rc3*d0*sin(th1+th3+th2)+m3*a2*d0*sin(th2+th1)-m3*a2*d0*sin(th2-th1)
+m2*rc2*d1*sin(th2+th1)-m2*rc2*d1*sin(th2-th1)+m2*rc2*d0*sin(th2+th1)-m2*rc2*d0*sin(th2-th1)
-m3*a2*d1*sin(th2-th1)+m3*a2*d1*sin(th2+th1)
NCM_{\tau 0}(1,4) = 1/2*I3yy*sin(2*th3+2*th2)+1/4*I3yy*sin(2*th2-2*th1+2*th3)
+1/4*I3yy*sin(2*th2+2*th1+2*th3)-1/2*I2xx*sin(2*th2)-1/4*I2xx*sin(2*th1+2*th2)
-1/4*I2xx*sin(-2*th1+2*th2)+2*m3*rc3*d0*cos(th3+th2)+1/4*I2vv*sin(2*th1+2*th2)
+2*m3*rc3*d1*cos(th3+th2)+1/4*m2*rc2^2*sin(2*th1+2*th2)+1/4*m2*rc2^2*sin(-2*th1+2*th2)
+1/2*m2*rc2^2*sin(2*th2)+m3*rc3*a2*sin(2*th2+th3)+1/4*I2vy*sin(-2*th1+2*th2)
+1/2*I2yy*sin(2*th2)+1/2*m3*rc3*a2*sin(th3+2*th2-2*th1)+1/2*m3*rc3*a2*sin(th3+2*th2+2*th1)
+1/2*m3*rc3^2*sin(2*th3+2*th2)+1/4*m3*rc3^2*sin(2*th2+2*th1+2*th3)
+1/4*m3*rc3^2*sin(2*th2-2*th1+2*th3)+1/4*m3*a2^2*sin(2*th1+2*th2)
+1/4*m3*a2^2*sin(-2*th1+2*th2)+1/2*m3*a2^2*sin(2*th2)-1/4*I3xx*sin(2*th2-2*th1+2*th3)
-1/4*I3xx*sin(2*th2+2*th1+2*th3)-1/2*I3xx*sin(2*th3+2*th2)+2*m2*cos(th2)*rc2*d0
+2*m3*cos(th2)*a2*d0+2*m3*cos(th2)*a2*d1+2*m2*cos(th2)*rc2*d1
NCM_{\tau 0}(1.5) = -1/4*I2xx*cos(-2*th1+2*th2)+1/4*m2*rc2^2*cos(-2*th1+2*th2)
-1/4*m3*a2^2*cos(2*th1+2*th2)+1/4*m3*a2^2*cos(-2*th1+2*th2)-1/4*m2*rc2^2*cos(2*th1+2*th2)
+1/4*I2xx*cos(2*th1+2*th2)+1/2*m3*rc3*a2*cos(th3+2*th2-2*th1)
-1/2*m3*rc3*a2*cos(th3+2*th2+2*th1)-1/4*I2vy*cos(2*th1+2*th2)+1/4*I2vy*cos(-2*th1+2*th2)
-1/4*I3vv*cos(2*th2+2*th1+2*th3)+1/4*I3vv*cos(2*th2-2*th1+2*th3)
+1/4*I3xx*cos(2*th2+2*th1+2*th3)-1/4*I3xx*cos(2*th2-2*th1+2*th3)
-1/4*m3*rc3^2*cos(2*th2+2*th1+2*th3)+1/4*m3*rc3^2*cos(2*th2-2*th1+2*th3)
NCM_{\tau 0}(1.6) = -\cos(th1)*(-2*m2*rc2^2-I3xx-I2yy+I3yy+I2xx-I3zz-I2zz+2*m2*rc2^2*\cos(th2)^2
+4*I3vy*cos(th3)^2*cos(th2)^2-4*I3xx*cos(th3)^2*cos(th2)^2+2*m3*a2^2*cos(th2)^2
-2*m3*rc3^2*cos(th2)^2-2*cos(th3)^2*rc3^2*m3-4*cos(th2)*sin(th3)*m3*rc3^2*cos(th3)*sin(th2)
-4*cos(th2)*sin(th3)*m3*rc3*sin(th2)*a2-2*m3*cos(th3)*sin(th2)*rc3*d1
-4*\cos(th2)*\cos(th3)*I3vv*\sin(th3)*\sin(th2)-2*m3*\sin(th3)*\cos(th2)*rc3*d1-2*m2*\sin(th2)*rc2*d1
-2*m3*sin(th2)*a2*d1-4*a2*rc3*m3*cos(th3)+2*I2yy*cos(th2)^2
+4*cos(th2)*cos(th3)*I3xx*sin(th3)*sin(th2) -2*m2*sin(th2)*rc2*d0-2*m3*sin(th2)*a2*d0
+4*m3*rc3^2*cos(th2)^2*cos(th3)^2+4*cos(th3)*m3*rc3*a2*cos(th2)^2
-2*m3*cos(th3)*sin(th2)*rc3*d0-2*m3*sin(th3)*cos(th2)*rc3*d0-2*I2xx*cos(th2)^2+2*cos(th3)^2*I3xx
-2*\cos(th3)^2*I3yy+2*I3xx*\cos(th2)^2-2*I3yy*\cos(th2)^2-2*m3*a2^2
NCM_{\tau 0}(1.7) = 1/2*I3vv*sin(2*th3+2*th2)+1/4*I3vv*sin(2*th2-2*th1+2*th3)
+1/4*I3yy*sin(2*th2+2*th1+2*th3)-3/2*sin(th3)*m3*rc3*a2-1/2*I3xx*sin(2*th3+2*th2)
+1/4*m3*rc3*a2*sin(th3+2*th1)+1/4*m3*rc3*a2*sin(th3-2*th1)-1/4*I3xx*sin(2*th2+2*th1+2*th3)
-1/4*I3xx*sin(2*th2-2*th1+2*th3)+1/2*m3*rc3^2*sin(2*th3+2*th2)
+1/4*m3*rc3^2*sin(2*th2+2*th1+2*th3)+1/4*m3*rc3^2*sin(2*th2-2*th1+2*th3)
+1/2*m3*rc3*a2*sin(2*th2+th3)+1/4*m3*rc3*a2*sin(th3+2*th2-2*th1)
+1/4*m3*rc3*a2*sin(th3+2*th2+2*th1)+2*m3*rc3*d0*cos(th3+th2)+2*m3*rc3*d1*cos(th3+th2)
```

 $-13zz*cos(2*th1)+1/2*rc3^2*m3*cos(2*th3+2*th2)$

```
NCM_{\tau 0}(1.8) = -1/4*m3*rc3*a2*cos(th3+2*th1)+1/4*m3*rc3*a2*cos(th3-2*th1)
-1/4*m3*rc3^2*cos(2*th2+2*th1+2*th3)+1/4*m3*rc3^2*cos(2*th2-2*th1+2*th3)
+1/4*I3xx*cos(2*th2+2*th1+2*th3)-1/4*I3xx*cos(2*th2-2*th1+2*th3)
-1/4*m3*rc3*a2*cos(th3+2*th2+2*th1)+1/4*I3yy*cos(2*th2-2*th1+2*th3)
+1/4*m3*rc3*a2*cos(th3+2*th2-2*th1)-1/4*I3yy*cos(2*th2+2*th1+2*th3)
NCM_{\tau 0}(1.9) = 1/2*I3xx*cos(2*th3+2*th2+th1)+1/2*I3xx*cos(2*th3+2*th2-th1)
-1/2*m3*rc3^2*cos(2*th3+2*th2-th1)-1/2*m3*rc3^2*cos(2*th3+2*th2+th1)
+m3*rc3*d0*sin(th1+th3+th2)+m3*rc3*d0*sin(-th1+th3+th2)-1/2*m3*rc3*a2*cos(2*th2+th3+th1)
-1/2*m3*rc3*a2*cos(2*th2+th3-th1)+m3*rc3*d1*sin(-th1+th3+th2)+m3*rc3*d1*sin(th1+th3+th2)
+\cos(th1)*m3*rc3^2-1/2*I3vv*cos(2*th3+2*th2+th1)-1/2*I3vv*cos(2*th3+2*th2-th1)
+1/2*m3*rc3*a2*cos(th3-th1)+1/2*m3*rc3*a2*cos(th3+th1)+cos(th1)*I3zz
NCM_{\tau 0}(2,1) = -4*I3vv*cos(th3)^2*cos(th2)^2*cos(th1)^2-I1xx+2*I1xx*cos(th1)^2+2*I2vv*cos(th1)^2
-13xx-12yy-13yy-12xx-11yy+11zz-2*cos(th2)^2*cos(th1)^2*12yy+2*cos(th2)^2*12xx*cos(th1)^2
-2*m3*rc3^2*cos(th1)^2+2*I3yy*cos(th2)^2*cos(th1)^2+2*I3xx*cos(th1)^2-2*cos(th1)^2*I3zz
-2*I1zz*cos(th1)^2-2*I2zz*cos(th1)^2-4*I3xx*cos(th3)*sin(th2)*sin(th3)*cos(th2)*cos(th1)^2
-4*m3*rc3*cos(th3)*cos(th2)^2*cos(th1)^2*a2+4*m3*rc3*sin(th3)*sin(th2)*cos(th1)^2*a2*cos(th2)
+4*m3*rc3^2*cos(th3)*sin(th2)*sin(th3)*cos(th2)*cos(th1)^2
-4*m3*rc3^2*cos(th3)^2*cos(th2)^2*cos(th1)^2+4*I3yy*cos(th3)*sin(th2)*sin(th3)*cos(th2)*cos(th1)^2
+4*I3xx*cos(th3)^2*cos(th2)^2*cos(th1)^2-2*m2*cos(th2)^2*cos(th1)^2*rc2^2
+2*m3*rc3^2*cos(th1)^2*cos(th2)^2+2*m3*rc3^2*cos(th1)^2*cos(th3)^2
-2*m3*cos(th1)^2 + a2^2 + cos(th2)^2 + 2*I3yy*cos(th3)^2 + cos(th1)^2 - 2*I3xx*cos(th3)^2 + cos(th1)^2 + (cos(th3)^2 + cos(th3)^2 + (cos(th3)^2 + (cos(th3)^2 + cos(th3)^2 + (cos(th3)^2 + (cos(th3)^2 + cos(th3)^2 + (cos(th3)^2 + (cos(th
-2*I3xx*cos(th2)^2*cos(th1)^2+I3zz+I2zz
NCM_{70}(2.2) = 2*\sin(th1)*\cos(th1)*(-m3*rc3^2-2*\cos(th2)^2*\cos(th3)^2*rc3^2*m3+I1xx+I3xx+I2vv
-I1zz+cos(th3)^2*I3yy-cos(th3)^2*I3xx-I3zz-cos(th2)^2*I2yy- I2zz+cos(th2)^2*I2xx
+2*cos(th2)*a2*sin(th2)*sin(th3)*rc3*m3+2*cos(th2)*sin(th3)*sin(th2)*cos(th3)*rc3^2*m3
-cos(th2)^2*I3xx-2*a2*cos(th2)^2*cos(th3)*rc3*m3-2*cos(th2)*sin(th3)*sin(th2)*cos(th3)*I3xx
+2*cos(th2)*sin(th3)*sin(th2)*cos(th3)*I3yy+cos(th2)^2*I3yy- a2^2*cos(th2)^2*m3
+2*cos(th2)^2*cos(th3)^2*I3xx-rc2^2*cos(th2)^2*m2+cos(th2)^2*rc3^2*m3
-2*\cos(th2)^2*\cos(th3)^2*I3yy+\cos(th3)^2*rc3^2*m3
NCM_{70}(2,3) = 1/2*I2xx*sin(2*th2-th1)-1/2*I2vy*sin(2*th2+th1)-1/2*m2*rc2^2*sin(2*th2-th1)
-1/2*m2*rc2^2*sin(2*th2+th1)+1/2*I2xx*sin(2*th2+th1)-1/2*I2yy*sin(2*th2-th1)
-m2*rc2*d0*cos(th2-th1)-m2*rc2*d0*cos(th2+th1)-m3*a2*d0*cos(th2-th1)-m3*a2*d0*cos(th2-th1)
-m3*rc3*d0*cos(th1+th3+th2)-m3*rc3*d0*cos(-th1+th3+th2)-m3*a2*d1*cos(th2-th1)
-m3*a2*d1*cos(th2+th1)-m3*rc3*d1*cos(-th1+th3+th2)-m3*rc3*d1*cos(th1+th3+th2)
-1/2*m3*a2^2*sin(2*th2+th1)-1/2*m3*a2^2*sin(2*th2-th1)-m3*rc3*a2*sin(2*th2+th3+th1)
-m3*rc3*a2*sin(2*th2+th3-th1)-m2*rc2*d1*cos(th2-th1)- m2*rc2*d1*cos(th2+th1)
+1/2*I3xx*sin(2*th3+2*th2-th1)+1/2*I3xx*sin(2*th3+2*th2+th1)-1/2*I3yy*sin(2*th3+2*th2-th1)
-1/2*I3yy*sin(2*th3+2*th2+th1)-1/2*m3*rc3^2*sin(2*th3+2*th2-th1)
-1/2*m3*rc3^2*sin(2*th3+2*th2+th1)
NCM_{\tau 0}(2,4) = -1/4*I3xx*cos(2*th2-2*th1+2*th3)+1/4*I3xx*cos(2*th2+2*th1+2*th3)
-1/4*m3*rc3^2*cos(2*th2+2*th1+2*th3)-1/4*I3yy*cos(2*th2+2*th1+2*th3)
+1/4*I3vv*cos(2*th2-2*th1+2*th3)+1/4*m3*rc3^2*cos(2*th2-2*th1+2*th3)
-1/4*m2*rc2^2*cos(2*th1+2*th2)+1/4*m2*rc2^2*cos(-2*th1+2*th2)
+1/2*m3*rc3*a2*cos(th3+2*th2-2*th1)-1/2*m3*rc3*a2*cos(th3+2*th2+2*th1)
-1/4*I2yy*cos(2*th1+2*th2)+1/4*I2yy*cos(-2*th1+2*th2)-1/4*m3*a2^2*cos(2*th1+2*th2)
+1/4*m3*a2^2*cos(-2*th1+2*th2)+1/4*I2xx*cos(2*th1+2*th2)-1/4*I2xx*cos(-2*th1+2*th2)
```

```
NCM_{\tau 0}(2.5) = -1/2*I3xx*sin(2*th3+2*th2)+1/4*I3xx*sin(2*th2+2*th1+2*th3)
+1/4*I3xx*sin(2*th2-2*th1+2*th3)-1/4*I3yy*sin(2*th2-2*th1+2*th3)-1/4*I3yy*sin(2*th2+2*th1+2*th3)
-1/4*m3*rc3^2*sin(2*th2-2*th1+2*th3)-1/4*m3*rc3^2*sin(2*th2+2*th1+2*th3)-1/2*I2xx*sin(2*th2)
+1/2*m3*rc3^2*sin(2*th3+2*th2)+1/2*I2yy*sin(2*th2)+1/2*I3yy*sin(2*th3+2*th2)
-1/4*m3*a2^2*sin(-2*th1+2*th2)+1/2*m3*a2^2*sin(2*th2)-1/4*m3*a2^2*sin(2*th1+2*th2)
-1/4*m2*rc2^2*sin(2*th1+2*th2)-1/4*m2*rc2^2*sin(-2*th1+2*th2)+1/2*m2*rc2^2*sin(2*th2)
+2*m3*rc3*d1*cos(th3+th2)+2*m3*rc3*d0*cos(th3+th2)+1/4*I2xx*sin(2*th1+2*th2)
+1/4*I2xx*sin(-2*th1+2*th2)+m3*rc3*a2*sin(2*th2+th3)-1/4*I2vv*sin(2*th1+2*th2)
-1/4*I2vv*sin(-2*th1+2*th2)+2*m2*cos(th2)*rc2*d1+2*m2*cos(th2)*rc2*d0
-1/2*m3*rc3*a2*sin(th3+2*th2-2*th1)-1/2*m3*rc3*a2*sin(th3+2*th2+2*th1)+2*m3*cos(th2)*a2*d1
+2*m3*cos(th2)*a2*d0
NCM_{\tau 0}(2,6) = -\sin(th1)*(-2*\cos(th3)^2*rc3^2*m3+2*m2*rc2^2*\cos(th2)^2-2*m3*rc3^2*\cos(th2)^2
-4*I3xx*cos(th3)^2*cos(th2)^2+4*I3yy*cos(th3)^2*cos(th2)^2+2*m3*a2^2*cos(th2)^2-4*I3yy*cos(th3)^2*cos(th2)^2+2*m3*a2^2*cos(th2)^2-4*I3yy*cos(th3)^2*cos(th2)^2+2*m3*a2^2*cos(th2)^2-4*I3yy*cos(th3)^2*cos(th2)^2+2*m3*a2^2*cos(th2)^2-4*I3yy*cos(th3)^2*cos(th2)^2+2*m3*a2^2*cos(th2)^2-4*I3yy*cos(th3)^2*cos(th2)^2+2*m3*a2^2*cos(th2)^2-4*I3yy*cos(th3)^2*cos(th2)^2+2*m3*a2^2*cos(th2)^2+2*m3*a2^2*cos(th2)^2+2*m3*a2^2*cos(th2)^2+2*m3*a2^2*cos(th2)^2+2*m3*a2^2*cos(th2)^2+2*m3*a2^2*cos(th2)^2+2*m3*a2^2*cos(th2)^2+2*m3*a2^2*cos(th2)^2+2*m3*a2^2*cos(th2)^2+2*m3*a2^2*cos(th2)^2+2*m3*a2^2*cos(th2)^2+2*m3*a2^2*cos(th2)^2+2*m3*a2^2*cos(th2)^2+2*m3*a2^2*cos(th2)^2+2*m3*a2^2*cos(th2)^2+2*m3*a2^2*cos(th2)^2+2*m3*a2^2*cos(th2)^2+2*m3*a2^2*cos(th2)^2+2*m3*a2^2*cos(th2)^2+2*m3*a2^2*cos(th2)^2+2*m3*a2^2*cos(th2)^2+2*m3*a2^2*cos(th2)^2+2*m3*a2^2*cos(th2)^2+2*m3*a2^2*cos(th2)^2+2*m3*a2^2*cos(th2)^2+2*m3*a2^2*cos(th2)^2+2*m3*a2^2*cos(th2)^2+2*m3*a2^2*cos(th2)^2+2*m3*a2^2*cos(th2)^2+2*m3*a2^2*cos(th2)^2+2*m3*a2^2*cos(th2)^2+2*m3*a2^2*cos(th2)^2+2*m3*a2^2*cos(th2)^2+2*m3*a2^2*cos(th2)^2+2*m3*a2^2*cos(th2)^2+2*m3*a2^2*cos(th2)^2+2*m3*a2^2*cos(th2)^2+2*m3*a2^2*cos(th2)^2+2*m3*a2^2*cos(th2)^2+2*m3*a2^2*cos(th2)^2+2*m3*a2^2*cos(th2)^2+2*m3*a2^2*cos(th2)^2+2*m3*a2^2*cos(th2)^2+2*m3*a2^2*cos(th2)^2+2*m3*a2^2*cos(th2)^2+2*m3*a2^2*cos(th2)^2+2*m3*a2^2*cos(th2)^2+2*m3*a2^2*cos(th2)^2+2*m3*a2^2*cos(th2)^2+2*m3*a2^2*cos(th2)^2+2*m3*a2^2*cos(th2)^2+2*m3*a2^2*cos(th2)^2+2*m3*a2^2*cos(th2)^2+2*m3*a2^2*cos(th2)^2+2*m3*a2^2*cos(th2)^2+2*m3*a2^2*cos(th2)^2+2*m3*a2^2*cos(th2)^2+2*m3*a2^2*cos(th2)^2+2*m3*a2^2*cos(th2)^2+2*m3*a2^2*cos(th2)^2+2*m3*a2^2*cos(th2)^2+2*m3*a2^2*cos(th2)^2+2*m3*a2^2*cos(th2)^2+2*m3*a2^2*cos(th2)^2+2*m3*a2^2*cos(th2)^2+2*m3*a2^2*cos(th2)^2+2*m3*a2^2*cos(th2)^2+2*m3*a2^2*cos(th2)^2+2*m3*a2^2*cos(th2)^2+2*m3*a2^2*cos(th2)^2+2*m3*a2^2*cos(th2)^2+2*m3*a2^2*cos(th2)^2+2*m3*a2^2*cos(th2)^2+2*m3*a2^2*cos(th2)^2+2*m3*a2^2*cos(th2)^2+2*m3*a2^2*cos(th2)^2+2*cos(th2)^2+2*cos(th2)^2+2*cos(th2)^2+2*cos(th2)^2+2*cos(th2)^2+2*cos(th2)^2+2*cos(th2)^
2*a2^2*m3+I2xx-I3xx+I3yy-I2yy-I2zz-I3zz+2*cos(th3)^2*I3xx-2*cos(th3)^2*I3yy+2*I2yy*cos(th2)^2
-2*I3vv*cos(th2)^2+2*I3xx*cos(th2)^2-2*I2xx*cos(th2)^2-2*m2*sin(th2)*rc2*d1-2*m2*rc2^2
-2*m3*sin(th2)*a2*d1-2*m3*sin(th3)*cos(th2)*rc3*d0-2*m3*cos(th3)*sin(th2)*rc3*d0
-4*cos(th2)*sin(th3)*m3*rc3*sin(th2)*a2-2*m3*sin(th3)*cos(th2)*rc3*d1
+4*cos(th3)*m3*rc3*a2*cos(th2)^2-2*m3*cos(th3)*sin(th2)*rc3*d1-2*m2*sin(th2)*rc2*d0
+4*m3*rc3^2*cos(th2)^2*cos(th3)^2-2*m3*sin(th2)*a2*d0
-4*\cos(th2)*\sin(th3)*m3*rc3^2*\cos(th3)*\sin(th2)
-4*cos(th2)*cos(th3)*I3yy*sin(th3)*sin(th2)+4*cos(th2)*cos(th3)*I3xx*sin(th3)*sin(th2)
-4*a2*rc3*m3*cos(th3))
NCM_{\tau 0}(2,7) = -1/4*m3*rc3*a2*cos(th3+2*th1)+1/4*m3*rc3*a2*cos(-th3+2*th1)
+1/4*I3vy*cos(-2*th2+2*th1-2*th3)-1/4*I3xx*cos(-2*th2+2*th1-2*th3)
-1/4*m3*rc3*a2*cos(th3+2*th2+2*th1)+1/4*I3xx*cos(2*th2+2*th1+2*th3)
-1/4*I3yy*cos(2*th2+2*th1+2*th3)+1/4*m3*rc3^2*cos(-2*th2+2*th1-2*th3)
-1/4*m3*rc3^2*cos(2*th2+2*th1+2*th3)+1/4*m3*rc3*a2*cos(-th3-2*th2+2*th1)
NCM_{\tau 0}(2.8) = 2*m3*rc3*d0*cos(th3+th2)-1/2*I3xx*sin(2*th3+2*th2)
+1/4*m3*rc3^2*sin(-2*th2+2*th1-2*th3)-1/4*m3*rc3^2*sin(2*th2+2*th1+2*th3)
-3/2*m3*sin(th3)*rc3*a2+1/2*m3*rc3^2*sin(2*th3+2*th2) +1/2*I3yy*sin(2*th3+2*th2)
+2*m3*rc3*d1*cos(th3+th2)-1/4*m3*rc3*a2*sin(th3+2*th2+2*th1)
+1/4*m3*rc3*a2*sin(-th3-2*th2+2*th1)-1/4*I3vv*sin(2*th2+2*th1+2*th3)
+1/4*I3vv*sin(-2*th2+2*th1-2*th3)+1/2*m3*rc3*a2*sin(th3+2*th2)
-1/4*m3*rc3*a2*sin(th3+2*th1)+1/4*m3*rc3*a2*sin(-th3+2*th1)+1/4*13xx*sin(2*th2+2*th1+2*th3)
-1/4*I3xx*sin(-2*th2+2*th1-2*th3)
NCM_{\tau 0}(2.9) = m3*rc3*d0*cos(-th2+th1-th3)-m3*rc3*d0*cos(th2+th1+th3)
-m3*rc3*d1*cos(th2+th1+th3)+m3*rc3*d1*cos(-th2+th1-th3)+sin(th1)*I3zz+sin(th1)*m3*rc3^2
+1/2*m3*rc3*a2*sin(th1+th3)+1/2*m3*rc3*a2*sin(th1-th3)-1/2*m3*rc3^2*sin(2*th2+th1+2*th3)
-1/2*m3*rc3^2*sin(-2*th2+th1-2*th3)+1/2*I3xx*sin(2*th2+th1+2*th3)+1/2*I3xx*sin(-2*th2+th1-2*th3)
-1/2*I3yy*sin(2*th2+th1+2*th3)-1/2*I3yy*sin(-2*th2+th1-2*th3)-1/2*m3*rc3*a2*sin(2*th2+th1+th3)
-1/2*m3*rc3*a2*sin(-2*th2+th1-th3)
NCM_{\tau 0}(3,1)=0
NCM_{\tau 0}(3,2)=0
NCM_{\tau 0}(3,3)=0
```

```
NCM_{\tau 0}(3,4) = \cos(th1) * (2*m3*rc3^2*\cos(th3)^2 + 2*m3*rc3^2*\cos(th2)^2 - 2*m2*\cos(th2)^2 + rc2^2
-4*I3yy*cos(th3)^2*cos(th2)^2+4*I3xx*cos(th3)^2*cos(th2)^2-2*m3*cos(th2)^2*a2^2-2*m3*rc3^2
-2*I2yy*cos(th2)^2+2*I2xx*cos(th2)^2-2*I3xx*cos(th2)^2+2*I3yy*cos(th2)^2+2*I3yy*cos(th3)^2
-2*I3xx*cos(th3)^2-4*sin(th2)*sin(th3)*I3xx*cos(th3)*cos(th2)
+4*sin(th2)*sin(th3)*I3yy*cos(th3)*cos(th2)- 4*cos(th3)*m3*rc3*cos(th2)^2*a2
+4*sin(th2)*sin(th3)*m3*rc3*cos(th2)*a2+4*sin(th2)*sin(th3)*m3*rc3^2*cos(th3)*cos(th2)+I3xx-I3vv
-4*m3*rc3^2*cos(th3)^2*cos(th2)^2-I3zz-I2zz+I2yy-I2xx)
NCM_{\tau 0}(3.5) = -\sin(th1)*(2*m3*rc3^2-I3xx+I3yy+I3zz-2*m3*rc3^2*cos(th3)^2
+4*I3yy*cos(th3)^2*cos(th2)^2+2*m3*cos(th2)^2*a2^2-4*I3xx*cos(th3)^2*cos(th2)^2
-4*sin(th2)*sin(th3)*m3*rc3^2*cos(th3)*cos(th2)+4*sin(th2)*cos(th3)*I3xx*sin(th3)*cos(th2)
+2*I3xx*\cos(th2)^2-4*\sin(th2)*\cos(th3)*I3yy*\sin(th3)*\cos(th2)-4*\sin(th2)*\sin(th3)*m3*rc3*\cos(th2)*a2
+4*cos(th3)*m3*rc3*cos(th2)^2*a2-2*I2xx*cos(th2)^2-2*I3yy*cos(th3)^2-2*I3yy*cos(th2)^2
+2*I3xx*\cos(th3)^2+2*I2yy*\cos(th2)^2+4*m3*rc3^2*\cos(th3)^2*\cos(th2)^2+2*m2*\cos(th2)^2+rc2^2
-2*m3*rc3^2*cos(th2)^2+I2zz-I2yy+I2xx
NCM_{\tau 0}(3.6) = 13xx*sin(2*th3+2*th2)-m3*rc3^2*sin(2*th3+2*th2)-13yy*sin(2*th3+2*th2)
-2*m3*rc3*a2*sin(th3+2*th2)+I2xx*sin(2*th2)-m3*a2^2*sin(2*th2)-I2yy*sin(2*th2)
-m2*rc2^2*sin(2*th2)
NCM_{\tau 0}(3,7) = -I3zz*cos(th1)-1/2*m3*rc3*a2*cos(2*th2+th1+th3)-m3*rc3^2*cos(th1)
-1/2*m3*rc3^2*cos(-2*th2+th1-2*th3)-1/2*m3*rc3^2*cos(2*th2+th1+2*th3)
+1/2*I3xx*cos(-2*th2+th1-2*th3)+1/2*I3xx*cos(2*th2+th1+2*th3)-1/2*I3yy*cos(-2*th2+th1-2*th3)
-1/2*I3yy*cos(2*th2+th1+2*th3)
NCM_{\tau 0}(3.8) = 1/2*I3xx*sin(-2*th2+th1-2*th3)-1/2*m3*rc3*a2*sin(2*th2+th1+th3)
-1/2*m3*rc3*a2*sin(-2*th2+th1-th3)-1/2*m3*rc3*a2*sin(th1+th3)-1/2*m3*rc3*a2*sin(th1-th3)
-I3zz*sin(th1)+1/2*I3xx*sin(2*th2+th1+2*th3)-1/2*I3yy*sin(2*th2+th1+2*th3)
-1/2*I3yy*sin(-2*th2+th1-2*th3)-1/2*m3*rc3^2*sin(-2*th2+th1-2*th3)
-1/2*m3*rc3^2*sin(2*th2+th1+2*th3)-m3*rc3^2*sin(th1)
NCM_{\tau_0}(3,9) = -m3*\sin(th3)*rc3*a2-m3*rc3*a2*\sin(th3+2*th2)+I3xx*\sin(2*th3+2*th2)
-m3*rc3^2*sin(2*th3+2*th2)-I3yy*sin(2*th3+2*th2)
                                                                                         (A-22)
```

A.1.3. Joint Torque Effects

Rigid Inertia Joint Torques

$$B_{\tau} = \begin{bmatrix} E + L - (G + E + J - K)c_{2}^{2} - (E + J)c_{3}^{2} + 2c_{2}c_{23}[N + (E + J)c_{3}] & 0 & 0 \\ 0 & E + H + K + 2Nc_{3} & E + I_{3zz} + Nc_{3} \\ 0 & E + I_{3zz} + Nc_{3} & E + I_{3zz} \end{bmatrix}$$
 (A-23)

Rigid Coriolis Joint Torques

```
\begin{array}{l} NR_{\tau}(1,1) = -Ksin(2*th2) - I2yy*sin(2*th2) - E*sin(2*th3+2*th2) - 2*B*a2*sin(2*th2+th3) \\ + I2xx*sin(2*th2) - I3yy*sin(2*th3+2*th2) + I3xx*sin(2*th3+2*th2) \\ NR_{\tau}(1,2) = -B*sin(th3)*a2 - E*sin(2*th3+2*th2) - B*a2*sin(2*th2+th3) - J*sin(2*th3+2*th2) \\ NR_{\tau}(2,3) = -2*sin(th3)*B*a2 \\ NR_{\tau}(1,3) = NR_{\tau}(2,1) = NR_{\tau}(2,2) = NR_{\tau}(3,1) = NR_{\tau}(3,2) = NR_{\tau}(3,3) = 0 \end{array} \tag{A-24}
```

Rigid Centrifugal Joint Torques

$$\label{eq:NRtilde} \begin{split} NR_{\tau}(2,1) &= 1/2*(E+J)*\sin(2*th3+2*th2) + 1/2*(K-G)*\sin(2*th2) + B*a2*\sin(2*th2+th3) \\ NR_{\tau}(2,3) &= -\sin(th3)*B*a2 \\ NR_{\tau}(3,1) &= 1/2*(E+J)*\sin(2*th3+2*th2) + 1/2*\sin(th3)*B*a2 + 1/2*B*a2*\sin(2*th2+th3) \\ NR_{\tau}(3,2) &= \sin(th3)*B*a2 \\ NC_{\tau}(1,1) &= NR_{\tau}(1,2) = NR_{\tau}(1,3) = NR_{\tau}(2,2) = NR_{\tau}(3,3) = 0 \end{split} \tag{A-25}$$

Rigid Gravitational Joint Torques

$$G_{\tau} = \begin{bmatrix} 0 \\ Bg\cos(\theta_2 + \theta_3) + Ag\cos\theta_2 \\ Bg\cos(\theta_2 + \theta_3) \end{bmatrix}$$
(A-26)

Flexible Body Inertia Joint Torques

```
 A_{\tau}(1,1) = -\sin(th1)^*(-B^*\sin(th3)^*\sin(th2) + \cos(th2)^*B^*\cos(th3) + A^*\cos(th2)) \\ A_{\tau}(1,2) = \cos(th1)^*(-B^*\sin(th3)^*\sin(th2) + \cos(th2)^*B^*\cos(th3) + A^*\cos(th2)) \\ A_{\tau}(1,3) = 0 \\ A_{\tau}(2,1) = -\cos(th1)^*(B^*\sin(th3)^*\cos(th2) + B^*\cos(th3)^*\sin(th2) + A^*\sin(th2)) \\ A_{\tau}(2,2) = -\sin(th1)^*(B^*\sin(th3)^*\cos(th2) + B^*\cos(th3)^*\sin(th2) + A^*\sin(th2)) \\ A_{\tau}(2,3) = B^*\cos(th2 + th3) + A^*\cos(th2) \\ A_{\tau}(3,1) = -B^*\cos(th1)^*(\sin(th3)^*\cos(th2) + \cos(th3)^*\sin(th2)) \\ A_{\tau}(3,2) = -B^*\sin(th1)^*(\sin(th3)^*\cos(th2) + \cos(th3)^*\sin(th2)) \\ A_{\tau}(3,3) = B^*\cos(th2 + th3)
```

Flexible Body Coriolis Joint Torques

```
NRC_{\tau}(1,1) = (2*\cos(th1)^2-1)*(2*I3yy*\cos(th2)^2*\cos(th3)^2-2*\sin(th2)*\cos(th3)*I3yy*\sin(th3)*\cos(th2) \\ +m3*\cos(th2)^2*a2^2-2*I3xx*\cos(th3)^2+\cos(th2)^2+I3xx*\cos(th3)^2-m3*rc3^2*\cos(th2)^2 \\ -m3*rc3^2*\cos(th3)^2+I1zz-I3xx-I2yy+I2yy*\cos(th2)^2-I2xx*\cos(th2)^2+I2zz+I3zz-I3yy*\cos(th2)^2 \\ +m3*rc3^2+I3xx*\cos(th2)^2-I3yy*\cos(th3)^2-I1xx+2*m3*rc3^2*\cos(th3)^2*\cos(th2)^2 \\ +m2*\cos(th2)^2*rc2^2+2*\cos(th3)*m3*rc3*\cos(th2)^2*a2+2*\sin(th2)*\sin(th3)*I3xx*\cos(th3)*\cos(th2) \\ -2*\sin(th2)*\sin(th3)*m3*rc3*\cos(th2)*a2-2*\sin(th2)*\sin(th3)*m3*rc3^2*\cos(th3)*\cos(th2) \\ \end{aligned}
```

 $NRC_{\tau}(1,2) = -\sin(th1) * (-\cos(th3) * 13yy * \sin(th3) + \sin(th2) * 12yy * \cos(th2) + \sin(th2) * 13xx * \cos(th2) + \sin(th3) * 13xx * \cos(th3) - \cos(th2) * 13yy * \sin(th2) + 2 * \cos(th3) * m3 * rc3 ^ 2 * \sin(th3) * \cos(th2) ^ 2 \\ + \cos(th2) * rc2 * m2 * d0 + \cos(th2) * m3 * d1 * a2 - 2 * \cos(th3) * 13xx * \sin(th3) * \cos(th2) ^ 2$

```
+\cos(th2)*\cos(th3)*m3*rc3*d0+2*m3*\sin(th3)*\cos(th2)^2*rc3*a2+\cos(th2)*\cos(th3)*m3*rc3*d1
+2*cos(th2)*cos(th3)*m3*rc3*sin(th2)*a2+cos(th2)*m3*sin(th2)*a2^2+cos(th2)*m2*sin(th2)*rc2^2
-\sin(th2)*m3*rc3^2*\cos(th2)-2*\cos(th2)*I3xx*\cos(th3)^2*\sin(th2)-\sin(th2)*\sin(th3)*m3*rc3*d0
-sin(th2)*sin(th3)*m3*rc3*d1-sin(th3)*m3*rc3*a2- sin(th3)*m3*rc3^2*cos(th3)+cos(th2)*m3*d0*a2
+2*\sin(th3)*I3yy*\cos(th3)*\cos(th2)^2+2*\sin(th2)*I3yy*\cos(th3)^2*\cos(th2)
+2*\cos(th2)*m3*rc3^2*\cos(th3)^2*\sin(th2)-\cos(th2)*I2xx*\sin(th2)+\cos(th2)*rc2*m2*d1
NRC_{\tau}(1,3) = \cos(th1)^*(-\cos(th2)^*13vv^*\sin(th2) + \sin(th2)^*13xx^*\cos(th2) - \cos(th3)^*13vv^*\sin(th3)
-\cos(th2)*I2xx*\sin(th2)+\sin(th2)*I2vv*\cos(th2)+\sin(th3)*I3xx*\cos(th3)
+2*cos(th3)*m3*rc3^2*sin(th3)*cos(th2)^2-sin(th3)*m3*rc3^2*cos(th3)- sin(th3)*m3*rc3*a2
+2*m3*sin(th3)*cos(th2)^2*rc3*a2-sin(th2)*sin(th3)*m3*rc3*d1-sin(th2)*m3*rc3^2*cos(th2)
+2*sin(th3)*I3yy*cos(th3)*cos(th2)^2-2*cos(th3)*I3xx*sin(th3)*cos(th2)^2
-2*\cos(th2)*I3xx*\cos(th3)^2*\sin(th2)-\sin(th2)*\sin(th3)*m3*rc3*d0
+2*cos(th2)*cos(th3)*m3*rc3*sin(th2)*a2+cos(th2)*m2*sin(th2)*rc2^2+cos(th2)*rc2*m2*d1
+\cos(th2)*rc2*m2*d0+\cos(th2)*m3*d0*a2+\cos(th2)*m3*d1*a2+\cos(th2)*\cos(th3)*m3*rc3*d1*a2+\cos(th2)*a2+\cos(th3)*m3*rc3*d1*a2+\cos(th3)*m3*rc3*d1*a2+\cos(th3)*m3*rc3*d1*a2+\cos(th3)*m3*rc3*d1*a2+\cos(th3)*m3*d1*a2+\cos(th3)*m3*rc3*d1*a2+\cos(th3)*m3*rc3*d1*a2+\cos(th3)*m3*rc3*d1*a2+\cos(th3)*m3*rc3*d1*a2+\cos(th3)*m3*rc3*d1*a2+\cos(th3)*m3*rc3*d1*a2+\cos(th3)*m3*rc3*d1*a2+\cos(th3)*m3*rc3*d1*a2+\cos(th3)*m3*rc3*d1*a2+\cos(th3)*m3*rc3*d1*a2+\cos(th3)*m3*rc3*d1*a2+\cos(th3)*m3*rc3*d1*a2+\cos(th3)*m3*rc3*d1*a2+\cos(th3)*m3*rc3*d1*a2+\cos(th3)*m3*rc3*d1*a2+\cos(th3)*m3*rc3*d1*a2+\cos(th3)*m3*rc3*d1*a2+\cos(th3)*m3*rc3*d1*a2+\cos(th3)*m3*rc3*d1*a2+\cos(th3)*m3*rc3*d1*a2+\cos(th3)*m3*rc3*d1*a2+\cos(th3)*m3*rc3*d1*a2+\cos(th3)*m3*rc3*d1*a2+\cos(th3)*m3*rc3*d1*a2+\cos(th3)*m3*rc3*d1*a2+\cos(th3)*m3*rc3*d1*a2+\cos(th3)*m3*rc3*d1*a2+\cos(th3)*m3*rc3*d1*a2+\cos(th3)*m3*rc3*d1*a2+\cos(th3)*m3*rc3*d1*a2+\cos(th3)*m3*rc3*d1*a2+\cos(th3)*m3*rc3*d1*a2+\cos(th3)*m3*rc3*d1*a2+cos(th3)*m3*rc3*d1*a2+cos(th3)*cos(th3)*cos(th3)*cos(th3)*cos(th3)*cos(th3)*cos(th3)*cos(th3)*cos(th3)*cos(th3)*cos(th3)*cos(th3)*cos(th3)*cos(th3)*cos(th3)*cos(th3)*cos(th3)*cos(th3)*cos(th3)*cos(th3)*cos(th3)*cos(th3)*cos(th3)*cos(th3)*cos(th3)*cos(th3)*cos(th3)*cos(th3)*cos(th3)*cos(th3)*cos(th3)*cos(th3)*cos(th3)*cos(th3)*cos(th3)*cos(th3)*cos(th3)*cos(th3)*cos(th3)*cos(th3)*cos(th3)*cos(th3)*cos(th3)*cos(th3)*cos(th3)*cos(th3)*cos(th3)*cos(th3)*cos(th3)*cos(th3)*cos(th3)*cos(th3)*cos(th3)*cos(th3)*cos(th3)*cos(th3)*cos(th3)*cos(th3)*cos(th3)*cos(th3)*cos(th3)*cos(th3)*cos(th3)*cos(th3)*cos(th3)*cos(th3)*cos(th3)*cos(th3)*cos(th3)*cos(th3)*cos(th3)*cos(th3)*cos(th3)*cos(th3)*cos(th3)*cos(th3)*cos(th3)*cos(th3)*cos(th3)*cos(th3)*cos(th3)*cos(th3)*cos(th3)*cos(th3)*cos(th3)*cos(th3)*cos(th3)*cos(th3)*cos(th3)*cos(th3)*cos(th3)*cos(th3)*cos(th3)*cos(th3)*cos(th3)*cos(th3)*cos(th3)*cos(th3)*cos(th3)*cos(th3)*cos(th3)*cos(th3)*cos(th3)*cos(th3)*cos(th3)*cos(th3)*cos(th3)*cos(th3)*cos(th3)*cos(th3)*cos(th3)*cos(th3)*cos(th3)*cos(th3)*cos(th3)*cos(th3)*cos(th3)*cos(th3)*cos(th3)*cos(th3)*cos(th3)*cos(th3)*cos(th3)*cos(th3)*cos(th3)*cos(th3)*cos(th3)*cos(th3)*cos(th3)*cos(th3)*cos(th3)*
+cos(th2)*cos(th3)*m3*rc3*d0+2*cos(th2)*m3*rc3^2*cos(th3)^2*sin(th2)+cos(th2)*m3*sin(th2)*a2^2
+2*\sin(th2)*I3yy*\cos(th3)^2*\cos(th2)
NRC_{t}(2.1) = -1/4*m3*rc3^2*cos(2*th2-2*th1+2*th3)+1/4*m3*rc3^2*cos(2*th2+2*th1+2*th3)
-1/4*I3xx*cos(2*th2+2*th1+2*th3)+1/4*I3yy*cos(2*th2+2*th1+2*th3)
-1/4*I3yy*cos(2*th2-2*th1+2*th3)+1/4*I3xx*cos(2*th2-2*th1+2*th3)+1/4*I2yy*cos(2*th1+2*th2)
-1/4*I2xx*cos(2*th1+2*th2)+1/4*I2xx*cos(-2*th1+2*th2)-1/4*I2yy*cos(-2*th1+2*th2)
+1/4*m3*a2^2*cos(2*th1+2*th2)-1/4*m3*a2^2*cos(-2*th1+2*th2)+1/4*m2*rc2^2*cos(2*th1+2*th2)
-1/4*m2*rc2^2*cos(-2*th1+2*th2)+1/2*m3*rc3*a2*cos(2*th2+th3+2*th1)
-1/2*m3*rc3*a2*cos(2*th2+th3-2*th1)
NRC_{\tau}(2,2) = \cos(th1)*(-4*I3xx*\cos(th3)^2*\cos(th2)^2+4*I3yy*\cos(th3)^2*\cos(th2)^2
+2*m2*cos(th2)^2*rc2^2-2*m3*rc3^2*cos(th3)^2+2*m3*cos(th2)^2*a2^2+m3*rc3^2-m2*rc2^2
-2*\cos(th2)^2 = 13xx + 2*13xx + \cos(th2)^2 - 2*13yy + \cos(th2)^2 + 2*13xx + \cos(th3)^2 - 13xx + 12xx - 12yy + 13yy + \cos(th2)^2 + 2*13xx + \cos(th3)^2 - 13xx + 12xx - 12yy + 13yy + \cos(th2)^2 + 2*13xx + \cos(th3)^2 - 13xx + 12xx - 12yy + 13yy + \cos(th2)^2 - 13xx + \cos(th3)^2 - \cos(th3)^2 -
-4*m3*rc3^2*cos(th3)*cos(th2)*sin(th3)*sin(th2)- 4*m3*rc3*sin(th3)*cos(th2)*a2*sin(th2)
+4*m3*rc3*cos(th3)*cos(th2)^2*a2-4*I3yy*cos(th3)*cos(th2)*sin(th3)*sin(th2)
-m3*rc3*cos(th3)*sin(th2)*d0-m3*rc3*sin(th3)*cos(th2)*d0+4*13xx*cos(th3)*cos(th2)*sin(th3)*sin(th2)
-m3*rc3*cos(th3)*sin(th2)*d1-rc2*m2*sin(th2)*d1-m3*a2^2-m3*rc3*sin(th3)*cos(th2)*d1
-2*m3*rc3^2*cos(th2)^2-rc2*m2*sin(th2)*d0-m3*sin(th2)*d1*a2-2*m3*rc3*cos(th3)*a2
-m3*sin(th2)*d0*a2+4*m3*rc3^2*cos(th3)^2*cos(th2)^2-2*I3yy*cos(th3)^2+2*cos(th2)^2*I2yy
 NRC_{\tau}(2.3) = -\sin(th1)*(m3*a2^2+rc2*m2*sin(th2)*d1+2*I3vv*cos(th3)^2+2*cos(th2)^2*I2xx
+m3*rc3*cos(th3)*sin(th2)*d0+4*m3*rc3*sin(th3)*cos(th2)*a2*sin(th2)-2*I3xx*cos(th2)^2
-2*I3xx*cos(th3)^2+m3*rc3*sin(th3)*cos(th2)*d1-4*m3*rc3*cos(th3)*cos(th2)^2*a2
+m3*rc3*cos(th3)*sin(th2)*d1-2*cos(th2)^2*I2yy+2*I3yy*cos(th2)^2
+4*I3yy*cos(th3)*cos(th2)*sin(th3)*sin(th2)+4*m3*rc3^2*cos(th3)*cos(th2)*sin(th3)*sin(th2)
+2*m3*rc3^2*cos(th3)^2-2*m3*cos(th2)^2*a2^2-4*I3yy*cos(th3)^2*cos(th2)^2-2*m2*cos(th2)^2*rc2^2
+4*I3xx*cos(th3)^2*cos(th2)^2+2*m3*rc3^2*cos(th2)^2+2*m3*rc3*cos(th3)*a2+m3*sin(th2)*d0*a2
+m3*sin(th2)*d1*a2+rc2*m2*sin(th2)*d0+I3xx-I2xx+I2yy-I3yy
-4*I3xx*cos(th3)*cos(th2)*sin(th3)*sin(th2) + m3*rc3*sin(th3)*cos(th2)*d0
-4*m3*rc3^2*cos(th3)^2*cos(th2)^2+m2*rc2^2-m3*rc3^2
NRC_{\tau}(3,1) = \frac{1}{4}m3*rc3^2*cos(2*th2+2*th1+2*th3)-\frac{1}{4}m3*rc3^2*cos(2*th2-2*th1+2*th3)}
-1/4*m3*rc3*a2*cos(th3-2*th1)+1/4*m3*rc3*a2*cos(th3+2*th1)+1/4*l3vy*cos(2*th2+2*th1+2*th3)
-1/4*I3vv*cos(2*th2-2*th1+2*th3)+1/4*I3xx*cos(2*th2-2*th1+2*th3)
-1/4*I3xx*cos(2*th2+2*th1+2*th3) +1/4*m3*rc3*a2*cos(2*th2+th3+2*th1)
-1/4*m3*rc3*a2*cos(2*th2+th3-2*th1)
```

```
NRC_{\tau}(3,2) = 1/2*I3yy*cos(-th1+2*th3+2*th2)+1/2*I3yy*cos(th1+2*th3+2*th2)
-1/2*I3xx*cos(-th1+2*th3+2*th2)-1/2*I3xx*cos(th1+2*th3+2*th2)
+1/2*m3*rc3^2*cos(-th1+2*th3+2*th2) +1/2*m3*rc3^2*cos(th1+2*th3+2*th2)
-1/2*m3*rc3*d0*sin(th2-th1+th3)+1/2*m3*rc3*a2*cos(2*th2-th1+th3)
+1/2*m3*rc3*a2*cos(2*th2+th1+th3)
NRC_{\tau}(3,3) = \frac{1}{2}m3*rc3*a2*sin(2*th2+th1+th3)-\frac{1}{2}m3*rc3*a2*sin(2*th2-th1+th3)
-1/2*m3*rc3*d0*cos(th2-th1+th3)+1/2*m3*rc3*d0*cos(th2+th1+th3)-1/2*I3yy*sin(-th1+2*th3+2*th2)
+1/2*I3yy*sin(th1+2*th3+2*th2)+1/2*I3xx*sin(-th1+2*th3+2*th2)-1/2*I3xx*sin(th1+2*th3+2*th2)
-1/2*m3*rc3*d1*cos(th2-th1+th3)+1/2*m3*rc3*d1*cos(th2+th1+th3)
-1/2*m3*rc3^2*sin(-th1+2*th3+2*th2) + 1/2*m3*rc3^2*sin(th1+2*th3+2*th2)
                                                                                                                                               (A-28)
                                             Flexible Body Coriolis Joint Torques
NCC_{\tau}(1,1) = -\sin(th1) *\cos(th1) *(2*m3*rc3*\cos(th3)*\cos(th2)^2*a2
-2*I3yy*cos(th3)*cos(th2)*sin(th3)*sin(th2) + 2*I3xx*cos(th3)*cos(th2)*sin(th3)*sin(th2)
+m2*cos(th2)^2*rc2^2+m3*cos(th2)^2*a2^2+2*I3yy*cos(th3)^2*cos(th2)^2
-2*I3xx*cos(th3)^2*cos(th2)^2-m3*rc3^2*cos(th3)^2-m3*rc3^2*cos(th2)^2+I3xx*cos(th3)^2
+I3xx*cos(th2)^2+I2yy*cos(th2)^2-I2xx*cos(th2)^2-I3yy*cos(th2)^2-I3yy*cos(th3)^2
-2*m3*rc3^2*cos(th3)*cos(th2)*sin(th3)*sin(th2)-2*m3*rc3*sin(th3)*cos(th2)*a2*sin(th2)
+2*m3*rc3^2*cos(th3)^2*cos(th2)^2+m3*rc3^2-I3xx-I2yy+I3zz+I2zz-I1xx+I1zz)
NCC_{\tau}(1,2) = \sin(th1) *\cos(th1) *(2*m3*rc3*\cos(th3)*\cos(th2)^2*a2
-2*I3vv*cos(th3)*cos(th2)*sin(th3)*sin(th2) + 2*I3xx*cos(th3)*cos(th2)*sin(th3)*sin(th2)
+m2*cos(th2)^2*rc2^2+m3*cos(th2)^2*a2^2+2*I3yy*cos(th3)^2*cos(th2)^2
-2*I3xx*cos(th3)^2*cos(th2)^2-m3*rc3^2*cos(th3)^2-m3*rc3^2*cos(th2)^2+I3xx*cos(th3)^2
+13xx*cos(th2)^2+12yy*cos(th2)^2-12xx*cos(th2)^2-13yy*cos(th2)^2-13yy*cos(th3)^2
-2*m3*rc3^2*cos(th3)*cos(th2)*sin(th3)*sin(th2)- 2*m3*rc3*sin(th3)*cos(th2)*a2*sin(th2)
+2*m3*rc3^2*cos(th3)^2*cos(th2)^2+m3*rc3^2-I3xx-I2vv+I3zz+I2zz-I1xx+I1zz)
NCC_{\tau}(1,3)=0
NCC_{\tau}(2.1) = -1/8*I3vv*\sin(2*th2-2*th1+2*th3) - 1/8*I3vv*\sin(2*th2+2*th1+2*th3)
+1/4*I3xx*sin(2*th3+2*th2)+1/8*I3xx*sin(2*th2-2*th1+2*th3)+1/8*I3xx*sin(2*th2+2*th1+2*th3)
-m3*rc3*d0*cos(th2+th3)-1/4*m3*rc3^2*sin(2*th3+2*th2)-1/8*m3*rc3^2*sin(2*th2+2*th1+2*th3)-1/8*m3*rc3^2*sin(2*th2+2*th1+2*th3)-1/8*m3*rc3^2*sin(2*th2+2*th1+2*th3)-1/8*m3*rc3^2*sin(2*th2+2*th1+2*th3)-1/8*m3*rc3^2*sin(2*th2+2*th3+2*th3)-1/8*m3*rc3^2*sin(2*th2+2*th3+2*th3)-1/8*m3*rc3^2*sin(2*th2+2*th3+2*th3)-1/8*m3*rc3^2*sin(2*th3+2*th3+2*th3)-1/8*m3*rc3^2*sin(2*th3+2*th3+2*th3+2*th3+2*th3+2*th3+2*th3+2*th3+2*th3+2*th3+2*th3+2*th3+2*th3+2*th3+2*th3+2*th3+2*th3+2*th3+2*th3+2*th3+2*th3+2*th3+2*th3+2*th3+2*th3+2*th3+2*th3+2*th3+2*th3+2*th3+2*th3+2*th3+2*th3+2*th3+2*th3+2*th3+2*th3+2*th3+2*th3+2*th3+2*th3+2*th3+2*th3+2*th3+2*th3+2*th3+2*th3+2*th3+2*th3+2*th3+2*th3+2*th3+2*th3+2*th3+2*th3+2*th3+2*th3+2*th3+2*th3+2*th3+2*th3+2*th3+2*th3+2*th3+2*th3+2*th3+2*th3+2*th3+2*th3+2*th3+2*th3+2*th3+2*th3+2*th3+2*th3+2*th3+2*th3+2*th3+2*th3+2*th3+2*th3+2*th3+2*th3+2*th3+2*th3+2*th3+2*th3+2*th3+2*th3+2*th3+2*th3+2*th3+2*th3+2*th3+2*th3+2*th3+2*th3+2*th3+2*th3+2*th3+2*th3+2*th3+2*th3+2*th3+2*th3+2*th3+2*th3+2*th3+2*th3+2*th3+2*th3+2*th3+2*th3+2*th3+2*th3+2*th3+2*th3+2*th3+2*th3+2*th3+2*th3+2*th3+2*th3+2*th3+2*th3+2*th3+2*th3+2*th3+2*th3+2*th3+2*th3+2*th3+2*th3+2*th3+2*th3+2*th3+2*th3+2*th3+2*th3+2*th3+2*th3+2*th3+2*th3+2*th3+2*th3+2*th3+2*th3+2*th3+2*th3+2*th3+2*th3+2*th3+2*th3+2*th3+2*th3+2*th3+2*th3+2*th3+2*th3+2*th3+2*th3+2*th3+2*th3+2*th3+2*th3+2*th3+2*th3+2*th3+2*th3+2*th3+2*th3+2*th3+2*th3+2*th3+2*th3+2*th3+2*th3+2*th3+2*th3+2*th3+2*th3+2*th3+2*th3+2*th3+2*th3+2*th3+2*th3+2*th3+2*th3+2*th3+2*th3+2*th3+2*th3+2*th3+2*th3+2*th3+2*th3+2*th3+2*th3+2*th3+2*th3+2*th3+2*th3+2*th3+2*th3+2*th3+2*th3+2*th3+2*th3+2*th3+2*th3+2*th3+2*th3+2*th3+2*th3+2*th3+2*th3+2*th3+2*th3+2*th3+2*th3+2*th3+2*th3+2*th3+2*th3+2*th3+2*th3+2*th3+2*th3+2*th3+2*th3+2*th3+2*th3+2*th3+2*th3+2*th3+2*th3+2*th3+2*th3+2*th3+2*th3+2*th3+2*th3+2*th3+2*th3+2*th3+2*th3+2*th3+2*th3+2*th3+2*th3+2*th3+2*th3+2*th3+2*th3+2*th3+2*th3+2*th3+2*th3+2*th3+2*th3+2*th3+2*th3+2*th3+2*th3+2*th3+2*th3+2*th3+2*th3+2*th3+2*th3+2*th3+2*th3+2*th3+2*th3+2*th3+2*th3+2*th3+2*th3+2*th3+2*th3
-1/8*m3*rc3^2*sin(2*th2-2*th1+2*th3)-rc2*m2*cos(th2)*d1-rc2*m2*cos(th2)*d0
-1/2*m3*rc3*a2*sin(2*th2+th3) -1/4*m3*rc3*a2*sin(2*th2+th3+2*th1)
-1/4*m3*rc3*a2*sin(2*th2+th3-2*th1) -m3*rc3*d1*cos(th2+th3)-1/4*I3yy*sin(2*th3+2*th2)
-m3*\cos(th2)*d0*a2-m3*\cos(th2)*d1*a2-1/4*m3*a2^2*\sin(2*th2)-1/8*m3*a2^2*\sin(2*th1+2*th2)
-1/8*m3*a2^2*sin(-2*th1+2*th2)-1/4*I2yy*sin(2*th2)-1/8*I2yy*sin(2*th1+2*th2)
-1/8*I2vv*sin(-2*th1+2*th2)+1/8*I2vx*sin(2*th1+2*th2)+1/8*I2vx*sin(-2*th1+2*th2)
+1/4*I2xx*sin(2*th2)-1/8*m2*rc2^2*sin(2*th1+2*th2)-1/8*m2*rc2^2*sin(-2*th1+2*th2)
-1/4*m2*rc2^2*sin(2*th2)
NCC_{\tau}(2,2) = \frac{1}{8} i3yy*sin(2*th2+2*th1+2*th3)-\frac{1}{4} i3yy*sin(2*th3+2*th2)+\frac{1}{4} i3xx*sin(2*th3+2*th2)}{1}
-1/8*I3xx*sin(2*th2-2*th1+2*th3)-1/8*I3xx*sin(2*th2+2*th1+2*th3)+1/8*I3yy*sin(2*th2-2*th1+2*th3)
-m3*cos(th2)*d0*a2-m3*cos(th2)*d1*a2-m3*rc3*d0*cos(th2+th3)
```

+1/4*m3*rc3*a2*sin(2*th2+th3+2*th1) +1/4*m3*rc3*a2*sin(2*th2+th3-2*th1)

```
-1/8*I2xx*sin(2*th1+2*th2)-1/8*I2xx*sin(-2*th1+2*th2)+1/4*I2xx*sin(2*th2)
+1/8*m3*a2^2*sin(2*th1+2*th2) +1/8*m3*a2^2*sin(-2*th1+2*th2) -1/4*m3*a2^2*sin(2*th2)
-1/4*I2yy*sin(2*th2)+1/8*I2yy*sin(2*th1+2*th2)+1/8*I2yy*sin(-2*th1+2*th2)
-1/4*m3*rc3^2*sin(2*th3+2*th2)+1/8*m2*rc2^2*sin(2*th1+2*th2)+1/8*m2*rc2^2*sin(-2*th1+2*th2)
-1/4*m2*rc2^2*sin(2*th2)+1/8*m3*rc3^2*sin(2*th2+2*th1+2*th3)
+1/8*m3*rc3^2*sin(2*th2-2*th1+2*th3)
NCC_{\tau}(2.3) = 1/2*m2*rc2^2*sin(2*th2) + 1/2*m3*a2^2*sin(2*th2) + 1/2*m3*rc3^2*sin(2*th3 + 2*th2)
-1/2*I3xx*sin(2*th3+2*th2)-1/2*I2xx*sin(2*th2)+m3*rc3*a2*sin(2*th2+th3)
+1/2*I3yy*sin(2*th3+2*th2)+1/2*I2yy*sin(2*th2)
NCC_{\tau}(3,1) = -1/4*m3*rc3^2*sin(2*th3+2*th2)-1/8*m3*rc3^2*sin(2*th2-2*th1+2*th3)
-1/8*m3*rc3^2*sin(2*th2+2*th1+2*th3)+1/4*I3xx*sin(2*th3+2*th2)+1/8*I3xx*sin(2*th2+2*th1+2*th3)
+1/8*I3xx*sin(2*th2-2*th1+2*th3)-1/8*m3*rc3*a2*sin(th3-2*th1)-1/8*I3yy*sin(2*th2-2*th1+2*th3)
-m3*rc3*d1*cos(th2+th3)-1/8*m3*rc3*a2*sin(th3+2*th1)+3/4*m3*rc3*a2*sin(th3)
-m3*rc3*d0*cos(th2+th3) - 1/8*m3*rc3*a2*sin(2*th2+th3-2*th1) - 1/8*m3*rc3*a2*sin(2*th2+th3+2*th1)
-1/8*I3vv*sin(2*th2+2*th1+2*th3)-1/4*I3vy*sin(2*th3+2*th2)-1/4*m3*rc3*a2*sin(2*th2+th3)-1/4*I3vy*sin(2*th3+2*th2)-1/4*m3*rc3*a2*sin(2*th2+th3)-1/4*I3vy*sin(2*th3+2*th2)-1/4*m3*rc3*a2*sin(2*th2+th3)-1/4*I3vy*sin(2*th3+2*th2)-1/4*m3*rc3*a2*sin(2*th2+th3)-1/4*I3vy*sin(2*th3+2*th2)-1/4*m3*rc3*a2*sin(2*th2+th3)-1/4*I3vy*sin(2*th3+2*th2)-1/4*m3*rc3*a2*sin(2*th2+th3)-1/4*I3vy*sin(2*th3+2*th2)-1/4*m3*rc3*a2*sin(2*th3+2*th3)-1/4*I3vy*sin(2*th3+2*th2)-1/4*m3*rc3*a2*sin(2*th3+2*th3)-1/4*I3vy*sin(2*th3+2*th2)-1/4*m3*rc3*a2*sin(2*th3+2*th3)-1/4*I3vy*sin(2*th3+2*th2)-1/4*m3*rc3*a2*sin(2*th3+2*th3)-1/4*m3*rc3*a2*sin(2*th3+2*th3)-1/4*m3*rc3*a2*sin(2*th3+2*th3)-1/4*m3*rc3*a2*sin(2*th3+2*th3)-1/4*m3*rc3*a2*sin(2*th3+2*th3)-1/4*m3*rc3*a2*sin(2*th3+2*th3)-1/4*m3*rc3*a2*sin(2*th3+2*th3)-1/4*m3*rc3*a2*sin(2*th3+2*th3)-1/4*m3*rc3*a2*sin(2*th3+2*th3+2*th3)-1/4*m3*rc3*a2*sin(2*th3+2*th3+2*th3+2*th3+2*th3+2*th3+2*th3+2*th3+2*th3+2*th3+2*th3+2*th3+2*th3+2*th3+2*th3+2*th3+2*th3+2*th3+2*th3+2*th3+2*th3+2*th3+2*th3+2*th3+2*th3+2*th3+2*th3+2*th3+2*th3+2*th3+2*th3+2*th3+2*th3+2*th3+2*th3+2*th3+2*th3+2*th3+2*th3+2*th3+2*th3+2*th3+2*th3+2*th3+2*th3+2*th3+2*th3+2*th3+2*th3+2*th3+2*th3+2*th3+2*th3+2*th3+2*th3+2*th3+2*th3+2*th3+2*th3+2*th3+2*th3+2*th3+2*th3+2*th3+2*th3+2*th3+2*th3+2*th3+2*th3+2*th3+2*th3+2*th3+2*th3+2*th3+2*th3+2*th3+2*th3+2*th3+2*th3+2*th3+2*th3+2*th3+2*th3+2*th3+2*th3+2*th3+2*th3+2*th3+2*th3+2*th3+2*th3+2*th3+2*th3+2*th3+2*th3+2*th3+2*th3+2*th3+2*th3+2*th3+2*th3+2*th3+2*th3+2*th3+2*th3+2*th3+2*th3+2*th3+2*th3+2*th3+2*th3+2*th3+2*th3+2*th3+2*th3+2*th3+2*th3+2*th3+2*th3+2*th3+2*th3+2*th3+2*th3+2*th3+2*th3+2*th3+2*th3+2*th3+2*th3+2*th3+2*th3+2*th3+2*th3+2*th3+2*th3+2*th3+2*th3+2*th3+2*th3+2*th3+2*th3+2*th3+2*th3+2*th3+2*th3+2*th3+2*th3+2*th3+2*th3+2*th3+2*th3+2*th3+2*th3+2*th3+2*th3+2*th3+2*th3+2*th3+2*th3+2*th3+2*th3+2*th3+2*th3+2*th3+2*th3+2*th3+2*th3+2*th3+2*th3+2*th3+2*th3+2*th3+2*th3+2*th3+2*th3+2*th3+2*th3+2*th3+2*th3+2*th3+2*th3+2*th3+2*th3+2*th3+2*th3+2*th3+2*th3+2*th3+2*th3+2*th3+2*th3+2*th3+2*th3+2*th3+2*th3+2*th3+2*th3
NCC_{\tau}(3,2) = 3/4*m3*rc3*a2*sin(th3) - 1/4*m3*rc3^2*sin(2*th3+2*th2)
+1/8*m3*rc3^2*sin(2*th2+2*th1+2*th3) +1/8*m3*rc3^2*sin(2*th2-2*th1+2*th3)
-1/4*I3vv*sin(2*th3+2*th2)+1/8*I3vv*sin(2*th2+2*th1+2*th3)+1/8*I3vv*sin(2*th2-2*th1+2*th3)
-1/4*m3*rc3*a2*sin(2*th2+th3)+1/8*m3*rc3*a2*sin(2*th2+th3+2*th1)
+1/8*m3*rc3*a2*sin(2*th2+th3-2*th1)+1/8*m3*rc3*a2*sin(th3+2*th1)+1/8*m3*rc3*a2*sin(th3-2*th1)
-m3*rc3*d1*cos(th2+th3)-1/8*I3xx*sin(2*th2+2*th1+2*th3)-1/8*I3xx*sin(2*th2-2*th1+2*th3)
-m3*rc3*d0*cos(th2+th3)+1/4*I3xx*sin(2*th3+2*th2)
NCC_{\tau}(3,3) = 1/2*m3*rc3*a2*sin(th3) + 1/2*m3*rc3*a2*sin(2*th2+th3) + 1/2*m3*rc3^2*sin(2*th3+2*th2)
                                                                                                                                                            (A-29)
-1/2*I3xx*sin(2*th3+2*th2)+1/2*I3yy*sin(2*th3+2*th2)
                                              Flexible Body Rotational Inertia Torques
B_{Wr}(1,1) = -\cos(th1)*(-\sin(th3)*I3vv*\cos(th3) - a2*rc3*\sin(th3)*m3+2*m3*\sin(th3)*\cos(th2)^2*rc3*a2
+cos(th2)*cos(th3)*m3*rc3*d1+cos(th2)*cos(th3)*m3*rc3*d0-sin(th3)*rc3^2*m3*cos(th3)
+cos(th2)*rc2*m2*d0+2*cos(th3)*m3*rc3^2*sin(th3)*cos(th2)^2
+2*cos(th2)*cos(th3)*m3*rc3*sin(th2)*a2+cos(th2)*rc2*m2*d1-sin(th2)*m3*rc3^2*cos(th2)
+2*cos(th3)*I3vy*sin(th3)*cos(th2)^2- sin(th2)*sin(th3)*m3*rc3*d0
+2*cos(th2)*m3*rc3^2*cos(th3)^2*sin(th2)-sin(th2)*sin(th3)*m3*rc3*d1+cos(th2)*m3*d1*a2
+2*cos(th2)*I3vv*cos(th3)^2*sin(th2)-2*I3xx*sin(th3)*cos(th3)*cos(th2)^2+cos(th2)*m2*sin(th2)*rc2^2
-2*\sin(th2)*I3xx*\cos(th3)^22*\cos(th2)+\sin(th2)*I3xx*\cos(th2)-\cos(th2)*I3yy*\sin(th2)
+\cos(th2)*I2yy*\sin(th2) -\sin(th2)*I2xx*\cos(th2) +\cos(th3)*\sin(th3)*I3xx
+\cos(th2)*m3*\sin(th2)*a2^2+\cos(th2)*m3*d0*a2)
B_{W\tau}(1,2) = -\sin(th1)*(-\sin(th3)*rc3^2*m3*cos(th3)-a2*rc3*sin(th3)*m3
```

 $+2*m3*sin(th3)*cos(th2)^2*rc3*a2+2*cos(th3)*m3*rc3^2*sin(th3)*cos(th2)^2+cos(th2)*rc2*m2*d1\\ -2*I3xx*sin(th3)*cos(th3)*cos(th2)^2-sin(th2)*m3*rc3^2*cos(th2)-2*sin(th2)*I3xx*cos(th3)^2*cos(th2)\\ +2*cos(th3)*I3yy*sin(th3)*cos(th2)^2+2*cos(th2)*I3yy*cos(th3)^2*sin(th2)+cos(th2)*m3*d1*a2$

 $+\cos(th2)*m2*\sin(th2)*rc2^2+\cos(th2)*m3*d0*a2+\cos(th2)*m3*\sin(th2)*a2^2+\cos(th2)*I3xx*\sin(th2)$

+cos(th2)*I2yy*sin(th2)-sin(th2)*I2xx*cos(th2)+cos(th3)*sin(th3)*I3xx-sin(th3)*I3yy*cos(th3)

+2*cos(th2)*cos(th3)*m3*rc3*sin(th2)*a2-sin(th2)*sin(th3)*m3*rc3*d0 +2*cos(th2)*m3*rc3^2*cos(th3)^2*sin(th2)- sin(th2)*sin(th3)*m3*rc3*d1

+cos(th2)*cos(th3)*m3*rc3*d1+cos(th2)*cos(th3)*m3*rc3*d0+cos(th2)*rc2*m2*d0

```
B_{Wr}(1.3) = \frac{1}{2}I2xx + \frac{1}{2}I2xy - \frac{1}{2}I3xx \cos(2*th^3 + 2*th^2) + m^3 \cos^2(2*th^2 + th^3)
+1/2*m3*rc3^2*cos(2*th3+2*th2)+1/2*I3yy*cos(2*th3+2*th2)+I1yy+1/2*m3*rc3^2+1/2*I3xx+1/2*m3*rc3^2+1/2*I3xx+1/2*m3*rc3^2+1/2*I3xx+1/2*m3*rc3^2+1/2*I3xx+1/2*m3*rc3^2+1/2*I3xx+1/2*m3*rc3^2+1/2*I3xx+1/2*m3*rc3^2+1/2*I3xx+1/2*m3*rc3^2+1/2*I3xx+1/2*m3*rc3^2+1/2*I3xx+1/2*m3*rc3^2+1/2*I3xx+1/2*m3*rc3^2+1/2*I3xx+1/2*m3*rc3^2+1/2*I3xx+1/2*m3*rc3^2+1/2*I3xx+1/2*m3*rc3^2+1/2*I3xx+1/2*m3*rc3^2+1/2*I3xx+1/2*m3*rc3^2+1/2*I3xx+1/2*m3*rc3^2+1/2*I3xx+1/2*m3*rc3^2+1/2*I3xx+1/2*m3*rc3^2+1/2*I3xx+1/2*m3*rc3^2+1/2*I3xx+1/2*m3*rc3^2+1/2*I3xx+1/2*m3*rc3^2+1/2*I3xx+1/2*m3*rc3^2+1/2*I3xx+1/2*m3*rc3^2+1/2*I3xx+1/2*m3*rc3^2+1/2*I3xx+1/2*m3*rc3^2+1/2*I3xx+1/2*m3*rc3^2+1/2*I3xx+1/2*m3*rc3^2+1/2*I3xx+1/2*m3*rc3^2+1/2*I3xx+1/2*m3*rc3^2+1/2*I3xx+1/2*m3*rc3^2+1/2*I3xx+1/2*m3*rc3^2+1/2*I3xx+1/2*m3*rc3^2+1/2*m3*rc3^2+1/2*m3*rc3^2+1/2*m3*rc3^2+1/2*m3*rc3^2+1/2*m3*rc3^2+1/2*m3*rc3^2+1/2*m3*rc3^2+1/2*m3*rc3^2+1/2*m3*rc3^2+1/2*m3*rc3^2+1/2*m3*rc3^2+1/2*m3*rc3^2+1/2*m3*rc3^2+1/2*m3*rc3^2+1/2*m3*rc3^2+1/2*m3*rc3^2+1/2*m3*rc3^2+1/2*m3*rc3^2+1/2*m3*rc3^2+1/2*m3*rc3^2+1/2*m3*rc3^2+1/2*m3*rc3^2+1/2*m3*rc3^2+1/2*m3*rc3^2+1/2*m3*rc3^2+1/2*m3*rc3^2+1/2*m3*rc3^2+1/2*m3*rc3^2+1/2*m3*rc3^2+1/2*m3*rc3^2+1/2*m3*rc3^2+1/2*m3*rc3^2+1/2*m3*rc3^2+1/2*m3*rc3^2+1/2*m3*rc3^2+1/2*m3*rc3^2+1/2*m3*rc3^2+1/2*m3*rc3^2+1/2*m3*rc3^2+1/2*m3*rc3^2+1/2*m3*rc3^2+1/2*m3*rc3^2+1/2*m3*rc3^2+1/2*m3*rc3^2+1/2*m3*rc3^2+1/2*m3*rc3^2+1/2*m3*rc3^2+1/2*m3*rc3^2+1/2*m3*rc3^2+1/2*m3*rc3^2+1/2*m3*rc3^2+1/2*m3*rc3^2+1/2*m3*rc3^2+1/2*m3*rc3^2+1/2*m3*rc3^2+1/2*m3*rc3^2+1/2*m3*rc3^2+1/2*m3*rc3^2+1/2*m3*rc3^2+1/2*m3*rc3^2+1/2*m3*rc3^2+1/2*m3*rc3^2+1/2*m3*rc3^2+1/2*m3*rc3^2+1/2*m3*rc3^2+1/2*m3*rc3^2+1/2*m3*rc3^2+1/2*m3*rc3^2+1/2*m3*rc3^2+1/2*m3*rc3^2+1/2*m3*rc3^2+1/2*m3*rc3^2+1/2*m3*rc3^2+1/2*m3*rc3^2+1/2*m3*rc3^2+1/2*m3*rc3^2+1/2*m3*rc3^2+1/2*m3*rc3^2+1/2*m3*rc3^2+1/2*m3*rc3^2+1/2*m3*rc3^2+1/2*m3*rc3^2+1/2*m3*rc3^2+1/2*m3*rc3^2+1/2*m3*rc3^2+1/2*m3*rc3^2+1/2*m3*rc3^2+1/2*m3*rc3^2+1/2*m3*rc3^2+1/2*m3*rc3^2+1/2*m3*rc3^2+1/2*m3*rc3^2+1/2*m3*rc3^2+1/2*m3*rc3^2+1/2*m3*rc3^2+1/2*m3*rc3^2+1/2*m3*rc3^2+1/2*
+1/2*I2yy*cos(2*th2)+1/2*I3yy-1/2*I2xx*cos(2*th2)+1/2*m3*a2^2+1/2*m3*a2^2*cos(2*th2)
+\cos(th3)*m3*rc3*a2+1/2*m2*rc2^2+1/2*m2*rc2^2*\cos(2*th2)
B_{Wr}(2,1) = \sin(th1)*(13zz+m3*\sin(th2)*d1*a2+m3*\sin(th2)*d0*a2+rc2*m2*\sin(th2)*d0
+rc2*m2*sin(th2)*d1+m2*rc2^2+m3*a2^2+m3*rc3*sin(th3)*cos(th2)*d1+m3*rc3*cos(th3)*sin(th2)*d0
+m3*rc3*cos(th3)*sin(th2)*d1+2*cos(th3)*m3*rc3*a2+m3*rc3*sin(th3)*cos(th2)*d0+m3*rc3^2+I2zz)
B_{Wr}(2,2) = -\cos(th1)*(I3zz+m3*\sin(th2)*d1*a2+m3*\sin(th2)*d0*a2+rc2*m2*\sin(th2)*d0
+rc2*m2*sin(th2)*d1+m2*rc2^2+m3*a2^2+m3*rc3*sin(th3)*cos(th2)*d1+m3*rc3*cos(th3)*sin(th2)*d0
+m3*rc3*cos(th3)*sin(th2)*d1+2*cos(th3)*m3*rc3*a2+m3*rc3*sin(th3)*cos(th2)*d0+m3*rc3^2+I2zz)
B_{Wr}(3,1) = \sin(th1)*(m3*rc3*\sin(th3)*\cos(th2)*d0+m3*rc3*\sin(th3)*\cos(th2)*d1
+m3*rc3*cos(th3)*sin(th2)*d0+m3*rc3*cos(th3)*sin(th2)*d1+m3*rc3*cos(th3)*a2+m3*rc3^2+I3zz)
B_{Wr}(3,2) = -\cos(th1)*(d0*\cos(th2)*\sin(th3)*rc3*m3+d1*\cos(th2)*\sin(th3)*rc3*m3
+d0*sin(th2)*cos(th3)*rc3*m3+d1*sin(th2)*cos(th3)*rc3*m3+a2*cos(th3)*rc3*m3+rc3^2*m3+I3zz)
B_{W\tau}(2,3)=B_{W\tau}(3,3)=0
                                                                                                                                                                                                                                     (A-30)
                                                                 Cross Coupling Interaction Torque Effects
N_{CM\tau}(1,1) = N_{CM\tau}(1,2) = N_{CM\tau}(1,3) = N_{CM\tau}(2,4) = N_{CM\tau}(2,5) = N_{CM\tau}(2,6) = N_{CM\tau}(2,9) = N_{CM\tau}(3,6) = N_{CM\tau}(3,7) = N_{C
N_{CM\tau}(3,8)=N_{CM\tau}(3,9)=0
N_{CMr}(1,4) = \cos(th1)*(-12xx-13zz-2*rc3^2*m3+2*\cos(th3)^2*rc3^2*m3-2*m2*\cos(th2)^2*rc2^2
+2*m3*rc3^2*cos(th2)^2-2*m3*cos(th2)^2*a2^2+4*I3xx*cos(th3)^2*cos(th2)^2
-4*I3yy*cos(th3)^2*cos(th2)^2-I3yy-I2zz+I2yy+I3xx+2*cos(th3)^2*I3yy-2*cos(th3)^2*I3xx
+2*I2xx*cos(th2)^2-2*I2yy*cos(th2)^2+2*I3yy*cos(th2)^2-2*I3xx*cos(th2)^2
+4*sin(th2)*sin(th3)*I3yy*cos(th3)*cos(th2)-4*sin(th2)*sin(th3)*I3xx*cos(th3)*cos(th2)
-4*cos(th3)*m3*rc3*cos(th2)^2*a2-4*m3*rc3^2*cos(th3)^2*cos(th2)^2
+4*sin(th2)*sin(th3)*m3*rc3*cos(th2)*a2+4*sin(th2)*sin(th3)*m3*rc3^2*cos(th3)*cos(th2))
N_{CMT}(1,5) = \sin(th1)*(-12xx-13zz+4*\sin(th2)*\sin(th3)*m3*rc3^2*\cos(th3)*\cos(th2)
+4*sin(th2)*cos(th3)*I3yy*sin(th3)*cos(th2)- 4*sin(th2)*cos(th3)*I3xx*sin(th3)*cos(th2)
+2*m3*rc3^2*cos(th2)^2+2*m3*rc3^2*cos(th3)^2-4*I3yy*cos(th3)^2*cos(th2)^2
+4*I3xx*cos(th3)^2*cos(th2)^2-2*m2*cos(th2)^2*rc2^2-2*m3*cos(th2)^2*a2^2-2*m3*rc3^2
-4*cos(th3)*m3*rc3*cos(th2)^2*a2-2*I3xx*cos(th3)^2+4*sin(th2)*sin(th3)*m3*rc3*cos(th2)*a2
-2*I2yy*cos(th2)^2-I3yy-I2zz+I2yy+I3xx-2*I3xx*cos(th2)^2+2*I3yy*cos(th2)^2+2*I3yy*cos(th2)^2
+2*I2xx*cos(th2)^2-4*m3*rc3^2*cos(th3)^2*cos(th2)^2
N_{CM\tau}(1,6) = -m3*a2^2*\sin(2*th2)-m2*rc2^2*\sin(2*th2)-I3yy*\sin(2*th3+2*th2)
-m3*rc3^2*sin(2*th3+2*th2)+I3xx*sin(2*th3+2*th2)-I2vy*sin(2*th2)+I2xx*sin(2*th2)
-2*m3*rc3*a2*sin(2*th2+th3)
N_{CMr}(1,7) = -1/2*m3*rc3^2*cos(th1+2*th3+2*th2)-1/2*m3*rc3^2*cos(-th1+2*th3+2*th2)
+1/2*I3xx*cos(-th1+2*th3+2*th2)+1/2*I3xx*cos(th1+2*th3+2*th2)-1/2*I3yy*cos(th1+2*th3+2*th2)
```

 $-\cos(th2)*I3yy*\sin(th2)$

```
-1/2*I3yy*cos(-th1+2*th3+2*th2)-m3*rc3^2*cos(th1)-I3zz*cos(th1)-1/2*m3*rc3*a2*cos(2*th2-th1+th3)
N_{CM\tau}(1,8) = 1/2*m3*rc3*a2*sin(2*th2-th1+th3)-1/2*m3*rc3*a2*sin(2*th2+th1+th3)
-1/2*m3*rc3*a2*sin(th1+th3)+1/2*m3*rc3*a2*sin(-th1+th3)-m3*rc3^2*sin(th1)-I3zz*sin(th1)
-1/2*I3vv*sin(th1+2*th3+2*th2)+1/2*I3vv*sin(-th1+2*th3+2*th2)
+1/2*m3*rc3^2*sin(-th1+2*th3+2*th2)- 1/2*m3*rc3^2*sin(th1+2*th3+2*th2)
+1/2*I3xx*sin(th1+2*th3+2*th2)-1/2*I3xx*sin(-th1+2*th3+2*th2)
N_{CMr}(1,9) = -m3*rc3^2*sin(2*th3+2*th2)-m3*rc3*a2*sin(2*th2+th3)-m3*sin(th3)*rc3*a2
-13yy*sin(2*th3+2*th2)+13xx*sin(2*th3+2*th2)
N_{CM_7}(2,1) = \cos(th1)*(2*m3*rc3^2+I3yy-I3xx-I2yy+I2xx+I2zz)
-4*m3*rc3^2*cos(th3)*sin(th2)*sin(th3)*cos(th2)+4*m3*rc3*cos(th3)*cos(th2)^2*a2
-4*I3vy*cos(th3)*sin(th2)*sin(th3)*cos(th2)+4*I3xx*cos(th3)*sin(th2)*sin(th3)*cos(th2)
-4*m3*rc3*sin(th3)*sin(th2)*a2*cos(th2)-2*m3*rc3^2*cos(th2)^2-2*m3*rc3^2*cos(th3)^2
+4*I3yy*cos(th3)^2*cos(th2)^2-4*I3xx*cos(th3)^2*cos(th2)^2-2*cos(th2)^2*I2xx-2*I3yy*cos(th2)^2
-2*I3vv*cos(th3)^2+2*cos(th2)^2*I2vv+2*I3xx*cos(th2)^2+2*I3xx*cos(th3)^2+2*m2*cos(th2)^2*rc2^2
+2*m3*cos(th2)^2*a2^2+4*m3*rc3^2*cos(th3)^2*cos(th2)^2+I3zz
N_{CMT}(2,2) = \sin(th1)*(2*13xx*\cos(th2)^2-2*\cos(th2)^2*12xx+2*\cos(th2)^2*12yy-2*13yy*\cos(th3)^2
-2*I3yy*cos(th2)^2 + 2*m3*rc3^2 + I3yy-I3xx-I2yy+I2xx-2*m3*rc3^2 *cos(th2)^2 + 2*m3*a2^2 *cos(th2)^2
+2*m2*cos(th2)^2*rc2^2-4*I3vv*cos(th3)*sin(th2)*sin(th3)*cos(th2)+4*I3vv*cos(th3)^2*cos(th2)^2
+4*I3xx*cos(th3)*sin(th2)*sin(th3)*cos(th2)+4*m3*rc3*cos(th3)*cos(th2)^2*a2+2*I3xx*cos(th3)^2
-4*m3*rc3^2*cos(th3)*sin(th2)*sin(th3)*cos(th2)-4*m3*rc3*sin(th3)*sin(th2)*a2*cos(th2)
-4*13xx*\cos(th3)^2\cos(th2)^2-2*m3*rc3^2\cos(th3)^2+4*m3*rc3^2\cos(th3)^2\cos(th2)^2+12zz+13zz
N_{CM}(2,3) = I3yy*\sin(2*th3+2*th2)-I2xx*\sin(2*th2)-I3xx*\sin(2*th3+2*th2)+m2*rc2^2*\sin(2*th2)
+I2yy*sin(2*th2)+m3*rc3^2*sin(2*th3+2*th2)+2*m3*rc3*a2*sin(2*th2+th3)+m3*a2^2*sin(2*th2)
N_{CM\tau}(2,7) = -2*m3*\sin(th3)*\sin(th1)*a2*rc3
N_{CM_7}(2.8) = 2*m3*\sin(th3)*\cos(th1)*a2*rc3
N_{CM\tau}(3,1) = m3*rc3^2*cos(th1) + 1/2*m3*a2*rc3*cos(-th1+th3) + 1/2*m3*a2*rc3*cos(th1+th3)
+13zz*cos(th1)+1/2*m3*a2*rc3*cos(2*th2-th1+th3)+1/2*m3*a2*rc3*cos(2*th2+th1+th3)
+1/2*m3*rc3^2*cos(th1+2*th3+2*th2)+1/2*m3*rc3^2*cos(-th1+2*th3+2*th2)
-1/2*I3xx*cos(-th1+2*th3+2*th2)-1/2*I3xx*cos(th1+2*th3+2*th2)+1/2*I3yy*cos(-th1+2*th3+2*th2)
+1/2*I3yy*cos(th1+2*th3+2*th2)
N_{CM}(3.2) = \frac{1}{2} I3xx * \sin(-th1 + 2*th3 + 2*th2) - \frac{1}{2} I3xx * \sin(th1 + 2*th3 + 2*th2) + m3*rc3^2 * \sin(th1)
+13zz*\sin(th1)+1/2*m3*rc3*a2*\sin(2*th2+th1+th3)-1/2*m3*rc3*a2*\sin(2*th2-th1+th3)
-1/2*m3*rc3*a2*sin(-th1+th3)+1/2*m3*rc3*a2*sin(th1+th3)+1/2*I3yy*sin(th1+2*th3+2*th2)
-1/2*I3yy*sin(-th1+2*th3+2*th2)-1/2*m3*rc3^2*sin(-th1+2*th3+2*th2)
+1/2*m3*rc3^2*sin(th1+2*th3+2*th2)
N_{CM}(3.3) = m3*rc3*sin(th3)*a2+m3*rc3*a2*sin(2*th2+th3)+m3*rc3^2*sin(2*th3+2*th2)
+I3vy*sin(2*th3+2*th2)-I3xx*sin(2*th3+2*th2)
N_{CM\tau}(3,4) = 2*m3*\sin(th3)*\sin(th1)*a2*rc3
                                                                                                                                                     (A-31)
N_{CM\tau}(3,5) = -2*m3*\sin(th3)*\cos(th1)*a2*rc3
```

A.2 Three Degree of Freedom Spherical Robot

The spherical robot was chosen as an alternate configuration for three reasons. First, it is a common robot configuration and modeling information is easily found in many robotics texts, including Craig [16] and Sciavicco and Siciliano [59]

Table A-2 Denavit-Hartenberg Parameters for Spherical Robot

| Link | a_i | $\alpha_{\rm i}$ | d_{i} | $\Theta_{ m i}$ |
|------|-------|------------------|---------|-----------------|
| 1 | 0 | $-\pi/2$ | 0 | θ_1 |
| 2 | 0 | $\pi/2$ | d_2 | θ_2 |
| 3 | 0 | 0 | d_3 | 0 |

Rotation Matrices:

$$R_1^0 = \begin{bmatrix} c_1 & 0 & -s_1 \\ s_1 & 0 & c_1 \\ 0 & -1 & 0 \end{bmatrix}$$

$$R_2^1 = \begin{bmatrix} c_2 & 0 & s_2 \\ s_2 & 0 & -c_2 \\ 0 & 1 & 0 \end{bmatrix}$$

$$R_3^2 = \begin{bmatrix} 1 & 0 & 0 \\ 0 & 1 & 0 \\ 0 & 0 & 1 \end{bmatrix} \tag{A-32}$$

Constants:

$$\begin{array}{c} A_s = m_2 r_2 + m_3 d_2 \\ B_s = m_3 r_3 \text{ (note } r_3 \text{ is not constant)} \\ E_s = m_3 r_3^2 \\ F_s = I_{2yy} + I_{3yy} \\ G_s = I_{2xx} + I_{3xx} \end{array}$$

$$\begin{array}{l} H_s = I_{3zz} + I_{2zz} \\ K_s = m_3 a_2^2 + m_2 r_2^2 \\ O_s = m_1 r_1 + (m_2 + m_3) d_1 \end{array} \tag{A-33}$$

Position Vector to CG

$$\mathbf{r}_{CG} = \begin{bmatrix} -A_s s_1 + B_s c_1 s_2 \\ A_s c_1 + B_s s_1 s_2 \\ O + B_s c_2 \end{bmatrix}$$
(A-34)

Rigid Inertia Forces

$$B_{F} = \begin{bmatrix} -A_{s}c_{1} - B_{s}s_{1}s_{2} & B_{s}c_{1}c_{2} & m_{3}c_{1}s_{2} \\ -A_{s}s_{1} + B_{s}c_{1}s_{2} & B_{s}s_{1}c_{2} & m_{3}s_{1}s_{2} \\ 0 & -B_{s}s_{2} & m_{3}c_{2} \end{bmatrix}$$

$$\begin{vmatrix} B_{f} | = -m_{3}^{3}s_{2}r_{3}^{2} \end{vmatrix}$$
(A-35)

Rigid Inertia Interaction Torques

$$B_{\tau 0}(1,1) = (H_{s} - E_{s} - G_{s})c_{1}c_{2}s_{2} + B_{s}(a_{1}c_{1}s_{2} + a_{2}s_{1}c_{2}) - A_{s}a_{1}s_{1}$$

$$B_{\tau 0}(1,2) = -(E_{s} + F_{s})s_{1} + B_{s}(a_{1}s_{1}c_{2} - a_{2}c_{1}s_{2})$$

$$B_{\tau 0}(1,3) = m_{3}(a_{1}s_{1}s_{2} + a_{2}c_{1}c_{2})$$

$$B_{\tau 0}(2,1) = (H_{s} - E_{s} - G_{s})s_{1}s_{2}c_{2} + B_{s}(a_{1}s_{1}s_{2} - a_{2}c_{1}c_{2}) + A_{s}a_{1}c_{1}$$

$$B_{\tau 0}(2,2) = (E_{s} + F_{s})c_{1} - B_{s}(a_{1}c_{1}c_{2} + a_{2}s_{1}s_{2})$$

$$B_{\tau 0}(2,3) = -m_{3}(a_{1}c_{1}s_{2} - a_{2}s_{1}c_{2})$$

$$B_{\tau 0}(3,1) = E_{s} + I_{1yy} + G_{s} + K_{s} + (H_{s} - E_{s} - G_{s})c_{2}^{2}$$

$$B_{\tau 0}(3,3) = -m_{3}a_{2}s_{2}$$

$$(A-36)$$

Rigid Nonlinear Coriolis Torques

 $NR_{\tau 0}(1,1) = -\cos(th1) * (2*m3*rc3^2*\cos(th2)^2 + 2*I3xx*\cos(th2)^2 - 2*I3zz*\cos(th2)^2 + 2*I2xx*\cos(th2)^2 - 2*I2zz*\cos(th2)^2 + I3zz+I3yy-I3xx+I2zz+I2yy-I2xx-2*m3*\cos(th2)*rc3*a1)$

 $NR_{\tau 0}(2,1) = -\sin(th1)*(2*m3*rc3^2*\cos(th2)^2 + 2*I3xx*\cos(th2)^2 - 2*I3zz*\cos(th2)^2 + 2*I2xx*\cos(th2)^2 - 2*I2zz*\cos(th2)^2 + I3zz+I3yy-I3xx+I2zz+I2yy-I2xx-2*m3*\cos(th2)*rc3*a1)$

 $NR_{\tau 0}(3,1) = 2*\sin(th2)*\cos(th2)*(m3*rc3^2+I3xx-I3zz+I2xx-I2zz)$

$$NR_{\tau 0}(1,2) = NR_{\tau 0}(1,3) = NR_{\tau 0}(2,2) = NR_{\tau 0}(2,3) = NR_{\tau 0}(3,2) = NR_{\tau 0}(3,3) = 0$$
 (A-37)

Rigid Nonlinear Centrifugal Torques

 $NC_{\tau 0}(1,1) = \cos(th1) *m3 *\cos(th2) *rc3 *a2 -\cos(th1) *m3 *a2 *a1 -\cos(th1) *m2 *rc2 *a1$

 $+\sin(th1)*\sin(th2)*m3*rc3^2*\cos(th2)+\sin(th1)*\sin(th2)*I3xx*\cos(th2)-\sin(th1)*\sin(th2)*I3zz*\cos(th2)\\ +\sin(th1)*\sin(th2)*I2xx*\cos(th2)-\sin(th1)*\sin(th2)*I2zz*\cos(th2)-\sin(th1)*m3*rc3*a1*\sin(th2)$

 $NC_{\tau 0}(1,2) = -m3*rc3*(cos(th1)*cos(th2)*a2+sin(th1)*a1*sin(th2))$

 $NC_{\tau 0}(2,1) = \sin(th1) *m3 *\cos(th2) *rc3 *a2 -\sin(th1) *m3 *a2 *a1 -\sin(th1) *m2 *rc2 *a1 \\ -\cos(th1) *m3 *rc3 ^2 *\cos(th2) *\sin(th2) -\cos(th1) *\cos(th2) *13 xx *\sin(th2) +\cos(th1) *\sin(th2) *13 zz *\cos(th2) \\ -\cos(th1) *\cos(th2) *12 xx *\sin(th2) +\cos(th1) *\sin(th2) *12 zz *\cos(th2) +\cos(th1) *m3 *rc3 *a1 *\sin(th2)$

 $NC_{\tau 0}(2,2) = -m3*rc3*(sin(th1)*cos(th2)*a2-cos(th1)*a1*sin(th2))$

 $NC_{\tau 0}(3,2) = m3*rc3*a2*sin(th2)$

$$NC_{\tau 0}(1,3) = NC_{\tau 0}(2,3) = NC_{\tau 0}(3,1) = NC_{\tau 0}(3,3) = 0$$
 (A-38)

Rigid Joint Torques

$$B_{\tau} = \begin{bmatrix} E + G + H + I_{1,yy} + (D - E - G)c_2^2 & -Ba_2c_2 & -m_3a_2s_2 \\ -Ba_2c_2 & E + F & 0 \\ -m_3a_2s_2 & 0 & m_3 \end{bmatrix}$$
(A-39)

A.3 Three Degree of Freedom Wrist

The third configuration chosen was a wrist configuration due to its common use in combination with other robots and availability for use in conjunction with the anthropomorphic robot on the experimental testbed.

Table A-3
Denavit-Hartenberg Parameters for Wrist

| Link | a_i | α_{i} | d_i | $\theta_{\rm i}$ |
|------|-------|--------------|-------|------------------|
| 3 | 0 | $\pi/2$ | d_3 | θ_3 |
| 4 | 0 | $-\pi/2$ | d_4 | θ_4 |
| 5 | 0 | $\pi/2$ | d_5 | θ_5 |
| 6 | 0 | 0 | d_6 | θ_6 |

Rotation Matrices

$$R_{4}^{3} = \begin{bmatrix} \cos(\theta_{4}) & 0 & -\sin(\theta_{4}) \\ \sin(\theta_{4}) & 0 & \cos(\theta_{4}) \\ 0 & -1 & 0 \end{bmatrix}$$

$$R_{6}^{5} = \begin{bmatrix} \cos(\theta_{6}) & -\sin(\theta_{6}) & 0 \\ \sin(\theta_{6}) & \cos(\theta_{6}) & 0 \\ 0 & 0 & 1 \end{bmatrix}$$

$$R_{5}^{4} = \begin{bmatrix} \cos(\theta_{5}) & 0 & \sin(\theta_{5}) \\ \sin(\theta_{5}) & 0 & -\cos(\theta_{5}) \\ 0 & 1 & 0 \end{bmatrix}$$
(A-40)

Constants

$$\begin{array}{c} A_w \!\!=\!\! m_5 r_5 \!\!+\!\! (d_5 \!\!+\!\! r_6) m_6 \\ E_w \!\!=\!\! m_6 r_6^2 \\ J_w \!\!=\!\! I_{6yy} \!\!-\!\! I_{6xx} \\ K_w \!\!=\!\! m_5 r_5^2 \!\!+\!\! m_6 d_5^2 \\ L_w \!\!=\!\! I_{5xx} \!\!-\!\! I_{5zz} \!\!+\!\! I_{6yy} \!\!-\!\! I_{6zz} +\!\! 2m_6 r_6 d_5 \\ M_w \!\!=\!\! I_{5yy} \!\!+\!\! I_{6xx} \!\!+\!\! 2m_6 r_6 d_5 \\ N_w \!\!=\!\! I_{4yy} \!\!+\!\! I_{5xx} \!\!+\!\! I_{6yy} \!\!+\!\! 2m_6 r_6 d_5 \end{array} \tag{A-41}$$

Position Vector to CG

$$\mathbf{r}_{CG} = \begin{bmatrix} m_6 \cos(\theta_4) \sin(\theta_5) \\ m_6 \sin(\theta_4) \sin(\theta_5) \\ m_3 (\cos(\theta_5) - r_3) \end{bmatrix}$$
(A-42)

Rigid Inertia Forces

$$B_f = \begin{bmatrix} -A_w s_4 s_5 & A_w c_4 c_5 & 0 \\ A_w c_4 s_5 & A_w s_4 c_5 & 0 \\ 0 & -A_w s_5 & 0 \end{bmatrix}$$
 (A-43)

Rigid Inertia Interaction Torques

$$\begin{split} B_{\tau 0}(1,1) &= -s_5 \left\{ (K_w + E_w + L_w) c_4 c_5 + A_w d_4 c_4 + J_w c_6 (s_4 s_6 - c_4 c_5 c_6) \right\} \\ B_{\tau 0}(1,2) &= -(M_w + E_w + L_w) s_4 - A_w d_4 s_4 c_5 - J_w c_6 (s_4 c_6 + c_4 c_5 s_6) \\ B_{\tau 0}(1,3) &= I_{6zz} c_4 s_5 \\ B_{\tau 0}(2,1) &= s_5 \left\{ -(K_w + E_w + L_w) s_4 c_5 - A_w d_4 s_4 + J_w c_6 (c_4 s_6 - s_4 c_5 c_6) \right\} \\ B_{\tau 0}(2,2) &= (M_w + E_w + L_w) c_4 + A_w d_4 c_4 c_5 + J_w c_6 (c_4 c_6 - s_4 c_5 s_6) \\ B_{\tau 0}(2,3) &= I_{6zz} s_4 s_5 \\ B_{\tau 0}(3,1) &= -s_5^2 (K_w + E_w + L_w) - J_w s_5^2 c_6^2 \\ B_{\tau 0}(3,2) &= J_w s_5 s_6 c_6 \\ B_{\tau 0}(3,3) &= I_{6zz} c_5 \end{split} \tag{A-44}$$

A.4 Six Degree of Freedom Anthropomorphic Robot with Wrist

Rotation Matrices

$$R_{1}^{0} = \begin{bmatrix} \cos(\theta_{1}) & 0 & \sin(\theta_{1}) \\ \sin(\theta_{1}) & 0 & -\cos(\theta_{1}) \\ 0 & 1 & 0 \end{bmatrix}$$

$$R_{2}^{1} = \begin{bmatrix} \cos(\theta_{2}) & -\sin(\theta_{2}) & 0 \\ \sin(\theta_{2}) & \cos(\theta_{2}) & 0 \\ 0 & 0 & 1 \end{bmatrix}$$

$$R_{3}^{2} = \begin{bmatrix} \cos(\theta_{3}) & -\sin(\theta_{3}) & 0 \\ \sin(\theta_{3}) & \cos(\theta_{3}) & 0 \\ 0 & 0 & 1 \end{bmatrix}$$

$$R_{4}^{3} = \begin{bmatrix} 0 & -1 & 0 \\ \cos(\theta_{4}) & 0 & \sin(\theta_{4}) \\ -\sin(\theta_{4}) & 0 & \cos(\theta_{4}) \end{bmatrix}$$

$$R_{5}^{4} = \begin{bmatrix} \cos(\theta_{5}) & 0 & \sin(\theta_{5}) \\ \sin(\theta_{5}) & 0 & -\cos(\theta_{5}) \\ 0 & 1 & 0 \end{bmatrix}$$

$$R_{6}^{5} = \begin{bmatrix} \cos(\theta_{6}) & -\sin(\theta_{6}) & 0 \\ \sin(\theta_{6}) & \cos(\theta_{6}) & 0 \\ 0 & 0 & 1 \end{bmatrix}$$
(A-45)

Constants

$$\begin{split} M_{aw} &= m_2 r_2 + (m_3 + m_4 + m_5 + m_6) a_2 \\ N_{aw} &= m_3 r_3 + (m_4 + m_5 + m_6) a_3 + m_4 r_4 + (m_5 + m_6) d_4 \\ O_{aw} &= m_5 r_5 + m_6 d_5 + m_6 r_6 \\ P_{aw} &= m_0 r_0 + d_0 (m_1 + m_2 + m_3 + m_4 + m_5 + m_6) + d_1 (m_2 + m_3 + m_4 + m_5 + m_6) + m_1 r_1 \\ M_{Taw} &= m_0 + m_1 + m_2 + m_3 + m_4 + m_5 + m_6 \end{split} \tag{A-46}$$

Position Vector To CG

$$\mathbf{r}_{CG} = \frac{1}{M_{Taw}} \begin{bmatrix} c_1 (M_{aw}c_2 + N_{aw}c_{23} + O_{aw}c_5c_{23} - O_{aw}c_4s_5s_{23}) - Os_1s_4s_5 \\ s_1 (M_{aw}c_2 + N_{aw}c_{23} + O_{aw}c_5c_{23} - O_{aw}c_4s_5s_{23}) + Oc_1s_4s_5 \\ P_{aw} + M_{aw}s_2 + N_{aw}s_{23} + O_{aw}c_5s_{23} + O_{aw}c_4s_5c_{23} \end{bmatrix}$$
(A-47)

Rigid Interaction Forces

 $B_f =$

$$\begin{bmatrix} -s_{1}\{Mc_{2}+c_{23}(N+Oc_{5})+Os_{23}c_{4}s_{5}\}-Oc_{1}s_{4}s_{5} & c_{1}\{Mc_{2}+c_{23}(N+Oc_{5})-Os_{23}c_{4}s_{5}\}-Os_{1}s_{4}s_{5} & 0 \\ -c_{1}\{Ms_{2}+s_{23}(N+Oc_{5})+Oc_{23}c_{4}s_{5}\} & -s_{1}\{Ms_{2}+s_{23}(N+Oc_{5})+Oc_{23}c_{4}s_{5}\} & c_{2}(M+N+Oc_{5})-Os_{23}c_{4}s_{5} \\ -c_{1}\{s_{23}(N+Oc_{5})+Oc_{23}c_{4}s_{5}\} & -s_{1}\{s_{23}(N+Oc_{5})+Oc_{23}c_{4}s_{5}\} & c_{23}(N+Oc_{5})-Os_{23}c_{4}s_{5} \\ Os_{5}(c_{1}s_{23}s_{4}-s_{1}c_{4}) & Os_{5}(s_{1}s_{23}s_{4}+c_{1}c_{4}) & -Oc_{23}s_{4}s_{5} \\ -O\{c_{1}(c_{23}s_{5}+s_{23}c_{4}c_{5})+s_{1}s_{4}c_{5}\} & O\{-s_{1}(c_{23}s_{5}+s_{23}c_{4}c_{5})+c_{1}s_{4}c_{5}\} & O(c_{23}c_{4}c_{5}-s_{5}s_{23}) \\ 0 & 0 & 0 \end{bmatrix}$$

$$(A-48)$$

Rigid Interaction Coriolis Forces

$$NR_f = \frac{1}{M_{Tow}} *$$

$$\begin{bmatrix} 2s_1\{M_{aw}s_2 + s_{23}(N_{aw} + O_{av}c_5) + O_{av}c_{23}c_4s_5\} & -2c_1\{M_{aw}s_2 + s_{23}(N_{aw} + O_{av}c_5) + O_{av}c_{23}c_4s_5\} & 0 \\ 2s_1\{s_{22}(N_{aw} + O_{av}c_5) + O_{av}c_{23}c_4s_5\} & -2c_1\{s_{23}(N_{aw} + O_{av}c_5) + O_{av}c_{23}c_4s_5\} & 0 \\ -2O_{av}s_5\{s_1s_{23}s_4 + c_1c_4\} & -2O_{av}s_5\{-c_1s_{23}s_4 + s_1c_4\} & 0 \\ 2O_{av}\{s_1(s_5c_{23} + s_{22}c_4c_5) - c_1s_4c_5\} & -2O_{av}\{c_1(c_{23}s_5 + s_{23}c_4s_5) + s_1s_4c_5\} & 0 \\ 0 & 0 & 0 \\ 2c_1\{-c_{23}(N_{aw} + O_{av}c_5) + O_{av}s_{23}c_4s_5\} & 2s_1\{-c_{23}(N_{aw} + O_{av}c_5) + O_{av}s_{23}c_4s_5\} & -2\{s_{23}(N_{aw} + O_{av}c_5) + O_{av}c_{23}c_4s_5\} \\ 2O_{av}s_1c_{23}s_4s_5 & 2O_{av}s_1c_{23}s_4s_5 & 2O_{av}s_2c_4s_5\} \\ -2O_{av}c_1\{-s_{23}s_5 + c_{23}c_4c_5\} & -2O_{av}s_1\{-s_{23}s_5 + c_{23}c_4c_5\} & -2O_{av}s_1s_2s_4c_5\} \\ 0 & 0 & 0 \\ 2O_{av}c_1\{-s_{23}s_5 + c_{23}c_4c_5\} & -2O_{av}s_1\{-s_{23}s_5 + c_{23}c_4c_5\} & -2O_{av}s_1s_2s_4c_5\} \\ -2O_{av}c_1\{-s_{23}s_5 + c_{23}c_4c_5\} & -2O_{av}s_1\{-s_{23}s_5 + c_{23}c_4c_5\} & -2O_{av}s_1s_2s_5c_4c_5\} \\ 0 & 0 & 0 \\ -2O_{av}c_1\{-s_{23}s_5 + c_{23}c_4c_5\} & -2O_{av}s_1\{-s_{23}s_5 + c_{23}c_4c_5\} & -2O_{av}s_2s_3s_4s_5 \\ -2O_{av}c_1\{-s_{23}s_5 + c_{23}c_4c_5\} & -2O_{av}s_1\{-s_{23}s_5 + c_{23}c_4c_5\} & -2O_{av}s_2s_3s_4s_5 \\ -2O_{av}c_1\{-s_{23}s_5 + c_{23}c_4c_5\} & -2O_{av}s_1\{-s_{23}s_5 + c_{23}c_4c_5\} & -2O_{av}s_2s_3s_4s_5 \\ -2O_{av}c_1\{-s_{23}s_5 + c_{23}c_4c_5\} & -2O_{av}s_1\{-s_{23}s_5 + c_{23}c_4c_5\} & -2O_{av}s_2s_3s_4s_5 \\ -2O_{av}c_1\{-s_{23}s_5 + c_{23}c_4c_5\} & -2O_{av}s_1\{-s_{23}s_5 + c_{23}c_4c_5\} & -2O_{av}s_2s_3s_4s_5 \\ -2O_{av}c_1\{-s_{23}s_5 + c_{23}c_4c_5\} & -2O_{av}s_2s_3s_4s_5 \\ -2O_{av}c_2\{s_3s_4 + s_1c_4\} & -2O_{av}c_2s_3s_4c_5 \end{bmatrix}$$

Rigid Interaction Centrifugal Forces

$$\begin{split} NC_{f}(1,1) &= \frac{1}{M_{Taw}} *c_{f}c_{4}s_{5} \{-M_{au}c_{2} - c_{22}(N_{av} + O_{au}c_{2}) + O_{au}s_{23}\} + O_{av}s_{1}s_{4}s_{5} \\ NC_{f}(1,2) &= \frac{1}{M_{Taw}} *c_{1} \{-M_{au}c_{2} - c_{23}(N_{aw} + O_{au}c_{5}) + O_{au}s_{22}c_{4}s_{5}\} \\ NC_{f}(1,3) &= \frac{1}{M_{Taw}} *c_{1} \{-c_{23}(N_{aw} + O_{au}c_{5}) + O_{au}s_{22}c_{4}s_{5}\} \\ NC_{f}(1,4) &= \frac{1}{M_{Taw}} *\{O_{av}(c_{1}s_{2}c_{4} + s_{1}s_{4})\} \\ NC_{f}(1,5) &= \frac{1}{M_{Taw}} *\{S_{1}[-M_{au}c_{2} - c_{23}(N_{aw} + O_{au}c_{5}) + O_{au}s_{22}c_{4}s_{5}] - Oc_{1}s_{4}s_{5} \\ NC_{f}(2,1) &= \frac{1}{M_{Taw}} *\{S_{1}[-M_{au}c_{2} - c_{23}(N_{aw} + O_{au}c_{5}) + O_{au}s_{22}c_{4}s_{5}] - Oc_{1}s_{4}s_{5} \\ NC_{f}(2,2) &= \frac{1}{M_{Taw}} *\{S_{1}[-M_{au}c_{2} - c_{23}(N_{aw} + O_{au}c_{5}) + O_{au}s_{22}c_{4}s_{5}] \\ NC_{f}(2,3) &= \frac{1}{M_{Taw}} *\{O_{au}s_{5}(s_{1}s_{2}c_{4} - c_{1}s_{4}) \\ NC_{f}(2,4) &= \frac{1}{M_{Taw}} *\{O_{au}s_{5}(s_{1}s_{2}c_{4} - c_{1}s_{4}) \\ NC_{f}(2,5) &= \frac{1}{M_{Taw}} *\{O_{au}s_{5}(s_{1}s_{2}c_{4} - c_{1}s_{4}) \\ NC_{f}(2,5) &= \frac{1}{M_{Taw}} *\{O_{au}s_{5}(s_{1}s_{2}c_{4} - c_{1}s_{4}) \\ NC_{f}(3,1) &= 0 \\ NC_{f}(3,1) &= 0 \\ NC_{f}(3,3) &= \frac{1}{M_{Taw}} *\{-s_{23}(N_{au} + O_{au}c_{5}) + O_{au}c_{25}c_{4}s_{5}\} \\ NC_{f}(3,5) &= \frac{1}{M_{Taw}} *\{-c_{23}(N_{au} + O_{au}c_{5}) + O_{au}c_{25}c_{4}s_{5}\} \\ NC_{f}(3,5) &= \frac{1}{M_{Taw}} *\{-c_{23}(N_{au} + O_{au}c_{5}) + O_{au}c_{25}c_{4}s_{5}\} \\ NC_{f}(3,5) &= \frac{1}{M_{Taw}} *\{-c_{23}(N_{au} + O_{au}c_{5}) + O_{au}c_{25}c_{4}s_{5}\} \\ NC_{f}(3,5) &= \frac{1}{M_{Taw}} *\{-c_{23}(N_{au} + O_{au}c_{5}) + O_{au}c_{25}c_{4}s_{5}\} \\ NC_{f}(3,5) &= \frac{1}{M_{Taw}} *\{-c_{23}(N_{au} + O_{au}c_{5}) + O_{au}c_{25}c_{4}s_{5}\} \\ NC_{f}(3,5) &= \frac{1}{M_{Taw}} *\{-c_{23}(N_{au} + O_{au}c_{5}) + O_{au}c_{5}c_{5}s_{5}\} \\ NC_{f}(3,5) &= \frac{1}{M_{Taw}} *\{-c_{23}(N_{au} + O_{au}c_{5}c_{5}s_{5}\} \\ NC_{f}(3,5) &= \frac{1}{M_{Taw}} *\{-c_{23}(N_{au} + O_{au}c_{5}s_{5}) + O_{au}c_{5}s_{5}\} \\ NC_{f}(3,5) &= \frac{1}{M_{Taw}} *\{-c_{23}(N_{au} + O_{au}c_{5}s_{5}) + O_{au}c_{5}s_{5}\} \\ NC_{f}(3,5) &= \frac{1}{M_{Taw}} *\{-c_{23}(N_{au} + O_{au}c_{5}s$$

REFERENCES

- [1] ATI Industrial Automation. *Installation and Operations Manual for Stand-Alone F/T Sensor Systems: Intelligent MultiAxis Force/Torque Sensor System.* Manual PN 9610-05-1001-14, Software Version 5.0, 2000.
- [2] Ballhaus, W.L., and S.M. Rock. "End-Point Control of a Two-Link Flexible Robotic Manipulator with a Mini-Manipulator: Initial Experiments." *Proceedings of the 1992 American Control Conference (IEEE)*. Vol. 3, pp. 2510-14, Chicago, IL, June 24-26, 1992.
- [3] Banerjee, Arun K. "Dynamics and Control of the WISP Shuttle-Antennae System." *Journal of the Astronautical Sciences*. Vol. 41, No. 1, pp. 73-90, Jan Mar 1993.
- [4] Bayo, E. and H. Moulin. "An Efficient Computation of the Inverse Dynamics of Flexible Manipulators in the Time Domain." *Proceedings of the IEEE Conference on Robotics and Automation.* pp. 710-715, 1989.
- [5] Bendat, Julius S. and Allan G. Piersol. *Engineering Applications of Correlation and Spectral Analysis*. New York: John Wiley and Sons, 1980.
- [6] Bevington, Philip R. and D. Keith Robinson. *Data Reduction and Error Analysis for the Physical Sciences*. Second Edition. Boston: WCB McGraw-Hill, 1992.
- [7] Biesel, Van. Matlab M-files "impactfrf.m" and "fftInOut.m" for signal processing of acclerometer data, November 2000.
- [8] Book, Wayne J. "Recursive Lagrangian Dynamics of Flexible Manipulator Arms." *The International Journal of Robotics Research.* Vol. 3, No. 3, pp. 87-101, Fall 1984.
- [9] Book, Wayne J. "Controlled Motion in an Elastic World (Final Report). Research

Project: Manipulation Strategies for Massive Space Payloads, November 15, 1989 – December 15, 1992." NASA-CR-191895, Georgia Institute of Technology, Atlanta, GA, 1992.

- [10] Book, Wayne J. "Controlled Motion in an Elastic World." *Transactions of the ASME Journal of Dynamic Systems, Measurement, and Control.* Vol. 115, No. 2B, pp. 252-261, June 1993.
- [11] Book, Wayne J. and Soo Han Lee. "Vibration Control of a Large Flexible Manipulator by a Small Robotic Arm." *Proceedings of the 1989 American Control Conference*. Vol. 2, pp. 1377-1380, Pittsburgh, PA, June 21-23, 1989.
- [12] Book, Wayne J. and Jeffery Cameron Loper. "Inverse Dynamics for Commanding Micromanipulator Inertial Forces to Damp Macromanipulator Vibration." *Proceedings of the 1999 IEEE Robot Society of Japan International Conference on Intelligent Robots and Systems, Human and Environment Friendly Robots with High Intelligence and Emotional Quotients.* Vol. 2, pp. 707-714, Kyongiu, Korea, October 17-21, 1999.
- [13] Book, Wayne and Klaus Obergfell. "Practical Models for Practical Flexible Arms." *Proceedings of the 2000 IEEE International Conference on Robotics and Automation Millennium Conference*. Vol. 1, pp. 835-842, San Francisco, CA, April 24-28, 2000.
- [14] Bradbury, Farel. *Hydraulic Systems and Maintenance*. New York: Von Nostand Reinhold, 1972.
- [15] Cannon, David Wayne. *Command Generation and Inertial Damping Control of Flexible Macro-Micro Manipulators*. Master of Science Thesis, Department of Mechanical Engineering, Georgia Institute of Technology, Atlanta, GA, 1996.
- [16] Cannon, David W., David P. Magee, Wayne J. Book, and Jae Y. Lew. "Experimental Study on Micro/Macro Manipulator Vibration Control." *Proceedings of the 1996 IEEE International Conference on Robotics and Automation*. Vol. 3, pp. 2549-2554, Minneapolis, MN, April 1996.
- [17] Cheney, Ward and David Kincaid. *Numerical Mathematics and Computing*. Second Edition. Monterey, CA:Brooks/Cole Publishing Company, 1985.

- [18] Craig, John J. *Introduction to Robotics: Mechanics and Control*. Reading, MA: Addison-Wesley. 1988.
- [19] Devasia, Santosh and Eduardo Bayo. "Inverse Dynamics of Articulated Flexible Structures: Simultaneous Trajectory Tracking and Vibration Reduction." *Journal of Dynamics and Control*. Vol. 4, No. 3, pp 299-309, 1994.
- [20] Doty, Keith L. "An Essay on the Application of Weighted Generalized-Inverses in Robotics." 5th Conference on Recent Advances in Robotics. Florida Atlantic University, Boca Raton, FL June 11-12, 1992.
- [21] Etter, Delores E. *Engineering Problem Solving with Matlab*. Second Edition. Upper Saddle River, NJ: Prentice Hall, 1997.
- [22] Featherstone, Roy. *Robot Dynamics Algorithms*. Boston: Kluwer Academic Press, 1987.
- [23] Friedland, Bernard. *Control System Design: An Introduction to State-Space Methods*. New York: McGraw-Hill Book Company, 1986.
- [24] Ginsberg, Jerry H. *Mechanical and Structural Vibration: Theory and Applications, Chapters 1-9.* Draft copy for Spring 2000 ME 6442 Mechanical Vibrations course, G.W. Woodruff School of Mechanical Engineering, Georgia Institute of Technology, Atlanta, GA, 2000.
- [25] Glassell, R.L., B.L. Burks, and W.H. Glover. "System Review of the Modified Light Duty Utility Arm After the Completion of the Nuclear Waste Removal From Seven Underground Storage Tanks at Oak Ridge National Laboratory." The Providence Group, Knoxville, TN, 2000.
- [26] Hibbeler, R.C. *Mechanics of Materials*. 3rd Edition. Upper Saddle River, NJ: Prentice Hall, 1997.

- [27] IBM Corporation. IBM 7565 Manufacturing System Archived data, news release, and technical information. Advanced Manufacturing Systems, Boca Raton, FL, 1983.
- [28] Jiang, Zhao Hui. "Dynamic Manipulation Characteristics of Robot Arms Mounted on a Flexible Space Structure." *Automatic Control in Aerospace, Proceedings Volume from the 14th International Federation of Automatic Control (IFAC) Symposium.* pp. 89-94, 1999.
- [29] Kernigham, Brian W. and Dennis M. Ritchie. *The C Programming Language*, Englewood Cliffs, NJ: Prentice-Hall, 1978.
- [30] Kuc, Roman. *Introduction to Digital Signal Processing*. New York: McGraw Hill, 1988.
- [31] Kwon, Dong-Soo, and Wayne J. Book. "A Time-Domain Inverse Dynamic Tracking Control of a Single-Link Flexible Manipulator." *Transactions of the ASME Journal of Dynamic Systems, Measurement, and Control.* Vol. 116, No. 2, pp. 193-200, June 1994.
- [32] Lee, Soo Han. *Robust Control of a Flexible Link Robot and Rigid Link Robot: Theory, Simulation, and Experiment.* Ph.D. Dissertation, Department of Mechanical Engineering, Georgia Institute of Technology, Atlanta, GA, March 1992.
- [33] Lee, Soo Han and Wayne J. Book. "Robot Vibration Control Using Inertial Damping Forces." *Proceedings of the VIII International Centre for Mechanical Sciences-International Federation for the Theory of Machines and Mechanisms (CISM-IFToMM) Symposium on the Theory and Practice of Robots and Manipulators.* pp. 252-259, Cracow, Poland, July 2-6, 1990.
- [34] Lew, Jae Young. *Control of Bracing Micro/Macro manipulators*. Ph.D. Dissertation, Department of Mechanical Engineering, Georgia Institute of Technology, Atlanta, GA, 1993.
- [35] Lew, Jae Y. and S.M. Moon. "Acceleration Feedback Control of Compliant Base Manipulators." *Proceedings of the 1999 American Control Conference*. Vol. 3, pp. 1955-1959, San Diego, CA, June 1999.

- [36] Lew, Jae Y. and Suk-Min Moon. "Active Damping Control of Compliant Base Manipulators." *Proceedings of the 1999 IEEE/RSJ International Conference on Intelligent Robots and Systems.* pp. 812-817, Kyongiu, Korea, October 1999.
- [37] Lew, Jae Young and Suk-Min Moon. "Experimental Study of Compliant Base Manipulator Control." *Proceedings of the 38th IEEE Conference on Decision and Control.* pp. 2969-2973, Phoenix, AZ, December 1999.
- [38] Lew, Jae Young and Suk-Min Moon. "A Simple Active Damping Control for Compliant Base Manipulators." *ASME/IEEE Transactions on Mechatronics*. Vol. 6, No. 3, pp. 305-310, 2001.
- [39] Lew, Jae Y. and Dan J. Trudnowski. "Vibration Control of a Micro/Macro Manipulator System." *IEEE Control Systems*. Vol. 16, No. 1, pp. 26-31, February 1996.
- [40] Lew, Jae Y., Dan J. Trudnowski, Mark S. Evans, and David W. Bennett. "Micro Manipulator Motion Control to Suppress Macro Manipulator Structural Vibrations." *Proceedings of the 1999 IEEE International Conference on Robotics and Automation*. Vol. 3, pp. 3116-3120, Nagoya, Japan, May 24-26, 1995.
- [41] Longman, Richard W. "Tutorial Overview of the Dynamics and Control of Satellite-Mounted Robots." *Teleoperation and Robotics in Space*. Progress in Astronautics and Aeronautics, Vol. 161, Eds. Steven B. Skaar and Carl F. Ruoff, Washington, D.C: American Institute of Aeronautics and Astronautics, pp. 237-258, 1994.
- [42] Loper, Jeffery Cameron. Vibration Cancellation and Disturbance Rejection in Serially Linked Micro/Macro Manipulators. Master of Science Thesis, Department of Mechanical Engineering, Georgia Institute of Technology, Atlanta, GA, March 1998.
- [43] Loper, J.C. "samii test.c" code, May, 1997.
- [44] MacKenzie, I. Scott. *The 68000 Microprocessor*. Englewood Cliffs, NJ: Prentice Hill, 1995.

- [45] Magee, David P. and Wayne J. Book. "Filtering Micro-Manipulator Wrist Commands to Prevent Flexible Base Motion." *Proceedings of the 1995 American Control Conference*. Vol. 1, pp. 924-928, Seattle, WA, June 21-23, 1995.
- [46] Mayes, Randall L. and G. Richard Eisler. "Experimental Characterization of a Flexible Two-link Manipulator Arm." *ASME Vibrations and Dynamics of Robotics and Multibody Structures*, DE-Vol 57, 1993.
- [47] McGill, David J. and Wilton W. King. *Engineering Mechanics: An Introduction to Dynamics*. 3rd Edition. Boston: PWS Publishing Company, 1995.
- [48] McKerrow, Phillip John. *Introduction to Robotics*. Sydney: Addison-Wesley. 1991.
- [49] Meirovitch, Leonard. *Elements of Vibration Analysis*. Second Edition. Boston, MA: McGraw Hill. 1986.
- [50] Merritt, Herbert E. Hydraulic Control Systems. John Wiley and Sons, 1967.
- [51] Moog, Flow Control Servovalves 30 and 30 Series Data Sheets, 2002.
- [52] Nataraj, C. "Flexibility Effects in a Single Link Robotic Manipulator." Vibrations and Dynamics of Robotic and Multibody Structures. ASME DE-Vol. 57, 1993.
- [53] Obergfell, Klaus. *End-Point Sensing and Control of Flexible Multi-Link Manipulators*. Ph.D. Dissertation, Department of Mechanical Engineering, Georgia Institute of Technology, Atlanta, GA, August 1998.
- [54] Ogata, Katsuhiko. *Discrete-Time Control Systems*. Englewood Cliffs, NJ: Prentice Hall, 1987.
- [55] Ogata, Katsuhiko. Modern Control Engineering. Third Edition. Upper Saddle

- River, NJ: Prentice-Hall, 1997.
- [56] Papadopoulos, Evangelos and Steven Dubowsky. "Dynamic Singularities in Free-Floating Space Manipulators." *Space Robotics: Dynamics and Control*. Eds. Y. Xu and T. Kanade, Norwell, MA: Kluwer Academic Publishers, pp. 77-100, 1993.
- [57] PCB Piezotronics. Specifications for Voltage Output Accelerometer Model 303 and 308.
- [58] Raab, F. J. and D. J. Trudnowski. "Experiments in Two-Axis Vibration Damping Using Inertial Torques Through Momentum Wheel Control." *Proceedings of the 1998 American Control Conference*. Vol. 6, pp. 3477-3481, Philadelphia, PA, June 1998.
- [59] Rao, Singiresu S. Mechanical Vibrations. Reading, MA: Addison-Wesley, 1986.
- [60] Schwartz, Eric M., Rachid Manseur, and Keith L. Doty. "Algebraic Properties of Noncommensurate Systems." *1999 Florida Conference on Recent Advances in Robotics*. April 29-30, 1999.
- [61] Sciavicco, Lorenzo and Bruno Siciliano. *Modeling and Control of Robot Manipulators*. Second Edition. London: Springer-Verlag, 2000.
- [62] Senda, Kei. *Dynamics and Control of Rigid/Flexible Space Manipulators*. Ph.D. Dissertation, Department of Aerospace Engineering, College of Engineering, University of Osaka Prefecture, Sakai, Osaka, Japan, 1993.
- [63] Sharf, I. "Active Damping of a Large Flexible Manipulator with a Short-Reach Robot." *Proceedings of the 1995 American Control Conference*. Vol. 5, pp. 3329-3333, Seattle, WA, June 21-23, 1995.
- [64] Sharon, Andre, Neville Hogan, and David E. Hardt. "The Macro/Micro Manipulator: An Improved Architecture for Robot Control." *Robotics and Computer-Integrated Manufacturing.* Vol. 10, No. 3, pp. 209-222, 1993.

- [65] Sharon, Andre, Neville Hogan, and David E. Hardt. "High Bandwidth Force Regulation and Inertia Reduction Using a Macro/Micro Manipulator System." *Proceedings of the IEEE Conference on Robotics and Automation.* pp. 126-132, May 1988.
- [66] Shearman, Sam. "Signal Processing Eases Vibration Transducer Selection." National Instruments Developer Zone Development Library, Analysis and Signal Processing, Signal Processing, National Instruments Corportation, 2002.
- [67] Sickle, Ted Van. *Programming Microcontrollers in C*, Solana Beach, CA: HighText Publication Inc., 1994
- [68] Singer, N.C. and W.P. Seering. "Preshaping Command Inputs to Reduce System Vibration," *ASME Journal of Dynamic Systems, Measurement, and Control*, Vol 112, pp. 76-82, March 1990.
- [69] Singh S.N. and A. A. Schy. "Control of Elastic Robotic Systems by Nonlinear Inversion and Modal Damping." *ASME Journal of Dynamic Systems Measurement and Control.* Vol. 108, No. 3, pp. 180-189, September 1986.
- [70] Singhose, William, Neil Singer, and Warren Seering. "Comparison of Command Shaping Methods for Reducing Residual Vibration." *Proceedings of the 1995 European Control Conference*. Vol. 2, pp. 1126-1131, 1993.
- [71] Singhose, William and Neil Singer. "Initial Investigations into the Effects of Input Shaping on Trajectory Following." *Proceedings of the 1994 American Control Conference*. Baltimore, MD, 1994.
- [72] Smart, David W. and Gloria J. Wiens. "Effect of Gravity on the Static and Dynamic Characteristics of a Single Link Component of Flexible Multibody Systems." *ASME Vibrations and Dynamics of Robotic and Multibody Structures*. DE-Vol. 57, 1993.
- [73] Strang, Gilbert. *Introduction to Linear Algebra*. Second edition. Wellesley, MA: Wellesley-Cambridge Press, 1998.
- [74] Tao, Gang, and Petar V. Kokotovic. Adaptive Control of Systems with Actuator and

Sensor Nonlinearities. New York: Wiley, 1996.

- [75] Thayer, W.J. "Transfer Functions for Moog Servovalves." Technical Bulleting 103. Moog Inc. Controls Division, East Aurora, NY, 1965.
- [76] Thayer, William J. "Specification Standards for Electrohydraulic Flow Control Servovalves." Technical Bulletin 117. Moog Inc. Controls Division, East Aurora, NY, June 1962.
- [77] Torres, Miguel A. and Steven Dubowsky. "Path Planning for Elastically Constrained Space Manipulator Systems." *Proceedings of the IEEE International Conference on Robotics and Automation*. Vol. 1, pp. 812-817, Atlanta, GA, May 2-7, 1993.
- [78] Torres, Miguel A., Steven Dubowsky, and Attilio C. Pisoni. "Path-Planning for Elastically-Mounted Space Manipulators: Experimental Evaluation of the Coupling Map." *Proceedings of the 1994 IEEE International Conference on Robotics and Automation.* pp. 2227-2233, San Diego, CA, May 1994.
- [79] Torres, Miguel A., Steven Dubowsky, and Attilio C. Pisoni. "Vibration Control of Deployment Structures' Long-Reach Space Manipulators: The P-PED Method." *Proceedings of the 1996 IEEE International Conference on Robotics and Animation*. Vol. 3, pp. 2498 2504, Minneapolis, MN, April 1996.
- [80] Vliet, Christopher John Van. *Predicted and Observed Active Damping Performance of Macro-Micro Manipulators*. Master of Applied Science Thesis, Department of Mechanical Engineering, University of Victoria, 1995.
- [81] Vliet, John Van and Inna Sharf. "A Frequency Matching Algorithm for Active Damping of Macro-Micro Manipulator Vibrations." *Proceedings of the 1998 IEEE/Robotics Society of Japan (RSJ) International Conference on Intelligent Robots and Systems.* Vol. 2, pp. 782-787, Victoria, B.C., Canada, October 1998.
- [82] Walters, R.B. *Hydraulic and Electrohydraulic Control Systems*. London: Elsevier Applied Science, 1991.

- [83] Weaver. W., Jr., S.P. Timoshenko, and D.H. Young. *Vibration Problems in Engineering*. Fifth Edition, NY: John Wiley and Sons, 1990.
- [84] Wilson, D.W., Boulanger, R.W., and Kutter, B.L. "Signal Processing for and Analysis of Dynamic Soil-Pile Interaction Experiments." *Proceedings, Centrifuge* 98. Kumura, Kusakabe, and Takemura, Eds. Balkema, Rotterdam, pp. 135-140, 1998.
- [85] Wind River Systems. VxWorks Programmer's Guide. Version 5.2, 1995.
- [86] Wind River Systems. VxWorks Reference Manual. Version 5.2, 1995.
- [87] Xie, H.P., S. Kalaycioglu, and R.V. Patel. "Control of Residual Vibrations in the Space Shuttle Remote Manipulator System." *International Journal of Robotics and Automation*. Vol. 15, No. 2, pp. 68-77, 2000.
- [88] Xu, Yangsheng and Heung-Yeung Shum. "Dynamic Control and Coupling of a Free-Flying Space Robotic System." *Journal of Robotic Systems*. Vol. 11, No. 7, pp. 573-589, 1994.
- [89] Yim, Woosoon and Sahjendra N. Singh. "Trajectory Control of Flexible Manipulator Using Macro-Micro Manipulator System." *Proceedings of the 34th Conference on Decision and Control*. pp. 2841-2846, New Orleans, LA, 1995.
- [90] Yim, Woosoon and Sahjendra N. Singh. "Nonlinear Inverse and Predictive End Point Trajectory Control of Flexible Macro-Micro Manipulators." *Proceedings of the 13th World Congress, International Federation of Automatic Control Vol. A: Robotics, Components, and Instruments.* pp. 97-102, San Francisco, CA, 1996.
- [91] Yim, W. and S.N. Singh. "Trajectory Control of Flexible Manipulator Using Rigid Micromanipulator System." *International Journal of Robotics and Automation*. Vol. 12, No. 3, pp. 93-99, 1997.
- [92] Yoshida, Kazuya and Dragomir N. Nenchev. "A General Formulation of Under-Actuated Manipulator Systems." *Robotics Research: The Eighth International*

Symposium. Edited by Y. Shirai and S. Hirose. London: Springer-Verlag, pp. 33-44, 1998.

[93] Yoshida, Kazuya, Dragomir N. Nenchev, and Masaru Uchiyama. "Vibration Suppression and Zero Reaction Maneuvers of Flexible Space Structure Mounted Manipulators." *Smart Materials and Structures*, Vol. 8, No. 6, pp. 847-856, December 1999.

[94] Yoshikawa, Tsuneo, Koh Hosoda, Toshitsugu Doi, and Hiroki Murakami. "Dynamic Trajectory Tracking Control of Flexible Manipulator by Macro-Micro Manipulator System." *Proceedings of the 1994 IEEE International Conference on Robotics and Automation.* Vol. 3, pp. 1804-1809, San Diego, CA, May 1994.

VITA

Lynnane George was born Joyce Lynnane Ellis in Decatur, Georgia on 25 October, 1966. She graduated from Newnan High in Newnan, Georgia in 1984. She attended Georgia Tech on an Air Force ROTC scholarship, where she graduated with High Honor with her B.S. in Mechanical Engineering on 2 September 1988. She stayed at Georgia Tech to complete her M.S. in Mechanical Engineering with a concentration in dynamics and control systems on 1 September 1989 and married on 2 September 1989. She then went on active duty in the U.S. Air Force, where she worked on the Titan IV launch vehicle, among other programs, at Los Angeles Air Force Base, CA from 1989 through 1995. Lynnane then went to Colorado Springs where she taught in the Department of Astronautics at the U.S. Air Force Academy from 1995 – 1999. When she is not studying engineering or working for the Air Force, Lynnane enjoys practicing karate and reading.